

**USE OF COMPUTATIONAL FLUID DYNAMICS IN THE  
DESIGN OF BUBBLE COLUMN REACTORS**

**GREGORY MARTIN CARTLAND GLOVER**

**Doctor of Philosophy**

**THE UNIVERSITY OF ASTON IN BIRMINGHAM**

**July 2008**

This copy of the thesis has been supplied on condition that anyone who consults it is understood to recognise that its copyright rests with its author and that no quotation from the thesis and no information derived from it may be published without proper acknowledgement.

# **Thesis Summary**

**THE UNIVERSITY OF ASTON IN BIRMINGHAM**

**USE OF COMPUTATIONAL FLUID DYNAMICS IN THE DESIGN OF BUBBLE  
COLUMN REACTORS**

**GREGORY MARTIN CARTLAND GLOVER**

**Doctor of Philosophy**

**July 2008**

Investigations into the modelling techniques that depict the transport of discrete phases (gas bubbles or solid particles) and model biochemical reactions in a bubble column reactor are discussed here. The mixture model was used to calculate gas-liquid, solid-liquid and gas-liquid-solid interactions.

Multiphase flow is a difficult phenomenon to capture, particularly in bubble columns where the major driving force is caused by the injection of gas bubbles. The gas bubbles cause a large density difference to occur that results in transient multi-dimensional fluid motion. Standard design procedures do not account for the transient motion, due to the simplifying assumptions of steady plug flow. Computational fluid dynamics (CFD) can assist in expanding the understanding of complex flows in bubble columns by characterising the flow phenomena for many geometrical configurations. Therefore, CFD has a role in the education of chemical and biochemical engineers, providing the examples of flow phenomena that many engineers may not experience, even through experimentation.

The performance of the mixture model was investigated for three domains (plane, rectangular and cylindrical) and three flow models (laminar, k- $\epsilon$  turbulence and the Reynolds stresses). This investigation raised many questions about how gas-liquid interactions are captured numerically. To answer some of these questions the analogy between thermal convection in a cavity and gas-liquid flow in bubble columns was invoked. This involved modelling the buoyant motion of air in a narrow cavity for a number of turbulence schemes. The difference in density was caused by a temperature gradient that acted across the width of the cavity. Multiple vortices were obtained when the Reynolds stresses were utilised with the addition of a basic flow profile after each time step.

To implement the three-phase models an alternative mixture model was developed and compared against a commercially available mixture model for three turbulence schemes. The scheme where just the Reynolds stresses model was employed, predicted the transient motion of the fluids quite well for both mixture models. Solid-liquid and then alternative formulations of gas-liquid-solid model were compared against one another. The alternative form of the mixture model was found to perform particularly well for both gas and solid phase transport when calculating two and three-phase flow. The improvement in the solutions obtained was a result of the inclusion of the Reynolds stresses model and differences in the mixture models employed. The differences between the alternative mixture models were found in the volume fraction equation (flux and deviatoric stress tensor terms) and the viscosity formulation for the mixture phase.

A biochemical reaction was then realized by modelling the transport of chemical species through the consumption of a substrate, the formation of a product and the growth of a cell culture. The cell culture was represented by the volume fraction equation for the solid phase with an extra term that predicted the increase in the solid fraction caused by cell growth. Gradients in the gas and solid fractions were observed over the height of the columns modelled, this influenced the location of the greatest rates of cell growth, product formation and substrate consumption. A gradient for the vertical velocity over the height of the columns was also observed that implied a gradient in the shear rate, which influences how the cell culture grows. To improve the biochemical reaction model studies into interphase mass transfer, the influence of shear rate and consideration of various stages of the culture life cycle are essential for further understanding to be gained for flow phenomena in bubble column reactors.

## **Dedication**

This thesis is dedicated to the memory of my grandparents Catherine Gibbs (1910-2000), John Harrison (1915-1999) who passed away during my PhD studies and Dr Jindrich Zahradnik (1944-1999), a distinguished project partner. I would also like to thank the support of my family and friends.

## **Acknowledgements**

I would like to acknowledge the following:

Dr Sotos Generalis who as my supervisor provided kind support and encouragement.

Inco-copernicus funded (ERB N° IC15-CT98-0904) programme to further the understanding of bubbling bed reactors (including bubble columns and air-lift reactors) in terms of the application to further understanding of the production of foods in aerobic biochemical reactors. The partners in this programme were the Czech Academy of Sciences, the Slovak Technical University, the University of Minho and Aston University between January 1999 and October 2001.

Dr Jindrich Zahradnik and Dr Marek Ruzicka at the Institute of Chemical Process Fundamentals, the Czech Academy of Sciences (Prague, Czech Republic), where experimental investigations into the hydrodynamics of bubbling beds were performed. I visited Prague for the CHISA 2000 conference, where a group meeting was held to discuss progress in the project (27/8/2000 to 31/8/2000).

Prof. Jozef Markoš at the Institute of Biochemical Engineering, the Slovak Technical University (Bratislava, Slovak Republic) performing studies of the biochemical production of food additives from flocculating micro-organisms. I visited the Institute twice, the first time (19/5/1999 to 21/5/1999) to see the equipment at the department and the second time for one month (30/1/2001 to 8/3/2001) to gain valuable experimental experience with the operation of airlift reactors. I would like to thank Ing. Michal Blazej for organising the experimental programme, to learn more about the hydrodynamics of airlift reactors. Two group meetings were also attended to discuss the project with group members (28/5/1999 and 26/5/2000). Ing. Michal Blazej visited Aston University between September and December 2001 to learn about the modelling of gas-liquid flows in airlift reactors using computational fluid dynamics.

Prof Jose Teixeira at the Department of Biological Engineering, University of Minho (Braga, Portugal) who studied the biochemical production of food additives from microorganisms inoculated onto support beads. I visited the Department for a group meeting (13/04/2000 to 16/04/2000). Other group meetings I attended were held at the Fourth International

Conference on Gas-Liquid-Solid Flows at Delft Technical University, The Netherlands (23/8/1999-25/8/1999) and the Third European Congress of Chemical Engineering (26/6/2001-28/6/2001).

Fluent Europe Ltd for providing the software and support, enabling the simulation of the flow phenomena in bubble column reactors. Dr Neale Thomas of FRED Ltd for valuable advice on multiphase flows and I would also wish to thank Craig Sivitar of Purac Limited and Andrew Lawson of Amchem Group Limited who helped to fund the continuation of the project.

Signed:

Dated:

## List of Contents

<b>1.0</b>	<b>INTRODUCTION</b>	<b>16</b>
1.1	Biochemical reactors: the need for research	16
1.2	Computational fluid dynamics	18
<b>2.0</b>	<b>RESEARCH STRATEGY</b>	<b>20</b>
2.1	Project statement	20
2.2	Aims	20
2.3	Simulation tactics	20
2.4	Equipment employed	21
<b>3.0</b>	<b>GAS-LIQUID FLOW MODELLING IN BUBBLE COLUMNS</b>	<b>23</b>
3.1	Plan	23
3.2	Mathematical models	23
3.3	Modelling parameters	29
3.4	Results and discussion	33
3.5	Conclusions	38
<b>4.0</b>	<b>MODELLING TURBULENT BUOYANCY DRIVEN FLOWS</b>	<b>40</b>
4.1	Plan	40
4.2	Mathematical models	40
4.3	Model parameters	44
4.4	Results and discussion	49
4.5	Conclusions	55
<b>5.0</b>	<b>GAS-LIQUID-SOLID FLOW MODELLING IN BUBBLE COLUMNS</b>	<b>57</b>
5.1	Plan	57
5.2	Mathematical models	58
5.3	Model parameters	59
5.4	Results and discussion	63
5.5	Conclusions	70
<b>6.0</b>	<b>A SIMPLE BIOCHEMICAL REACTION</b>	<b>72</b>
6.1	Plan	72
6.2	Mathematical models	74
6.3	Model parameters	77
6.4	Results and discussion	81
6.5	Conclusions	85
<b>7.0</b>	<b>CONCLUSIONS</b>	<b>87</b>
7.1	Current investigations	87
7.2	Further investigations	91
<b>8.0</b>	<b>LIST OF REFERENCES</b>	<b>93</b>
<b>9.0</b>	<b>NOMENCLATURE</b>	<b>99</b>
9.1	Model equations	99
9.2	User-defined functions	103
<b>10.0</b>	<b>APPENDIX 1: FLOW AND REACTION MODELS</b>	<b>111</b>
10.1	Mixture model equations	111
10.2	Two fluid model equations	112
10.3	Discrete phase model equations	113
10.4	Turbulence transport equations	114
10.5	Thermal convection equations	116
10.6	Scalar equations	117
10.7	Biochemical reaction equations	118

<b>11.0</b>	<b>APPENDIX 2: SOURCE CODE FOR USER-DEFINED FUNCTIONS</b>	<b>121</b>
11.1	Lateral convection in a high aspect ratio cavity	121
11.2	Gas-liquid flow using a scalar transport equation	122
11.3	Gas-liquid-solid flow and reaction using four scalar transport equations	125
<b>12.0</b>	<b>APPENDIX 3: CASE SPECIFICATIONS</b>	<b>131</b>
12.1	Physical properties	131
12.2	User defined functions	132
12.3	Domain specifications	135
12.4	Solver specifications	139
<b>13.0</b>	<b>APPENDIX 4: RESULTS</b>	<b>158</b>
13.1	Gas-liquid results	158
13.2	Turbulence modelling of buoyancy driven flows results	170
13.3	Gas-liquid-solid flow results	180
13.4	Biochemical reaction results	195

## List of Figures

Figure 1: Reactors where air is bubbled through a liquid. The liquid can be stagnant, flow co- or counter currently to the gas phase.	16
Figure 2: Bubble and liquid phase velocities are calculated by using the drift (difference between the phase and mixture phase), slip (gradient between bubble and liquid) and mixture (mass weighted average of bubble and liquid) velocities.	24
Figure 3: Time series of the vertical mixture velocity ( $\text{m s}^{-1}$ ) for plane gas-liquid flow;	158
Figure 4: Vertical mixture velocity profile ( $\text{m s}^{-1}$ ) for plane gas-liquid flow;	158
Figure 5: Vertical liquid velocity profile ( $\text{m s}^{-1}$ ) for plane gas-liquid flow;	159
Figure 6: Vertical gas velocity profile ( $\text{m s}^{-1}$ ) for plane gas-liquid flow;	159
Figure 7: Volume fraction of the gas phase profile (-) for plane gas-liquid flow;	160
Figure 8: Vectors of mixture velocity magnitude ( $\text{m s}^{-1}$ ) for plane gas-liquid flow;	160
Figure 9: Vectors of gas velocity magnitude ( $\text{m s}^{-1}$ ) for plane gas-liquid flow;	161
Figure 10: Contours of volume fraction of gas (-) for plane gas-liquid flow;	161
Figure 11: Time series of the vertical mixture velocity ( $\text{m s}^{-1}$ ) for rectangular gas-liquid flow;	162
Figure 12: Vertical mixture velocity profile ( $\text{m s}^{-1}$ ) for rectangular gas-liquid flow;	162
Figure 13: Vertical liquid velocity profile ( $\text{m s}^{-1}$ ) for rectangular gas-liquid flow;	163
Figure 14: Vertical gas velocity profile ( $\text{m s}^{-1}$ ) for rectangular gas-liquid flow;	163
Figure 15: Volume fraction of gas phase profile (-) for rectangular gas-liquid flow;	164
Figure 16: Vectors of mixture velocity magnitude ( $\text{m s}^{-1}$ ) for rectangular gas-liquid flow;	164
Figure 17: Vectors of gas velocity magnitude ( $\text{m s}^{-1}$ ) for rectangular gas-liquid flow;	165
Figure 18: Contours of gas phase volume fraction (-) for rectangular gas-liquid flow;	165
Figure 19: Time series of the vertical mixture velocity ( $\text{m s}^{-1}$ ) for cylindrical gas-liquid flow;	166
Figure 20: Vertical mixture velocity profile ( $\text{m s}^{-1}$ ) for cylindrical gas-liquid flow;	166
Figure 21: Vertical liquid velocity profile ( $\text{m s}^{-1}$ ) for cylindrical gas-liquid flow;	167
Figure 22: Vertical gas velocity profile ( $\text{m s}^{-1}$ ) for cylindrical gas-liquid flow;	167
Figure 23: Volume fraction of gas phase profile (-) for cylindrical gas-liquid flow;	168
Figure 24: Vectors of mixture velocity magnitude ( $\text{m s}^{-1}$ ) for cylindrical gas-liquid flow;	168
Figure 25: Vectors of gas velocity magnitude ( $\text{m s}^{-1}$ ) for cylindrical gas-liquid flow;	169
Figure 26: Contours of volume fraction of gas (-) for cylindrical gas-liquid flow;	169
Figure 27: Contours of stream function ( $\text{kg s}^{-1}$ ) for lateral convection;	170

Figure 28: Lateral convection plots for the 50:1 height to width aspect ratio mesh;	171
Figure 29: Time series of the vertical mixture velocity ( $\text{m s}^{-1}$ ) for gas-liquid flow;	173
Figure 30: Profile plots of the vertical mixture velocity ( $\text{m s}^{-1}$ ) for gas-liquid flow;	174
Figure 31: Profile plots of the vertical liquid velocity ( $\text{m s}^{-1}$ ) for gas-liquid flow;	175
Figure 32: Profile plots of the vertical gas velocity ( $\text{m s}^{-1}$ ) for gas-liquid flow;	176
Figure 33: Profile plots of the gas volume fraction (-) for gas-liquid flow;	177
Figure 34: Vectors of mixture velocity magnitude ( $\text{m s}^{-1}$ ) for gas-liquid flow;	178
Figure 35: Contours of gas phase volume fraction (-) for gas-liquid flow;	179
Figure 36: Time series of the solid phase volume fraction (-) for solid-liquid flow;	180
Figure 37: Time series of the vertical mixture velocity ( $\text{m s}^{-1}$ ) for solid-liquid flow;	180
Figure 38: Profile plots of the vertical mixture velocity ( $\text{m s}^{-1}$ ) for solid-liquid flow;	181
Figure 39: Profile plots of the vertical liquid phase velocity ( $\text{m s}^{-1}$ ) for solid-liquid flow;	181
Figure 40: Profile plots of the vertical solid phase velocity ( $\text{m s}^{-1}$ ) for solid-liquid flow;	182
Figure 41: Profile plots of the solid phase volume fraction (-) for solid-liquid flow;	182
Figure 42: Experimental gas and solid phase extracted from Warsito <sup>56</sup> . Chart B describes the solid holdup for a similarly size particle to the particles used in the scalar transport and algebraic slip mixture models <sup>9</sup> found in Figure 41.	183
Figure 43: Vectors of mixture velocity magnitude ( $\text{m s}^{-1}$ ) for solid-liquid flow;	184
Figure 44: Contours of solid phase volume fraction (-) for solid-liquid flow;	185
Figure 45: Time series of the solid phase volume fraction (-) for gas-liquid-solid flow;	186
Figure 46: Time series of the vertical mixture velocity ( $\text{m s}^{-1}$ ) for gas-liquid-solid flow;	186
Figure 47: Profiles of the vertical mixture velocity ( $\text{m s}^{-1}$ ) for gas-liquid-solid flow;	187
Figure 48: Profiles of liquid-phase vertical velocities ( $\text{m s}^{-1}$ ) for gas-liquid-solid flow;	187
Figure 49: Profiles of the gas-phase vertical velocities ( $\text{m s}^{-1}$ ) for gas-liquid-solid flow;	188
Figure 50: Profiles of the solid-phase vertical velocities ( $\text{m s}^{-1}$ ) for gas-liquid-solid flow;	188
Figure 51: Profiles of the gas phase volume fraction (-) for gas-liquid-solid flow;	189
Figure 52: Profiles of the solid phase volume fraction (-) for gas-liquid-solid flow;	189
Figure 53: Vectors of mixture velocity magnitude ( $\text{m s}^{-1}$ ) for GLS1 gas-liquid-solid flow;	190
Figure 54: Contours of gas phase volume fraction (-) for GLS1 gas-liquid-solid flow;	190
Figure 55: Contours of solid phase volume fraction (-) for GLS1 gas-liquid-solid flow;	191
Figure 56: Vectors of mixture velocity magnitude ( $\text{m s}^{-1}$ ) for GLS2 gas-liquid-solid flow;	191
Figure 57: Contours of gas phase volume fraction (-) for GLS2 gas-liquid-solid flow;	192
Figure 58: Contours of solid phase volume fraction (-) for GLS2 gas-liquid-solid flow;	192
Figure 59: Vectors of mixture velocity magnitude ( $\text{m s}^{-1}$ ) for GLS3 gas-liquid-solid flow;	193

Figure 60: Contours of gas phase volume fraction (-) for GLS3 gas-liquid-solid flow;	193
Figure 61: Contours of solid phase volume fraction (-) for GLS3 gas-liquid-solid flow;	194
Figure 62: Time series for the volume fraction of the solid phase (-) for both gas-liquid-solid flow and reaction models;	195
Figure 63: Time series for the substrate concentration ( $\text{kg m}^{-3}$ ) for both gas-liquid-solid flow and reaction models;	196
Figure 64: Time series for the product concentration ( $\text{kg m}^{-3}$ ) for both gas-liquid-solid flow and reaction models;	197
Figure 65: Profiles of vertical mixture velocity ( $\text{m s}^{-1}$ ) for both gas-liquid-solid flow and reaction models;	198
Figure 66: Profiles of volume fraction of the gas phase (-) for both gas-liquid-solid flow and reaction models;	198
Figure 67: Profiles of volume fraction of the solid phase (-) for both gas-liquid-solid flow and reaction models;	199
Figure 68: Profiles of cell growth rate ( $\text{kg m}^{-3} \text{ s}^{-1}$ ) for both gas-liquid-solid flow and reaction models;	199
Figure 69: Profiles of substrate consumed per time step ( $\text{kg m}^{-3}$ ) for both gas-liquid-solid flow and reaction models;	200
Figure 70: Profiles of product formed per time step ( $\text{kg m}^{-3}$ ) for both gas-liquid-solid flow and reaction models;	200
Figure 71: Fields of the gas-liquid-solid flow and reaction models for the 5:1 bubble column after 100 s, where $\lambda=6.5*10^{-5} \text{ s}^{-1}$ ;	201
Figure 72: Fields of the gas-liquid-solid flow and reaction models for the 5:1 bubble column after 100 s, where $\lambda=1.52*10^{-4} \text{ s}^{-1}$ ;	202
Figure 73: Bottom half of the fields for the gas-liquid-solid flow and reaction models in the 20:1 bubble column after 100 s, where $\lambda=6.5*10^{-5} \text{ s}^{-1}$ ;	203
Figure 74: Top half of the fields for the gas-liquid-solid flow and reaction models in the 20:1 bubble column after 100 s, where $\lambda=6.5*10^{-5} \text{ s}^{-1}$ ;	204
Figure 75: Bottom half of the fields for the gas-liquid-solid flow and reaction models in the 20:1 bubble column after 100 s, where $\lambda=1.52*10^{-4} \text{ s}^{-1}$ ;	205
Figure 76: Top half of the fields for the gas-liquid-solid flow and reaction models in the 20:1 bubble column after 100 s, where $\lambda=1.52*10^{-4} \text{ s}^{-1}$ ;	206

## List of Tables

Table 1: Material properties for all cases between §3.0 and §6.0.	131
Table 2: External functions used in §3.0 and §4.0.	132
Table 3: External functions used in §5.0 for solid-liquid flow and gas-liquid-solid flow.	133
Table 4: External functions used in §6.0 for three-phase flow and reaction.	134
Table 5: Boundaries for the 5:1 height to width ratio plane mesh (§3.0, §4.0 and §6.0).	135
Table 6: Boundaries for the 5:1 height to diameter ratio, 3D cylinder used in §3.0.	135
Table 7: Boundaries for the 3D rectangular mesh used in §3.0.	136
Table 8: Boundaries for the 50:1 height to width ratio mesh used in §4.0.	136
Table 9: Boundaries for the 5:1 height to width ratio plane used for solid-liquid flow.	137
Table 10: Boundaries for the 5:1 height to width ratio plane used for gas-liquid-solid flow.	137
Table 11: Boundaries for the 20:1 height to width ratio plane used in §6.0.	138
Table 12: Laminar mixture models for 2D and 3D domains described in §3.0.	139
Table 13: k- $\epsilon$ turbulence mixture model for 2D and 3D domains described in §3.0.	140
Table 14: Reynolds stresses mixture model for 2D and 3D domains described in §3.0.	141
Table 15: Lateral convection with under-relaxation adjustment in §4.0.	142
Table 16: Lateral convection for a number of k- $\epsilon$ turbulence modelling methods (§4.0).	143
Table 17: Lateral convection for a number of Reynolds stresses modelling methods (§4.0).	144
Table 18: Gas-liquid flow using the algebraic slip mixture model in §4.0.	145
Table 19: Gas-liquid flow using the modified scalar equation mixture model in §4.0.	146
Table 20: Solid-liquid flow using the algebraic slip mixture model in §5.0.	147
Table 21: Solid-liquid flow using the modified scalar equation mixture model in §5.0.	148
Table 22: Gas-liquid-solid flow for the GLS1 case described in §5.0.	149
Table 23: Gas-liquid-solid flow for the GLS2 case described in §5.0.	150
Table 24: Solver controls for the GLS1 and GLS2 cases (Table 22 and Table 23).	151
Table 25: Solver conditions for the GLS3 case (Table 26).	151
Table 26: Gas-liquid-solid flow for the GLS3 case described in §5.0.	152
Table 27: Gas-liquid-solid flow and reaction for the 5:1 aspect ratio bubble column.	153
Table 28: Gas-liquid-solid flow and reaction for the 5:1 aspect ratio bubble column.	154
Table 29: Gas-liquid-solid flow and reaction for the 20:1 aspect ratio bubble column.	155
Table 30: Gas-liquid-solid flow and reaction for the 20:1 aspect ratio bubble column.	156
Table 31: Solver conditions for gas-liquid-solid flow and reaction (Table 27 to Table 30).	157

## List of Equations

Equation 1: continuity equation for the mixture phase	111
Equation 2: momentum equation for the mixture	111
Equation 3: volume fraction equation for the mixture model	111
Equation 4: mixture density	111
Equation 5: mixture viscosity	111
Equation 6: mass averaged velocity	111
Equation 7: drift velocity	112
Equation 8: slip velocity equation	112
Equation 9: friction factor for the mixture model	112
Equation 10: particle Reynolds number for the mixture model	112
Equation 11: continuity equation for the two-fluid model	112
Equation 12: momentum equation for the two-fluid model	112
Equation 13: volume fraction equation for the two-fluid model	112
Equation 14: shear stress equation from the momentum equation for the two-fluid model	112
Equation 15: two-fluid density ratio	112
Equation 16: two-fluid model phase interaction force equation	113
Equation 17: two-fluid model momentum exchange coefficient	113
Equation 18: lift force for the two-fluid model	113
Equation 19: virtual mass effect for the two-fluid model	113
Equation 20: particle force balance equation	113
Equation 21: particle drag force	113
Equation 22: particle Reynolds number for the discrete phase model	113
Equation 23: particle virtual mass force effect	113
Equation 24: particle pressure force effect	113
Equation 25: turbulent kinetic energy transport equation	114
Equation 26: rate of dissipation of energy from turbulent flow, transport equation	114
Equation 27: turbulent viscosity formulation	114
Equation 28: total derivative for the turbulent kinetic energy	114
Equation 29: total derivative for the rate of dissipation of energy from the turbulent flow	114
Equation 30: constant that determines the orientation buoyant shear layers	114
Equation 31: exact transport equation for the transport of Reynolds stresses	115
Equation 32: turbulent diffusive transport	115

Equation 33: buoyancy effects	115
Equation 34: stress production	115
Equation 35: system rotation effects	115
Equation 36: pressure-strain term	115
Equation 37: decomposition of pressure-strain term	115
Equation 38: slow pressure-strain term	116
Equation 39: rapid pressure-strain term	116
Equation 40: wall reflection term	116
Equation 41: energy transport equation	116
Equation 42: conservation of mass equation	116
Equation 43: conservation of momentum equation	116
Equation 44: deviatoric stress tensor	116
Equation 45: Boussinesq approximation	116
Equation 46: Grashof Number	117
Equation 47: characteristic velocity based on the Grashof number	117
Equation 48: Prandtl number	117
Equation 49: temperature difference	117
Equation 50: update the flow field variables, references a profile	117
Equation 51: velocity profile for the lateral convection problem	117
Equation 52: temperature profile for the lateral convection problem	117
Equation 53: momentum equation	117
Equation 54: convective scalar equation	117
Equation 55: momentum source term	118
Equation 56: scalar equation source term	118
Equation 57: mixture viscosity	118
Equation 58: solid phase $\mu^*$	118
Equation 59: gas phase $\mu^*$	118
Equation 60: empirical velocity profile for air-water flow in a bubble column	118
Equation 61: cell mass balance	119
Equation 62: substrate mass balance	119
Equation 63: product formation mass balance	119
Equation 64: cell growth rate of reaction	119
Equation 65: reaction rate for the cell growth associated substrate consumption	119
Equation 66: reaction rate for the citric acid formation associated substrate consumption	119

Equation 67: reaction rate for product formation	119
Equation 68: volume of liquid	120
Equation 69: mass of cells grown per unit time	120
Equation 70: volume of cells grown per unit time	120
Equation 71: volume fraction of the cell culture that is grown	120
Equation 72: transport of the solid phase as a volume fraction	120
Equation 73: transport and consumption of glucose as a concentration	120
Equation 74: transport and formation of citric acid as a concentration	120

## 1.0 INTRODUCTION

### 1.1 Biochemical reactors: the need for research

The study of biochemical engineering is increasingly becoming important as the biotechnology industry is expanding with activities in the production of beverages, food, fuel, pharmaceuticals and the processing of waste materials. Many such processes are often operated with multiple phases where mass transport and reaction exists across these phases. This leads to highly complicated flow phenomena that are dependent on many factors from diverse aspects of the engineering knowledge base.

Biochemical process reactors come in many forms, from stirred tanks to bubbling beds. These processes can be either operated in batch (stirred tank, airlift or bubble beds) or continuous modes (stirred tank, packed bed or tubular reactors). General practice within the industry involves the use of aerated stirred tanks, which provide a stable operating environment. Agitators drive the flow phenomena in stirred tank reactors, but the more reactor internals that are used the greater the chance there is of contaminating the contents through the ingress of "undesirable" organisms. Damage and fragmentation of cell cultures increase with the high shear rates that are associated with the use of agitator blades in stirred tank reactors<sup>1</sup>.

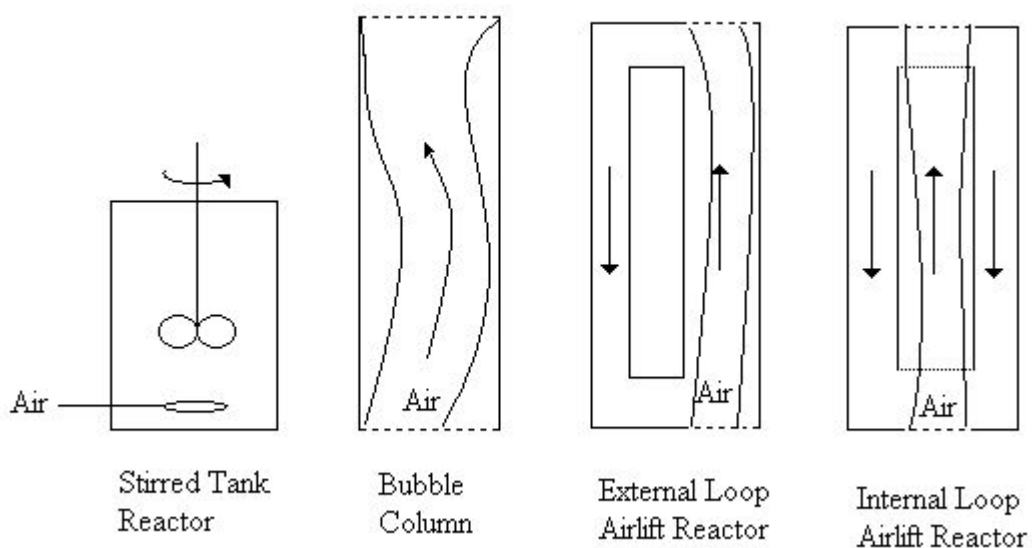


Figure 1: Reactors where air is bubbled through a liquid. The liquid can be stagnant, flow co-currently or counter-currently to the gas phase.

Over the past three decades, investigations into the operating characteristics of bubble columns and airlift reactors have shown that there is a viable alternative to stirred tank reactors<sup>2</sup>. Bubble columns display increased power efficiency through the lack of mechanical parts and their simplistic construction leads to a reduction in the number of regions with high shear rates. High thermal stability with good heat and mass transfer characteristics are also associated with the effective operation of such equipment<sup>2</sup>. The effective prediction of the process performance is limited due to the lack of definitive mathematical models that account for multi-dimensional unsteady flow effects. It is believed that the mechanical efficiency of the flow in existing bubbling bed reactors can be improved by between 10 and 30%<sup>1</sup>, where the major factor in improving the design of bubbling beds is characterising the turbulent interactions between the gas, liquid and solid phases. These interactions influence many other effects such as the transport of nutrients (e.g. oxygen, glucose, lactose etc), the size distribution and shape of bubbles, the coalescence and break-up of bubbles and the prediction of viscosity for the turbulent gas-liquid-solid mixtures<sup>1-3</sup>. Just some of these effects were investigated with computational fluid dynamics to model the transport of gas, liquid and solid phases as a mixture in a biochemical reactor with the inclusion of a simple reaction to describe the effect that the phases have on such reactions.

The emphasis of this research is as part of a thematic network of institutes collaborating through the investigation of different aspects of the fundamental phenomena of bioreactor operation<sup>4</sup>. This included the development of relationships between the effects of gas entry on the near field and the modal implications of this along with the representation of bubble-bubble interactions through non-linear paradigms<sup>5-6</sup>. The regime transition associated with reactor scale and the analogy of the instability inception between bubble columns and thermal convection for single-phase fluid heated from below was studied<sup>4</sup>. Another effect investigated was the influence of the fluid phenomena on the performance of biochemical reactions such as the production of citric and gluconic acids using *Aspergillus niger* and ethanol using a flocculating yeast<sup>4</sup>. Aspects also studied include circulation correlations, oxygen transfer with operational affects including gas phase pulsing and the influence of mass loading on the dynamics of flocculating cultures<sup>4</sup>.

---

<sup>1</sup> See Acknowledgements referring the project meetings held as part of the Inco-copernicus funded (ERB N° IC15-CT98-0904) programme

## 1.2 Computational fluid dynamics

An excellent tool for investigating flow phenomena is computational fluid dynamics or CFD. Commercial CFD software gives an opportunity for engineers to investigate the fluid phenomena in devices used in industry and everyday life. The numerical solution of equations (i.e. the Navier-Stokes transport equations) requires that the equations employed be applied to boundary conditions that are based on either the finite element approach or the finite volume method. The Navier-Stokes equations are partial differential equations that are derived from Newton's second law (force is equivalent to the product of mass and acceleration) that represents the starting point for the solution of fluid flow problems. Solving these equations is difficult, as the equations cannot be solved analytically except for a few specific cases. This leads to the use of solution procedures that solve the variables locally by dividing the region modelled into a mesh or grid of small volumes or elements.

The solution of such transport equations can provide detailed information about specific flow phenomena associated with a piece of equipment or the flow characteristics modelled i.e. multi-fluid models, the influence of heat or electro-magnetic fields. The accuracy of the resultant solution is heavily dependent on the defining assumptions made to simplify the problem tackled. From this information, the flow phenomena can be used to design a piece of engineering equipment, or it can be used to demonstrate important aspects or factors that influence the flow's nature that can be taken account of in design procedures. Engineering education can also benefit from the use of CFD in a descriptive nature to help explain such factors that impinge on the performance of process equipment to engineering students of all levels.

The use of CFD to simulate multiphase flows is widely available through the use of commercial software codes such as CFX<sup>7</sup>, ESTET-ASTRID<sup>8</sup>, FLUENT<sup>9</sup> and STAR-CD<sup>10</sup> which utilise the finite volume technique to define the domain and the methods used to apply the transport models to the domain. These codes<sup>7-10</sup> enable the simulation of the complex turbulent flows in bubble columns and many other engineering problems. In the modelling of multiphase flow, each of the above codes can apply models such as the discrete particle, the two-fluid and mixture-phase models<sup>11</sup> to depict the interactions between the phases in bubble columns and other examples of process equipment. Other functions of the software packages

include the embodiment of physical phenomena such as heat and mass transport, phase change, moving surfaces and turbulence.

To be able to replicate the flow-field within process equipment most software packages supply separate programs to define, solve and analyse the problems. These programs are known as pre-processors, solvers and post-processors. Pre-processors are used to specify the extent and boundaries of the regions in which the flow occurs. This domain is then entered into the solver where boundary values and flow models are administered to the domain and the solution is obtained through the application of the initial values to the discretised form of the transport equations. The solver is run until a converged solution (when the change in the variables is very small) is obtained, with or without the influence of time. After which the results are analysed by a post processor that displays the results as contour maps, particle traces, vector and profile plots of parameters including pressure, temperature, velocity, volume fraction, etc.

## **2.0 RESEARCH STRATEGY**

### **2.1 Project statement**

*To create a simulation that can depict the operation of a biochemical reactor in a multiphase bubbling bed.*

### **2.2 Aims**

- To develop modelling methods for three-phase (gas-liquid-solid) flow for use in simulating macro-scale flow structures in biochemical reactors in the form of bubbling beds, using a commercially available CFD code.
- To develop and apply a mass transport and reaction model that represents the consumption of a substrate and the excretion of a product through a biochemical reaction found in a specific microorganism.

### **2.3 Simulation tactics**

The tactics for the simulation of multiphase flows includes decisions about the following:

- processor architecture (alpha microprocessors<sup>12</sup>, AMD Athlon<sup>13</sup> or Intel x86<sup>14</sup>)
- operating system (Linux<sup>15</sup>, Windows NT or 2000<sup>16</sup> or Tru64-UNIX<sup>12</sup>)
- CFD pre-processor and solver (CFX<sup>7</sup>, ESTET-ASTRID<sup>8</sup>, FLUENT<sup>9</sup> or STAR-CD<sup>10</sup>)
- multiphase model (discrete phase, two fluid or mixture models<sup>11</sup>)
- domain (planar, rectangular or cylindrical)
- mesh resolution (fine or coarse)
- variables analysed (velocity, phase fraction or turbulence parameters)
- flow models applied (laminar, k- $\epsilon$  turbulence or Reynolds stress turbulence)
- discretisation procedures (first or second order, power law or QUICK methods)
- pressure-velocity coupling (SIMPLE or SIMPLEC<sup>11</sup>)
- under-relaxation factors (between 0 and 1)
- phases and their physical properties (air, nitrogen, oxygen, oil, silicone, ethanol, water, glass, biomass)

- substrate (oxygen, glucose, sucrose, lactose, carbon dioxide)
- biochemical reaction (organism and the kinetics i.e. Monod)
- metabolic product (organism chosen and specific parameters such as pH etc)
- mass transport processes for the substrate and the products (gas-liquid and liquid-solid transport and vice versa)
- steady state or transient plus the length of simulation time plus the time step size

The choice of each of the above parameters requires the application of assumptions to simplify the flow modelled. This affects the accuracy of the solutions obtained from the simulation (apart from the processor architecture and the operating system). The development of the proposed research for simulating a biochemical reaction in a bubble column reactor proceeded as follows:

- two-phase flow, where the two phases are gas and liquid phases
- three-phase flow, where the three phases are gas, liquid and solid phases
- mass transport and reaction, where the reaction occurs in the solid phase representing a microbial culture, either as flocculating particles or suspended on support beads.

## **2.4 Equipment employed**

### ***The Computers***

Two computers powered by Intel Pentium Microprocessor Chips (PII 400 MHz and PIII 850 MHz)<sup>14</sup> both of which employ Windows NT 4<sup>16</sup> as the operating system.

### ***The CFD Software***

Fluent Incorporated provided the software used to simulate the multiphase flow<sup>9</sup>. The reasons for the choice of software and hardware was to provide a solution with a recognised code that is known to provide a reasonable solution and make it widely accessible for use in the education of engineers when applying design principles to the construction and operation of bubble bed and airlift reactors.

### ***The Multiphase Model***

The discrete phase model represents the transport of individual phases as a series of discrete particles in Lagrangian frame of reference to calculate their motion in a continuum fluid and the influence that this has on the continuous phase. The advantages of this method are that the influence of individual bubbles and the associated wake dynamics are calculated, but this increases the computational loading for large numbers of bubbles reducing the efficiency of the calculations<sup>17-19</sup>.

The two-fluid model represents both phases as continuum phases with continuity and momentum conservation equations applied to each phase, good examples of the application of simulation techniques were presented by Eigenberger et al<sup>17,20-23</sup>.

The mixture model is similar to the two-fluid model in that the application of discrete phase is as a continuum fluid. This model differs from the two-fluid model, as there is only one set of continuity and momentum conservation equations, which are used to calculate the variables to predict the motion of the mixture. To do this source terms and volume fraction equations are applied to the model calculate the inter-phase interactions. Computationally this approach is efficient when compared to the dispersed phase and two-fluid models<sup>11,24-28</sup>.

In multiphase calculations the mixture model was employed, as it provided the most efficient method to perform the macro-scale simulations, whereas the more accurate discrete particle method is focused on the influence of the micro-scale structures such as bubble wakes and clusters for example. In the interest of the project, the macro-scale fluctuations in the flow structure were investigated and to do this all calculations that were performed were time-dependent. To enable comparison of the flow characteristics between simulated and empirical data, long time-periods of simulation were applied to reduce the influence of the fluctuations on the averaged parameter profiles. Thus ensuring the fluctuations influence on the averaged profiles such as those of velocity and discrete phase hold-up is minimal. Therefore, time dependent simulations of the order of 600 seconds or 10 minutes were performed.

## **3.0 GAS-LIQUID FLOW MODELLING IN BUBBLE COLUMNS**

### **3.1 Plan**

Modelling of gas-liquid flow in three domains:

- two-dimensional planar mesh
- three-dimensional rectangular mesh
- three-dimensional cylindrical mesh

For three flow models:

- laminar
- k- $\epsilon$  turbulence
- Reynolds stresses

The emphasis of this section is to introduce the modelling of multiphase flows in bubble columns and to show the difficulties encountered in providing solutions that are characteristic of flow regimes experimental columns. This depends on whether the structure of the flow fields for both phases and the magnitudes of the velocities observed are of relevance. Different turbulent flow models are used to compare the structures that such schemes depict with buoyancy driven flows. In addition, the three domains are used to determine the relevance of the two-dimensional plane to the three-dimensional flow regimes and whether the plane is more representative of either the rectangular mesh or the cylindrical mesh.

### **3.2 Mathematical models**

The modelling of multiphase flow using computational fluid dynamics or CFD has led to the application of additional techniques to improve the accuracy of the results obtained. Three basic flow models can be employed to assess the phase interactions. These are the discrete phase, two-fluid and mixture models<sup>11</sup>.

As explained in the previous section each model differs by how the discrete phase is defined, this influences the computational demand on the solver and the scale of the interactions, i.e. micro, meso or macro-scale motions. The accuracy of the solution obtained depends on the application of the viscous flow model and the relevant boundary condition to initialise a solution. The choice of models includes laminar flow model, k- $\epsilon$  turbulence transport and the transport of turbulent Reynolds stresses, which offer viable alternatives to the representation of the flow phenomena associated with the simulation of multiphase flows. Each model requires a different mesh resolution and form to be able to describe the fluctuating vortices that are present i.e. laminar flow requires fine meshes to accurately capture vortices, whereas k- $\epsilon$  and Reynolds transport can use coarser grids to capture similar effects. The equations cross-referenced in the next sub-sections can be found between §10.1 and 10.4.

### ***The mixture model***

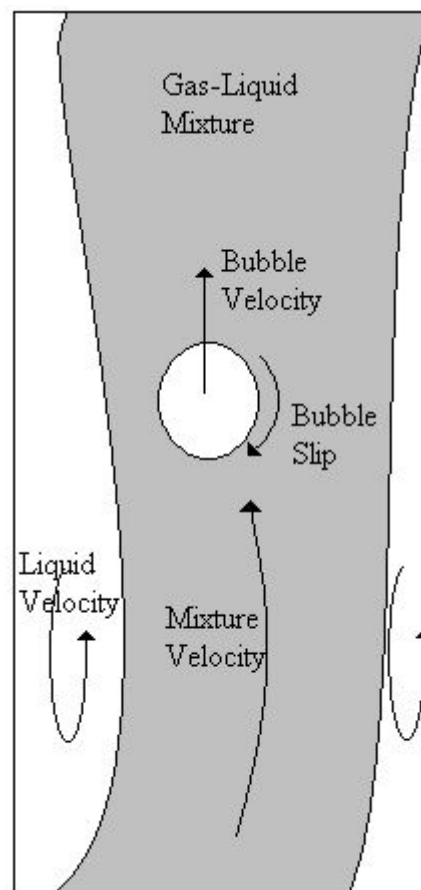


Figure 2: Bubble and liquid phase velocities are calculated by using the drift (difference between the phase and mixture phase), slip (gradient between bubble and liquid) and mixture (mass weighted average of bubble and liquid) velocities.

The mixture model is a continuum model, but only one phase is considered in the calculation of the flow phenomena and this comprises of a mixture of the discrete and continuous phases. The equations used in obtaining a numerical solution of the gas-liquid mixture are a modified form of the Navier-Stokes equations for incompressible flow. The Navier-Stokes equations consist of an equation of the conservation of mass (Equation 1) in this case for the mixture phase only, which is used to calculate the pressure field and check the solution of the transport equations through the imbalance of mass in the domain<sup>25-26</sup>. The general transport equations are the mixture momentum conservation equation (Equation 2) used to calculate the flow phenomena of the mixture phase and a volume fraction equation (Equation 3) of the discrete or secondary phases, which assesses the impact of the secondary phase on the multiphase mixture. Both transport equations contain an extra term that calculates the phase interactions, by using a diffusion velocity or drift flux in the form of a diffusion stress (last term on the right hand side of Equation 2 and Equation 3). This was based on the work of Zuber and Findlay<sup>24</sup> and these terms were implemented into commercial software codes by Manninen et al<sup>25</sup> and Sanyal et al<sup>26</sup>. The physical properties of the mixture phase are calculated using the sum of the product of the physical property and the phase's volume fraction (Equation 4 and Equation 5)<sup>24-25</sup>. There is a major limitation with this model for the viscosity (Equation 5) as this reduces the validity of the simulation, if a sum of the individual viscosities is used. Thus, a more representative model would be the use of a viscosity formulation such as that of Ishii and Zuber<sup>27</sup> or Ishii and Mishima<sup>28</sup>. Ishii et al<sup>27-28</sup> improved the application of the formulations to include the effect of the different flow regimes such as homogeneous, heterogeneous and churn turbulent flows. By considering parameters such as the mixture viscosity, particle drag in a pure liquid and for a multiphase mixture and the effect that this has on the diffusion velocity of the mixture and the relative velocity between the phases. To calculate the influence of the secondary phase on the primary phase, drift and slip velocity formulations as used (Equation 6 to Equation 10) by Sanyal et al<sup>26</sup> are available as a standard model with the Fluent code<sup>9</sup>. The slip or relative velocity was obtained by averaging a combined momentum equation for the discrete phase and the mixture according to the principles of local equilibrium and Favre averaging. Assumptions made as part of the averaging procedure are that the pressure is the same for all phases and that only viscous drag influences particle motion leading to a fluctuating form of the slip velocity. A constitutive equation is then employed to account for the fluctuating terms to further simplify the relative velocity<sup>25</sup>.

### ***The two-fluid model***

This model treats both the gas and liquid phases as continuum phases, where the discrete phase is considered as a pseudo-continuous phase and both fluids are treated as incompressible fluids, with a single pressure field being shared by all phases<sup>26</sup>. The model predicts both the gas and liquid motion through continuity (Equation 11) and momentum (Equation 12) conservation equations for each phase<sup>26</sup>. The momentum equation for each phase is linked by an inter-phase interaction term, which is essentially an alternative representation of the slip velocity (Equation 16 and Equation 17)<sup>26</sup>. The lift force (Equation 18) and the virtual mass effect (Equation 19) are included in the gas phase Navier-Stokes equations through the additional forces term<sup>26</sup>. Examples of the application of CFD simulation techniques in modelling gas-liquid flow in bubble columns include the steady<sup>29-31</sup> and unsteady flow models<sup>20-21</sup>, comparison with discrete phase models, investigation of discretisation techniques<sup>17</sup> and the consideration of turbulence modelling techniques<sup>22-23</sup>.

### ***The discrete phase model***

This model defines the phases as a continuous fluid phase through which discrete particles move (either as bubbles, drops or solid particles). The continuous phase is calculated in an Eulerian frame of reference, i.e. the calculations are based on a fluid passing through a control volume. The particulate phase calculations are based on a Lagrangian reference frame, where the calculations are based on the motion of fluid or solid particles that move through a domain. From this the motion of the particles is calculated by using a force balance equation for each particle (Equation 20). The force balance includes the influence of particle drag (Equation 21 and Equation 22), the virtual mass effect (Equation 23) and the pressure force effect (Equation 24).

The forces balance equations for all particles are then coupled to the Navier-Stokes equations of motion using source terms and thus determine the influence that the particulate phase has on the fluid continuum. Examples of the application of the discrete phase model to gas-liquid flow in bubbles include the initial unsteady applications to two-dimensional domains for gas-liquid flows<sup>18-19</sup>, comparisons between discrete and continuum based approaches for the bubbly phase<sup>17</sup> and the application to three-dimensional flow domains<sup>19</sup>. Other applications

include the addition of a third, solid phase to a gas-liquid mixture, and to test the use of a continuum approach for the simulation of gas-liquid-solid motion in bubbling bed reactors<sup>32-33</sup>.

### ***The modeling method employed***

The discrete phase model is by far the most accurate formulation as it accounts for the individual impact of each particle. As this is a computationally intensive technique when large numbers of bubbles are required to represent a phase fraction of up to 10%<sup>17-19</sup>. Therefore, to use this model requires the use of very powerful computers to perform such comprehensive simulations. As the intention of the project is to use widely available equipment then it would not be worthwhile employing this technique, as the computers employed cannot cope with such a large number of bubbles. In addition, the focus of the discrete phase model is on the micro-scale, whereas the generation of macro-scale flow structures that influence the mixing characteristics of bubble column reactors is of interest here<sup>1-3</sup>.

This leaves the two-fluid and mixture models, and asking the question:

*Is the accuracy of using the two-fluid model good enough to justify not using the computationally efficient mixture model?*

The efficiency of the code is a major factor in the choice of flow model particularly when the intention of the project is to add complexity to situations modelled. Adding a third solid-phase with complex turbulence transport models and then finally including the transport of reactive species and products will increase the complexity of the models employed. These effects are used in answering the above question deciding the emphasis of the work with the pitfalls of the simplifying assumptions, limiting the representative nature of each model.

The two-fluid model is widely regarded as the most effective model to simulate multiphase flow, with the individual depiction of the phases. The mixture model is the most efficient of the models discussed above, but there is some controversy about the specific formulation of the mixture phase and whether this accurately represents the gas-liquid mixture. This is due to the formulation of the mixture phase viscosity, an important parameter in the modelling of

turbulent flows. From the understanding that turbulence is a characteristic of the flow and not the fluid, this means that the laminar viscosity is a contributing factor to a total viscosity including the viscous effects of the turbulent flow<sup>34</sup>. Therefore, if the application of the viscosity formulation is not correct then errors will be introduced into the fluid flow calculations, as discussed by Manninen et al<sup>25</sup>.

From the comparison of the results obtained between the two-fluid model and the mixture model in the homogeneous regime<sup>26</sup>, it was found that the difference between the computational results was negligible. Especially when the flow profiles from the simulations were compared with the experimental observations, the simulations were found to agree with one another<sup>26,35-37</sup>. Therefore, from this I determined that the most efficient method was the mixture model. This allows the expansion of the model by using turbulence models and including the third-phase with a biochemical reaction, without a drastic reduction in the efficiency of the code.

### ***Transport of turbulence***

Apart from the application of the equations that define the phase motion and influences the solution obtained, the viscous flow model used also controls the flow phenomena that are captured. Three methods to depict the transport of turbulent vortices are the laminar flow model, the k- $\epsilon$  turbulence model and the Reynolds stresses model. The transport equations for turbulence can be found in §10.4.

The laminar flow model is the basic representation of viscous flow, with just the Navier-Stokes equations providing the model for the transport of fluid. The k- $\epsilon$  model includes the use of a pair of coupled transport equations to model the generation of kinetic energy by the flow (Equation 25) and the rate of dissipation of that energy from the flow (Equation 26). The remaining equations (Equation 27 to Equation 30) expand the terms for the turbulent viscosity and the total derivatives plus the equation for the determination of the  $C_{3\epsilon}$  constant. This approach to the solution of turbulent flow parameters is based on the work of Launder and Spalding<sup>38</sup>.

The transport of Reynolds stresses can be predicted by the exact transport equation (Equation 31). The Fluent<sup>9</sup> solver splits this equation into at least four equations for two-dimensional

flow and seven equations for three-dimensional flow in order to attain closure of the exact equation as there are several unknowns (some of these equations are described between equations Equation 32 and Equation 40). Investigations into natural convection across the width of a cavity with a large aspect ratio of the cavity height to width, utilising basic or reference flow profiles, were used to update parameters such as temperature and the velocity parallel to the cavity walls<sup>39-40</sup>.

From this and the analogy between natural convection and buoyancy driven multiphase flow in bubble columns or fluidised beds<sup>41</sup> the updating approach is applied to the vertical velocity by either Equation 50 or Equation 60. The solver employed allows the user to implement a series of functions to manipulate the mathematical models used, Therefore, enabling the widening of the functionality of the solver. These functions are called user-defined functions (UDF) and they include effects such as source terms, boundary profiles, variable adjustment and definition, properties of the fluids and solids. To update parameters such as vertical velocity and the gas phase fraction, the DEFINE\_ADJUST function was used. This updates each variable before every iteration<sup>9,i</sup>.

### **3.3 Modelling parameters**

#### ***Boundary conditions***

The experimental investigations of Degaleesan<sup>35-36</sup> and Kumar<sup>37</sup>, plus the simulations of Sanyal et al<sup>26</sup>, were used to provide a comparison of both experimental and simulated profiles for multiphase flow in bubble columns with a height to diameter ratio of 5:1 or ~1 m high by 0.19 m diameter. From these comparisons, it was obvious that the efficiency of the mixture model outweighed the increase in accuracy of the two-fluid model. The data provided by Degaleesan<sup>35-36</sup> and Sanyal et al<sup>26</sup> provides a useful comparative aid for justifying the use of the mixture model.

To accurately model the flow, the type of mesh used is just as important as the choice of viscous flow model<sup>17</sup>. Therefore, three simple meshes that describe the flow domain are employed; these include rectangular and cylindrical domains for three-dimensional flow and a

---

<sup>i</sup> See §11.1 for the source code to update the flow variables and Table 2 in §12.2 for user function definitions

two-dimensional plane for reduced computational expense simulations. Each mesh is used to demonstrate how well each mesh captures the turbulent vortices and oscillations that occur in bubbling beds and to determine whether the planar case is more representative of the rectangular or cylindrical cases. The planar mesh has dimensions of 1 by 0.2 m with the resolution of 100 cells high by 20 cells across giving a 2000 cell grid. The three-dimensional rectangular column is 1 m high by 0.2 m wide with a depth of 0.2, with a respective mesh specification of 33 by 20 by 20 cells to give a 13200-cell mesh. Finally, the cylindrical column with the dimensions of 1.00 m in height by 0.20 m in diameter has a mesh resolution of 75 cells by 19 cells across the column width and 20 cells about the perimeter of the column giving 12375 cells. Note that the inlet condition for all of the meshes was 80% of the area of the column's bottom surface. A free slip surface was used to represent the liquid surface<sup>i</sup> as an outlet condition for the whole of the top surface of the column.

In applying the multiphase models to the domains as constructed above conditions such as the acceleration due to gravity, physical properties of the phase including density and viscosity, the inlet velocity and diameter conditions for the particle or bubble phase. The gravitational force was set to  $9.81 \text{ m s}^{-2}$ , acting as an accelerating force on both phases in the vertical plane of the domain. The physical properties of the dispersed phase were defined as air, with the density as  $1.225 \text{ kg m}^{-3}$  and the viscosity as  $1.7894 \cdot 10^{-5} \text{ kg m}^{-1} \text{ s}^{-1}$ . The bubbles representing the gas phase were treated as spherical bubbles that were assumed to have a constant diameter of 5 mm. The gas phase is injected through the inlet condition at the base of the column and is quantified as a superficial velocity; this was defined as the volumetric flow of gas per unit area of the column and was set to  $2 \text{ cm s}^{-1}$ . Finally, the liquid phase was defined as having no net flow in and out of the column and with the properties of water, i.e. density at  $998.2 \text{ kg m}^{-3}$  and the viscosity at  $1.003 \cdot 10^{-3} \text{ kg m}^{-1} \text{ s}^{-1}$ <sup>9,11,ii</sup>.

### ***Modelling strategies***

The strategies used to improve the depiction of reality in the modelling of bubble columns, include the use of alternative discretisation procedures to define the application of the transport equation variables to the domain modelled. Other parameters include the under-

---

<sup>i</sup> See Table 5 to Table 7 in §12.3 where boundaries conditions are defined

<sup>ii</sup> See Table 1 in §12.1 where material properties are specified

relaxation of the equations and the use of steady or unsteady flow to represent the flow characteristics<sup>i</sup>.

The application of discretisation procedures in Fluent<sup>9</sup> can be generally divided into the transport equations applied, with the exception of the pressure variable. The pressure variable requires special treatment because it is unable to be isolated from the Navier-Stokes equations, thus any attempted solution of the equation results in the loss of the pressure gradient term. This leaves us with the application of three discretisation procedures for the simplest flow model, which is laminar flow.

As the acceleration due to gravity is applied to the momentum transport equation the pressure discretisation procedure applied is known as the "body-force weighted method". This method works well for buoyancy driven flows, where the defining assumption of the method is that the normal gradient of difference between the pressure and the body force is constant<sup>11</sup>.

The momentum equation is discretised by either using a first or second order UPWIND method or the QUICK form of the method<sup>42-43</sup>. These are control volume based approaches of discretisation between the actual form of the transport equation and the algebraic equations used to calculate the flow variables by deriving values from the upstream cells of the domain<sup>44</sup>. The first order scheme is where the variable at the centre of a cell holds for all regions of the cell<sup>44</sup>. The second order scheme uses a Taylor expansion series of the cell centred solution<sup>45</sup>. A more accurate method is the QUICK<sup>42</sup> (Quadratic Upstream Interpolation for Convective Kinematics) scheme, which interpolates centre values in the cell using a weighted quadratic equation.

Sokolichin, Eigenberger, Lapin and Lüebbert<sup>17</sup> compared the effect of the upwind and the total variation diminishing of the solution discretisation when simulating multiphase flow in bubble columns. They concluded that it is important to reduce the impact that numerical diffusion has on the prediction of the secondary phase for the simulation of multiphase flows. From comparison of these methods further conclusions were made discussing the improvement in the results obtained when more complex discretisation procedures were used in the solution of gas-liquid flow problems<sup>17</sup>. From these conclusions to improve the flow

---

<sup>i</sup> See Table 12 to Table 14 in §12.4 where flow models and variables plus solver are described

modelling the most complex scheme available to use in Fluent<sup>9</sup> was employed and this is the QUICK scheme<sup>42</sup>.

The choice of the pressure velocity scheme between the SIMPLE<sup>43</sup> and SIMPLER<sup>45</sup> methods is important as it defines how the pressure field links to the velocity field. The SIMPLE scheme employs a relationship between the pressure and velocity corrections to link the conservation of mass and the pressure field. The SIMPLER method is basically the same method except for how the cells' face flow rate is expressed. This difference allows for improvement in the rate of convergence of a solution if there are problems associated with the coupling of the pressure and the velocity<sup>11</sup>.

As the motion of the gas-phase through the liquid-phase is highly unstable<sup>i</sup>, it would be prudent to use time dependent formulations of the transport equations as the turbulent nature of the flow is important to the inclusion of models such as the reaction of a biochemical agent. From the unsteady nature of the flow it is necessary to consider the discussion of time-averaged variables such as the vertical velocity to be able make comparisons between simulated and experimental results.

To ensure that the influence of all the fluctuations of the variables is absorbed by the averaged profile, a long simulation must be run to the order of 600 seconds or more. If we choose a reasonable time step size of 0.1 due to the unstable nature of the flow, then there are 6000 steps for 600 seconds of simulated time. As the plan suggests there are three grids of varying complexity, the more complex the grid the longer the simulation will run. For a 2D plane with 2000 cells the simulation will run for approximately 24 hours, but for the 3D grid with ~10000 cells these simulations will run for the best part of a week. Therefore, for any smaller time size, you will be looking for a much longer simulation time, but for a step-size any much larger than this and the solution becomes divergent.

The influence each transport equation has on the stability of the solution can be controlled by the use of under-relaxation factors. Under-relaxation reduces the influence of equations and potentially increases the stability of the solution. These factors are generally between values of 0 and 1. The default values for the momentum and pressure terms are 0.7 and 0.3

---

<sup>i</sup> See Acknowledgements referring to experimental experience gained in the Slovak Republic

respectively<sup>9</sup> and in the solution of the mixture model these factors will be kept the same. Due to reduced stability of the solution, the factor for the volume fraction equation is kept to 0.5 and the secondary phase slip equation at 0.1. All the remaining factors were assigned the value 1.

### **3.4 Results and discussion**

The simulation of gas phase transport in a continuum liquid was implemented through various meshes from two-dimensional planes to three-dimensional volumes. These simulations also included the effect that fluid transport models have on the motion of gas and liquid mixtures such as laminar, k- $\epsilon$  turbulence and turbulent Reynolds stresses models. Each simulation was performed for 600 seconds of flow time, where data were recorded at half-second intervals for parameters of gas phase hold-up and the vertical component of the velocities of the gas, liquid and mixture phases. These parameters were recorded at the height of 0.5m for the plane and rectangular meshes and 0.5225m for the column across the x-direction or horizontal axis of the mesh. The data obtained by the Fluent<sup>9</sup> solver is presented in §13.1.

#### ***Two-dimensional plane***

Between Figure 3 and Figure 10, the results for the two-dimensional plane with a height to diameter aspect ratio of 5:1 can be found. These include time series, flow profiles, vector and contour plots for the flow representations modelled.

Figure 3 describes how the mixture velocity in the vertical direction changes with time for the plane mesh. Each solution shows the influence of the transport equations used has on the fluctuation in the velocity. The laminar case displays many oscillations between flow states that have been observed experimentally, whereas both the k- $\epsilon$  and the Reynolds stresses turbulence transport cases do not display any oscillation.

Figure 4 to Figure 6 are the corresponding time-averaged profile plots for the vertical velocity of the mixture, gas and liquid phases in the plane mesh. Each profile is parabolic with the bulk flow in the centre of the column moving upwards and down the column at the walls for all three cases and phase velocities, except for the gas phase, which only moves up the

column. The profiles for each phase are exactly the same apart from the magnitude of the velocities in the profile, due to the influence of the slip velocity equation. Again, the influence of the turbulence transport equations can be noted by the change in the shape of the profiles. The laminar case shows a symmetric parabolic profile with velocities ranging between  $-0.5$  and  $0.35 \text{ m s}^{-1}$  in Figure 4. When comparing the experimental and simulated flow cases, the laminar case over-predicts velocity profile and the turbulent flow cases are flatter and closer to the experimental result. These profiles more accurately represent the magnitudes of the velocity in the column. The fluctuation of the parameters observed in the laminar solution is not present in the turbulence cases (Figure 3).

The volume fraction profiles are presented in Figure 7 and again the laminar case is not representative of reality with peaks where there are troughs in the turbulence case results and troughs where there are peaks. The profiles of the Reynolds stresses cases are suspect as the implementation of the model includes the updating of the vertical velocity and the volume fraction of the gas phase for all iterations. This results in constant values for the parameters as observed in Figure 3 and as the profiles used were derived from the experimental data, this result does not portray the dynamic behaviour of experimental flows. The same could be said for the  $k-\epsilon$  turbulence case when comparing the profiles with the fluctuations in the parameters as virtually negligible.

The reasons for the lack of fluctuation in the flow variables in the turbulence cases can also be explained by the vortical flow structures observed in the vector fields for the mixture and gas phases (Figure 8 and Figure 9). For both turbulence cases there are only two vortices observed with dimensions that are equivalent to the column height and radius, whereas multiple vortical structures arise while using the laminar flow specifications. Figure 10 shows the contour plots of volume fraction of the gas phase for the corresponding instantaneous vector plots (Figure 8 and Figure 9). Comparing these plots demonstrates that the flow structure and the volume fraction of the gas phase are coupled or intrinsically linked. The turbulence transport models used also affects the volume fraction observed with a nearly uniform distribution in the vertical direction, whereas for the laminar case, the volume fraction is heavily influenced by the smaller vortices giving a non-uniform distribution in the vertical direction.

### ***Three-dimensional rectangular mesh***

The three-dimensional mesh is used to determine whether the flow regime depicted in the plane mesh is more representative of rectangular or cylindrical flow regime. This is important for developing flow models as a lower number of mesh cells in a plane mesh improves the speed at which solutions are obtained and the implementation of the flow models is simplified when compared with three-dimensional cylindrical and rectangular domains. The results of the rectangular cases are presented from Figure 11 to Figure 18, with time series, flow profiles, vector field and contour plots.

Again, the time series in Figure 11 illustrates the change between the turbulence flow cases and the laminar flow case where fluctuations are large and frequent. The turbulence flow cases are steady except for a step change in the flow regime after 300 seconds of simulation time with the Reynolds stresses turbulence case.

The laminar and Reynolds stresses profiles of the velocity and volume fraction are symmetric and of the form of a plug flow profile. The profiles are unlike the  $k-\epsilon$  turbulence profiles, which are asymmetric (Figure 12 to Figure 15) and remain asymmetric for the entire simulation. The time series for the  $k-\epsilon$  turbulence equations becomes constant after a stable flow structure is obtained, explaining why the profile is asymmetric. The reason for the difference in the flow regime shown for this case can be explained by the fact that the  $k-\epsilon$  turbulence transport model is known to perform poorly for non-cylindrical flows<sup>46</sup>. Therefore, the flow regimes for two-dimensional plane and the three-dimensional rectangular configurations are different so that leaves the cylindrical cases to confirm the relevance of the two-dimensional case. As well as producing plug flow profiles, the three-dimensional case over-predicts the magnitude of the velocities for both the laminar and Reynolds stresses profiles particularly close to the column walls.

Figure 16 to Figure 18 describes the vectors of velocity and contours of volume fraction in the vertical and horizontal directions across the depth plane. The velocity vectors (Figure 16 and Figure 17) for both phases show why the time series in Figure 11 are variable for the laminar case as the flow structure consists of multiple vortices with the diameter no greater than the width of the column. The results are also displayed for the  $k-\epsilon$  turbulence case, which shows a steady asymmetric form with the majority of the flow moving up the left wall and down the

right. For the Reynolds stresses case where two steady solutions are observed, with the change in the solution occurring after 300 seconds of simulation time. The vector and contour fields exhibit this shift between states with a significant effect on the flow profiles by changing from the parabolic form to a plug flow profile.

### ***Three-dimensional cylindrical mesh***

The cylindrical mesh results can be found between Figure 19 and Figure 26, again presenting the time series, profiles and field plot for vectors and contours. Figure 19 is the time series where both the laminar and Reynolds stresses turbulence cases show similar results to the plane and rectangular domains. With an oscillating curve for the laminar case and a steady trace for the Reynolds stresses model application. The k- $\epsilon$  turbulence case produces a very different solution when compared with the alternative meshes used in this investigation. Instead of the steady trace obtained in the previous solutions, a regular oscillation between two states is found to occur. The oscillation has an estimated time-period of ten seconds, which first appears twenty seconds after the simulation was initialised.

The velocity profiles for the mixture, air and liquid phases can be found between Figure 20 and Figure 22. The k- $\epsilon$  turbulence profile is of a different form again and when comparing with the previous solutions only a slight asymmetry occurs, whereas the rectangular case was fully asymmetric and the laminar mesh was symmetric. Both the laminar and Reynolds stresses profiles indicate similarities to the plane and rectangular meshes, with symmetric and plug flow forms except for the laminar plane case which is parabolic (Figure 4 and Figure 12). Figure 23 displays the volume fraction of the gas phase profiles and as before the volume fraction profile is dependent on the velocity profiles observed. Therefore, both the laminar and Reynolds stresses profiles have a plug flow form and the k- $\epsilon$  turbulence case has a parabolic curve that is asymmetric.

The final three figures illustrate the vector and contour fields, which can be found from Figure 24 to Figure 26. The behaviour of these fields helps to explain the behaviour of the profiles and time series discussed earlier by describing the dynamic flow phenomena. The structure of the motion when solving with the laminar flow model is similar to the plane and rectangular results with many unstable vortices. As for the laminar case the Reynolds stresses turbulence case displays similar flow phenomena to the plane and rectangular meshes, but this time the

flow consists of two vortices of a size equivalent to the height and radius of the column. The k- $\epsilon$  turbulence case flow-fields consist of a column diameter wide vortex at the base of the column and elongated vortices above this vortex whose width are approximately equal to the radius of the column. As mentioned before these fields can explain the dynamic phenomena occurring in the time series (Figure 19) for example the two vortices in the Reynolds stresses case and a limiting condition in updating the velocity for all iterations resulting in the steady series. The laminar case produces an unsteady result due to the many unstable vortices transporting the gas phase about the column resulting in the irregular oscillating profile. The time series for the k- $\epsilon$  turbulence case has a regular oscillation; this instability is caused by large vortex at the base of the column influencing the remainder of the flow-field as the gas phase is transported through this vortex. As this vortex rotates about the bottom of the column, the flow variables oscillate between the states.

### ***Implications***

From the laminar flow results, the dynamic behaviour consists of vortices of the scale of the column diameter that are free to move about the column. The difference in flow characteristics between meshes is minimal, except for the two-dimensional case, which has a parabolic flow profile. For the modelling of a turbulent two-phase flow, the laminar model does not include the calculation of energy transport and the influence the turbulent viscosity has on the fluid mixture. Therefore, many of the important interactions that characterise turbulent flow are missing from the solution of the flow-field. Reasonable results are presented, though they are not definitive solutions to what is essentially a turbulent flow, as the terms calculated do not include the effects described above, the results cannot be fully trusted.

The nature of the three flows in all three meshes for the k- $\epsilon$  turbulence cases produce different solutions (c.f. plane: steady symmetric profile; rectangular: steady asymmetric profile; cylindrical: unsteady parabolic profile with a slight asymmetry;). These results introduce doubt into the validity of the k- $\epsilon$  turbulence model to produce a consistent answer for a multiphase flow, as the laminar and Reynolds stresses turbulence case produce consistent flow structures across all three meshes. Particularly with the dynamic flow behaviour as two of the cases produced steady solutions, with only the cylindrical case producing an unsteady structure. This can be seen as being the correct result for the flow, as a cylindrical mesh was

used with cylindrical coordinates to produce a flow with a regular oscillation in the flow variables with time. However, there are too many questions raised about the remaining meshes as to why the results are different to fully trust the solutions obtained. Especially with the steady flow observed in the k- $\epsilon$  turbulence plane and rectangular mesh results that could be caused by the strength of the model equations used or the application of boundary conditions when employing these transport equations. In using these models default specifications of Fluent<sup>9</sup> are used for both the boundary conditions and constants applied to the transport equations in the solver. Therefore, to change these settings could change the solutions, but the results would require the backup of experimental investigations into the turbulent nature of the flow. The investigation must determine the magnitude of the constants used in the k- $\epsilon$  turbulence equations or characterise appropriate boundary conditions for the application of turbulence equations.

The results for all three of the Reynolds stresses cases show steady solutions, this is not what is expected even though profiles are near perfect, as dynamic changes in the flow variables are expected due to the unsteady flow characteristics caused by a bubbly flow. This result is not as accurate as it suggests, as experimental flow profiles are used to update the vertical velocity and the gas phase fraction for all iterations. This method does not allow the unknown secondary velocities to have an influence on the solution. Therefore, alternative updating methods must be used or calculate the flow-field without using the addition of a basic profile.

### **3.5 Conclusions**

The modelling of two-phase flow using alternative turbulence methods emphasises how difficult it is to obtain an accurate solution of bubbly flow in column devices. Using the standard (algebraic slip mixture) model available in the Fluent<sup>9</sup> software provides an excellent basis for investigating the influence that the domain and the turbulent flow representations have on the outcome of the simulations performed. To model gas-liquid-solid flow simultaneously along with biochemical reactions is limited by the standard model specifications. Therefore, there are two approaches to make from here by either the use of independent flow models influenced by the mixture phase velocity of the gas-liquid simulation or adapt scalar equations to represent the volume fraction transport equation of

each discrete phase. These individual phase representations can be implemented easily, but some of the instantaneous interaction is lost through solving for each phase separately and then for substrate transport and reaction in a further calculation. This leads to further movement away from the driving forces caused by the density difference of the gas and liquid phases. Therefore, in the next section (§4.0) the adaptation of scalar transport equations will be investigated for the simultaneous application transport equations for both discrete gas and solid phases in a continuous liquid phase.

Concluding this first models section (§3.0), the rectangular cases were used to determine how relevant the two-dimensional plane is to the cylindrical reality of the experimental specifications. Therefore, further developments of the code can be harnessed using the more efficient two-dimensional plane. It was found that the rectangular results for all flow representations were significantly different to the phenomena depicted by plane and cylindrical cases. Further to this the application of the flow models did not indicate significant improvements of the unsteady flow phenomena and raised questions about the suitability of the  $k-\varepsilon$  turbulence model for the modelling of two-phase flow in bubble columns. These questions can only be answered by combining an experimental and numerical investigation, as the value of specific constants used in the calculations above may not be applicable to a bubbly flow. As the aim of this work is to provide a simulation model for gas-liquid-solid flow in which a biochemical reaction occurs, such an investigation would move away from the remit of the research<sup>i</sup>. Therefore, to make improvements in the calculation of the turbulent flow interactions between both phases driven by buoyancy, the next section (§4.0) will also investigate the applicability of the Reynolds stresses turbulence model to such flows. To do this an example of buoyancy driven flow was investigated in §4.0 that was based on lateral convection in a narrow vertical cavity<sup>39-40</sup>.

---

<sup>i</sup> See Acknowledgements, §1.0 and §2.0 referring to the scope of the project ERB N° IC15-CT98-0904

## 4.0 MODELLING TURBULENT BUOYANCY DRIVEN FLOWS

### 4.1 Plan

Determine the application of the turbulence transport schemes:

- model thermally buoyant flow in a cavity using a two-dimensional plane mesh with a height to width ratio of 50:1
- employ various turbulence models for thermal convection, i.e. k- $\epsilon$  turbulence, Reynolds stresses etc
- model buoyant gas phase motion in a manner that is similar to that of the thermal convection simulation except that a two-dimensional plane mesh with a height to diameter ratio of 5:1 is used
- use both the mixture model available in Fluent<sup>9</sup> and a modified scalar equation form of the model

The purpose of this section is to provide an assessment of the use of turbulence models for buoyancy driven flow through the analogy between thermal convection and multiphase flow in bubble columns<sup>41</sup>. To develop the use of a scalar equation for the transport of the gas phase with the need for further application to modelling the motion of more than one discrete phase<sup>i</sup>.

### 4.2 Mathematical models

#### *Energy transport*

Heat transport has long been established in the modelling of turbulent flows particularly when simulating natural convection in cavities with large height to diameter ratios<sup>39-40</sup>. The simulation of lateral convection of heat the across the width of the mesh provides an excellent example of how to simulate the turbulence in buoyancy driven flows. As there is an analogy between both multiphase flow in bubble columns and natural convection it would seem prudent to attempt to model the transport of the discrete phase in a similar manner<sup>41</sup>. To use this technique effectively it would be wise to test the capacity of Fluent<sup>9</sup> to simulate natural

---

<sup>i</sup> See §5.0 for the modelling of gas-liquid-solid flows in bubble columns

convection, utilising the work of Chait and Korpela as an example of how to simulate such flows for reasons of geometric consistency<sup>40</sup>.

The thermal transport equation (Equation 41) has the general form of a transport equation with time dependent and the non-linear velocity terms on the left hand side. On the right hand side is the temperature gradient and the velocity coupling term. These last two terms are intrinsic to the accurate prediction of the structure of both the velocity and temperature fields and how each of the variables influences the other parameter. Along with the energy transport equation, the conservation of mass and momentum (Equation 42 and Equation 43) are used to predict and check the pressure and velocity fields. The fluid density varies with temperature and this variation is calculated through the use of the Boussinesq approximation (Equation 45), which is then applied to the transport equations (Equation 41 to Equation 43).

### ***Transport of turbulence***

The k- $\epsilon$  turbulence equations are used to depict the transport of energy between large and small vortices in the velocity field. The energy transport is modelled through the use of a pair of coupled transport equations (Equation 25 and Equation 26) that describes the generation of energy due to motion (conversion from one source i.e. density difference to another) in the one equation (Equation 25) and dissipation of that energy in the other (Equation 26). This effectively characterises the growth and evolution of vortices caused by some form energy input be that agitation from heat, another fluid or the motion of a solid object.

Previous investigations into gas-liquid motion<sup>i</sup> suggest the use of a more complex model for the closure of the transport equations, by the use of Reynolds stresses; Equation 31 shows the exact Reynolds stresses turbulence transport equation. The equation utilised in Fluent<sup>9,11</sup> is simplified into several different equations to reduce the complexity of the formulation and to enable closure of the exact equation in the mathematical models. This includes the use of both the k- $\epsilon$  equations (Equation 25 and Equation 26) and the inclusion of the effects of buoyancy, pressure, pressure-strain and any rotation (Equation 32 to Equation 40). Note that the number equations used depends on whether the domain used is two or three-dimensional.

---

<sup>i</sup> See §3.0 for discussion of the effects of turbulence transport models on multiphase flow

In the prediction of natural convection it is beneficial to the numerical solution of the transport equations to split the flow into basic and secondary flow (Equation 50) quantities<sup>39-40</sup>. The basic flow quantity is a known profile that was determined by the laminar flow conditions. The secondary flow is determined by taking an x-y average of the Navier-Stokes equation and this then represents the effect of the Reynolds stresses. Using such a profile is relevant to multiphase flow based on the density difference driving force by analogy with natural convection<sup>41</sup>. The profiles used for both types of flow can be found for temperature, volume fraction and the velocity parallel to the direction of the flow (Equation 51, Equation 52 and Equation 60). A series of functions in Fluent<sup>9</sup> are employed to update parameters such as temperature, velocity and volume fraction of the gas phase. The functions used are defined as the DEFINE\_ADJUST, DEFINE\_INIT and DEFINE\_ON\_DEMAND functions, where the DEFINE\_ADJUST functions updates the variable for every iteration and the DEFINE\_ON\_DEMAND function is utilised when an execute command is exercised in a defined sequence enabling the quantity to be updated when the user specifies. The DEFINE\_INIT function is used to initialise the flow-field with the basic profiles<sup>1</sup>.

### *Algebraic slip mixture model<sup>9,26</sup>*

The investigations of Zuber, Findlay, Ishii and Mishima provide the physical and theoretical basis for the application of a continuum mixture approach to the simulation of multiphase flow<sup>24,27-28</sup>. Allowing the discrete and continuous phases to be considered as a pseudo-continuous mixture, a single continuity equation (Equation 1) and a single momentum equation (Equation 2) were employed to assess mixture phase transport. To predict the mixture phase composition a volume fraction equation for the discrete phase (Equation 3), a mixture density (Equation 4) and a mixture viscosity (Equation 5) must be employed to characterise gas-liquid or solid-liquid interactions. However, the phases have distinct interactions that influence the transport of each phase and this is characterised by the use of mass-averaged, drift and slip velocities (Equation 6, Equation 7 and Equation 8) for the mixture. The slip or relative velocity was obtained by averaging a combined momentum equation for the discrete phase and the mixture according to the principles of local equilibrium and Favre averaging. Assumptions made as part of the averaging procedure are that the pressure is the same for all phases and that only viscous drag influences particle

---

<sup>1</sup> See §11.1 for the source code to update the flow variables and Table 2 in §12.2 for user function definitions

motion leading to fluctuating form of slip velocity. A constitutive equation is then employed to account for the fluctuating terms to further simplify the relative velocity<sup>25</sup>.

The formulation of the mixture phase for one flow regime is not the same for another and this has a critical influence on how the driving forces and frictional effects (employing Equation 9 where the Reynolds number, Equation 10, is based on the particle diameter as the characteristic dimension) are considered when modelling such flows<sup>24-28</sup>. The regimes vary according to discrete particle size, the volume fraction and the distribution of particle sizes. Predicting flow phenomena in the heterogeneous regime increases the complexity of the description of the mixture phase, as different bubble sizes are more prevalent. Therefore, to simplify the models employed we concentrate on flow predictions in the homogeneous regime, where a single bubble size is assumed.

### ***Modified scalar equation mixture model***

The scalar transport model can be used to model the transport of any parameter such as volume fraction of a phase, heat, the influence of electromagnetism etc<sup>9</sup> and is used in conjunction with basic continuity (Equation 42) and momentum (Equation 53) equations. The scalar equation employed here models the transport of a pseudo-continuous discrete phase that has the form of Equation 54 where the diffusion coefficient used,  $\Gamma$ , was defined as 0.1 for the discrete phase volume fraction equation. To depict the transport of the discrete phase, Equation 55 and Equation 56 are source terms that are applied to Equation 53 and Equation 54 respectively. The first term in both source terms is the deviatoric stress tensor and the last term is the inter-phase interaction term as calculated by the drift velocity. The second term in Equation 56 is the convective flux of the discrete phase noting that there are two convective fluxes with one for the mixture phase. The scalar volume fraction equation is different to the volume fraction formulation used in algebraic slip mixture model<sup>26</sup> where the diffusive flux term and deviatoric stress tensor are not included. The drift velocity is calculated through the use of the mixture density (Equation 4), mass-averaged, drift and slip velocity formulations (Equation 6 to Equation 10). The mixture viscosity is calculated using

Equation 57 to Equation 59, this differs from the algebraic slip mixture model<sup>9,26</sup> which only employs Equation 5<sup>i</sup>.

### 4.3 Model parameters

From §2.0 the plan for this investigation of multiphase flows in bubble columns, the development of the solid phase transport scheme can be split into four stages. The first two are dealt with in this section by examining Fluent's<sup>9</sup> energy model to determine how to model buoyancy driven flow with the appropriate turbulence models and conditions and then applying these specifications to the transport of the gas phase motion in a liquid medium. The final two stages involve the transport of gas and solid phases through a liquid medium, which will be investigated in the next section<sup>ii</sup>. Of the two stages in this section the first stage is a test of the ability of Fluent to model turbulent buoyancy driven flow, where the density difference driving force is caused by changes in temperature across the domain. The second stage is application of the appropriate turbulence models to two mixture model formulations representing the gas phase, from which comparisons of the efficacy of the models between the experimental and simulated data is made. The two mixture models investigated are the standard scheme available in Fluent<sup>9</sup> and a modified scalar transport equation that represents the volume fraction equation for the gas phase.

#### *Boundary conditons*

The meshed domains are two-dimensional planes with height to width ratios of 50:1 (in an attempt to model a vertical cavity of infinite extent) and 5:1. The high aspect ratio mesh contains 5000 cells (500 by 10) and the lower aspect ratio mesh contains 2000 cells (100 by 20). Four walls surround the large aspect ratio mesh to which temperature conditions are applied, whereas for the small height to width ratio mesh, the velocity inlet and outlet conditions are applied to the bottom and the top of the mesh. The inlet condition is only applied to 80% of the base of the column, with the remaining boundaries being treated as

---

<sup>i</sup> See §11.1 and §11.2 for the source code consisting of source terms and variable adjustments and Table 2 in §12.2 for user function definitions

<sup>ii</sup> See §5.0 for solid-liquid and gas-liquid-solid flow implementations

walls. The conditions applied to the boundaries include the volume fraction and the inlet velocity of the discrete phase modelled<sup>i</sup>.

The physical properties of the fluids simulated include the density, the viscosity, the specific heat capacity, the thermal expansion coefficient and the thermal conductivity of each of the fluids. The fluid phase density and viscosity are defined as  $1.225 \text{ kg m}^{-3}$  and  $1.7894 \cdot 10^{-5} \text{ kg m}^{-1} \text{ s}^{-1}$  for air,  $998.2 \text{ kg m}^{-3}$  and  $1.003 \cdot 10^{-3} \text{ kg m}^{-1} \text{ s}^{-1}$  for water. The diameter for the air bubbles was 5 mm assuming that the form of the particles is spherical. The definition of the fluid phase when predicting the transport of energy through the fluid, air, required the specific heat capacity, the thermal expansion coefficient and the thermal conductivity to be defined as  $1006.43 \text{ J kg}^{-1} \text{ K}^{-1}$ ,  $1.766069 \cdot 10^{-8} \text{ K}^{-1}$  and  $2.42 \cdot 10^{-2} \text{ W m}^{-1} \text{ K}^{-1}$ . The expansion coefficient was determined by using the Grashof number formulation (Equation 46) by assuming a value of 8500 and using the fluid parameters, the Prandtl number (Equation 48) was assumed to be 0.74<sup>ii</sup>.

### ***Solution strategies***

For the solution of lateral convection where a linear temperature gradient over the range 300 to 310 K was applied to the domain through the use of wall boundary conditions at 300 K for the left wall and 310 K on the right wall using Equation 52. A cubic velocity profile is applied to the vertical velocity field, with an inflection point at the mid-point of the mesh in the horizontal direction (Equation 51)<sup>iii,iv</sup>.

To obtain a comparable converged solution of the temperature and velocity fields, a series of twenty cases were performed to determine the best solution strategy. The first ten cases involved the adjustment of the under-relaxation factors for the Reynolds stresses transport model by changing the value between 0.1 and 1, incrementing the factor by 0.1 for each case simulated. The application of the basic flow profiles to the domain for the ten cases were based on the DEFINE\_ON\_DEMAND and DEFINE\_INIT user functions, to update the parameter fields for the temperature and the vertical velocity after every time-step and to

---

<sup>i</sup> See Table 5 and Table 8 in §12.3 where the flow domains are specified

<sup>ii</sup> See Table 1 in §12.1 for physical property definitions and Table 2 in §12.2 for user function definitions

<sup>iii</sup> See Table 15 to Table 17 in §12.4 for solver specifications for thermal convection

<sup>iv</sup> See §11.1 for the coding required to update the turbulent flow variables and Table 2 in §12.2 for user function definitions

initialise the solution at the beginning of the simulation. This approach provides the most relevant solution of all the cases specified in the next the ten cases and is, therefore, a more accurate test of the influence of the under-relaxation factor.

To describe the influence of each method in order to obtain a solution the next ten cases were applied, five utilising the k- $\epsilon$  turbulence transport model and the remaining five cases employing the Reynolds stresses transport of turbulence. The following approaches were implemented:

- no basic profiles for the temperature and the velocity
- no basic profile for the temperature, but the profile for the velocity is updated before every iteration, using the DEFINE\_INIT and DEFINE\_ADJUST functions
- no basic profile for the temperature, but the profile for the velocity is updated once every time-step, using the DEFINE\_INIT and DEFINE\_ON\_DEMAND functions
- profiles for both the temperature and the velocity, which are updated every iteration, using the DEFINE\_INIT and DEFINE\_ADJUST functions
- profiles for both the temperature and the velocity, which are updated once every time-step, using the DEFINE\_INIT and DEFINE\_ON\_DEMAND functions.

Each of the above cases were run for 500 seconds with a time-step size of 0.2 seconds to ensure that the correct flow phenomena was observed for validating the use of the energy and turbulence transport models in the software code<sup>9</sup>. All under-relaxation factors for the last ten cases were set to 1 except for the k- $\epsilon$  and Reynolds stresses transport equations, which were 0.1.

Applying the above turbulence models to the prediction of gas-liquid flow in a bubble column is the next part of this section. The gas (air) and liquid (water) mixture is represented by either the (standard) algebraic slip mixture model<sup>9</sup> or the modified scalar equation form of the mixture model for these simulations<sup>i</sup>.

The standard mixture model<sup>9</sup> is applied using the techniques described in §3.3, with the use of the body force weighted, QUICK<sup>42</sup> and the SIMPLEC<sup>45</sup> methods for the discretisation and

---

<sup>i</sup> See Table 18 and Table 19 in §12.4 for gas-liquid flow model, solver and variable specifications and Table 2 in §12.2 for user function definitions

solution of the continuity and momentum equations and the coupling of the velocity and pressure. With under-relaxation factors including 0.1, 0.3, 0.7 for slip velocity, pressure, volume fraction and momentum equations respectively, all remaining terms are set to 1<sup>26,32-33</sup>. Except for the Reynolds stresses model, which has an under-relaxation factor of 0.1, the scalar transport equation is solved in a similar manner to the mixture model, but to couple the effect of the volume fraction equation of the gas phase to the momentum equation, a series of user-defined functions were employed. These include calculation of the mixture phase properties, momentum and scalar equation source terms, plus variable adjustment to calculate drift, phase and slip velocities<sup>i</sup>.

The subroutines that calculate the mixture phase properties are the DEFINE\_PROPERTY routines and are applicable to any of the physical properties used for prediction of flow, energy or mass parameters. To calculate mixture phase density and viscosity Equation 4, Equation 57 and Equation 59 describe how the functions GLMU and MR are defined. The next subroutines are used to calculate the source terms and introduce additional force terms into the transport equations. The momentum equation source terms calculate the inter-phase interaction term, i.e. the square of the drift velocity for each discrete phase and the appropriate deviatoric stress tensor for the respective momentum equation<sup>25</sup>. The source term for the volume fraction equation also has an inter-phase interaction term, but the drift velocity is not squared<sup>25</sup>. The other terms are the deviatoric stress tensor for both the x and y directions (remembering that the mesh used is two dimensional) and a mass-flow rate term for the gas phase. The mass-flow rate term is a product of the gas phase fraction, density and gradient of the component velocities with respect to the height and width of mesh cells for the evenly spaced two-dimensional mesh.

To predict the gas-liquid interactions a DEFINE\_ADJUST function was employed to perform calculations of the drift, phase and slip velocities. To do this, user-defined memory arrays are accessed (C\_UDMI(c,t,i) where c is the cell volume, t is the cell surface thread, i is the index of the allocated memory array) to store calculated velocity variables as global variables for use in the DEFINE\_SOURCE subroutines. In predicting the slip velocity<sup>26</sup>, the particle Reynolds number is assessed through the RE macro, which in turn is used in the drag coefficient macros CD1 and CD2 to predict the terminal velocity of the particle. The resultant

---

<sup>i</sup> See §11.2 for the source code consisting of source terms and variable adjustments and Table 2 in §12.2 for user function definitions

terminal velocity is then multiplied by the sum of the total velocity derivative and the gravitational acceleration, i.e. the slip velocity equation (Equation 8)<sup>24-28</sup>. Then drift velocity was determined by subtracting the mixture velocity (employing Equation 7). As only two-phase interactions are calculated the drift velocity equation can be used to predict the gas velocity, but this relationship is multiplied by the gas fraction. Next the liquid phase velocity is back calculated from a rearranged form of the mixture phase velocity (Equation 6) with the previously calculated gas and mixture phase velocities and then the mixture phase velocity is recalculated using Equation 6. Depending on the turbulence modelling method the mixture phase velocity is substituted into Fluent's<sup>9</sup> component velocity arrays in the DEFINE\_ADJUST or DEFINE\_ON\_DEMAND subroutine where an experimental vertical velocity profile is updated after every time-step (noting that the vertical velocity field is initialised by the DEFINE\_INIT subroutine prior to the solution of the flow field proceeding).

To test comparisons between alternative turbulence transport formulations of the scalar transport equation, these results were then matched with the results of the experimental investigations of Degaleesan and Kumar<sup>26,35-37</sup> and the standard mixture model results<sup>9</sup>. In this investigation the turbulence models applied to the fluid mixture include:

- k-ε turbulence transport
- Reynolds stresses turbulence transport
- Reynolds stresses turbulence transport with the “updating” of the vertical velocity profile using DEFINE\_ON\_DEMAND function every time-step and the DEFINE\_INIT function to initialise the velocity field.

The fraction of the gas phase at the inlet was defined as 0.6 and as a flux rather than as a specific value. The outlet condition at the top being treated as a free slip fixed boundary with a scalar flux condition. For reasons of repeatability with previous multiphase calculations<sup>i</sup>, the superficial gas velocity applied to the inlet was 2 cm s<sup>-1</sup> (within the homogeneous flow regime) and the time step-size remains as 0.1 seconds for 6000 steps.

---

<sup>i</sup> See §3.3 for the gas-liquid model boundary condition

## 4.4 Results and discussion

The calculations performed for this section involves the unsteady convective transfer of thermal energy across a long thin vertical cavity and the turbulent transport of a bubbly gas in a liquid medium with the results presented in §13.2. Therefore, discussion of the results is split into two sub-sections for the respective transport models.

### *Thermal convection in a cavity*

Figure 27 presents the change in the stream function calculated after 500 seconds of simulation time for the linear temperature problem for the 50:1 height to width aspect ratio mesh. Each solution is dependent on the under-relaxation factor applied to the turbulence equations (i.e. the  $k$ ,  $\varepsilon$  and Reynolds stresses equations). As Figure 27 shows the only solution that has vortical structures of less than five mesh widths are for the result with an under-relaxation of 0.1. This result corresponds to the solutions obtained by Nagata and Busse<sup>39</sup> plus Chait and Korpela<sup>40</sup> to a reasonable standard of accuracy for the purposes of this investigation. The smaller vortices vanish for the simulations with under-relaxation factors that are greater than 0.1 for the turbulent flow models. The fact that the smaller vortices occur at such a low relaxation factor on the turbulence models raises a few questions to the validity of the mesh, boundary conditions and the turbulence and energy transport models employed in the prediction of heat transport by lateral convection<sup>9</sup>.

The results from Figure 28 in §13.2 are calculated through the application of different secondary flow methods and turbulence transport model for which there are ten cases<sup>i</sup> and these are presented as:

- A, no basic profiles for the temperature and the velocity using Reynolds stresses turbulence transport
- B, basic profile for the velocity only, which is updated before each iteration using Reynolds stresses turbulence transport
- C, basic profile for the velocity, which is updated after each time-step using Reynolds stresses turbulence transport

---

<sup>i</sup> Referring to the Solution Strategies in §4.3.

- D, profiles for both the temperature and the velocity, which are updated before each iteration using Reynolds stresses turbulence transport
- E, profiles for both the temperature and the velocity, which are updated after each time-step using Reynolds stresses turbulence transport
- F, no basic profiles for the temperature and the velocity using Reynolds stresses turbulence transport
- G, basic profile for the velocity only, which is updated before each iteration using Reynolds stresses turbulence transport
- H, basic profile for the velocity, which is updated after each time-step using Reynolds stresses turbulence transport
- I, profiles for both the temperature and the velocity, which are updated before each iteration using Reynolds stresses turbulence transport
- J, profiles for both the temperature and the velocity, which are updated after each time-step using Reynolds stresses turbulence transport

Of the results obtained vectors of velocity (Figure 28 I), contours of stream function (Figure 28 II) and total temperature (Figure 28 III) are presented to show the effectiveness of the techniques used. It is observed that vectors of velocity in Figure 28 I display vortical structures that are only just over the width of the mesh in cases H and J that were solved with the Reynolds stresses model application and the “updating” of flow parameters after the completion of each time-step. The corresponding contours of stream-function and temperature for cases H and J also show the effects of the buoyancy driven flow influencing the structure of temperature field. All the remaining cases presented in the vector and contour plots of Figure 28 do not show any of the characteristics observed in the results of cases H and J. The velocity vectors and contours of stream function in these two cases correspond to the results presented by Nagata and Busse<sup>39</sup> plus Chait and Korpela<sup>40</sup> with column wide vortical structures. By analysing the differences between cases H and J, it was found that the inclusion of a temperature profile in the “updating” of parameters has little or no effect on the predicted velocity or temperature fields. Therefore, using the analogy between the transport of heat and discrete phases caused by differences in density<sup>41</sup> in considering the solution of the transport equations it would be prudent to consider using the basic profile “updating”<sup>i</sup> in the calculation of the buoyancy driven flow in gas-liquid and gas-liquid-solid simulations of bubble columns.

---

<sup>i</sup> i.e. the addition of a laminar flow profile to the secondary flow quantities (discussed in §4.2 and §4.3)

Particularly with the “updating” of the vertical velocity after the completion of each time-step when using Reynolds stresses turbulence transport model with an under-relaxation factor of 0.1.

### ***Gas-liquid transport***

The gas-liquid simulations for both the standard and the modified scalar transport equations were performed for a period of 600 seconds of simulation time, for reasons of consistency with the results of §3.0. Again to characterise the flow phenomena modelled, time series of the vertical mixture velocity plus time-averaged profiles of vertical velocity and the gas fraction are presented between Figure 29 and Figure 33. Along with the profiles plots describing the flow characteristics, field plots of vectors of velocity for the mixture phase (Figure 34) and contours of the gas fractions are also provided (Figure 35).

Figure 29 presents a time series of the vertical mixture velocity at a height of 0.5 m above the base of the column and was located in the centre of the column. As in §3.0 the parameters that are presented here are recorded at half-second intervals to give the curves observed. There are two sets of data for the curves, derived from the modified scalar equation (A) and the algebraic slip (standard) mixture model<sup>9</sup> (B), each series presents the data for the k- $\epsilon$  turbulence (Black curve), the Reynolds stresses (Red curve) and the basic profile “updating” with Reynolds stresses (Blue curve) models.

For the k- $\epsilon$  turbulence calculations in series B, there is little or no change to the solution for the majority of the simulation. Except for an initial 50-second period during which time the gas-liquid flow interactions and structures develop. The scalar time series with k- $\epsilon$  turbulence displays a regular oscillation with a time period of 25 seconds that first appears within 50 seconds of the gas flow starting (Figure 29). The time-period for the two-dimensional scalar equation case is almost 1.5 times greater than the regular oscillation that was observed for the three-dimensional simulation with the standard model (Figure 19). The increase in the time-period for the scalar equation model could be as a result of ignoring the third dimension and therefore, suppressing the motion of the vortices through the tangential axis of the column.

The use of the Reynolds stresses case produced an unsteady result for both the scalar equation and the standard mixture model<sup>9</sup>. There is a difference between the results in that the scalar

case does not produce the regular oscillations that were observed with the standard model. The time period for the standard model was approximately 10 seconds and becomes regular after 50 seconds of simulation time<sup>9</sup>. The interactions modelled by the scalar equation begin to oscillate within 5 to 10 seconds of the flow being initialised, though using the scalar equation resulted in a random variation in the velocity observed.

The effect of adding<sup>i</sup> the basic velocity profile to the predicted velocities after each time-step increased the average velocity that was observed for both modelling methods. The basic profile obtained from the experimentation of Degaleesan<sup>35-36</sup> influences the velocities observed even when the profile was multiplied by a factor of 0.1. For the simulations with the scalar equation model for gas-liquid flow, the difference between the two Reynolds stresses cases for the averaged velocity was  $6.7 \text{ cm s}^{-1}$ . In contrast when the standard model<sup>9</sup> was employed with the velocity “updating” the oscillation also develops after 50 seconds but at a higher average velocity than the case without the velocity “updating” giving a difference of  $4.9 \text{ cm s}^{-1}$ . A distinct regular oscillation occurs with a time-period of 10 to 15 seconds for the standard and the turbulent Reynolds stresses models with the velocity “updating”.

Profile plots of the vertical mixture velocity across the width of the mesh for the scalar (A) and standard<sup>9</sup> (B) mixture modelling methods can be found in Figure 30. The  $k$ - $\epsilon$  turbulence ( $\Delta$ ) curves show parabolic forms though the velocity magnitudes for both modelling methods; there is over-prediction of the profiles though this is less significant for the standard model compared to the scalar equation form of the mixture model. The form of the two curves produced by the each scheme is different, with a symmetric profile for the standard model curve and an asymmetric profile for the modified scalar profile. The differences can also be observed in the location at which the velocity has a value of  $0 \text{ m s}^{-1}$  by the fact that the radius for the scalar result is greater than the experimental curve<sup>35-37</sup> ( $\times$ ) and the standard model<sup>9</sup> is less than the experiment.

The magnitude of the average velocities as discussed before for Figure 29 showed that the basic profile “updating” over-predicts the simulated cases solved without the basic profile ( $\ast$ ) by approximately  $5 \text{ cm s}^{-1}$ , but the average velocity for the standard model at this point is  $8 \text{ cm s}^{-1}$  larger than the experimental case. The corresponding difference between the velocities

---

<sup>i</sup> i.e. the addition of a laminar flow profile to the secondary flow quantities (discussed in §4.2 and §4.3)

for the experimental result and the modified scalar equation case without velocity “updating” was  $1 \text{ cm s}^{-1}$ . Therefore, from the form of the profiles the scalar transport model is more representative of gas-liquid transport in a bubble column than the standard mixture model available in Fluent<sup>9</sup>. The use of the Reynolds stresses model with the scalar equation in capturing the turbulent gas-liquid interactions results in a profile that has a greater accuracy than both the k- $\epsilon$  turbulence case and the Reynolds stresses model where the velocity was updated.

Both the mixture models that are solved with the Reynolds stresses turbulence model show the change in magnitude when “updating” the basic flow profile ( $\diamond$ ). The form of the profiles for each model does not change, just the scale of the velocities observed as discussed above. Note that the form of parabolic profile is flatter and wider for the scalar equation model compared to the standard mixture model<sup>9</sup>. This is confirmed by the location at which the velocities changing from positive to negative. The scalar equation cases and the profile updated standard model case cross over the zero velocity within 0.005 m of the experimental case. The standard mixture model case without “updating” the profile is much less than all the remaining profiles Figure 31 displays the liquid velocity corresponding to the mixture velocities presented in Figure 30. As the gas phase fraction is relatively small compared with the liquid fraction, there is little change in the form of the curve and the magnitude of the velocities; this effect is valid for both of the modelling methods when comparing the mixture and liquid phase velocities.

Figure 32 depicts the gas phase vertical velocity across the width of the column for the modified scalar (A) and standard mixture models (B). The standard model produces similar curves to that of the liquid and mixture phases, with narrow parabolic profiles for the Reynolds stresses turbulence cases and a wider/flatter profile for the k- $\epsilon$  turbulence transport model. The only difference from the previous curves for the liquid and mixture phases (Figure 30 and Figure 31) being that the magnitude of the velocities is always positive and the maximum velocities are of the order of  $65 \text{ cm s}^{-1}$ .

The gas phase velocities for the modified scalar equation profiles are wholly different. The shape of the profiles for both turbulent Reynolds stresses methods are the same with three shallow peaks, one peak at either wall and a peak in the column centre between 25 and 50  $\text{cm s}^{-1}$ . The k- $\epsilon$  turbulence case has one large peak to the right side of the domain with velocities

up to  $2.25 \text{ m s}^{-1}$ . The gas velocity profile for the k- $\epsilon$  turbulence case helps to explain why there is an asymmetry in both of the mixture and liquid phase profiles.

The gas phase fractions are presented in Figure 33. The modified scalar equation hold-up (A) profiles lies across the range of the experimental data with a flat, plug flow profile. The standard model under-predicts the volume fraction by 2 % but instead of the plug flow form the standard model has a parabolic form. Both models produce curves that are unlike the experimental data, which has a discontinuous form though could be said to peak at  $\sim 14\%$  gas between  $|0.03|$  and  $|0.07|$  m from the column centre. The profiles predicted by scalar equation do correspond to hold-up profiles presented by Joshi<sup>47</sup>.

Figure 34 illustrates the vector fields for the different turbulence modelling methods applied to the scalar (Figure 34I) and standard<sup>9</sup> (Figure 34II) mixture model formulations. As discussed in §3.4 the vector fields produced by the k- $\epsilon$  turbulence with the standard mixture model<sup>9</sup> are steady and consist of two large circulation patterns, with the bulk of the flow in the vertical direction (plots A and B in Figure 34II). The flow pattern that arises for the scalar mixture model when solved with k- $\epsilon$  turbulence case (plots A and B in Figure 34 I) is different with unsteady elongated vortices on top of a large column diameter eddy at the base of the column. The vector fields observed in plots A and B of Figure 34 I correspond to phenomena observed from the k- $\epsilon$  turbulence simulations with the cylindrical column (plots C and D in Figure 24).

Unsteady flow structures of smaller, column diameter scaled vortices are observed with the Reynolds stresses model applications of the turbulence models for both multiphase models (C-F plots in Figure 34). The vector fields resemble the complex structures that were predicted in simulations by Sokolichin and Eigenberger<sup>17,20-23</sup>. The scalar equation case with basic flow profile “updating” depicts smaller vortices that are comparable to the vector fields for standard model<sup>9</sup>, where the velocity “updating” has little or no influence on the vector field. This leaves plots, C and D, for the vector fields derived from the scalar equation model (Figure 34I) displaying elongated vortices that spread either side of the column diameter.

The effect of the vector field on the gas fraction is observed in the contour profiles for the volume fraction in Figure 35 where there is little difference between the respective Reynolds

stresses turbulence modelling methods. The scalar equation cases (plots C-F in Figure 35 I) show a diffuse gas field with subtle influence of the vector field, but the standard model<sup>9</sup> shows a greater influence of the flow structure with eddies flicking the bubble plume from the left side of the column to right and vice versa (plots C-F in Figure 35 II). The k- $\epsilon$  turbulence cases show the influence of the vector structures with a steady diffuse plume for the standard model<sup>9</sup> and the equivalent scalar equation case depicts gas phase motion that is influenced by the vector field as for the cylindrical simulation as displayed in Figure 26.

## 4.5 Conclusions

The linear thermal transport problem across a large height to width ratio cavity indicates the methods of turbulence model applications required to obtain an unsteady flow structure with eddies that have a diameter equivalent to the mesh width. The only method to produce an unsteady flow structure was the Reynolds stresses model where the “updating” of vertical velocity profile took place after each time-step. The principles derived from this method of solving thermal convection in a cavity were then applied to gas phase transport through a liquid medium according to the analogy between buoyant thermal convection and multiphase flow in bubble columns<sup>41</sup>. Two modelling approaches testing the solution of the gas-phase transport and the slip velocity equations combined with the k- $\epsilon$  and Reynolds stresses turbulence models to predict the unsteady motion of a continuum gas phase.

Comparing the influence of different turbulence modelling methods on the gas phase transport, it was determined that the Reynolds stresses model captures the unsteady nature of bubble columns through the variation in the velocity. The gas hold-up and velocity profiles were averaged with respect to time correspond to the profiles presented by Sanyal et al<sup>26</sup>, Degaleesan et al<sup>35-36</sup>, Kumar<sup>37</sup> and Joshi<sup>47</sup>. The influence of k- $\epsilon$  turbulence model on the solution of the gas flow models results in a steady flow for the standard model<sup>9</sup> and an unsteady flow for the modified scalar equation where the flow structure corresponds to the cylindrical simulations that were described in §3.0. The time-averaged profiles were asymmetric for the modified scalar equation model that was solved with k- $\epsilon$  turbulence. This is particularly prevalent in the gas phase velocity, where velocities of up to 2.25 m s<sup>-1</sup> were predicted resulting in an asymmetric profile. All the other gas-liquid simulations presented in this thesis predicted maximum gas velocities between 40 and 70 cm s<sup>-1</sup>. Therefore, the

modified scalar equation when used with Reynolds stresses is appropriate for representing the volume fraction of the discrete phase when considering solid phase transport, particularly for the low fractions that are observed in biochemical reactors. The scalar equation is important in attempting to solve gas-liquid-solid flows, as each discrete phase requires a volume fraction equation and this cannot be achieved with the standard mixture model currently available in Fluent 5<sup>9</sup>.

Further improvements to bubbly flows would be to model the transport of multiple gas phases where each volume fraction equation is solved for a specific bubble size. This allows for the simulation of coalescence and bubble break-up caused by turbulent fluid interactions and enabling a more accurate representation of the gas phase fraction in bubble columns and airlift reactors. The aim of this investigation is to provide first case scenario for a gas-liquid-solid flow where a biochemical reaction occurs<sup>i</sup>. Investigating the effect of multiple bubble sizes with bubble coalescence and break-up would move away from the remit of the research discussed. Other effects that have not been included in the models and require investigation are comprehensively discussed in Joshi's review of bubble column investigations, such as the influence of multi-dimensional flows, bubble wakes, energy transport due to bubble motion etc<sup>47</sup>.

---

<sup>i</sup> See Acknowledgements, §1.0 and §2.0 referring to the scope of the project ERB N° IC15-CT98-0904

## 5.0 GAS-LIQUID-SOLID FLOW MODELLING IN BUBBLE COLUMNS

### 5.1 Plan

To model solid phase motion through a liquid phase in 5:1 height to width ratio mesh, a slug of solid particles was injected through a small inlet at the top of the column for ten seconds of simulation time and continuing the simulation for a further 190 seconds for:

- standard mixture model<sup>9</sup>
- scalar transport equation<sup>9</sup> with the subroutines used in §4.0 to represent the transport of a solid phase

To model gas-liquid-solid flow in a 5:1 height to diameter aspect ratio bubble column, in a similar fashion as the solid-liquid flow, utilising three modelling approaches:

- implementing the scalar transport equation<sup>9</sup> to predict gas phase motion and the standard mixture model<sup>9</sup> to predict solid phase transport
- using the scalar transport equation<sup>9</sup> to predict solid phase motion and the standard mixture model<sup>9</sup> to predict gas phase transport
- employing two scalar transport equations<sup>9</sup> to predict the motion of both phases, with one equation assessing the volume fraction of the solid phase and the other equation calculating the gas phase volume fraction.

This section continues the development of schemes that predict the transport of a solid phase in a bubble column, where the major driving force is the difference in density between the gas and liquid phases. Before the gas-liquid-solid flow models are implemented for low solid fractions (<1%), the mixture models must be tested for their efficacy in solving solid phase transport assuming that the accuracy of the gas-liquid mixture models from §4.0 is retained. This is difficult to achieve without experimental validation of these “toy” tests, as velocity and phase fraction profiles are not easy to obtain. Both of these models do not allow for particle collisions and interactions as described by Gidaspow<sup>48-49</sup>, Padial<sup>50</sup>, Fan<sup>51-52</sup> and Michele<sup>53-55</sup> but as low fractions are used the influence of these effects are assumed to be small. After this both phases can be simulated either as a combination of both modelling

methods (see above) or by using two scalar equations to represent the volume fraction of each phase. This is so that the influence of one discrete phase over the other phases can be determined, though no quantitative results can be used for design of columns as no experimental comparisons are made between parameters such as velocity, volume fraction and the physical properties.

## 5.2 Mathematical models

### *Mixture models*

The models described in the previous sections, when modelling multiphase flows in bubble columns, were based on the studies of Findlay, Ishii, Mishima and Zuber<sup>24,27-28</sup>. The studies provide the physical and theoretical basis for the application of a continuum mixture approach as single set of continuity (Equation 1) and momentum (Equation 2) equations employed in the simulation of multiphase flow<sup>24-28</sup>. Their investigations present a comprehensive discussion of the features of such flows, through the provision of equations that enable the calculation of the mixture phase composition, i.e. density (Equation 4), viscosity (Equation 5) and volume fraction (Equation 3). From these relationships, the influence each component phase has on the continuum mixture was predicted through the use of drift, mass-averaged and slip velocities (Equation 7, Equation 6 and Equation 8) for the mixture. For the purposes of the investigations into the application of the turbulence models and gas-liquid-solid flow in a bubble column required the use of user-defined functions with a scalar transport equation along side the standard mixture model<sup>9</sup>. Prior to three-phase model implementation, the ability of each mixture model to capture solid phase motion was tested and compared against one another.

For the homogenous flow regime of discrete phase motion the solid particle phase can be treated in a similar fashion to the bubbly gas phase<sup>24-28</sup>, so there is little change to equations used. As in the previous section<sup>i</sup> the scalar transport equation is used in conjunction with the standard continuity (Equation 42) and momentum (Equation 53) equations. The conservation equations are used to model the transport of a pseudo-continuous discrete phase that has the form of Equation 54 where the diffusion coefficient used,  $\Gamma$ , was defined as 0.1. The

---

<sup>i</sup> See §3.2 and §4.2 for further discussion of mixture and multiphase flow models

diffusion coefficient is kept the same for both volume fraction equations. To model the transport the discrete phase, Equation 55 and Equation 56 are source terms that are applied to Equation 53 and Equation 54, respectively. The first term in both source terms is the deviatoric stress tensor and the last term is the inter-phase interaction term as calculated by the drift velocity utilising Equation 4 and Equation 6 to Equation 10. The mixture viscosity was calculated using Ishii et al<sup>28</sup> viscosity formulation (Equation 57 to Equation 59), differing from the standard mixture model<sup>9</sup> which only uses Equation 5.

### ***Transport of turbulence***

The transport of turbulent energy is difficult to predict with many unknown and immeasurable parameters that influence the transport of energy and vortices in a turbulent flow. Therefore, to capture all these effects requires the use of a complex model such as the Reynolds stresses model. Equation 31 shows the exact Reynolds stresses equation, with many unknown terms. The solver employs the Reynolds stresses in a series of equations to enable closure of the unknown terms in the exact equation<sup>9,11</sup>. This includes the use of both the k- $\epsilon$  turbulence equations (Equation 25 and Equation 26) and the inclusion of the effects of buoyancy, pressure, pressure-strain and any rotation (Equation 32 to Equation 40).

## **5.3 Model parameters**

Here we continue the development of the solid phase transport from the first two stages that were examined in the previous section through investigations into the efficacy of turbulence models in buoyancy driven flows<sup>i</sup>. The remaining stages involve the reapplication of the mixture model where the discrete phase represents a heavier or solid phase and the implementation of gas and solid discrete phases for gas-liquid-solid flow in a bubble column. The two mixture models used in §4.0 are also used to investigate the solid phase motion, as a comparative technique in the effectiveness of the models, though no comparisons with experimentation are made here, the numerical comparisons must be used to prove the efficacy of the models that represent solid phase transport.

---

<sup>i</sup> See §4.0 for the modelling of turbulence in buoyancy driven flows

### ***Boundary conditons***

The domain used was a two-dimensional plane with a height to width ratio of 5:1 containing 2000 cells (100 by 20). The boundary conditions through which the discrete phases were injected into the domain consist of velocity inlets. The conditions applied to the boundaries include the volume fraction and the inlet velocity of the discrete phase modelled. There are four zones to which the velocity-inlet, pressure-inlet or wall conditions can be applied and these are located at the top and bottom of the column, also on the left and right hand boundaries only wall conditions are applied. Depending on the multiphase model implementation, different conditions are applied to the four zones. When injecting a slug of solid phase, the zone at the base of the domain was defined as a wall and the three zones at the top are defined as velocity inlets with the middle zone used to inject the solid phase. When injecting the gas phase, the inlet conditions at the top are redefined as pressure-inlet conditions with the base zone being redefined as a velocity-inlet condition that injects the gas phase<sup>i</sup>.

The physical properties of the fluids simulated include the density, the particle size and the viscosity of each phase. The density and viscosity of the fluid phases are defined as  $1.225 \text{ kg m}^{-3}$  and  $1.7894 \cdot 10^{-5} \text{ kg m}^{-1} \text{ s}^{-1}$  for air,  $998.2 \text{ kg m}^{-3}$  and  $1.003 \cdot 10^{-3} \text{ kg m}^{-1} \text{ s}^{-1}$  for water,  $1080 \text{ kg m}^{-3}$  and  $1 \text{ kg m}^{-1} \text{ s}^{-1}$  for the solid phase. Note that the “solid phase” viscosity for the standard model<sup>9</sup> is  $1 \text{ kg m}^{-1} \text{ s}^{-1}$  only, whereas the modified scalar equation employs Equation 57 to Equation 59. The particle size of the discrete phase is an important parameter, defining the magnitude of the buoyancy driven forces applied to the liquid phase. The diameter of the particle is used in defining the air phase was 5 mm and the solid phase was 0.1mm, where it was assumed that the form of both types of particle was spherical<sup>ii</sup>.

### ***Solution strategies***

The discretisation techniques applied to model the solid phase transport, are as described in §3.3 and §4.3 with the use of the body force weighted, QUICK<sup>42</sup> and the SIMPLEC<sup>45</sup> methods for the discretisation and solution of the continuity and momentum equations and

---

<sup>i</sup> See Table 9 and Table 10 in §12.3 for the solid-liquid and gas-liquid-solid flow domains

<sup>ii</sup> See Table 1 in §12.1 for the definitions of the gas, liquid and solid phases and Table 3 in §12.2 for user function definitions

coupling the velocity field to the pressure field. With under-relaxation factors set at 0.1 for the Reynolds stresses turbulence model, the slip velocities and the volume fraction equations. Except for the pressure and momentum equations, where the under-relaxation factors are 0.3 and 0.7 respectively. All other remaining factors are defined as 1, such as the body forces, density and viscosity<sup>26,32-33,i</sup>.

The scalar transport equation is solved in a similar manner to the mixture model, but to couple the effect of the volume fraction equation to the momentum equation a series of user-defined functions are employed. These include calculation of the mixture phase properties, momentum and scalar equation source terms, plus variable adjustment to calculate drift, phase and slip velocities<sup>ii</sup>.

The DEFINE\_PROPERTY subroutines calculate the mixture phase properties such as the mixture phase density and viscosity, as predicted by Equation 4, Equation 57, Equation 58 and Equation 59 and instead of using GLMU and MR, the alternative forms (SLMU, GLSMU etc) are used to define the mixture phase. The density equation is of the same form as for the gas-liquid simulations in §4.0, except for the density of discrete phase is higher than that of the liquid phase and the solid-liquid mixture viscosity equations used accounts for the effect of the solid-liquid phase interactions. When calculating the gas-liquid-solid mixture viscosity, the solid-liquid mixture viscosity is calculated first, following the assumption that the solid phase is not transported in the gas side of the bubbly flow. From this assumption the gas-liquid-solid (GLSMU) mixture viscosity was calculated by substituting the solid-liquid mixture viscosity into the liquid phase viscosity term used in the prediction of gas-liquid (GLMU) phase viscosity.

The next subroutines used introduce additional force terms into the transport equations employed through source terms (i.e. DEFINE\_SOURCE routines). As for §4.0 there are inter-phase interaction terms and the deviatoric stress tensor for each of the transport equations plus the convective phase term for the discrete phase in the volume fraction equation. The three-phase model differs from the two-phase models in that there are two

---

<sup>i</sup> See Table 20 to Table 26 in §12.4 for the flow model, solver and variable specifications

<sup>ii</sup> See §11.2 and §11.3 for the source code consisting of source terms and variable adjustments and Table 3 in §12.2 for user function definitions

inter-phase terms, one for liquid-solid interactions and the other for gas phase interactions with the liquid-solid mixture.

To predict the discrete and continuous phase interactions a DEFINE\_ADJUST function was employed to perform calculations of the drift, phase and slip velocities. For the modelling of the solid-liquid motion the form of the function is exactly the same as for gas-liquid motion. When simulating more than one discrete phase, consideration of the individual phase effects such as the particle Reynolds number and drag coefficient must be determined prior to the velocity calculation of the slip velocity of each phase. Again, the slip velocity for the gas phase is calculated in terms of the liquid-solid mixture rather than in terms of just the liquid phase. The remaining terms in the adjust subroutine are calculated in a similar manner to the gas-liquid mixture<sup>1</sup> except for the mixture velocity, which includes the solid phase velocity as well and terms for the gas and liquid velocities.

The boundary conditions for the test cases of the solid-liquid motion were  $0.1 \text{ m s}^{-1}$  for the inlet velocity, at a solid phase fraction of 0.1 for both mixture models<sup>9</sup>. The solid phase was injected for a period of 10 seconds at a time step size of 0.1 seconds, followed by 190 seconds where the solid phase is allowed to accumulate at the base of the mesh. The boundary condition for the top of the mesh was specified as a velocity inlet through which only a 10% portion of 0.2 m wide boundary at the midpoint through which the solid phase was injected.

The boundary conditions for the test cases of the gas-liquid-solid motion were  $0.1 \text{ m s}^{-1}$  for the solid inlet velocity, at a solid phase fraction of 0.1 for both the scalar and standard mixture models<sup>9</sup>. At the top of the mesh the boundary condition was specified as a velocity inlet through which the solid phase was injected, this was only a small portion (0.02 cm wide) of the whole top surface and was located across the centreline. The solid phase was injected for a period of 10 seconds at a time step size of 0.1 seconds, followed by 10 seconds where the solid phase is allowed to drop towards the base of the mesh. After this time the top boundary condition was changed to a pressure-inlet condition and the bottom boundary was redefined as a velocity-inlet condition for the prediction of gas-liquid-solid motion. The fraction of the gas phase at the gas inlet was then defined as 0.6 and as a flux rather than a specific value, at a

---

<sup>1</sup> See Table 2 and Table 3 in §12.2 for the definition of the adjust subroutines discussed here (gl2de\_calc, sl2da\_calc and gls2da\_calc)

superficial gas velocity of  $2 \text{ cm s}^{-1}$ . The simulation of gas-liquid-solid motion is then calculated for a further 1800 steps or 180 seconds of time.

## 5.4 Results and discussion

### *Liquid-solid flow*

The purpose of this investigation is to examine “toy” tests of solid-liquid motion in order to determine the capability of each of the gas-liquid multiphase models as discussed in §3.0 and §4.0. This was done by observing the motion of a continuum solid phase that was injected into the liquid phase at the top boundary condition. The results of these simulations are found in §13.3 between Figure 36 to Figure 44 as time series and time-averaged flow profiles across the width of the mesh, plus vector and contour field plots.

Figure 36 displays the time series of the solid fraction at a height of 0.5 m on the mesh centreline. The red curve represents the solid fraction as calculated by the modified scalar transport equation and the blue curve is the solid fraction determined by the standard mixture model<sup>9</sup>. Both curves are characterised by two sharp peaks at approximately 25 and ~40 seconds of simulation time, after which there is a gradual reduction in the fraction for the next 100 seconds. These peaks arise when the first solids from the slug passes the halfway point and is followed by the wake entrained solids. There is a significant difference between the solid fractions observed here that also occurred with the gas-liquid models presented in §4.0.

The next time series, Figure 37, charts the vertical velocity of the mixture phase at the same location that was used for the solid fraction in Figure 36. The profiles show corresponding peaks at 25 and ~40 seconds with a difference in the velocity that is proportional to one another. The time series shows the influence that the solid hold-up has on the velocity with peaks and troughs in velocity that occur with the increases and decreases in the driving force caused by the changes in volume fraction and thus the mixture density. The solid fraction becomes steady as the bulk of the solid descends to the bottom of the domain. The slug of solid displaces the liquid phase and creates an unsteady flow pattern that is confirmed with the curve for the mixture phase velocity. The velocity series eventually settles as the solid particles move towards the bottom of the mesh and the turbulence dissipates.

Profiles of the mixture, liquid and solid phase vertical velocities are found between Figure 38 and Figure 40. These profiles were averaged with respect to time, where the velocities for the modified scalar equation ( $\diamond$ ) and Fluent's mixture model<sup>9</sup> ( $\square$ ) are depicted. The mixture and liquid phase velocities (Figure 38 and Figure 39) are little different with parabolic curves that have maximums at the mesh walls and the centre of the mesh. It is noted that both curves are asymmetric, with higher velocities observed for the modified scalar case at the right wall and in the bulk downward flow. The unsteady injection process causes the development and dissipation of wake structures and leads to the asymmetries observed in both velocity profiles.

The profiles in Figure 40 are for the vertical component of the solid phase velocity. The scale on the left hand side is for the standard mixture model<sup>9</sup> ( $\square$ ) and the scale on the right hand side represents the change in velocity for modified scalar equation ( $\diamond$ ). The scales show that there is a difference of  $10^4$  in the velocities observed. The viscosity formulations used in the prediction of the solid-liquid mixture (Equation 5, Equation 57 and Equation 58) properties could cause these differences. Other equations that could influence the velocities observed are the functions that predict the slip velocity of the solid phase (Equation 6 to Equation 10). The standard mixture model<sup>9</sup> curve consists of two peaks at the domain walls where the liquid phase is displaced by the solid particles moving down the column. The bulk of the flow is in the downward direction in the central section of the domain where the motion of the solid is the major driving force. The modified scalar equation does not show these peaks at the edge of the domain with just a discontinuous profile in the downward direction that shows the temporary influence that the solid phase has on the flow-field. Both curves show asymmetries that occur as a result of the short slug of the solid particles that were injected into the domain. This short burst of particles has a large bearing on the development and dissipation of the turbulent flow field.

The next plot, Figure 41, is the volume fraction of the solid phase. The difference between the two volume fractions is small, though the profile forms are not the same. The volume fraction profile for modified scalar equation corresponds to the solid phase velocity profile with the asymmetric curve that nearly has a plug flow form. The profile for the standard model<sup>9</sup> has two distinct regions corresponding to the wall regions and the central section of the domain between a radius  $\pm 0.04$  m where the fraction is relatively constant. From the central section to the domain walls the fraction reduces in value. The difference in form is explained by the differing form of the volume fraction equations employed i.e. Equation 3

was used in the standard mixture model<sup>9</sup> and the modified scalar model utilised Equation 54 and Equation 56.

Figure 43 and Figure 44 present the velocity vector field and contour plots for the modified scalar equation (I) and standard<sup>9</sup> (II) modelling methods. Figure 43 describes the liquid-solid motion as vectors of the mixture velocity and Figure 44 presents the volume fraction contours for the solid phase. The plots in Figure 43 capture the development of turbulent vortices caused by the introduction of the solid phase. Figure 44 shows how these vortices influence the discrete phase transport as the solids disperse through the liquid phase. As mentioned when discussing Figure 41 the volume fraction and slip velocity equations influence the profile of the volume fraction of the solid phase that is observed. The influence of the equations that were employed is displayed in the speed at which the solid particles disperse throughout the domain. From the volume fraction contours (Figure 44) it is obvious that the standard mixture model<sup>9</sup> reaches the bottom of the domain more quickly than for the modified scalar equation. As there are no comparisons with detailed experimentation it is difficult to determine the accuracy of the models used. Despite this lack of verification, the effects that are predicted by the models show plausible characteristics of solid motion through a liquid medium.

### ***Gas-liquid-solid flow***

Three simulations of gas-liquid-solid flow were performed using the two modelling methods. The standard<sup>9</sup> and the modified scalar equation models were combined for two cases (GLS1 and GLS2). For the GLS1 case the standard scheme<sup>9</sup> represents the solid phase and the modified scalar equation characterises the gas phase and vice versa for the second test case (GLS2). The final test was where two scalar equations were used to predict the transport of each discrete phase (GLS3).

Results of the simulations are presented in §13.3 between Figure 45 and Figure 61 with time series plots of the volume fraction and vertical mixture velocity (Figure 45 and Figure 46). The time averaged profile plots of the vertical velocity for each phase i.e. the gas, liquid, mixture and solid phases follow the times from Figure 47 to Figure 50. Then volume fraction profiles for the gas and solid phases are illustrated in Figure 51 and Figure 52. Finally vectors

of velocity and volume fraction contour field plots for all three cases are found between Figure 53 and Figure 61.

The time series plots of the solid phase volume fraction for all the approaches of capturing three-phase flow are found in Figure 45. The red line represents the variation in the solid fractions for the GLS1 case, the blue line depicts the fluctuation for the GLS2 case and the black line characterises the GLS3 case. As for the solid-liquid simulations there is a sharp rise in the volume fraction between 25 and 40 seconds of simulation time, as the bulk of the solids pass the height of 0.5 m from the base of the domain. In the GLS1 case there is a reduction in fraction as solid phase is transported about the column. The time series for the GLS2 and GLS3 cases oscillate about an average fraction. The average solid fraction for the GLS2 case was 0.015 and the GLS3 was 0.02. Note that the GLS3 case shows a greater influence of the gas-liquid interactions than both the GLS1 and GLS2 cases. This is shown by the narrow range of the fluctuations in the volume fraction for the GLS2 case (between 0.01 and 0.02) compared to the variations for the GLS3 case (between 0.01 and 0.04). There is a difference in the form of the time-series, where the fluctuation in the hold-up is regular for the GLS2 series and is irregular for the GLS3 curve. The mixture model employed for the gas phase transport causes the difference between the GLS2 and GLS3 cases.

The next time series, Figure 46, is for the variation in the velocity magnitude with the individual series coloured in a similar fashion to that of Figure 45. Comparing the series to the gas-liquid simulations in Figure 29 found that all three-phase simulations produced fluctuations in the mixture velocity that were equivalent to the two-phase velocity fluctuations. Note that on average the GLS3 series is slightly less than the GLS1 series showing the influence that the scalar equation for solid phase has on the liquid motion.

Again comparing the vertical component of the mixture and liquid phase velocities in Figure 47 and Figure 48, there is little difference between the profiles for each case. Both the time averaged profiles for GLS1 ( $\diamond$ ) and GLS2 ( $\square$ ) show asymmetries, while the GLS3 ( $\triangle$ ) case is symmetric with respect to the column centreline. The GLS3 case also has a similar flattened parabolic form to the velocity profiles for the gas-liquid scalar equation model observed in Figure 30 and Figure 31. The profiles therefore, show the influence that the modelling method used has on the flow profile. Particularly, the asymmetries observed in the GLS1 and GLS2

cases, appear to be introduced by the algebraic slip mixture model. These asymmetries may be eliminated by extending the length of the unsteady simulations.

The profiles for the gas phase velocity are found in Figure 49 where it is obvious from the form of the curves which modelling method has been used to predict the volume of the gas phase. The GLS1 and GLS3 curves have a similar form to that of the modified scalar equation profile observed in Figure 32 with two small peaks near to the walls of the column and a third wider peak in the column centre, noting that the central peak is much larger for the GLS1 case. The GLS2 case, where the standard model predicted gas phase motion, was parabolic with a slight asymmetry on the right-hand side. When comparing the gas velocities for the two- and three-phase models each of the curves are different in scale, where the maximum observed velocities in Figure 32 for the gas-liquid simulations were up to  $0.6 \text{ m s}^{-1}$ . The GLS3 method saw gas phase velocities of up to  $0.6 \text{ m s}^{-1}$  and the GLS1 method velocities in excess of  $1.2 \text{ m s}^{-1}$ , both significantly larger than the two-phase flow velocities. The gas velocities for the GLS2 case are  $0.1$  to  $0.15 \text{ m s}^{-1}$  less than the two-phase flow results<sup>i</sup>, indicating that the solid phase model used here suppresses the gas phase motion. Therefore, the solid-phase prediction method influences the gas phase velocities observed with the modified scalar equation increasing the gas phase velocity and the standard mixture model<sup>9</sup> decreasing the velocities observed.

Figure 50 presents the profiles for the vertical component of the solid phase velocities. The scale on the left-hand side characterises the velocities calculated by the modified scalar equation and the right-hand scale describes the range of velocities predicted by the standard mixture model<sup>9</sup>. As observed in Figure 40 there is a sizable difference between the predicted solid phase velocities and as for the solid-liquid flow the three-phase flow is of the order of  $10^4$ . In Figure 40 velocities were of the order of  $10^{-2}$  and  $10^{-6}$  and the velocities observed in Figure 50 were of the order of  $10^{-1}$  and  $10^{-5}$ , the increase in velocity by an order of magnitude can be attributed to the introduction of the gas phase.

The solid phase as modelled by the standard mixture model<sup>9</sup> ( $\diamond$ ) produces a parabolic profile where the bulk of the flow in the centre of the column is in the upward direction, and the solid phase travels down the walls, corresponding to the motion of the gas phase. The solid phase

---

<sup>i</sup> See §4.4 for the discussion of the results of gas-liquid flow simulations

results as modelled by the modified scalar equation produce different results with the majority of the solid phase for the GLS3 case travels down the centre of the column. This is counter to the flow of the gas phase; even though the velocities are very small (of the order of  $10^{-5}$ ) there is an influence on the gas phase velocities observed. For the GLS2 profile the solid motion is down the column but the motion of the gas phase causes a reduction in the solid velocity in the central section of the column. At the mesh walls the solid particles motion is at a faster rate (see inverse peaks) where there is a reduction in the gas fraction. Again each of the flow profiles is different as the influence of multiphase models varies.

The next two profiles are of the gas phase (Figure 51) and solid phase (Figure 52) volume fractions. Comparing Figure 51 with Figure 33 the form of the curves are similar, except that each fraction displays an asymmetry that was not present in equivalent simulations performed in §4.0. The GLS3 case continues the similarity to the modified scalar equation for gas motion, where the profiles are flat, though the GLS3 case is nearly 2 % less than the gas-liquid profile. The GLS1 case displays the influence of the asymmetries in the velocity profile with a change in the fraction from the left to right sides of the column, as the bulk of the flow moves to the right hand side of the column. The GLS2 curve is parabolic with a flattened peak. The differences in the phase fraction profiles for the GLS1 and GLS2 cases can again be attributed to the mixture model employed either for the solid or gas phases. Therefore, the solid phase interactions introduce asymmetries to the profiles, showing there is some impact on the motion of the gas phase. As the simulation times are much shorter than two-phase cases, asymmetries maybe introduced into the flow profiles. Therefore, increasing the length of the simulations may result in the elimination of these asymmetries. In Figure 52 the solid fraction varies between 0.1 % and 2 % and the form of GLS1 profile is comparatively flat in contrast to the plug flow profiles with distinct asymmetries that the GLS2 and GLS3 cases display. Examining the gas and solid phase fractions with the experimental investigations of Warsito<sup>56-58</sup> shows that the form of the profiles are plausible (Figure 42), even with differences in the experimental rig and the solid phase densities employed.

Fields of velocity vectors and the contours of the volume fraction of each discrete phase predicted by the GLS1 case are found between Figure 53 and Figure 55. The vector fields for the modified scalar equation are similar to the flow fields depicted in fields C and D from Figure 34I, where the equivalent gas-liquid simulation results are presented. Figure 54

depicts the gas hold-up as a series of contour plots that display equivalent structures to fractions presented in plots C and D of Figure 35I. The next contour (Figure 55) plot is of the solid fraction and as only a slug of the solid is injected into the column the plots show the solid concentration gradually reducing with time until no discernable fraction occurs. Note that the reason for the reduction in the solid fraction could be due to losses of the solid out of the inlet and outlet conditions as the mixture crosses these boundaries.

As for GLS1, field plots of velocity vectors and contours of phase fraction for the GLS2 simulations are described in Figure 56 to Figure 58. The vectors in Figure 56 display flow structures and oscillating behaviour that is equivalent to the vector fields C and D presented in Figure 34II. Here the meandering flow is more obvious with the main flow (where the larger vectors move up the column) flicking from one side to the other. It is also noted that the highest velocities occur at the wall where the flow is in the downward direction at heights equivalent to 0.5, 1.5 and 3 column diameters. The location of the highest velocities corresponds to the places where the macro-scale vortices interact with the column wall. The influence of the vortices are seen through the meandering plume moving from left to right as the large vortices push the gas phase across the column (Figure 57). The regions of the high downward velocities correspond to zones that are low in the gas fraction and there is some entrainment of the gas phase in the downward flow section of these vortices. These effects are confirmed as originating from the gas-liquid flow models by comparing both the vector fields (Figure 34II and Figure 56) and gas phase fraction contours (Figure 35 II and Figure 57) and observing the same phenomena. The solid fractions in Figure 58 display the influence of the meandering bubble plume, with fractions that were higher where the gas fraction was lower and vice versa.

Finally the field plots (Figure 59 and Figure 61) for the GLS3 case where both of the discrete phases are predicted by the modified scalar equation are depicted. The vector fields in Figure 59 correspond to vector fields produced by the scalar equation when modelling gas-liquid motion, referring to fields C and D in Figure 34I and Figure 53. The gas phase fraction (Figure 60) is also comparable to the contour plots of Figure 35I and Figure 54. The solid fraction contours in Figure 61 also show similar effects to the contours displayed in Figure 58. The difference from Figure 58 is that fraction was higher for the GLS3 simulation results and the vortices are elongated resulting in the different form of the contours. Both the GLS2 and GLS3 cases show dispersed fractions of the solid phase, though fractions of up to 5% were

observed in the lower half of the column in Figure 58 and Figure 61. At the higher solid phase fraction accuracy could be limited when not employing models for the granular flow effects such as particle collisions, conductivity etc<sup>49</sup>.

## 5.5 Conclusions

This leaves the question of recommending one of the mixture models to use when considering the simulation of gas-liquid-solid flows in bubble columns. The only way to assess the efficacy of each approach is to consider how well the solid phase is captured by the models employed for predicting the volume fraction. This is important, as there are no comparisons between simulated and experimental models of the motion of the solid particles in two or three phase flows. This was done by examining Figure 45, Figure 52, Figure 55, Figure 58 and Figure 61 where the transport of solid phase was depicted as time series, flow profiles and contours plots.

The standard mixture model<sup>9</sup> captures the motion of the solid phase (GLS1) quite well, except that there is a problem in the application of the boundary conditions as solid is lost through the flow boundaries at the top and bottom of the column resulting in the reducing solid fraction of Figure 45. In addition, the viscosity formulation employed by the standard model<sup>9</sup> does not account for the maximum solid fraction, 0.62. This means that the solid fraction can exceed the maximum value, producing solutions that are physically non-realistic in these regions.

The transport of the solid phase in the GLS2 and GLS3 simulations captures the physicality of solid motion, when employing the modified scalar equation form of the mixture model. In contrast to the standard model<sup>9</sup>, the scalar equation method employed Equation 57 to Equation 59 for the prediction of the mixture viscosity where a maximum fraction term was included in these formulations. Note that the profiles of the solid fraction are comparable to the experimental profiles (Figure 42) derived from the investigations of Warsito<sup>56-58</sup>.

Earlier in §5.0 it was noted that the aim of this thesis is the modelling of a biochemical reaction, where a microorganism that absorbs and excretes many chemical species requires an appropriate model to mimic the organism. The scalar equation model provides a reasonable

approximation of the gas and solid phases and therefore, the solid phase can be directly treated as a microbial cell culture. When using the standard mixture model<sup>9</sup> to predict the solid phase results needed to predict the organism, the reaction models must be applied independently of the mixture model. As far as preliminary investigations into reaction processes the accuracy of the modified scalar equation version of the mixture model is more than adequate for the demonstrative purposes of this thesis. Note that future work for effective design procedures must include the effects of granular<sup>48-55</sup> representations of the solid phase motion and bubble particle interactions that were ignored in the models employed. Further comparisons with detailed experimentation into gas-liquid-solid flow phenomena in bubble columns must be performed.

## 6.0 A SIMPLE BIOCHEMICAL REACTION

### 6.1 Plan

To model the transport of a substrate that is absorbed into a cell culture. The substrate is then converted into metabolic products (i.e. internal and external products) by the culture.

- treat the cell culture as a suspended solid
- model the solid as a volume fraction, with a modified scalar equation with mixture and reaction model interaction terms
- the gas phase provides agitation of the solid-liquid mixture
- use the mixture model in the form of the modified scalar equation to determine the gas phase interactions with the solid-liquid mixture
- model the substrate and the product with modified scalar equations that predict the concentration of the chemical species
- assume that the all reactions and phase interactions are isothermal
- assume pseudo-steady state conditions apply to the biofilm
- use the reaction models that are applied to the substrate and product scalar equations to depict the conversion of the substrates into a product
- investigate the influence of the aspect ratio on flow and reaction phenomena by using meshes with 5:1 and 20:1 height to diameter aspect ratios

A good example of a biochemical reaction that could be employed in gas-liquid-solid flow simulations with CFD is the fermentation of sugars to form citric acid. In the 80 years since citric acid was first commercially manufactured many process routes have been developed that can be grouped into either surface or submerged cell cultures<sup>59-60</sup>. Surface cultures consist of warm air blown over shallow pans of inoculated media and submerged cultures generally occur in stirred tank or airlift reactors where the gas phase agitates and oxygenates the solid and liquid phases.

A large number of fungal organisms are known to excrete citric acid including various species of the moulds *Aspergillus*, *Penicillium* and *Candida*. The mould known as *Aspergillus niger* is widely preferred for the manufacture of citric acid in the submerged cultures<sup>59</sup>. When

considering fermentation processes, the broth composition and the conditions applied have a direct influence on the cell growth. Particularly as fungal moulds are vegetative organisms that grow aerobically and obtain their energy by oxidising organic substances. The product formed by the fungal mould is usually a result of metabolic processes within the organism<sup>61</sup>. These metabolic pathways dominate the development of cells where the composition and temperature of the broth determines what pathways are employed by the microbe to function<sup>1,59,62-66</sup>.

The time scale of fermentations is measured in days, for the life cycle of the culture during which stages of non-growth, accelerated growth and product formation occur<sup>65</sup>. To provide conditions that promote cell growth and ultimately product formation, the broth or medium composition needs to be a complex mixture of carbohydrates, sources of nitrogen, phosphorous and sulphur. Carbohydrates provide energy and material for the formation of metabolic products (including the growth of cells) and because of this the form of carbohydrate is usually pure glucose, starch or sucrose. The energy and materials for metabolic processes can also be derived from raw starch, sugar or molasses. Other forms of carbohydrates include waste vegetable matter such as fruit peels or mashes. The sources of nitrogen, phosphorous and sulphur are provided in the form of inorganic salts of ammonium, magnesium and potassium. Other factors that affect the production of citric acid using *Aspergillus niger* include the pH of the broth (1.5-2.8), the temperature (28-33°C) and length of the fermentation (6 to 25 days)<sup>59-60</sup>.

It is important to note that how the culture develops is heavily dependent on the trace metals and the anionic complexes that are added to the broth with the carbohydrate source. Trace metals used in broths include copper, iron, manganese and zinc where the concentration of each metal has a bearing on the growth and product formation rates. Too much iron or too little copper in the broth could cause formation of various types of pellet or even a viscous mixture<sup>60,64</sup>. Note that the most effective form the cell culture is grown as loose fluffy pellets. Mass transfer rates across phase boundaries (gas-liquid and liquid-pellet) are greater, with greater surface areas and low broth viscosities for the loose, fluffy pellets.

A great deal of effort has been invested in understanding how citric acid is formed by micro-organisms at scales that range from the single cell (>5µm) up to process scale bio-reactors (several metres in diameter)<sup>59-60</sup>. Therefore, it is still difficult to understand many of the

reactions that take place in fermentation processes, as direct observation of the reactions that take place is tricky. The impact that the environmental factors have on growth of a fungal mould during each stage of fermentation increase the complexity of the design and operational procedures for biochemical reactors. This is apparent when each individual cell acts in a different manner due the age of the cell and changes in the local environment for the entire fermentation (i.e. local substrate concentrations plus the presence of nitrates, sulphates and specific trace metals)<sup>59,62, and 64-66</sup>. CFD can help improve understanding that changes in the local environment have on the cell culture and the formation of extracellular products such as citric acid at different stage of the culture life cycle.

## 6.2 Mathematical models

### *Species transport and reaction models*

The modelling of the biochemical reaction can be treated in many ways from the simple to the very complex. The complex models involve mimicking the metabolic pathways for product synthesis in a single cell, observing how simple changes to the environmental conditions influence the pathways that are utilized<sup>67</sup>. As reactions in a cell are highly non-linear, a power law model was employed in modelling of each of the component reactions to enable the prediction of chemical reactions under specific conditions<sup>67</sup>. However, single cell representations of the culture are far too complex for implementing with the continuum representation of multiphase flow models employed in CFD<sup>1</sup>. Therefore, it would be prudent to consider a volume-averaged approach such as those applied to diffusion and reaction in the biofilm of pellets formed by cell growth<sup>68-71</sup>.

The definition of the volume-averaged model that is employed in predicting biochemical reactions is dependent on the scale at which the biofilm is regarded. Wood and Whitaker<sup>68</sup> described six levels of the different length scales from the aquifer (i.e. from trickling filters commonly used in water treatment) to length scales associated with microbes (i.e. membrane thickness, length, width etc). The focus of the models derived by Wood and Whitaker<sup>68</sup> through the volume averaging of length scales was associated with the biofilm thickness and a two-phase system that consisted of microbes and a polysaccharide matrix that forms the

---

<sup>1</sup> See §3.0 to §5.0 for models employed in predicting multiphase motion in bubble columns

biofilm structure. The scales considered were far below that of the macroscopic flow structures described by the methods in chapters §3.0 and §5.0, so this leaves the implementation of models that consider mass transport and reaction on a larger scale<sup>69-71</sup>. For reasons of simplifying the models derived, Wanner<sup>69</sup> and McCarty et al<sup>70-71</sup> considered the biofilm as a single continuum phase where reaction and diffusion occurred throughout the film and not just in the microbes. This increased the length scale at which the diffusion coefficients were calculated, ignoring the effects of the geometry of the microbes and the surrounding environment even though competing organisms were considered in the treatment of the models<sup>69,71</sup>.

Recently Sakurai et al<sup>62</sup> presented a model that calculated the production of citric acid by fermenting sugars in the presence of *Aspergillus niger* using a rotating disc contactor. Employing experimentally derived reaction rates and yield-coefficients, Sakurai et al<sup>62</sup> solved the mass balances numerically and provided a good comparison with changes in cell mass, product and substrate concentrations. The model expressed cell growth and product formation in terms of Monod and Luedeking-Piret rate equations<sup>1,59,61,72</sup>. Oxygen transport was considered along with the transport of sugars, as oxygen is a limiting substrate in the growth and maintenance metabolic pathways of which citric acid is a by-product<sup>61-62</sup>. This introduces many difficulties into modelling with changes in the molecular weight and density of the gas phase. The transfer of oxygen influences the pressure acting on the bubbles and would therefore influence the size and shape of the bubbles. The biofilm in the rotating disc contactor<sup>62</sup> (the film is supported by the disc) differs from the biofilms that occur in a bubble column (biomass is in the form of pellets or a viscous broth). Therefore, the boundary conditions applied to the species transport and reaction models must be reconsidered.

A monologue on the development of fermentation models by Sinclair and Kristiansen<sup>72</sup> was then used to provide the basis for models of the growth of the cell cultures through the consumption of a substrate and the formation of an extracellular product. Three equations for change in the concentration of cells, substrate and product were obtained (Equation 61 to Equation 63)<sup>i</sup>. The equations are based on the whole reactor volume. All the derivatives for the species concentrations in Equation 61 to Equation 63 are proportional to the reaction rate for cell growth. Yield coefficients are then applied to the cell growth rate to determine the

---

<sup>i</sup> See §10.7 for the assumptions made in deriving the reaction model equations

substrate consumption rate with respect to cell growth and product formation (Equation 65 and Equation 66). The rate of product formation (Equation 67) is also related to the cell growth rate and is used to predict the mass of substrate consumed in the formation of the product. Therefore, to determine the influence of the flow field in a bubble column reactor on the transport and reaction of these species, extra terms must be introduced that model the convection and diffusion of the species across the reactor.

When solving a computational flow model, the volume of the reactor is divided into many small volumes<sup>9,46</sup>. These small volumes allow the discretisation of partial differential equations that predict transport of some species (be that chemical, electromagnetic fields, flow, heat or different phases). The multiphase flow models discussed in §4.0 and §5.0 were implemented with scalar equations. In Equation 54 there are four terms, these are the unsteady flow term, the diffusive flux, convective flux and the source term and by linking source term subroutines to specific scalar equations, this makes the modelling of the transport and reaction of a biochemical species possible<sup>1</sup>.

The cell culture is treated as a solid phase and therefore, all that is needed to model the cell culture is an additional source term for the increase in the volume fraction of the solid phase that is caused by the growth of cells. As the reaction model is in terms of concentration, a few equations are required to convert the concentration into a volume fraction and these are found between Equation 68 and Equation 71. A term for the volume fraction of cell growth can be found in Equation 72, which is the volume fraction equation for the reactive solid phase. Now that the increase in the volume fraction due to cell growth has been defined, equations for the consumption of the substrate (Equation 73) and the formation of a biochemical product (Equation 74) are then defined.

### ***Multiphase flow models***

To predict the volume fraction of discrete phases and their motion through a bubble column, a number of scalar equations (Equation 54) were employed with the continuity (Equation 42) and momentum (Equation 53) equations. In depicting the transport of the discrete phase, the diffusion coefficient was defined as 0.1 for the volume fraction equations and  $10^{-3}$  for the

---

<sup>1</sup> See §10.7 for the species transport equations and §11.3 for the associated coding of the source and sink terms that model cell growth and product formation through the consumption of a substrate

concentration equations. Equation 55 and Equation 56 were used as source terms that are applied to Equation 53 and Equation 54 respectively. The first term in both source terms is the deviatoric stress tensor and the last term is the inter-phase interaction term as calculated by the drift velocity. The second term in Equation 56 is the convective flux of the discrete phase noting that there are two convective fluxes with one for the mixture phase. The drift velocity was calculated through the use of the mixture density (Equation 4), mass-averaged, drift and slip velocity formulations (Equation 6 to Equation 10). We note that the slip or relative velocity was obtained by averaging a combined momentum equation for the discrete phase and the mixture according to the principles of local equilibrium and Favre averaging<sup>25</sup>. Finally the mixture viscosity is calculated using Equation 57 to Equation 59 in the form of the macros SLMU and GLSMU<sup>i</sup>.

### ***Transport of turbulence***

After modelling the lateral convection of heat and two-phase flow in a bubble column<sup>ii</sup>, it was determined that the most appropriate method for the prediction of the turbulence parameter required the use of a complex model such as the Reynolds stresses turbulence transport model. Equation 31 shows the exact Reynolds stresses equation that is employed in the solver<sup>9,11</sup> as a series of equations that enable closure of the unknown terms. This includes the use of both the k- $\epsilon$  equations (Equation 25 and Equation 26) and the inclusion of the effects of buoyancy, pressure, pressure-strain and any rotation (Equation 32 to Equation 40).

## **6.3 Model parameters**

### ***Boundary conditions***

The domains employed for the simple biochemical reaction are a pair of two-dimensional plane meshes with height to width aspect ratios of 5:1 (2000 cells) and 20:1 (4500 cells)<sup>iii</sup>. The 5:1 mesh employed here is based on the experimental and numerical investigations<sup>iv</sup>. The 20:1 mesh is based on an experimental rig that was used to investigate the morphological

---

<sup>i</sup> See §11.3 for the coding of three-phase mixture model subroutines and macros

<sup>ii</sup> See §4.0 for discussion of lateral convection and two phase flow

<sup>iii</sup> See Table 5 and Table 11 for the dimensions and boundary definitions in §12.3

<sup>iv</sup> See References 26,35-37 and §3.0 to §5.0 for previous numerical investigations with the 5:1 height to diameter aspect ratio column

and rheological properties of an *Aspergillus niger* fermentation in a bubble column<sup>63</sup>. Solving the gas-liquid-solid flow field for a large aspect ratio mesh is useful in understanding how the flow characteristics of bubble column and airlift fermentation reactors change with column height. Generally large aspect ratio columns are employed for submerged culture fermentations, as the effect of the greater hydrostatic head increases the transfer of oxygen from the gas phase to the liquid phase<sup>60</sup>. Oxygen is critical to many fermentation processes as the organism employed requires dissolved oxygen to convert carbohydrates into energy and materials for metabolic products<sup>1,59-61</sup>.

Velocity inlet conditions are applied to the base of both meshes, with the volume fraction and vertical velocity of the gas phase defined as a flux. The 5:1 column the inlet condition was applied to 80% of the base of the column and the inlet for the 20:1 mesh employed the whole of the bottom surface of the column was specified as the inlet condition. At the top boundary, pressure inlet conditions are applied to the whole of the top surface of the mesh. The remaining boundaries are treated as walls, where no species fluxes were defined i.e. the discrete phase or the solutes were specified as zero and without gradients. These specifications were also applied to the bottom and top surfaces for the solid, substrate and product species. Only the gas phase was defined differently with the gas entering through the bottom surface and leaving the domain through the top surface.

### ***Physical properties***

In solving the reaction models applied to the solid phase, substrate and product species, experimental rates of reaction and yield coefficients<sup>i</sup> are required to relate the physicality of a fermentation to the influence of the computational flow field. Haq et al<sup>64</sup> presented experimentally derived reaction rates for cell growth, substrate consumption and product formation for two strains of the *Aspergillus niger* species of mould. The models derived ignored the influence of oxygen on the biomass.

By varying the concentration of copper ion with copper sulphate, copper chloride, copper nitrate or copper carbonate differences in cell growth and morphology were observed, which

---

<sup>i</sup> Reaction models are presented in §10.7 with the reaction rates and yield coefficients employed in the subroutines (see §11.3 and Table 4 in §12.1) for each case modelled as discussed between Table 27 and Table 30 (§12.4).

in turn influenced the molasses consumed and the product that was formed. It was found that when  $2 \times 10^{-5}$  M of copper sulphate was added to the fermentation medium, an increase of 20 % of the yield of citric acid was observed when compared to the fermentations where no copper salts were added to the broth. The improvement in the citric acid concentration occurred even when there was no significant increase in carbohydrate consumption rate. The addition of copper sulphate promoted the formation of pellets that were loose and fluffy. This improved mass transfer rates of chemical species into and out of the pellets and therefore, growth rates and product formation rates increased.

Haq et al<sup>64</sup> presented growth rates and the yield coefficients of sugar consumption and citric acid formation for the control fermentations of both mould strains and the fermentations where  $2 \times 10^{-5}$  M of copper sulphate was added. Focusing on the conditions that promoted the desired pellet formation for high rates of mass transfer and reaction, the growth rates for the two mould strains were selected for the use in the reaction models from the fermentations where  $2 \times 10^{-5}$  M of copper sulphate was added to the broth. The specific growth rates of these strains were  $6.5 \times 10^{-5}$  and  $1.52 \times 10^{-4}$  s<sup>-1</sup>. The associated substrate consumption yield-coefficients were 0.118 or 0.148 (kg cells) (kg substrate)<sup>-1</sup> and 0.442 or 1.087 (kg product) (kg substrate)<sup>-1</sup> for each respective strain. Finally the respective yield coefficients of citric acid formed per unit mass of cells grown were 3.752 and 7.360 kg cells (kg substrate)<sup>-1</sup>.

The physical properties of the gas, liquid and solid phases that are represented in this model include the density, the particle size and the viscosity of each phase. The density and viscosity of the fluid phases are defined as  $1.225 \text{ kg m}^{-3}$  and  $1.7894 \times 10^{-5} \text{ kg m}^{-1} \text{ s}^{-1}$  for air,  $998.2 \text{ kg m}^{-3}$  and  $1.003 \times 10^{-3} \text{ kg m}^{-1} \text{ s}^{-1}$  for water. The density for the solid phase was  $1080 \text{ kg m}^{-3}$  with Equation 57 and Equation 58 relating the impact that the solid phase on the fluid viscosity. The particle size of the discrete phase is an important parameter that defines the magnitude of the buoyancy driven forces that are applied to the liquid phase. For the gas phase, this was 5 mm and for the solid phase, the diameter was 0.1mm, where the form of both types of particle was assumed spherical. The diameters were kept the same as the particle diameters from previous investigations for reasons of consistency. The particle diameter of the solid phase was assumed constant for whole length of the simulation.

Therefore, there was no increase in the solid particle diameter, just an increase in the number of particles as the mass of cells increased<sup>i,ii</sup>.

### ***Solution strategies***

The discretisation techniques applied used to model three-phase flow and reaction are similar to the techniques described in §3.3, §4.3 and §5.3. The body force weighted, QUICK<sup>42</sup> and the SIMPLER<sup>45</sup> methods were employed for the discretisation and solution of the continuity and momentum equations and then coupling the velocity field to the pressure field. First order UPWIND<sup>43-46</sup> methods were applied for the solution of the turbulent flow parameters and second order UPWIND<sup>43-46</sup> methods were employed for all the scalar transport equations. Under-relaxation factors were set at 0.1 for the Reynolds stresses turbulence model, slip velocities and the scalar equations. The pressure and momentum equations under-relaxation factors were 0.3 and 0.7 respectively. All other remaining factors were defined as 1 for models that include the body forces, density, k-ε turbulence and viscosity equations<sup>26,32-33,iii</sup>.

In addition to solving the scalar transport equations with the second order UPWIND<sup>43-46</sup> methods a series of user-defined functions were implemented and linked to specific equations within the solver. The effects included in the prediction of flow phenomena, were the calculation of the mixture phase properties, source terms for the momentum and scalar equation, including the volume fraction of the discrete phase and the consumption and formation of chemical species in the reactor. Variable initialisation and adjustment subroutines were then used to calculate the deviatoric stress tensor and drift, phase and slip velocities<sup>iv</sup>.

The mixture phase properties such as the mixture density and viscosity are predicted by Equation 4, Equation 57, Equation 58 and Equation 59 through the macros MR and GLSMU that define the mixture phase. Assumptions made when calculating the mixture viscosity encompass the solid phase remaining on liquid side of the mixture and that the substrates and extra-cellular products bear no influence on the liquid phase viscosity. From these

---

<sup>i</sup> See Table 1 in §12.1 for the definitions of the gas, liquid and solid phases

<sup>ii</sup> See §4.0 and §5.0 for discussion of two- and three-phase flow modelling parameters

<sup>iii</sup> See Table 27 to Table 31 in §12.4 for the flow model, solver and variable specifications

<sup>iv</sup> For the source term and variable adjustment subroutines see §11.2 and §11.3 with definitions of the user functions in Table 4 (§12.2). Note subroutine `a_gls_s1_calc` in §11.3 is where the coding for three-phase flow and reaction is found

assumptions the gas-liquid-solid (GLSMU) mixture viscosity is calculated by first assessing the solid-liquid (SLMU) mixture viscosity using the solid dispersion form of the viscosity model. SLMU mixture viscosity is then substituted into the liquid phase viscosity term of gas-liquid (GLMU) phase form of the viscosity equation.

The DEFINE\_SOURCE subroutines allow the introduction of additional phase interaction terms into the volume fraction (gas and solid phases) and momentum equations (where each phase is represented by an individual interaction term) as well as deviatoric stress tensors and convective fluxes. The source terms for the scalar equations that model the transport of the chemical species (i.e. the substrate and product species) assess the consumption and formation of species by the cell culture. The cell culture is represented by the scalar equation for the volume fraction of the solid phase (Equation 72) with an extra term in the volume fraction equation of the solid phase that predicts the increase in the volume fraction caused by the growth of the cell culture (Equation 71). As depicted in §4.3 and §5.3 the discrete and continuous phase interactions were predicted by employing a DEFINE\_ADJUST function, with additional commands to extract reaction rate and phase volume data from the user-defined calculations.

The fraction of the gas phase at the inlet at the bottom of the column was then defined as 0.6 and as a flux at a superficial gas velocity of  $2 \text{ cm s}^{-1}$ . This resulted in different velocities for each mesh, with the velocity for 5:1 case defined as  $0.032 \text{ m s}^{-1}$  and the 20:1 case requiring a velocity of  $0.036 \text{ m s}^{-1}$ . The volume fraction of the gas and solid phases, substrate and product concentrations were initialised for the whole of the column as 0, 0.005,  $150 \text{ kg m}^{-3}$  and  $0 \text{ kg m}^{-3}$  assuming that each species was perfectly mixed prior to the injection of the gas phase. The flow fields were then solved for 2000 steps or 200 seconds of time.

## 6.4 Results and discussion

The modelling of a pair of simple biochemical reactions using two meshes with height to diameter aspect ratios of 5:1 and 20:1 were investigated in this section. From the analysis of these results, it is possible to infer regions of high substrate consumption and product formation. This is possible by using times series (Figure 62 to Figure 64), profile (Figure 65

---

<sup>i</sup> For the three-phase flow and reaction model specifications, see §12.4 between Table 27 and Table 31.

to Figure 70) and field plots (Figure 71 to Figure 76). It must be noted that caution must be used in drawing conclusions from the solutions presented, as a simplistic model was used to mimic a complex process that is dependent on many factors<sup>1</sup>.

The time series for the volume fraction of the solid phase for the both cell growth rates (specific growth rate was  $6.5 \cdot 10^{-5} \text{ s}^{-1}$  for series I and  $1.52 \cdot 10^{-4} \text{ s}^{-1}$  for series II) are depicted in Figure 62. A single point location was used for 5:1 mesh (red line) and was at the midpoint of the column (i.e. on the centre line at a height of 2.5 diameters from the base of the column or half the column height). Two points were employed for the 20:1 mesh with one at the midpoint of the column (black line) and a second point location at 2.5 column diameters in height from the base of the column (blue line). The series for both of the 5:1 cases are little different from the series observed for the equivalent gas-liquid-solid flow model (Figure 45) with a rapid increase to  $\sim 2\%$  within 25 seconds of the gas phase being first injected. The same effects are observed for both of the 20:1 cases at the lower point location, though higher up the column the variation in the fraction is not as great as for the lower point. Much lower fractions are also observed at the higher point location, showing that there is a negative gradient in the vertical direction for the solid fraction. The reduction in the frequency of the oscillation is also an indication of the reduction in the intensity of the turbulence that occurs the further away from the gas injection location that has been observed in many turbulent flow investigations<sup>34</sup>.

Figure 63 and Figure 64 present the respective concentrations for the substrate and product species. There is little difference in the rate at which the substrate is consumed for both specific growth rates (Figure 63). Yet the product formation rate for the higher specific growth rate series (Figure 64II) is four times that of the lower rate (Figure 64I). This can be explained by the rates applied for the consumption of the substrate due to product formation and the rate of product formation per unit cell mass being 2 to 2.5 times greater for the higher specific growth rate, which itself is 2.3 times greater<sup>64</sup>. As Haq et al<sup>64</sup> discussed, the second strain of the mould (specific growth rate was  $1.52 \cdot 10^{-4} \text{ s}^{-1}$ ) was a faster growing organism that had the ability to produce large quantities of citric acid. Note that the series in Figure 63 and Figure 64 are power law functions, as the rates at which the substrate was consumed and the product was formed reduce as the concentration of the substrate species reduces.

---

<sup>1</sup> For discussion of the model employed and the assumptions used see §6.1, §6.2 and §10.7.

The profiles for vertical velocity of the mixture for the 5:1 and 20:1 height to diameter aspect ratio bubble are found in Figure 65. All the profiles are parabolic and comparing the influence of the mould strain, there is little impact on the velocities observed, noting that the profiles for the 5:1 column are equivalent to the gas-liquid (Figure 30) and gas-liquid-solid (Figure 47) cases. The profiles for the 20:1 column are lower in magnitude when compared to the 5:1 column. At half the 20:1 column's height the profile varies between  $0.05 \text{ m s}^{-1}$  at the column centre and  $-0.05 \text{ m s}^{-1}$  at the column walls, whereas at a height of 2.5 column diameters the maximums are up to  $|0.09| \text{ m s}^{-1}$ . Note that the two points next to the walls, the velocities are the same for the 20:1 case, this is because there are more points in the profile than there are cells across the width of the mesh, therefore, some computational cells contain two point locations. Comparing the equivalent column diameter heights, i.e. 2.5 column diameters for the 5:1 and 20:1 column, the 5:1 column is nearly one and half times that of the 20:1 column at  $|0.12| \text{ m s}^{-1}$ .

Figure 66 and Figure 67 depict the profiles for the volume fraction of the gas and solid phases, respectively. The profiles for both phases display the plug flow form as observed with the equivalent models for gas-liquid (Figure 33) and gas-liquid-solid flows (Figure 51 and Figure 52). Note that asymmetries occur in the gas phase profile for the second mould strain ( $1.52 \cdot 10^{-4} \text{ s}^{-1}$ ) when used with the 5:1 column. The asymmetries in the gas fraction profile can be explained by the increase in the solid fraction that occurs on the left-hand side of the column. Both of the solid fraction profiles display asymmetries, but there is a noticeable difference between the solid fractions for the two moulds on the left-hand side compared to the fractions on the right. Therefore, it was determined that the specific growth rate of the cell culture has an influence on the flow structures that developed. The profiles for the gas phase at a height of 2.5 column diameters for the 20:1 column, as with the 5:1 column are not flattened across the diameter of the column. The increase in the gas fraction that occurs in the centre of the column corresponds to a decrease in the solid fraction that does not occur for the 5:1 column. Yet higher up the 20:1 column the influence of each discrete phase over the other is not as distinct as much lower fractions are observed for both phases.

Figure 68, Figure 69 and Figure 70 illustrate the profiles for the rate of cell growth, the substrate consumed per time step and the product formed per time step, respectively. The profiles display the same characteristics as the corresponding solid fraction profiles with plug

flow forms (Figure 67). Except that the magnitude of the profiles derived from the simulations for the mould strain with the higher specific growth rate were significantly greater than the profiles derived from the cases with the lower specific growth rate. Note that the substrate consumption values are negative. The consumption of the substrate is caused by the formation of biomass and product, where the values are positive (c.f. Figure 63 and Figure 64 for the change in substrate and product concentrations with time).

Between Figure 71 and Figure 76 field plots for both meshes and mould strains are presented during the thousandth time-step (i.e. 100 s). Each figure contains eight field plots and these are:

- A, velocity vectors ( $\text{m s}^{-1}$ ),
- B, contours of the volume fraction of the solid phase (-),
- C, contours of the volume fraction of the gas phase (-),
- D, contours of the concentration of the substrate ( $\text{kg m}^{-3}$ ),
- E, contours of the concentration of the product ( $\text{kg m}^{-3}$ ),
- F, contours of the cell growth rate ( $\text{kg m}^{-3} \text{ s}^{-1}$ ),
- G, contours of the substrate consumed ( $\text{kg m}^{-3}$ ),
- H, contours of the product formed ( $\text{kg m}^{-3}$ ),

Figure 71 and Figure 72 describe how both the phases and species move and react about the 5:1 height to diameter aspect ratio bubble column where specific growth rates of  $6.5 \cdot 10^{-5} \text{ s}^{-1}$  and  $1.52 \cdot 10^{-4} \text{ s}^{-1}$  were respectively employed in the reaction models. Examining Figure 68, the influence that the velocity vector field has on the phases and chemical species can be seen with contours of each parameter displaying patterns that match the vortical structures. Note that the gas phase motion is driving the turbulent motion and that where the gas fraction is lower, the solid fraction tends to be higher and this corresponds to the earlier gas-liquid-solid investigations<sup>1</sup>. As discussed with Figure 68, Figure 69 and Figure 70 the solid fraction determines the cell growth rate, substrate consumed and the product formed. Therefore, where solid fraction is greatest, there are maximums for cell growth rate, species consumption and formation. Comparing Figure 71 and Figure 72 it is observed that the flow structures are not the same. The change in the flow structure is related to changes in the reaction models

---

<sup>1</sup> Plots of the gas-liquid-solid flow field for the two-scalar equation mixture model are found between Figure 59 and Figure 61 in §13.3.

through the specific growth rate and the yield coefficients used. The influence of the reaction model specifications was also observed in the profiles of the gas hold-up and solid fraction (Figure 66 and Figure 67).

Figure 73 and Figure 74 depict the flow fields at the bottom and top of the 20:1 bubble column where the specific growth rate was  $6.5 \cdot 10^{-5} \text{ s}^{-1}$ . Figure 75 and Figure 76 display the corresponding flow fields where the mould with the higher specific growth rate was employed. The velocity vector field shows a marked reduction in the velocity magnitude in the top half of the column and associated with this was an observed reduction in the gas and solid phase fractions. Comparing the fields with the findings of Berovič et al<sup>63</sup>, it is noted that there was a reduction in the shear rate at the top of the experimental column and this also occurred in the simulated columns. The lower shear rates lead to an increase in the cell concentration, as a different pellet type was formed<sup>63</sup>. The pellets found in the top half of the experimental column were less dense due to lower levels of cell damage, leading to the accumulation of cells here<sup>63</sup>. Therefore, the maximum rates of cell growth occurred at the top of the column, whereas the reverse occurred in the simulations as only a single pellet form and density were considered. This led to a higher solid phase fraction at the base of the column and therefore, higher reaction rates occurred in this region (Figure 73 and Figure 75).

## 6.5 Conclusions

Biochemical reaction models were implemented with the gas-liquid-solid mixture model that utilised two modified scalar equations. The reactions mimicked processes that occur within a microbial culture quite well. Two strains of the mould *Aspergillus niger* were used to test the application of the reaction models and displayed an influence on the flow phenomena observed. The flow structures that were produced were similar to the earlier gas-liquid and gas-liquid-solid flow cases<sup>i</sup>. The simulations that employed the higher specific growth rate produced a flow-field that differed from the flow-field for the lower growth rate. This implies that the amount of suspended solids present influences the flow structure, as a higher solid fraction was observed for the second strain of the mould.

The consumption of a substrate displayed power law properties that have long been associated with fermentation of sugars by *Aspergillus niger*<sup>1,59-61 and 65</sup>. Yet the rate of consumption was

---

<sup>i</sup> For further discussion of the multiphase models employed see §4.0 and §5.0

high for the length of the simulation considered (i.e. 200 seconds). This was probably due to defining the substrate in terms of concentration and the lack of diffusion models for transport through the pellets and across cell membranes. Other reasons could include how the yield coefficients and growth rates were defined, either in terms of the whole fermentation or for specific stages of the life cycle of the culture. The formation of a product also showed power law tendencies as the mass of the product increased, but this was at a much lower rate than was observed for the substrate consumption.

Improvements that need to be considered include modelling the transport of oxygen across the gas-liquid interface and the diffusion of chemical species into and out of the cell culture. Other aspects that are influential encompass effects such as the local shear rate, and the local concentration of species display on the growth of the cell culture (i.e. trace metals, nitrogen, phosphorous and sulphur). Therefore, more detailed cell growth and maintenance models are required to examine the majority of the effects of the species in the culture broth. Note that the impact that the shear rate has on the discrete phase flow phenomena includes particle break-up, pellet formation and particle collisions and to effectively model the biochemical reaction it is essential to model the shear rate effects.

## 7.0 CONCLUSIONS

### 7.1 Current investigations

#### *Two-phase flow*

The algebraic slip mixture model from the Fluent<sup>9</sup> solver was initially used to study the influence that the domain and the turbulent flow models have on the structure of two-phase flow. Three domains (plane, rectangular and cylindrical) were used to test how well the turbulence models (laminar, k- $\epsilon$  turbulence and turbulent Reynolds stresses) captured the unsteady motion of vortices. The k- $\epsilon$  turbulence model predicted three very different flow structures in each of the meshes. The structures varied from the steady elongated vortices for the plane and rectangular meshes to column diameter wide vortices at the base of the cylindrical domain that corresponded to flow structures depicted by Sanyal et al<sup>26</sup> and Degaleesan<sup>35</sup>. Both the laminar flow and the turbulent Reynolds stresses models produced similar solutions when respectively applied to all three domains. The method used to implement the Reynolds stresses model (adding the basic flow profile before each iteration) suppressed the development and motion of vortices. The flow profiles for the plane and cylindrical cases were not significantly different for the laminar flow and k- $\epsilon$  turbulence models. Therefore, it was concluded that the plane mesh could be used in the development of two and three-phase models. The implementation of the turbulence models raised questions about the suitability of the k- $\epsilon$  turbulence and the Reynolds stresses model for the predicting of two-phase flow in bubble columns.

Further experimental and numerical investigations are required to determine the boundary conditions and model constants for the turbulence flow models. As the aim of the project was to provide a simulation of gas-liquid-solid flow with a biochemical reaction, an experimental investigation into the constants and boundary conditions for k- $\epsilon$  turbulence would move away from the remit of the research<sup>i</sup>. Therefore, improvements to gas-liquid flow modelling were studied numerically by modelling buoyancy driven flow in a narrow cavity<sup>39-40</sup> that was heated laterally for various turbulence models. By adding the basic flow profile for the vertical velocity after each time-step was solved, vortices of two to three mesh widths formed.

---

<sup>i</sup> See Acknowledgements, §1.0 and §2.0 referring to the scope of the project ERB N° IC15-CT98-0904

All other schemes produced stable, laminar structures apart from the model that included the addition of the basic profile of the temperature after each time-step. However, the phenomena observed were little different from the method where the just velocity profile was added to the solution after each time-step.

Using the analogy<sup>41</sup> between buoyant convection driven by density differences that is caused by the addition of either heat or a different phase (i.e. gas or solid), three turbulence schemes were employed to model the motion of a gas phase in a column of liquid. Two of the turbulence schemes used were the k- $\epsilon$  and the Reynolds stresses turbulence models. The final turbulence scheme involved solving the flow-field with the Reynolds stresses model, where only the basic velocity profile was added to the flow-field after each time-step. Alternative mixture models were also employed, one of which was derived from a scalar equation and the other was the algebraic slip mixture model<sup>9</sup>.

The default Reynolds stresses model adequately captured the unsteady flow of a gas-liquid mixture in a bubble column. The scheme where a basic velocity profile was used did not display significant improvements to the solution of the flow field. The mixture model that employed the scalar equation with the Reynolds stresses model predicted velocity profiles that were comparable in magnitude and form to the experimental profiles presented by Sanyal et al<sup>26</sup> and Degaleesan et al<sup>35-36</sup>. The corresponding profiles predicted by algebraic slip mixture model were narrow compared to the profiles for the scalar equation model and over-predicted the velocity on the column centre-line. The gas hold-up profile for the scalar equation model was consistent with the flat profiles that were presented by Joshi<sup>47</sup>, whereas the profile for the algebraic slip mixture model was parabolic. Therefore, the modified scalar equation when solved with the Reynolds stresses model is appropriate for representing the volume fraction of the discrete phase in a bubble column.

The next phase of the project was to implement and test the application of the alternative mixture models to the motion of a pseudo-continuous solid phase prior to the use of both gas and solid phase forms of the mixture model in modelling gas-liquid-solid flow. Relying on the accuracy of the gas-liquid form of the mixture models, a slug of solid was injected into a domain to compare the performance of either mixture model using the algebraic slip or scalar equation models. Note that the no comparisons with experimentation were made. It was found that the motion of the solid phase predicted by either model was similar with the only

differences caused by the alternative formulations of the mixture viscosity (Equation 5 and Equation 57 to Equation 59) and the volume fraction (Equation 3, Equation 54 and Equation 56). A note of caution must be mentioned about the mixture viscosity for algebraic slip mixture model not including a term for the maximum fraction of the discrete phase (i.e. 0.99 or 1 for gas bubbles and 0.62 for solid particles). This means that fractions that exceed or approach the maximum fraction are likely to be inaccurate, though this did not occur for the test cases described here.

### ***Three-phase flow***

The algebraic slip and scalar equation forms of the mixture models were combined to model gas-liquid-solid flow in a bubble column as the cases GLS1, GLS2 and GLS3<sup>i</sup>. Again no direct comparisons were made with experimentation due to the mesh configurations employed. The motion of the solid phase for the GLS1 case is captured quite well, except that there is a problem in the application of the boundary conditions as solid is lost through the flow boundaries at the top and bottom of the column. The transport of the solid phase in the GLS2 and GLS3 cases capture the physicality of solid motion without the loss of the solid phase from the top and bottom boundary conditions. Only the profiles of the solid fraction for the GLS2 and GLS3 cases are comparable to the experimental profiles (Figure 42) of Warsito<sup>56-58</sup>. Therefore, the scalar equation model provides a reasonable approximation of the gas and solid phases thus the solid phase can be directly treated as a microbial cell culture.

### ***Three-phase flow and reaction***

The reaction rates and yield coefficients of two strains of the mould *Aspergillus niger* were used to model the transport of molasses, the cell culture (represented by the solid phase) and the metabolic product, citric acid. The reactions mimicked processes that occur within a microbial culture adequately, where the consumption of molasses and the formation of citric acid displayed power law properties that have long been associated with fermentation of carbohydrates by *Aspergillus niger*<sup>1,59-61 and 65</sup>. Note that where the solid fraction or cell culture concentration was at the greatest observed value, the molasses consumed and the citric acid formed were also at their greatest. The simulations that employed the higher specific

---

<sup>i</sup> For the specifications of the GLS1, GLS2 and GLS3 cases refer to Table 22, Table 23 and Table 26, respectively.

growth rate predicted a flow-field that differed from the flow-field predicted by the cases that used the lower growth rate. This implies that the amount suspended solids present influences the flow structure, as a higher solid fraction was observed for the second strain of the mould.

Two meshes were employed in the transport and reaction of the biochemical species with height to diameter ratios of 5:1 and 20:1. The flow structures and profiles for the 5:1 mesh were equivalent to the earlier gas-liquid and gas-liquid-solid models where the scalar equation form of the mixture model was used to represent the volume fraction for both of the discrete phases (GLS3 case). Direct comparisons between biochemical species concentrations, volume fractions and the velocity profiles could not be made for the 20:1 mesh, as the flow profiles were not experimentally investigated<sup>63</sup>. Berovič et al<sup>63</sup> noted that there was a reduction in the shear rate in the upper half of the column. This was also observed for the 20:1 simulations, with a reduction in the frequency of the velocity oscillations and a reduction in the magnitude of flow profiles between column heights of 2.5 and 10 diameters of the column. Note that the fraction of the solid phase was greater in the lower half of the 20:1 column for the simulated flows, but the fraction of the cell culture was great in the upper half of the experimental column<sup>63</sup>. The reason for the greater cell concentration at the top of the experimental column was a result of the change in the shear rate influencing the growth of the cell culture. The effect of the shear rate on cell growth was not included in the reaction models and this caused the differences observed for the solid fraction.

### ***Overall***

The operating characteristics of bubble columns and airlift reactors have shown that there is a viable alternative to stirred tank reactors for the biotechnology industry. However, the design of the bubble column reactors is difficult because there is a lack of fundamental understanding of the transport and reaction processes that exist. Design procedures for the construction and operation of bubble columns are simplified to steady, one-dimensional flows<sup>2</sup>. Yet many experimental and numerical investigations into fluid flow in bubble columns have described unsteady, multi-dimensional flows<sup>4-6,17-33,35-37,41 and 48-58</sup>. Just some of the many effects that influence the motion of gas bubbles and solid particles were modelled here with a commercial computational fluid dynamics (CFD) code for a biochemical reactor where a simple reaction was employed. The gas-liquid-solid flow models performed well for the low solid phase fractions considered, but the reaction models need the inclusion of many multiphase flow

effects and factors that affect the growth and maintenance of a cell culture, to be able to design a bubble column reactor using just CFD. The models discussed here are good enough to assist in the design of bubble column reactors when using standard design procedures, so that the transient multi-dimensional flows are accounted for in the design of reactors.

The multiphase models used in CFD codes can currently provide information about the mixing characteristics of bubble columns and airlift reactors. This information can be used to educate biochemical and chemical engineers across many process (petroleum, biochemical, chemical, pharmaceutical and waste treatment) industries about the instabilities and transport capabilities of such reactors.

## **7.2 Further investigations**

Multiphase model improvements should include:

- further tests in the viability of the  $k$ - $\epsilon$  turbulence and Reynolds stresses models for the boundary conditions and the constants that define the influence of each parameter modelled are required,
- test the consistency of the gas-liquid model across three domains, i.e. plane, rectangular and cylindrical flows
- model complex three-dimensional geometries for gas-liquid, gas-liquid-solid flows,
- detailed comparison of gas-liquid-solid flow with experimentation,
- the effect that temperature has on multiphase transport processes through the energy equation,
- inclusion of multiple bubble sizes for the gas phase with coalescence and break-up of bubbles,
- influence of the solid phase on the gas phase i.e. the coalescence and break-up of bubbles through particle-bubble interactions,
- solid-solid particle interactions i.e. van der Waals forces, repulsive forces and other electrostatic effects, conductivity, granular temperature, particle collision and break-up
- equipment specifications i.e. aspect ratios of height to diameter, riser to downcomer area etc

- the motion of the gas-liquid interface at the top surface and the expansion of the bubble bed that occurs as the gas phase is bubbled through the bubble column.

Biochemical reaction model improvements should include:

- modelling specific stages of the micro-organism life cycle,
- mass transport between the gas and liquid phases, i.e. transport of oxygen and carbon dioxide,
- include diffusion models i.e. from the bulk liquid to the pellet, through the polysaccharide matrix that exists in the pellet and across the cell membrane,
- the effect that temperature has on the diffusion and reaction processes through the energy equation,
- inclusion of cell maintenance rates of substrate consumption along with cell growth and the influence that cell maintenance has on product formation,
- influence of the mixture viscosity when biochemical reactions occur i.e. pseudo-plastic fluids from the polysaccharide matrix excreted by the micro-organism,
- the influence of pH level changes in the reactor on biochemical reactions critical to design of fermenters,
- the effect that chemical species such as trace metals, nitrogen, phosphorous and sulphur sources display on cell growth and product formation rates, Therefore, model different culture types i.e. cultures in the form of suspended pellets, viscous broths etc
- three-dimensional models for multiphase flow and reaction and the effect of the equipment specifications.

## 8.0 LIST OF REFERENCES

1. Bailey, J. E. and Ollis, D. F., Biochemical Engineering Fundamentals, McGraw-Hill, 1986, London, England
2. Deckwer, W. -D., Bubble Column Reactors, Jon Wiley and Sons Ltd, 1992, Chichester, England
3. Chisti, M. Y., Airlift Bioreactors, Elsevier Science Publishers Ltd, 1989, London, England
4. Zahradník, J. Růžicka, M. Markoš, J. Teixeira, J. Generalis, S. and Thomas, N. Modelling Design of Multiphase Bubble-Bed Reactors for Advanced Food-Industry Applications, Third European Congress of Chemical Engineering, Nuremberg, Germany 26-28th June 2001
5. Růžicka, M. Drahoš, J. Zahradník, J. and Thomas, N. (1999) Natural modes of multi-orifice bubbling from a common plenum, *Chemical Engineering Science* **54**, 5223-5229
6. Růžicka M, (2000), On bubbles rising in a line, *International Journal of Multiphase Flow* **26**, 1146-1181
7. CFX Solvers, AEA Technology plc, The Gemini Building, Fermi Avenue, Harwell International Business Centre, Didcot, Oxfordshire OX11 0QR, United Kingdom ([www.aeat.com](http://www.aeat.com))
8. Estet-Astrid Solver, 1 rue James Joule 78286 GUYANCOURT Cedex ([www.simulog.fr](http://www.simulog.fr))
9. Fluent Solvers, Fluent Europe Ltd, Sheffield Airport Business Park, Europa Link, Sheffield S9 1XU ([www.fluent.co.uk](http://www.fluent.co.uk))
10. Star-CD, Computational Dynamics, 200 Shepherds Bush Road, London, W6 7NY, ENGLAND ([www.cd.co.uk](http://www.cd.co.uk))
11. FLUENT 5 Users Guide, Fluent Incorporated, Centerra Park, 10 Cavendish Court, Lebanon, NH03766, USA, 1998
12. Compaq Computer Corporation, P.O. Box 692000, Houston, Texas 77269-2000, USA ([www.compaq.com](http://www.compaq.com))
13. Advanced Micro Devices, Incorporated, AMD Headquarters, One AMD Way, P.O. Box 3453 Sunnyvale, CA94088 ([www.amd.com](http://www.amd.com))
14. Intel Corporation, 2200 Mission College Blvd., P.O. Box 58119, Santa Clara, CA 95052-8119, USA ([www.intel.com](http://www.intel.com))
15. Linux Online Incorporated, Linux Online 59 East River St, #2 Ogdensburg, NY 13669, U.S.A. ([www.linux.org](http://www.linux.org))

16. Windows NT or 2000 Servers, Microsoft Corporation, One Microsoft Way Redmond, WA 98052-6399, USA ([www.microsoft.com](http://www.microsoft.com))
17. Sokolichin, A. Eigenberger, G. Lapin, A. and Lübbert, A. (1997) Dynamic numerical simulation of gas-liquid two-phase flows, *Chemical Engineering Science* **52**, 611-626
18. Lapin, A. and Lübbert, A. (1994) Numerical simulation of the dynamics of two-phase gas-liquid flows in bubble columns, *Chemical Engineering Science* **49**, 3661-3674.
19. Delnoij, E., Fluid dynamics of gas-liquid bubble columns - a theoretical and experimental study, PhD Thesis, Twente University, The Netherlands, 1998, ISBN 90-36512085
20. Sokolichin, A. and Eigenberger, G. (1994) Gas-liquid flow in bubble columns and loop reactors: Part I. Detailed modelling and numerical simulation, *Chemical Engineering Science* **49**, 5735-5746
21. Becker, S. Sokolichin, A. and Eigenberger, G. (1994) Gas-liquid flow in bubble columns and loop reactors: Part II. Comparisons of detailed experiments and flow simulations, *Chemical Engineering Science* **49**, 5747-5762
22. Sokolichin, A. and Eigenberger, G. (1999) Applicability of the standard k- $\epsilon$  turbulence model to the dynamic simulation of bubble columns: Part I. Detailed numerical simulations, *Chemical Engineering Science* **54**, 2273-2284
23. Borchers, O. Busch, A. Sokolichin, A. and Eigenberger, G. (1999) Application of the standard k- $\epsilon$  turbulence model to the dynamic simulation of bubble columns. Part II: Comparison of detailed experiments and flow simulations, *Chemical Engineering Science* **54**, 5927-5935
24. Zuber, N. and Findlay, J. A. (1965) Average volumetric concentrations in two-phase flow systems, *Journal of Heat Transfer* **87**, 453-468
25. Manninen, M. Taivassalo V. and Kallio, S. (1996) On the mixture model for multiphase flow, *VTT Publications*, **288**, ISBN 951-38-4946-5
26. Sanyal, J. Vásquez, S. Roy, S. and Dudukovic, M. P. (1999) Numerical simulation of gas-liquid dynamics in cylindrical bubble column reactors, *Chemical Engineering Science*, **54**, 5071-5083
27. Ishii, M. and Zuber, N. (1979) Drag coefficient and relative velocity in bubbly, droplet and particulate flow, *AIChE Journal*, **25**, 843-854
28. Ishii, M. and Mishima, K. (1984) Two-fluid model and hydrodynamic constitutive relations, *Nuclear Engineering and Design* **82**, 107-126
29. Torvik, R. and Svendsen, H. F. (1990) Modeling of slurry reactors: A fundamental approach, *Chemical Engineering Science* **45**, 2325-2332

30. Svendsen, H. F. Jakobsen, H. A. and Torvik, R. (1992) Local flow structure in internal loop and bubble column reactors, *Chemical Engineering Science* **47**, 3297-3304
31. Ranade, V. V. (1997) Modeling of turbulent flow in a bubble column reactor, *Transactions of the Institution of Chemical Engineers* **75A**, 14-23
32. Cartland Glover, G. M., Generalis, S. C. and Thomas, N. H. (2000) Dynamic simulations of multiphase flow in bubble columns, Proceedings of the 14<sup>th</sup> International Congress of Chemical and Process Engineering, CHISA 2000, 27-31 August 2000, Prague, Czech Republic, Lecture G5.5, ISBN 80-86059-30-8
33. Cartland Glover, G. M., Generalis, S. C. and Thomas, N. H. (2001) Three phase flow in bubble columns, 3<sup>rd</sup> European Congress of Chemical Engineering, Session 16 Multiphase Flows, Posters, 26<sup>th</sup>-28<sup>th</sup> June 2001, Nuremberg, Germany, (<http://www.dechema.de/veranstaltung/ecce/cd/table16.htm>)
34. Hinze, J. O. Turbulence, McGraw-Hill, 1976, New York,
35. Degaleesan, S. (1997) Fluid dynamic measurements and modelling of liquid mixing in bubble columns. D.Sc. Thesis, Washington University, St Louis, Missouri, USA
36. Degaleesan, S. Dudukovic, M. P. and Yan, P. (2001) Experimental study of gas-induced liquid-flow structures in bubble columns, *AIChE Journal*, **47**, 1913-1931
37. Kumar, S. B. (1994) Computed tomographic measurements of void fraction and modelling of the flow in bubble columns. PhD Thesis, Florida Atlantic University: Boca Raton, Florida, USA
38. Launder, B. E. and Spalding, D. B., The numerical computation of turbulent flows, *Computer Methods in Applied Mechanics and Engineering*, **3**, 269-289, 1974
39. Nagata, M. and Busse, F. H. (1983) Three-dimensional tertiary motions in a plane shear layer, *Journal of Fluid Mechanics* **135**, 1-26
40. Chait, A. and Korpela, S. A. (1989) The secondary flow and its stability for natural convection in a tall vertical enclosure, *Journal of Fluid Mechanics* **200**, 189-216
41. Van Den Akker, H. A. (1998) Coherent structures in multiphase flows, *Powder Technology* **100**, 123-136
42. Leonard, B. P. (1979), A stable and accurate convective modelling procedure based on quadratic upstream interpolation, *Computer Methods in Applied Mechanics and Engineering*, **19**, 59-98
43. Patanakar, S. V., Numerical Heat Transfer and Fluid-Flow, Hemisphere Publishing, 1980, New York, London

44. Barth, T. J. and Jespersen, D. (1989) The design and application of upwind schemes on unstructured meshes, Technical Report AIAA-890366, AIAA 27<sup>th</sup> Aerospace Sciences Meeting, Reno, Nevada, USA.
45. Vandoormaal, J. P. and Raithby, G. D. (1984) Enhancement of the SIMPLE method for predicting incompressible fluid-flows, *Numerical Heat Transfer*, **7**, 147-163
46. Versteeg, H.K. and Malalasekera, W., An introduction to Computational Fluid Dynamics, Longman Group Ltd, 1995, London, England
47. Joshi, J. B. (2001) Computational flow modelling and design of bubble column reactors, *Chemical Engineering Science* **56**, 5893-5933
48. Ding, J. and Gidaspow, D. (1990) A bubbling fluidization model using kinetic theory of granular flow, *AIChE Journal* **36**, 523-538
49. Wu, Y. X. and Gidaspow, D. (2000) Hydrodynamic simulation of methanol synthesis in gas-liquid slurry bubble column reactors, *Chemical Engineering Science* **55**, 573-587
50. Padial, N. T., Vander Heyden, W. B., Rauenzahn, R. M. and Yarbrow, S. L. (2000) Three-dimensional simulation of a three-phase draft-tube bubble column, *Chemical Engineering Science* **55**, 3261-3273
51. Li, Y., Zhang, J. P. and Fan L. S. (1999) Numerical simulation of gas-liquid-solid fluidization systems using a combined CFD-VOF-DPM method: bubble wake behavior, *Chemical Engineering Science* **54**, 5101-5107
52. Li, Y., Yang, G. Q., Zhang, J. P. and Fan, L. S. (2001) Numerical studies of bubble formation dynamics in gas-liquid-solid fluidization at high pressure, *Powder Technology* **116**, 246-260
53. Dziallas, H., Michele, V. and Hempel, D. C. Measurement and modeling of local phase holdup and flow structure in three-phase bubble columns, Proceedings of the International Symposium on Multiphase Flow and Transport Phenomena, Antalya Turkey November 5-10 2000
54. Michele, V., Enss, J., Dziallas, H. and Hempel, D. C., Liquid flow structure in three-phase bubble columns and airlift loop reactors, Proceedings of the Fourth International Conference on Multiphase Flow, New Orleans, May 27 to June 6 2001
55. Michele, V., Dziallas, H. Enss, J. and Hempel, D. C. Three-phase flow in bubble columns – measurement and modelling, Proceedings of the Third European Congress in Chemical Engineering 26-28 June 2001
56. Warsito, Ohkawa, M., Maezawa, A. and Uchida, S. (1997) Flow structure and phase distributions in a slurry bubble column, *Chemical Engineering Science* **52**, 3941-3947

57. Warsito, Ohkawa, M., Kawata, N. and Uchida, S. (1999) Cross-sectional distributions of gas and solid holdups in slurry bubble column investigated by ultrasonic computed tomography, *Chemical Engineering Science* **54**, 4711-4728
58. Warsito, W. and Fan, L.-S. (2001) Measurement of real-time flow structures in gas-liquid and Gas-liquid-solid flow systems using electrical capacitance tomography (ECT), *Chemical Engineering Science* **56**, 6455 –6462
59. Atkinson, K. and Mavituna, F., *Biochemical Engineering and Biotechnology*, Macmillan Publishers Ltd, 1983, UK
60. Zidwick, M. J., *Organic Acids*, §11 of *Biotechnology of filamentous fungi: technology and products*, Edited by Finkelstein, D. B. and Ball, C., Butterworth-Heinemann, 1991, Stoneham, Massachusetts, USA
61. Coulson, J. M. and Richardson, J. F., *Chemical Engineering Volume 3*, Third Edition, Edited by Richardson, J. F. and Peacock, D. G., Elsevier Science Limited, 1994, Oxford, UK
62. Sakurai, A., Imai, H., Takenaka, Y. and Sakakibara, M. (1997) Simulation of citric acid production by rotating disk contactor, *Biotechnology and Bioengineering* **56**, 689-696
63. Berovič, M., Koloini, T., Olsvik, E. S. and Kristiansen, B. (1993) Rheological and morphological properties of submerged citric acid fermentation in stirred tank and bubble column reactors, *The Chemical Engineering Journal and The Biochemical Engineering Journal* **53**, B35-B40
64. Haq, I. -U., Ali, S., Qadeer, M. A. and Iqbal, J. (2002) Effect of copper ions on mould morphology and citric acid productivity by *Aspergillus niger* using molasses based media, *Process Biochemistry* **37**, 1085-1090
65. Roehr, M., Zehentgruber, O. and Kubicek, C. P. (1981) Kinetic of biomass formation and citric acid production by *Aspergillus niger* on pilot plant scale, *Biotechnology and Bioengineering* **23**, 2433-2445
66. Sankpal, N. V., Joshi, A. P. and Kulkarni, B. D. (2001) Citric acid production by *Aspergillus niger* immobilized on cellulose microfibrils: influence of morphology and fermenter conditions on productivity, *Process Biochemistry* **36**, 1129-1139
67. Alvarez-Vasquez, F., González-Alcón, C., and Torres, N. V. (2000) Metabolism of citric acid production by *Aspergillus niger*: Model definition, steady-state analysis and constrained optimisation of citric acid production rate, *Biotechnology and Bioengineering* **70**, 82-108

68. Wood, B.D. and Whitaker, S. (1998) Diffusion and reaction in biofilms, *Chemical Engineering Science* **53**, 397-425
69. Wanner, O. and Gujer, W. (1986) A multispecies biofilm model, *Biotechnology and Bioengineering* **28**, 314-328
70. Rittmann, B. E. and McCarty, P. L. (1980) Model of steady-state-biofilm kinetics, *Biotechnology and Bioengineering* **22**, 2343-2357
71. Kissel, J. C., McCarty, P. L. and Street, R. L (1984) Numerical simulation of mixed-culture biofilm, *Journal of Environmental Engineering* **110**, 393-411
72. Sinclair, C. G. and Kristiansen, B., Fermentation kinetics and modelling, Edited by J. D. Bu'Lock, Open University Press, 1987, Milton Keynes, England

## 9.0 NOMENCLATURE

### 9.1 Model equations

#### *General symbols*

B	buoyancy effect term from Reynolds stresses model
C	coefficient
$C'_1$	constant in the linear pressure-strain model, for the wall reflection term, 0.5
$C'_2$	constant in the linear pressure-strain model, for the wall reflection term, 0.3
c	specific heat capacity ( $\text{J kg}^{-1} \text{K}^{-1}$ )
d	particle diameter (m)
E	enthalpy
F	external forces ( $\text{kg m s}^{-2}$ )
f	dimensionless friction factor (-)
G	generation of turbulent energy
Gr	Grashof Number
g	acceleration due to gravity vector ( $0 -9.81 0 \text{ m s}^{-2}$ )
k	kinetic energy ( $\text{m}^2 \text{s}^{-2}$ )
K	interphase momentum exchange coefficient
$\mathbf{K}'$	interaction force vector between the phases
L	characteristic length (m)
M	mass (kg)
m	characterises the mass transfer between the phases
n	unit normal vector (where the subscript defines the direction of the vector)
P	stress production term for the Reynolds stresses model
p	pressure ( $\text{N m}^{-2}$ )
q	variable (i.e. velocity)
$q'$	primary flow variable (i.e. velocity)
$q''$	secondary flow variable (i.e. velocity)
R	effect of system rotation of the Reynolds stresses model

Re	Reynolds number (-)
r	density ratio
r'	rate of reaction ( $\text{kg m}^{-3} \text{ s}^{-1}$ )
S	source term
t	time (s)
tanh	hyperbolic tangent function
U	mean velocity ( $\text{m s}^{-1}$ )
u	velocity component ( $\text{m s}^{-1}$ )
V	volume ( $\text{m}^3$ )
v	slip velocity component ( $\text{m s}^{-1}$ )
W	distance to the wall (m)
x	spatial co-ordinate (m)
$Y_{P/Q}$	yield coefficient of unit mass of P per unit mass of Q ( $(\text{kg P}) (\text{kg Q})^{-1}$ )

***Mathematical operators***

D	total differential operator
d	differential operator
$\partial$	partial differential operator
$\nabla$	del operator
$\Delta$	difference between two quantities of a variable
$\Sigma$	summation
$\times$	curl
$\cdot$	dot product
$\otimes$	dyadic product
$\rightarrow$	vector form of variable (i.e. representing i, j and k forms of the variable as a matrix)
$\bar{\quad}$	bar denoting an averaged product

### ***Greek symbols***

$\alpha$	volume fraction
$\beta$	coefficient of thermal expansion ( $\text{K}^{-1}$ )
$\delta$	Kronecker symbol
$\varepsilon$	rate of dissipation of turbulent energy ( $\text{m}^2 \text{s}^{-2}$ )
$\phi$	scalar function variable, in this case representing the volume fraction of the discrete phase
$\phi'$	volume fraction
$\phi''$	concentration ( $\text{kg m}^{-3}$ )
$\Gamma$	diffusion coefficient for the scalar function
$\gamma$	pressure strain
$\eta$	constant for the linear pressure-strain model wall reflection term, 0.41
$\kappa$	thermal conductivity ( $\text{W m}^{-1} \text{K}^{-1}$ )
$\lambda$	specific growth rate ( $\text{s}^{-1}$ )
$\mu$	dynamic viscosity ( $\text{kg m}^{-1} \text{s}^{-1}$ )
$\nu$	kinematic viscosity ( $\text{m}^2 \text{s}^{-1}$ )
$\theta$	temperature (K)
$\rho$	density ( $\text{kg m}^{-3}$ )
$\sigma$	Prandtl number (for the kinetic energy equation is 1 for k- $\varepsilon$ turbulence transport or 0.82 for the Reynolds stresses and 1.3 for the dissipation rate)
$\tau$	deviatoric stress tensor
$\Omega$	mean rate of rotation tensor

### ***Subscripts and superscripts***

0	reference value for a physical property at a corresponding quantity for an associated variable i.e. density of fluid at a specific temperature
1	constant for the linear pressure-strain model, 1.8
2	constant for the linear pressure-strain model, 0.6

1 $\epsilon$	constant for the turbulent dissipation of energy, 1.44
2 $\epsilon$	constant for the turbulent dissipation of energy, 1.92
3 $\epsilon$	constant for the turbulent dissipation of energy
b	buoyancy
CA	citric acid concentration
CC	computational cell/reactor volume
c	continuous phase
D	drag
DS	solid phase drift velocity
D <sub>q</sub>	drift velocity of the qth phase
eff	effective value in reference to the addition of turbulent and non-turbulent contributions of a variable
GAS	gas phase
h	heat source for the conservation of heat
i	co-ordinate index
j	co-ordinate index normal to i
k	kinetic energy
L	liquid phase
l	co-ordinate index
lift	lift force
M	molasses substrate
m	co-ordinate index
mp	mixture phase index
n	number of phases
P	species P i.e. S or CA
p	pressure context for the specific heat capacity
Q	species Q i.e. S or M
q	discrete or particulate phase (including bubbles, drops and particles)
qm	maximum discrete phase fraction (i.e. 0.62 for solids and 1 for bubbles)
r	phase index
ref.	reference value of a variable
rq	denotes interphase interaction terms for the two-fluid models

S	solid phase volume fraction
SG	parameter where the concentration, mass or volume is increased by cell growth
s	mass source for the conservation of mass
t	turbulent context
w	wall effects
w,1	variable at wall 1, i.e. specified as the right wall
w,2	variable at wall 2, i.e. specified as the left wall
vm	virtual mass force
x	co-ordinate depend force effect
$\varepsilon$	rate of dissipation of turbulent energy
$\phi$	diffusion coefficient of the scalar equation, 0.1
$\phi'$	diffusion coefficient of the volume fraction equations, 0.1
$\phi''$	diffusion coefficient of the concentration equations, 0.001
$\mu$	turbulent viscosity constant, 0.09
*	viscosity power function, different for solid and gas phases
•	rate of mass transport between phases

## 9.2 User-defined functions

### *Array identifiers and pointers*

c	array identifier for the cell, to apply the function to a specific part of the simulated domain
domain	array identifier for the whole mesh array
dS	array for the derivative in the DEFINE_SOURCE subroutine
eqn	array for the equation in the DEFINE_SOURCE subroutine
f	array identifier for the face, to apply the function to a specific part of the simulated domain
ND_ND	array of the dimensions of the mesh
t	array identifier for the thread, to apply the function to a specific part of the simulated domain
*domain	pointer to the domain array
*n0	pointer to the n0 node array

*t	pointer to the thread array
*t0	pointer to the t0 thread array
*tf	pointer to the tf thread array

### ***Descriptive commands***

define	statement to declare variables, as functions, real numbers or integers
else	else logic statement
enum	declare multiple variables for a specific function that has multiple attributes
fabs	modulus function, e.g. fabs(SLIP) is equivalent to $ SLIP $
if	if logic statement
include	statement link the file to another file to access global variables
pow	power function, e.g. pow(1,2) is equivalent to $1^2$
return	returns a function or value to the program code from the function
sqrt	square root function e.g. sqrt(9) is equivalent to 3
udf.h	header file for user-defined functions, enabling access to macros, subroutines and variables

### ***Global variables***

CG	acceleration due to gravity
CT	redefinition of the cell temperature
CU	horizontal velocity redefinition
CV	redefinition of the cell vertical velocity
CVOL	computational cell volume
Ci	general constant with index i
C_i	constant of the value of -10 used in the temperature profile
GD	gas bubble diameter
GF	gas phase volume fraction
GLF	liquid fraction for the three-phase model
GLMU	gas-liquid mixture viscosity

GLSMU	gas-liquid-solid mixture viscosity
GMU	gas phase viscosity
GR	gas density
GV	gas phase volume
i	profile or constant index number
LF	liquid phase volume fraction
LR	liquid phase density
LMU	liquid phase viscosity
LV	liquid phase volume
MUE	effective viscosity
MR	mixture density
PC	concentration of the product
PFR	product formation rate
Pi	velocity profile constant with index i
RC	concentration of the substrate
RCR	overall substrate consumption rate
RPR	product formation rate due to consumption of substrate
RPY	yield of product per unit mass of substrate
RSY	yield of cells per unit mass of substrate
RSR	cell growth rate due to consumption of substrate
SC	solid phase concentration
SD	solid phase particle diameter
SF	solid phase volume fraction
SGF	volume of cells grown
SGM	mass of cells grown
SGR	rate of cell growth
SGV	volume of cells grown
SLA	specific growth rate
SLF	fraction for the mixture of the gas and liquid phases in the three-phase model
SLMU	solid-liquid mixture viscosity
SM	solid phase mass
SPY	yield of product per unit mass of cells
SR	solid phase density

SV	solid phase volume
TS	time step size

***Local variables***

c0	local variable for the cell array c
cdu	horizontal direction drag coefficient
cdv	vertical direction drag coefficient
dotix	dot product with respect to the horizontal direction
dotiy	dot product with respect to the vertical direction
gdu	gas phase horizontal direction drag coefficient
gdv	gas phase vertical direction drag coefficient
gru	gas phase horizontal direction Reynolds number
grv	gas phase vertical direction Reynolds number
i	index number for dot product, either deviatoric stress tensor, drift velocity or flux term
n	local variable for the node array n0
physical-time-step	used in the RP_Get_Real function to return the time-step size
rate	local variable to determine the value of reaction source or sink term
ri	local variable to determine the value of reaction source or sink term
reu	horizontal direction Reynolds number
rev	vertical direction Reynolds number
sdu	gas phase horizontal direction drag coefficient
sdv	gas phase vertical direction drag coefficient
sru	gas phase horizontal direction Reynolds number
srv	gas phase vertical direction Reynolds number
te	difference between the temperature profile and the predicted temperatures
tp	temperature profile variable
vi	variable for #define macros, local to the macro in question
vp	profile variable
x[0]	position in the [ND_ND] vector/array at location 0

xc	coordinate index
y	square of horizontal location, z
z	non-dimensional position across the width of the mesh

### ***Macros***

CDi	calculates one of two drag coefficients with index i
C_CENTROID	function to return the centroid of a cell
C_FACE	extract cell number
C_FACE_THREAD	extract thread number on face c
C_NODE	determine node n0
C_T	temperature calculated in the solver
C_UDMI	user defined memory
C_UDSI	scalar function variable
C_U	vertical velocity calculated in the solver
C_V	vertical velocity calculated in the solver
C_VOLUME	returns the volume of a computational cell
DEFINE_ADJUST	adjustment routine, returning as a void or no variable
DEFINE_INIT	initialises the value of the variables at the start of the simulation
DEFINE_ON_DEMAND	defines the value of the variables on demand, returns as a void
DEFINE_PROPERTY	subroutine to enter physical properties into the solver
DEFINE_SOURCE	subroutine to enter transport equation source terms into the solver
F_C0	returns the cell identity for a specific face
Get_Domain	function to return the domain array
NODE_X	returns the x location for node n0
NODE_Y	returns the y location for node n0
RE	returns the particle Reynolds number
RP_Get_Real	returns the time-step size from the solver
SQR	square root function
THREAD_T0	returns the thread identity from the solver
TV	terminal velocity of the particle
VERTVP	macro to calculate the vertical velocity profile

### ***Loop commands***

<code>begin_c_loop</code>	macro to loop cells
<code>begin_c_loop_all</code>	macro to loop all cells
<code>c_face_loop</code>	macro to loop faces in a cell
<code>c_node_loop</code>	macro to loop nodes in a cell
<code>end_c_loop</code>	end looping macro
<code>end_c_loop_all</code>	macro to end all loops
<code>thread_loop_c</code>	looping macro to loop over all cell threads in the domain

### ***Scalar equation identifiers***

<code>GAS</code>	gas phase scalar equation identifier
<code>N_REQUIRED_UDS</code>	command that notifies the solver of the end of the scalar equation list
<code>PROD</code>	product concentration identifier
<code>SOL</code>	solid phase volume fraction identifier
<code>SUB</code>	substrate concentration equation identifier

### ***Symbolic commands***

<code>#</code>	used to notify the compiler of a define or include statement
<code>;</code>	end of line for a function
<code>"..."</code>	start and end of filename to be read as the code is performed
<code>(...)</code>	brackets that group variables together, passing variables onto another subroutine
<code>[...]</code>	array brackets, where the number is an integer
<code>{...}</code>	function/routine brackets
<code>/*...*/</code>	commented text brackets
<code>=</code>	term on the left-hand side is equal to the relationship on the right-hand side
<code>+</code>	add
<code>-</code>	subtract
<code>*</code>	multiply, or pointer to an array in the form <code>Thread *t</code>

/	divide
<	less than
<=	less than or equal to
>	greater than
>=	greater than or equal to
^	superscript in commented text
e	exponent, e.g. 1e-5 is equivalent to $1 \cdot 10^{-5}$

### ***Type definition***

cell_t	variable type, to apply the functions to the volumes that are component parts of the whole domain
Domain	variable type, to apply the whole mesh domain
face_t	variable type, to apply the functions to the surfaces that are component parts of a cell
Node	point in space defined by the geometry
Thread	variable type, to apply the functions to threads, component parts of a face
real	defines the type of variable, this case it is a real number (also represented by float)

### ***User defined function names***

a_gls_s1_calc, domain	calculates variables during each iteration
b_gls_s1_calc, domain	initialises x and y direction deltas
gas_s1_vof	calculates the gas volume fraction equation source
gl2d_mu1	calculates the gas-liquid viscosity
gl2d_vof	calculates the scalar equation source term
gl2d_xmom	calculates the x-direction momentum equation source term
gl2db_calc	updates the velocity profile after each time step
gl2dc_calc	initialises the velocity profile and the x and y direction deltas
gl2dd_calc	calculates variables during each iteration
gl_s1_rho	calculates the gas-liquid density
gl_s1_xmom	calculates the x-direction momentum equation source term

gls_s1_ymom	calculates the y-direction momentum equation source term
prod_s1_conc	calculates the cell concentration equation source
sol_s1_vof	calculates the solid volume fraction equation source
sub_s1_conc	calculates the cell concentration equation source
velo_calc1	calculates lateral convection profiles when requested
velo_calc4	calculates lateral convection profiles before every iteration
velo_calc5	initialises lateral convection profiles

## 10.0 APPENDIX 1: FLOW AND REACTION MODELS

The following equations are discretised and used in Fluent code to model multiphase flow, turbulence, thermal convection and reaction <sup>9,11,25-26,72</sup>.

### 10.1 Mixture model equations

Equation 1: continuity equation for the mixture phase

$$\frac{\partial}{\partial t}(\rho_{mp}) + \frac{\partial}{\partial X_i}(\rho_{mp} u_{mp,i}) = 0$$

Equation 2: momentum equation for the mixture

$$\begin{aligned} \frac{\partial}{\partial t}(\rho_{mp} u_{mp,j}) + \frac{\partial}{\partial X_i}(\rho_{mp} u_{mp,i} u_{mp,j}) = & -\frac{\partial p}{\partial X_j} + \rho_{mp} g_j + F_j \\ & + \frac{\partial}{\partial X_i} \sum_{q=1}^n \alpha_q \rho_q u_{Dq,i} u_{Dq,j} + \frac{\partial}{\partial X_j} \mu_{mp} \left( \frac{\partial}{\partial X_j} (u_{mp,i}) + \frac{\partial}{\partial X_i} (u_{mp,j}) \right) \end{aligned}$$

Equation 3: volume fraction equation for the mixture model

$$\frac{\partial}{\partial t}(\alpha_q \rho_q) + \frac{\partial}{\partial X_i}(\alpha_q \rho_q u_{mp,i}) = -\frac{\partial}{\partial X_i}(\alpha_q \rho_q u_{Dq,i})$$

Equation 4: mixture density

$$\rho_{mp} = \sum_{q=1}^n \alpha_q \rho_q$$

Equation 5: mixture viscosity

$$\mu_{mp} = \sum_{q=1}^n \alpha_q \mu_q$$

Equation 6: mass averaged velocity

$$\bar{u}_{mp} = \frac{\sum_{q=1}^n \alpha_q \rho_q \bar{u}_q}{\rho_{mp}}$$

Equation 7: drift velocity

$$\vec{u}_{Dq} = \vec{u}_q - \vec{u}_{mp} = \vec{v}_{q,c} - \frac{1}{\rho_{mp}} \sum_{r=1}^{n-1} \alpha_r \rho_r \vec{v}_{r,c}$$

Equation 8: slip velocity equation

$$\vec{v}_{q,c} = \vec{u}_q - \vec{u}_c = \frac{d_q^2 (\rho_{mp} - \rho_q)}{18\mu_c f} \left( \vec{g}_j - \frac{D\vec{u}_{mp}}{Dt} \right)$$

Equation 9: friction factor for the mixture model

$$f = 1 + 0.05 \text{Re}^{0.687} \quad \text{Re} < 1000$$

$$f = 0.018 \text{Re} \quad \text{Re} \geq 1000$$

Equation 10: particle Reynolds number for the mixture model

$$\text{Re} = \frac{d_q u_{mp} \rho_c}{\mu_c}$$

## 10.2 Two fluid model equations

Equation 11: continuity equation for the two-fluid model

$$\frac{\partial}{\partial t} (\alpha_r r_r) + \nabla \cdot (\alpha_r r_r \vec{u}_r) = \frac{1}{\rho_{r,\text{ref}}} \sum_{r=1}^n \dot{m}_{rq}$$

Equation 12: momentum equation for the two-fluid model

$$\frac{\partial}{\partial t} (\alpha_r \rho_r \vec{u}_r) + \nabla \cdot (\alpha_r \rho_r \vec{u}_r \otimes \vec{u}_r) = -\alpha_r \nabla p + \nabla \bar{\tau}_r + \alpha_r \rho_r \vec{g} + \vec{F}_r + \sum_{r=1}^n (\vec{K}'_{rq} + \dot{m}_{rq} \vec{u}_{rq})$$

Equation 13: volume fraction equation for the two-fluid model

$$\sum_{r=1}^n \alpha_r = 1$$

Equation 14: shear stress equation from the momentum equation for the two-fluid model

$$\tau_{r,ij} = \alpha_r \mu_r \left( \frac{\partial u_{r,i}}{\partial x_j} + \frac{\partial u_{r,j}}{\partial x_i} \right) - \frac{2}{3} \alpha_r \mu_r \delta_{ij} \frac{\partial u_{r,l}}{\partial x_l}$$

Equation 15: two-fluid density ratio

$$r_r = \frac{\rho_r}{\rho_{r,\text{ref}}}$$

Equation 16: two-fluid model phase interaction force equation

$$\sum_{r=1}^n \vec{K}'_{rq} = \sum_{r=1}^n K_{rq} (\vec{u}_r - \vec{u}_q)$$

Equation 17: two-fluid model momentum exchange coefficient

$$K_{rq} = \frac{3}{4} C_D \frac{\alpha_q \rho_r |\vec{u}_q - \vec{u}_r|}{d_q}$$

Equation 18: lift force for the two-fluid model

$$F_{\text{lift}} = -0.5 \rho_q \alpha_q |\vec{u}_q - \vec{u}_r| \times (\nabla \times \vec{u}_r)$$

Equation 19: virtual mass effect for the two-fluid model

$$F_{\text{vm}} = 0.5 \alpha_q \rho_r \left( \frac{\partial \mathbf{u}_r}{\partial t} - \frac{\partial \mathbf{u}_q}{\partial t} \right)$$

### 10.3 Discrete phase model equations

Equation 20: particle force balance equation

$$\frac{d\mathbf{u}_q}{dt} = F_D (\mathbf{u} - \mathbf{u}_q) + \mathbf{g}_i \frac{(\rho - \rho_q)}{\rho_q} + F_x$$

Equation 21: particle drag force

$$F_D = \left( \frac{18\mu}{\rho_p d_p^2} \right) \left( \frac{C_D \text{Re}_p}{24} \right)$$

Equation 22: particle Reynolds number for the discrete phase model

$$\text{Re}_q = \frac{\rho d_q |\mathbf{u}_q - \mathbf{u}|}{\mu}$$

Equation 23: particle virtual mass force effect

$$F_x = \frac{1}{2} \frac{\rho}{\rho_q} \frac{d}{dt} (\mathbf{u} - \mathbf{u}_q)$$

Equation 24: particle pressure force effect

$$F_x = \left( \frac{\rho}{\rho_q} \right) \mathbf{u}_q \frac{\partial \mathbf{u}}{\partial \mathbf{x}}$$

## 10.4 Turbulence transport equations

### *k-ε turbulence transport equations*

Equation 25: turbulent kinetic energy transport equation

$$\rho \frac{Dk}{Dt} = \frac{\partial}{\partial x_i} \left[ \left( \mu + \frac{\mu_t}{\sigma_k} \right) \frac{\partial k}{\partial x_i} \right] + G_k + G_b - \rho \varepsilon$$

Equation 26: rate of dissipation of energy from turbulent flow, transport equation

$$\rho \frac{D\varepsilon}{Dt} = \frac{\partial}{\partial x_i} \left( \mu + \frac{\mu_t}{\sigma_\varepsilon} \right) \frac{\partial \varepsilon}{\partial x_i} + C_{1\varepsilon} \frac{\varepsilon}{k} (G_k + C_{3\varepsilon} G_b) - C_{2\varepsilon} \frac{\varepsilon^2}{k}$$

Equation 27: turbulent viscosity formulation

$$\mu_t = \rho C_\mu \frac{k^2}{\varepsilon}$$

Equation 28: total derivative for the turbulent kinetic energy

$$\frac{Dk}{Dt} = \frac{\partial k}{\partial t} + \frac{\partial k u}{\partial x_i}$$

Equation 29: total derivative for the rate of dissipation of energy from the turbulent flow

$$\frac{D\varepsilon}{Dt} = \frac{\partial \varepsilon}{\partial t} + \frac{\partial \varepsilon u}{\partial x_i}$$

Equation 30: constant that determines the orientation buoyant shear layers

$$C_{3\varepsilon} = \tanh \left| \frac{u_j}{u_i} \right|$$

**Reynolds stresses model for turbulence transport**

Equation 31: exact transport equation for the transport of Reynolds stresses

$$\begin{aligned} \frac{\partial}{\partial t} (\overline{\rho u_i u_j}) + \frac{\partial}{\partial x_1} (\overline{\rho U_1 u_i u_j}) = & - \frac{\partial}{\partial x_1} \left[ \overline{\rho u_i u_j u_1} + \overline{p(\delta_{lj} u_i + \delta_{il} u_j)} \right] \\ & + \frac{\partial}{\partial x_1} \left[ \overline{\mu \frac{\partial}{\partial x_1} (u_i u_j)} \right] - \rho \left( \overline{u_i u_1} \frac{\partial U_j}{\partial x_1} + \overline{u_j u_1} \frac{\partial U_i}{\partial x_1} \right) + \overline{p \left( \frac{\partial u_i}{\partial x_j} + \frac{\partial u_j}{\partial x_i} \right)} \\ & - \rho \beta (\overline{g_i u_j \theta} + \overline{g_j u_i \theta}) - 2 \overline{\mu \frac{\partial u_i}{\partial x_1} \frac{\partial u_j}{\partial x_1}} - 2 \rho \Omega_1 (\overline{u_j u_m \varepsilon_{ikm}} + \overline{u_i u_m \varepsilon_{jkm}}) \end{aligned}$$

Equation 32: turbulent diffusive transport

$$\frac{\partial}{\partial x_1} \left[ \overline{\rho u_i u_j u_1} + \overline{p(\delta_{lj} u_i + \delta_{il} u_j)} \right] = \frac{\partial}{\partial x_1} \left( \frac{\mu_t}{\sigma_k} \frac{\partial}{\partial x_1} (\overline{u_i u_j}) \right)$$

Equation 33: buoyancy effects

$$B_{ij} = \rho \beta (\overline{g_i u_j \theta} + \overline{g_j u_i \theta}) = \beta \frac{\mu_t}{\sigma_t} \left( g_i \frac{\partial \rho}{\partial x_j} + g_j \frac{\partial \rho}{\partial x_i} \right)$$

Equation 34: stress production

$$P_{ij} = \rho \left( \overline{u_i u_1} \frac{\partial U_j}{\partial x_1} + \overline{u_j u_1} \frac{\partial U_i}{\partial x_1} \right)$$

Equation 35: system rotation effects

$$R_{ij} = 2 \rho \Omega_1 (\overline{u_j u_m \varepsilon_{ikm}} + \overline{u_i u_m \varepsilon_{jkm}})$$

Equation 36: pressure-strain term

$$\gamma_{ij} = \overline{p \left( \frac{\partial u_i}{\partial x_j} + \frac{\partial u_j}{\partial x_i} \right)}$$

Equation 37: decomposition of pressure-strain term

$$\gamma_{ij} = \gamma_{ij,1} + \gamma_{ij,2} + \gamma_{ij}^w$$

Equation 38: slow pressure-strain term

$$\gamma_{ij,1} = -C_1 \rho \frac{\varepsilon}{k} \left[ \overline{u_i u_j} - \frac{2}{3} \delta_{ij} k \right]$$

Equation 39: rapid pressure-strain term

$$\gamma_{ij,2} = -C_2 \left[ \begin{aligned} & \left( P_{ij} + R_{ij} + B_{ij} + \frac{\partial}{\partial x_1} (\rho U_1 \overline{u_i u_j}) \right) \\ & + \frac{2}{3} \delta_{ij} \left( \frac{1}{2} P_{11} + \frac{1}{2} B_{11} - \frac{1}{2} \frac{\partial}{\partial x_1} (\rho U_1 \overline{u_1 u_1}) \right) \end{aligned} \right]$$

Equation 40: wall reflection term

$$\gamma_{ij}^w = C'_1 \frac{\varepsilon}{k} \left( \overline{u_i u_m n_l n_m} \delta_{ij} - \frac{3}{2} \overline{u_i u_l n_j n_l} - \frac{3}{2} \overline{u_j u_l n_i n_l} \right) \frac{k^{3/2}}{(C_\mu^{3/4} / \eta) \varepsilon W}$$

$$C'_2 \left( \gamma_{lm,2} n_l n_m \delta_{ij} - \frac{3}{2} \gamma_{il,2} n_j n_l - \frac{3}{2} \gamma_{jl,2} n_i n_l \right) \frac{k^{3/2}}{(C_\mu^{3/4} / \eta) \varepsilon W}$$

## 10.5 Thermal convection equations

Equation 41: energy transport equation

$$\frac{\partial}{\partial t} (\rho E) + \frac{\partial}{\partial x_i} [u_i (\rho E + p)] = \frac{\partial}{\partial x_i} \left[ \left( \kappa + \frac{c_p \mu_t}{\sigma_t} \right) \frac{\partial \theta}{\partial x_i} + u_j (\tau_{ij})_{\text{eff}} \right] + S_h$$

Equation 42: conservation of mass equation

$$\frac{\partial \rho}{\partial t} + \frac{\partial}{\partial x_i} (\rho u_i) = S_s$$

Equation 43: conservation of momentum equation

$$\frac{\partial}{\partial t} (\rho u_i) + \frac{\partial}{\partial x_j} (u_i u_j) = -\frac{\partial p}{\partial x_i} + \frac{\partial \tau_{ij}}{\partial x_j} - \rho_0 \beta (\theta - \theta_0) g_i + F_i$$

Equation 44: deviatoric stress tensor

$$(\tau_{ij})_{\text{eff}} = \mu_{\text{eff}} \left( \frac{\partial u_j}{\partial x_i} + \frac{\partial u_i}{\partial x_j} \right) - \frac{2}{3} \mu_{\text{eff}} \frac{\partial u_i}{\partial x_i} \delta_{ij}$$

Equation 45: Boussinesq approximation

$$\rho = \rho_0 (1 - \beta \Delta \theta)$$

Equation 46: Grashof Number

$$\text{Gr} = \frac{g\beta\Delta\theta L^3}{\nu^2} = \frac{UL}{\nu}$$

Equation 47: characteristic velocity based on the Grashof number

$$U = \frac{g\beta\Delta\theta L^2}{\nu}$$

Equation 48: Prandtl number

$$\sigma = \frac{\nu}{\kappa}$$

Equation 49: temperature difference

$$\Delta\theta = \theta_{w,1} - \theta_{w,2}$$

Equation 50: update the flow field variables, references a profile

$$q(x_i, x_j, t) = q''(x_i, x_j, t) + q'(x_i)$$

Equation 51: velocity profile for the lateral convection problem

$$q'(x_i) = u_j(x_i) = -\frac{x_i}{24} + \frac{x_i^3}{6}$$

Equation 52: temperature profile for the lateral convection problem

$$q'(x_i) = \theta(x_i) = -10 * x_i + 305$$

## 10.6 Scalar equations

Equation 53: momentum equation

$$\frac{\partial}{\partial t}(\rho_{mp} \mathbf{u}_{mp,i}) + \frac{\partial}{\partial x_j}(\rho \mathbf{u}_{mp,i} \mathbf{u}_{mp,j}) = -\frac{\partial p}{\partial x_i} + \rho_{mp} \mathbf{g}_i + F_i$$

Equation 54: convective scalar equation

$$\frac{\partial \phi_q \rho_q}{\partial t} + \frac{\partial}{\partial x_i} \left( \rho_{mp} \mathbf{u}_{mp,i} \phi_q - \Gamma \frac{\partial \phi_q}{\partial x_i} \right) = S_\phi$$

Equation 55: momentum source term

$$F_i = \nabla \left( \mu_{\text{eff}} \left( \frac{\partial}{\partial x_j} (u_{\text{mp},i}) + \frac{\partial}{\partial x_i} (u_{\text{mp},j}) \right) + \sum_{q=1}^n \phi_q \rho_q u_{\text{Dq},i} u_{\text{Dq},j} \right)$$

Equation 56: scalar equation source term

$$S_\phi = \nabla \left( \mu_{\text{eff}} \left( \frac{\partial}{\partial x_j} (u_{\text{mp},i}) + \frac{\partial}{\partial x_i} (u_{\text{mp},j}) \right) + \phi_q \rho_q u_{\text{mp},i} + \sum_{q=1}^n \phi_q \rho_q u_{\text{Dq},i} \right)$$

Equation 57: mixture viscosity

$$\mu_{\text{mp}} = \mu_c \left( 1 - \frac{\phi}{\phi_{\text{qm}}} \right)^{-2.5 \phi_{\text{qm}} \mu^*}$$

Equation 58: solid phase  $\mu^*$

$$\mu^* = 1$$

Equation 59: gas phase  $\mu^*$

$$\mu^* = \frac{\mu_q + 0.4 \mu_c}{\mu_q + \mu_c}$$

Equation 60: empirical velocity profile for air-water flow in a bubble column

$$q'(x_i) = u_j(x_i) = -0.9254 * x_i^2 - 0.1076 * x_i + 0.1425$$

## 10.7 Biochemical reaction equations

### *Assumptions for the transport and reaction of a micro-organism*

The following assumptions were made to obtain reaction models for the consumption of substrates by a cell culture:

- the reaction and transport of chemical species occur in a batch reactor
- the cell culture as a suspension of loose pellets where only viable cells exist
- isothermal transport and reaction of the species
- isothermal transport of each phase
- oxygen transport is a limiting factor in the growth and maintenance of the cell culture, but spatial changes in the gas phase fraction of oxygen add to the complexity of the model
- to effectively model the dissolution of oxygen into the liquid phase the change in the gas phase fraction of oxygen must be included
- therefore, for reasons of complexity, mass transfer across the gas-liquid interface is ignored and thus its influence on the metabolic function of the cell culture is ignored

- from this a single substrate is consumed as a result of the cell growth and maintenance mechanisms
- one extra-cellular product species is formed as a result of cell growth and maintenance metabolisms
- cell growth and maintenance rates are combined into one rate and is expressed as a specific growth rate
- when the concentration of the substrate reaches zero, both the substrate consumption, cell growth and product formation rates are assumed to be zero
- pseudo-steady state conditions apply to the biofilm, therefore, diffusion of species into the biofilm has little influence on the concentration of the substrates
- the viscosity of the broth is only influenced by the gas bubbles and cell concentration or solid particles, i.e. the substrate, product are assumed to have no effect on the viscosity

### ***Transport and reaction equations***

Equation 61: cell mass balance

$$\frac{d\phi_S''}{dt} = r_S'$$

Equation 62: substrate mass balance

$$\frac{d\phi_M''}{dt} = -(r_{MS}' + r_{MCA}')$$

Equation 63: product formation mass balance

$$\frac{d\phi_{CA}''}{dt} = r_{CA}'$$

Equation 64: cell growth rate of reaction

$$r_S' = \lambda \phi_S''$$

Equation 65: reaction rate for the cell growth associated substrate consumption

$$r_{MS}' = \frac{r_S'}{Y_{S/M}}$$

Equation 66: reaction rate for the citric acid formation associated substrate consumption

$$r_{MCA}' = \frac{r_{CA}'}{Y_{CA/M}}$$

Equation 67: reaction rate for product formation

$$r_{CA}' = Y_{CA/S} r_S'$$

Equation 68: volume of liquid

$$V_L = (1 - (\phi'_{GAS} + \phi'_S))V_{CC}$$

Equation 69: mass of cells grown per unit time

$$M_{SG} = r'_S V_L = \lambda \phi''_S V_L$$

Equation 70: volume of cells grown per unit time

$$V_{SG} = M_{SG} / \rho_S$$

Equation 71: volume fraction of the cell culture that is grown

$$\phi'_{SG} = \frac{V_{SG}}{V_{CC}}$$

Equation 72: transport of the solid phase as a volume fraction

$$\begin{aligned} \frac{\partial \phi'_S}{\partial t} + \frac{\partial}{\partial x_i} \left( \rho u_{mp,i} \phi'_S - \Gamma_{\phi'} \frac{\partial \phi'_S}{\partial x_i} \right) = \phi'_{SG} + \nabla \left( \mu_{eff} \left( \frac{\partial}{\partial x_j} (u_{mp,i}) + \frac{\partial}{\partial x_i} (u_{mp,j}) \right) \right) \\ + \nabla \left( \phi'_S \rho_S u_{mp,i} + \sum_{S=1}^n \phi'_S \rho_S u_{DS,i} \right) \end{aligned}$$

Equation 73: transport and consumption of glucose as a concentration

$$\frac{\partial \phi''_M}{\partial t} + \frac{\partial}{\partial x_i} \left( \rho u_{mp,i} \phi''_M - \Gamma_{\phi''} \frac{\partial \phi''_M}{\partial x_i} \right) = - \left( \frac{r'_S}{Y_{S/M}} + \frac{r'_{CA}}{Y_{CA/M}} \right)$$

Equation 74: transport and formation of citric acid as a concentration

$$\frac{\partial \phi''_{CA}}{\partial t} + \frac{\partial}{\partial x_i} \left( \rho u_{mp,i} \phi''_{CA} - \Gamma_{\phi''} \frac{\partial \phi''_{CA}}{\partial x_i} \right) = Y_{CA/S} r'_S$$

## 11.0 APPENDIX 2: SOURCE CODE FOR USER-DEFINED FUNCTIONS

The user-defined functions presented below are used to model thermal convection and multiphase flow with reaction through the modification of scalar equations<sup>9,11,26,72</sup>. The model equations are found in §10.1, §10.5, §10.6 and §10.7 and were implemented using the C programming language through conventions devised by Fluent Incorporated<sup>9</sup>. These conventions enable the Fluent<sup>9</sup> user to add code to the program, to modify the application of the mathematical models. To improve the ease of use when linking the additional code to the software, a series of functions or subroutines were created and stored in a header file and are labelled, DEFINE\_<sub>11</sub>.

### 11.1 Lateral convection in a high aspect ratio cavity

*/\* Source UDF to up vertical velocity and temperature value for the linear temperature profile for 50:1 mesh heated from the left with asymmetric vertical velocity profile \*/*

```
#include "udf.h" /* udf header file */
#define C3 3.0 /* constant of the value 3 */
#define C6 6.0 /* constant of the value 6 */
#define C_24 -24.0 /* constant of the value -24 */
#define C_10 -10.0 /* temperature gradient for linear profile */
#define CT C_T(c, t) /* cell temperature, K */
#define CV C_V(c, t) /* cell velocity, m s^-1 */
#define C305 305.0 /* midpoint temperature */
DEFINE_ON_DEMAND(velo_calc1)
{
    Domain *domain=Get_Domain(1); /* mesh assignment command (whole mesh domain) */
    Thread *t; /* mesh assignment command (threads) */
    cell_t c; /* mesh assignment command (cells) */
    face_t f; /* mesh assignment command (faces) */
    real x[ND_ND],z,vp; /* local variables definition */
    thread_loop_c (t,domain)
    {
        begin_c_loop_all (c,t)
        {
            C_CENTROID(x,c,t); /* cell identification */
            z = x[0]; /* non-dimensional width */
            vp=((z/C_24)+(pow(z,C3)/C6)); /* vertical velocity profile */
            C_V(c,t)=CV+vp; /* assigning the velocity to the cell */
        }
        end_c_loop_all (c,t)
    }
}
DEFINE_ADJUST(velo_calc4,domain)
{
    Thread *t; /* mesh assignment command (threads) */
    cell_t c; /* mesh assignment command (cells) */
    face_t f; /* mesh assignment command (faces) */
    real x[ND_ND],z,vp,tp,te; /* local variables definition */
    thread_loop_c (t,domain)
    {
        begin_c_loop_all (c,t)
        {
            C_CENTROID(x,c,t); /* cell identification */
            z=x[0]; /* non-dimensional width */
            vp=((z/C_24)+(pow(z,C3)/C6)); /* vertical velocity profile */
```

```

        tp=(C_10*z+C305);          /* linear temperature profile */
        te=CT-tp;
        C_V(c,t)=CV+vp;          /* assigning the velocity to the cell */
        C_T(c,t)=CT+te;          /* assigning the temperature to the cell */
    }
    end_c_loop_all (c,t)
}
}
}
DEFINE_INIT(velo_calc5,domain)
{
    Thread *t;                    /* mesh assignment command (threads) */
    cell_t c;                      /* mesh assignment command (cells) */
    face_t f;                      /* mesh assignment command (faces) */
    real x[ND_ND],z,vp;            /* local variables definition */
    thread_loop_c (t,domain)
    {
        begin_c_loop_all (c,t)
        {
            C_CENTROID(x,c,t);     /* cell identification */
            z=x[0];                 /* non-dimensional width */
            vp=((z/C24)-(pow(z,C3)/C6)); /* vertical velocity profile */
            C_V(c,t)=vp;           /* assigning the velocity to the cell */
        }
        end_c_loop_all (c,t)
    }
}

```

## 11.2 Gas-liquid flow using a scalar transport equation

```

/*-----*/
/*-----Source UDF to vertical velocity and volume fraction profiles for two-phase flow -----*/
/*-----*/
#include "udf.h" /* udf header file */
enum
{
    GAS,
    N_REQUIRED_UDS
};
/*-----Fluent Variables-----*/
#define CU C_U(c,t) /* cell x-velocity, m s^-1 */
#define CV C_V(c,t) /* cell y-velocity, m s^-1 */
#define MUE C_MU_EFF(c,t) /* effective viscosity, m s^-1 */
#define TS RP_Get_Real("physical-time-step") /* function to extract the time-step size used by the solver */
/*-----Constants-----*/
#define P1 0.2 /* constant of the value 0.2 */
#define P2 -0.9254 /* constant of the value -0.9254 */
#define P3 -0.1076 /* constant of the value 0.1076 */
#define P4 0.1425 /* constant of the value 0.1425 */
#define VERTVP(z,y) ((P2*y)+(P3*z)+P4) /* vertical velocity profile v1=z*z, v2=z*/
#define C0 0 /* constant of the value 0 */
#define C1 1.0 /* constant of the value 1. */
#define C2 2.0 /* constant of the value 2. */
#define C3 3.0 /* constant of the value 3. */
#define C4 0.1 /* constant of the value 0.1 */
#define C5 18.0 /* constant of the value 18. */
#define C6 -2.5 /* mixture viscosity constant =-2.5 */
#define C7 0.4 /* drop ratio for continuous phase viscosity=0.4 */
#define C8 0.01 /* constant of the value 0.01 */
#define C9 1000.0 /* constant of the value of 0.1 */

```

```

#define C10 0.05 /* constant of the value 0.05 */
#define C11 0.687 /* constant of the value 0.687 */
#define C12 0.018 /* constant of the value of 0.018 */
#define C17 0.5 /* constant of the value of 0.5 */
#define CG -9.81 /* gravitational acceleration, m s^-2 */
/*-----Multiphase property macros (gas, liquid, solid)-----*/
#define GD 0.005 /* gas bubble diameter, m */
#define GR 1.225 /* gas density, kg m^-3 */
#define GF C_UDSI(c,t,GAS) /* cell volume fraction */
#define GMU 1.7894e-5 /* gas viscosity, kg m^-1 s^-1 */
#define LR 998.2 /* liquid density, kg m^-3 */
#define LF (C1-GF) /* liquid volume fraction */
#define LMU 0.001003 /* liquid viscosity, kg m^-1 s^-1 */
/*-----Flow variable macros-----*/
#define MR ((GF*GR)+(LF*LR)) /* mixture density, kg m^-3 */
#define GLMU LMU*pow((C1-(GF/C1)),(C6*C1*((GMU+C7*LMU)/(GMU+LMU)))
/* mixture viscosity, kg m^-1 s^-1 */
#define TV(v1,v2,v3,v4,v5) (((v1-v2)*pow(v3,C2))/(C5*v4*v5))
/* terminal velocity of particle, m s^-1, where v1=discrete density, v2=continuous density, v3=particle diameter,
v4=continuous phase viscosity, v5=drag force */
#define RE(v1,v2,v3,v4) fabs(v1)*v2*v3/v4
/* Reynolds number, where v1=phase velocity, v2=diameter of particle, v3=continuous phase density,
v4=mixture phase viscosity */
#define CD1(v) (C1+C10*pow(v,C11)) /* drag coefficient for RE<1000*/
#define CD2(v) (C12*v) /* drag coefficient for RE>1000*/
/*-----Subroutines-----*/
DEFINE_PROPERTY(gl2d_mu1,c,t)
{
    return (GLMU); /* mixture viscosity for the gas-liquid mixture */
}
/* dot products of gas-liquid mixture interaction term, fluxes and the appropriate deviatoric stress tensors for the
x momentum and the gas fraction equations */
DEFINE_SOURCE(gl2d_xmom, c, t, dS, eqn)
{
    real dot1x,dot1y,dot2x,dot2y;
    dot1x=C8*GF*GR*C_UDMI(c,t,1)*C_UDMI(c,t,6)/C_UDMI(c,t,10);
    dot1y=C8*GF*GR*C_UDMI(c,t,6)*C_UDMI(c,t,1)/C_UDMI(c,t,11);
    dot2x=C8*(C_UDMI(c,t,12)+C_UDMI(c,t,13))/C_UDMI(c,t,10);
    dot2y=C8*(C_UDMI(c,t,12)+C_UDMI(c,t,13))/C_UDMI(c,t,11);
    return C17*C17*C8*(dot1x+dot1y+dot2x+dot2y);
}
DEFINE_SOURCE(gl2d_vof,c,t,dS,eqn)
{
    real dot1x,dot1y,dot2x,dot2y,dot3x,dot3y;
    dot1x=C8*GF*GR*(C_UDMI(c,t,1)+C_UDMI(c,t,6))/C_UDMI(c,t,10);
    dot1y=C8*GF*GR*(C_UDMI(c,t,6)+C_UDMI(c,t,1))/C_UDMI(c,t,11);
    dot2x=C17*GF*GR*(CV+CU)/C_UDMI(c,t,10);
    dot2y=C17*GF*GR*(CV+CU)/C_UDMI(c,t,11);
    dot3x=C8*(C_UDMI(c,t,12)+C_UDMI(c,t,13)+C_UDMI(c,t,14)+C_UDMI(c,t,15))/C_UDMI(c,t,10);
    dot3y=C8*(C_UDMI(c,t,12)+C_UDMI(c,t,13)+C_UDMI(c,t,14)+C_UDMI(c,t,15))/C_UDMI(c,t,11);
    return C17*C8*(dot1x+dot1y+dot2x+dot2y+dot3x+dot3y);
}
DEFINE_ON_DEMAND(gl2db_calc)
{
    Domain *domain=Get_Domain(1); /* accessing the domain used in the solver */
    Thread t; /* local mesh array variable definition */
    cell_t c;
    real x[ND_ND],y,z; /* local dimension variable definition */
    thread_loop_c (t,domain)
    {

```

```

        begin_c_loop (c,t)
        {
            C_CENTROID(x,c,t);          /* cell identification */
            z=fabs(x[0])/P1;             /* non-dimensional width */
            y=z*z;                       /* square of non-dimensional width */
            C_U(c,t)=C_UDMI(c,t,4);     /* add the mixture velocity to the horizontal velocity */
            C_V(c,t)=C_UDMI(c,t,9)+C4*VERTVP(z,y);
/* Assigning the velocity to the cell, as the vertical mixture velocity and the velocity profile */
        }
        end_c_loop (c,t)
    }
}
DEFINE_INIT(gl2dc_calc, domain)
{
    Node *n0;                          /* local mesh array variable definition */
    Thread *t,*t0,*tf;
    cell_t c;
    face_t f;
    int c0,n;
    real xc[ND_ND],y,z;                 /* local dimension variable definition */
    thread_loop_c (t, domain)
    {
        begin_c_loop (c,t)
        {
            c_face_loop(c,t,n)
            {
                f=C_FACE(c,t,n);        /* identifying face f */
                tf=C_FACE_THREAD(c,t,n); /* Identifying thread tf for f */
                c0=F_C0(f,tf);          /* Identifying cell c0 for f and tf */
                t0=THREAD_T0(tf);       /* extracting tf as t0 */
                c_node_loop(c,t,n)
                {
                    C_CENTROID(xc,c,t);
                    n0=C_NODE(c0,t0,n);
                    C_UDMI(c,t,10)=C17*sqrt(SQR(NODE_X(n0)-xc[0]));
                    C_UDMI(c,t,11)=C17*sqrt(SQR(NODE_Y(n0)-xc[1]));
/* Calculating the difference between the cell nodes and the cell centroids to act as the spatial derivatives */
                }
            }
        }
        end_c_loop (c,t)
        begin_c_loop (c,t)
        {
            C_CENTROID(xc,c,t);          /* cell identification */
            z=fabs(xc[0])/P1;             /* non-dimensional width */
            y=z*z;                       /* square of non-dimensional width */
            C_V(c,t)=VERTVP(z,y);       /* assigning the velocity to the cell */
        }
        end_c_loop (c,t)
    }
}
DEFINE_ADJUST(gl2dd_calc, domain)
{
    Thread *t;
    cell_t c;
    real cdu,cdv,reu,rev;
    thread_loop_c (t, domain)
    {
/* Calculating and assessing the particle Reynolds numbers to determine the drag coefficients*/
        begin_c_loop (c,t)

```

```

    {
        reu=RE(CU,GD,LR,LMU);
        if (reu<C9) cdu=CD1(reu);
        else if (reu>=C9) cdu=CD2(reu);
        rev=RE(CV,GD,LR,LMU);
        if (rev<C9) cdv=CD1(rev);
        else if (rev>=C9) cdv=CD2(rev);
    }
    end_c_loop (c,t)
/* Calculates slip, drift, gas, liquid and mixture phase velocities in the horizontal direction */
    begin_c_loop (c,t)
    {
        C_UDMI(c,t,0)=(C0-(CU*CU/C_UDMI(c,t,10))-(CV*CV/C_UDMI(c,t,11)) -(CU/TS))
                    *TV(GR,MR,GD,LMU,cdu);/* slip velocity */
        C_UDMI(c,t,1)=(C_UDMI(c,t,0)-CU);/* drift velocity */
        C_UDMI(c,t,2)=GF*(CU+C_UDMI(c,t,1));/* gas phase velocity */
        C_UDMI(c,t,3)=((CU*MR)-C_UDMI(c,t,2)*GR*GF)/(LR*LF);/* liquid phase velocity */
        C_UDMI(c,t,4)=(GR*GF*C_UDMI(c,t,2)+LR*LF*C_UDMI(c,t,3))/MR;/* mixture
velocity */
    }
    end_c_loop (c,t)
/* Calculates slip, drift, gas, liquid and mixture phase velocities in the vertical direction */
    begin_c_loop (c,t)
    {
        C_UDMI(c,t,5)=(CG-(CU*CV/C_UDMI(c,t,10))-(CV*CV/C_UDMI(c,t,11))-(CV/TS))
                    *TV(GR,MR,GD,LMU,cdv);
        C_UDMI(c,t,6)=(C_UDMI(c,t,5)-CV);
        C_UDMI(c,t,7)=GF*(CV+C_UDMI(c,t,6));
        C_UDMI(c,t,8)=((CV*MR)-C_UDMI(c,t,7)*GR*GF)/(LR*LF);
        C_UDMI(c,t,9)=(GR*GF*C_UDMI(c,t,7)+LR*LF*C_UDMI(c,t,8))/MR;
    }
    end_c_loop (c,t)
/* Calculates the deviatoric stress tensor components udm-12: i=j=1; udm-13: i=1, j=2; udm-14: i=2, j=1; udm-
15: i=j=2; */
    begin_c_loop (c,t)
    {
        C_UDMI(c,t,12)=CU*MUE*((CU/C_UDMI(c,t,10)+CU/C_UDMI(c,t,10))
                    -((C1*C2*CU/C_UDMI(c,t,10))/C3));
        C_UDMI(c,t,13)=CV*MUE*((CU/C_UDMI(c,t,11)+CV/C_UDMI(c,t,10))
                    -((C0*C2*CU/C_UDMI(c,t,10))/C3));
        C_UDMI(c,t,14)=CU*MUE*((CV/C_UDMI(c,t,10)+CU/C_UDMI(c,t,11))
                    -((C0*C2*CV/C_UDMI(c,t,11))/C3));
        C_UDMI(c,t,15)=CV*MUE*((CV/C_UDMI(c,t,11)+CV/C_UDMI(c,t,11))
                    -((C1*C2*CV/C_UDMI(c,t,11))/C3));
    }
    end_c_loop (c,t)
}
}
}

```

### 11.3 Gas-liquid-solid flow and reaction using four scalar transport equations

```

/*-----*/
/*--Source UDF to vertical velocity and volume fraction for 2D three-phase flow and reaction--*/
/*-----*/
#include "udf.h" /* udf header file */
enum
{
    SOL,

```

```

    GAS,
    SUB,
    PROD,
    N_REQUIRED_UDS
};
/* scalar-uds-0 = volume fraction of solid (SOL); s-u-1 = volume fraction of gas (GAS); s-u-2 = concentration of
substrate (SUB); s-u-3 = concentration of product (PROD); */
#define SF C_UDSI(c,t,SOL) /* microbial cell volume fraction */
#define GF C_UDSI(c,t,GAS) /* cell volume fraction */
#define RC C_UDSI(c,t,SUB) /* concentration of the substrate */
#define PC C_UDSI(c,t,PROD) /* concentration of the product */
/*-----Constants-----*/
/* See §11.2 for the definitions of C0 to C12, C17 and CG */
#define C16 0.62 /* maximum solid fraction 0.62 */
/*-----Fluent Variables-----*/
/* See §11.2 for the definitions of CU, CU, MUE and TS */
#define CVOL C_VOLUME(c,t) /* volume of each computational cell, m^3 */
/*-----Multiphase property macros (gas, liquid, solid)-----*/
/* See §11.2 for the definitions of GD, GR, GMU, LR and LMU */
#define GV (GF*CVOL) /* gas phase volume, m^3 */
#define SD 0.0001 /* solid bubble diameter, m */
#define SR 1080.0 /* solid density, kg m^-3 */
#define SV (SF*CVOL) /* solid phase volume, m^3 */
#define SM (SV*SR) /* solid phase mass, kg */
#define SLF (C1-SF) /* liquid fraction for solid liquid mixture, - */
#define GLF (SLF-GF) /* liquid fraction for gas-solid-liquid, - */
#define LV (GLF*CVOL) /* liquid phase volume, m^3 */
#define SC (SM/LV) /* solid phase concentration, kg m^-3 */
/*-----Species transport and reaction macros (substrates and product)-----*/
#define RSY 0.118 /* yield coefficient of cell growth per unit mass of
substrate: 0.118, 0.148 (kg cell) (kg substrate)^-1 */
#define RPY 0.442 /* yield coefficient of product formation per unit mass
of substrate: 0.442, 1.087 (kg citric acid) (kg substrate)^-1 */
#define SPY 3.752 /* yield coefficient of product formation per unit cell
mass: 3.752, 7.360 (kg citric acid) (kg cells)^-1 */
#define SLA 6.500e-5 /* specific growth rates: 6.500e-5, 1.522e-4 s^-1 */
#define SGR (SC*SLA) /* rate of growth kg m^-3 s^-1 */
#define SGM (C4*SGR*CVOL*TS) /* mass of cells grown per time step kg */
#define SGV (SGM/SR) /* volume of cells grown per time step m^3 */
#define SGF (SGV/CVOL) /* volume fraction of cells grown - */
#define PFR (TS*C4*(SGR*SPY)) /* concentration of product formed kg m^-3 */
#define RSR (SGR/RSY) /* cell growth substrate rate kg m^-3 s^-1 */
#define RPR (PFR/RPY) /* product formation substrate rate kg m^-3 s^-1 */
#define RCR -(TS*C4*(RSR+RPR)) /* concentration of substrate consumed kg m^-3 */
/*-----Flow variable macros-----*/
/* See §11.2 for the definitions of CD1, CD2, CU, CV, MUE, RE and TV */
#define MR ((GF*GR)+(GLF*LR)+(SF*SR)) /* mixture density, kg m^-3 */
#define SLMU LMU*pow((C1-(SF/C16)),(C6*C16*C1))
/* mixture viscosity for the liquid-solid mixture, kg m^-1 s^-1 */
#define GLSMU SLMU*pow((C1-(GF/C1)),(C6*C1*((GMU+C7*SLMU)/(GMU+SLMU)))
/* mixture viscosity for the gas-liquid-solid mixture, kg m^-1 s^-1 */
/*-----Subroutines-----*/
DEFINE_PROPERTY(gls_s1_rho,c,t)
{
    return (MR); /* mixture density for the liquid-solid mixture */
}
/* dot products of gas-liquid-solid mixture interaction term, fluxes and the appropriate deviatoric stress tensors
for the x and y momentum equations and the discrete phase fraction equations */
DEFINE_SOURCE(gls_s1_xmom, c, t, dS, eqn)
{

```

```

real dot1x,dot1y,dot2x,dot2y,dot3x,dot3y;
dot1x=C8*GF*GR*C_UDMI(c,t,7)*C_UDMI(c,t,10)/C_UDMI(c,t,14);
dot1y=C8*GF*GR*C_UDMI(c,t,10)*C_UDMI(c,t,7)/C_UDMI(c,t,15);
dot2x=SF*SR*C_UDMI(c,t,1)*C_UDMI(c,t,4)/C_UDMI(c,t,14);
dot2y=SF*SR*C_UDMI(c,t,4)*C_UDMI(c,t,1)/C_UDMI(c,t,15);
dot3x=C8*(C_UDMI(c,t,16)+C_UDMI(c,t,17))/C_UDMI(c,t,14);
dot3y=C8*(C_UDMI(c,t,16)+C_UDMI(c,t,17))/C_UDMI(c,t,15);
return C17*C8*(dot1x+dot1y+dot2x+dot2y+dot3x+dot3y);
}
DEFINE_SOURCE(gls_s1_ymom,c,t,dS,eqn)
{
real dot1x,dot1y,dot2x,dot2y,dot3x,dot3y;
dot1x=C8*GF*GR*C_UDMI(c,t,10)*C_UDMI(c,t,7)/C_UDMI(c,t,14);
dot1y=C8*GF*GR*C_UDMI(c,t,7)*C_UDMI(c,t,10)/C_UDMI(c,t,15);
dot2x=SF*SR*C_UDMI(c,t,4)*C_UDMI(c,t,1)/C_UDMI(c,t,14);
dot2y=SF*SR*C_UDMI(c,t,1)*C_UDMI(c,t,4)/C_UDMI(c,t,15);
dot3x=C8*(C_UDMI(c,t,18)+C_UDMI(c,t,19))/C_UDMI(c,t,14);
dot3y=C8*(C_UDMI(c,t,18)+C_UDMI(c,t,19))/C_UDMI(c,t,15);
return C17*C8*(dot1x+dot1y+dot2x+dot2y+dot3x+dot3y);
}
DEFINE_SOURCE(gas_s1_vof,c,t,dS,eqn)
{
real dt1x,dt1y,dt2x,dt2y,dt3x,dt3y;
dot1x=C8*GF*GR*(C_UDMI(c,t,7)+C_UDMI(c,t,10))/C_UDMI(c,t,14);
dot1y=C8*GF*GR*(C_UDMI(c,t,10)+C_UDMI(c,t,7))/C_UDMI(c,t,15);
dot2x=C17*GF*GR*(CV+CU)/C_UDMI(c,t,14);
dot2y=C17*GF*GR*(CV+CU)/C_UDMI(c,t,15);
dot3x=C8*(C_UDMI(c,t,16)+C_UDMI(c,t,17)+C_UDMI(c,t,18)+C_UDMI(c,t,19))/C_UDMI(c,t,14);
dot3y=C8*(C_UDMI(c,t,16)+C_UDMI(c,t,17)+C_UDMI(c,t,18)+C_UDMI(c,t,19))/C_UDMI(c,t,15);
return C17*C8*(dt1x+dt1y+dt2x+dt2y+dt3x+dt3y);
}
DEFINE_SOURCE(sol_s1_vof,c,t,dS,eqn)
{
real dt1x,dt1y,dt2x,dt2y,dt3x,dt3y,rate;
if(RC<=C0) rate=C0;
else if(RC>C0) rate=SGF;
dot1x=SF*SR*(C_UDMI(c,t,1)+C_UDMI(c,t,4))/C_UDMI(c,t,14);
dot1y=SF*SR*(C_UDMI(c,t,4)+C_UDMI(c,t,1))/C_UDMI(c,t,15);
dot2x=C17*SF*SR*(CV+CU)/C_UDMI(c,t,14);
dot2y=C17*SF*SR*(CV+CU)/C_UDMI(c,t,15);
dot3x=C8*(C_UDMI(c,t,16)+C_UDMI(c,t,17)+C_UDMI(c,t,18)+C_UDMI(c,t,19))/C_UDMI(c,t,14);
dot3y=C8*(C_UDMI(c,t,16)+C_UDMI(c,t,17)+C_UDMI(c,t,18)+C_UDMI(c,t,19))/C_UDMI(c,t,15);
return (rate+C17*C8*(dt1x+dt1y+dt2x+dt2y+dt3x+dt3y));
}
/* source terms for the concentration equations, involving the consumption and formation of the species
described */
DEFINE_SOURCE(sub_s1_conc,c,t,dS,eqn)
{
real rate;
if(RC<=C0) rate=C0;
else if(RC>C0) rate=RCR;
return rate;
}
DEFINE_SOURCE(prod_s1_conc,c,t,dS,eqn)
{
real rate;
if(RC<=C0) rate=C0;
else if(RC>C0) rate=PFR;
return rate;
}

```

```

DEFINE_ADJUST(a_gls_s1_calc,domain)
{
  Thread *t;
  cell_t c;
  real gdu,gdv,gru,grv,sdu,sdv,sru,svr;
  thread_loop_c (t,domain)
  {
/* Calculating and assessing the particle Reynolds numbers to determine the drag coefficients*/
    begin_c_loop (c,t)
    {
      sru=RE(CU,SD,LR,LMU);          /* solid particles */
      if (sru<C9) sdu=CD1(sru);
      else if (sru>=C9) sdu=CD2(sru);
      svr=RE(CV,SD,LR,LMU);
      if (svr<C9) sdv=CD1(svr);
      else if (svr>=C9) sdv=CD2(svr);
      gru=RE(CU,GD,LR,LMU);          /* gas bubbles */
      if (gru<C9) gdu=CD1(gru);
      else if (gru>=C9) gdu=CD2(gru);
      grv=RE(CV,GD,LR,LMU);
      if (grv<C9) gdv=CD1(grv);
      else if (grv>=C9) gdv=CD2(grv);
    }
    end_c_loop (c,t)
/* slip, drift and discrete phase velocities for the solid phase in the horizontal direction */
    begin_c_loop (c,t)
    {
      C_UDMI(c,t,0)=(C0-(CU*CU/C_UDMI(c,t,14))-(CV*CU/C_UDMI(c,t,15))-(CU/TS))
                    *TV(SR,MR,SD,LMU,sdu);/* slip velocity */
      C_UDMI(c,t,1)=(C_UDMI(c,t,0)-CU); /* drift velocity */
      C_UDMI(c,t,2)=SF*(CU+C_UDMI(c,t,1)); /* discrete phase velocity */
    }
    end_c_loop (c,t)
/* slip, drift and discrete phase velocities for the solid phase in the vertical direction */
    begin_c_loop (c,t)
    {
      C_UDMI(c,t,3)=(CG-(CU*CV/C_UDMI(c,t,14))-(CV*CV/C_UDMI(c,t,15))-(CV/TS))
                    *TV(SR,MR,SD,LMU,sdv);
      C_UDMI(c,t,4)=(C_UDMI(c,t,3)-CV);
      C_UDMI(c,t,5)=SF*(CV+C_UDMI(c,t,4));
    }
    end_c_loop (c,t)
/* slip, drift and discrete phase velocities for the gas phase in the horizontal direction */
    begin_c_loop (c,t)
    {
      C_UDMI(c,t,6)=(C0-(CU*CU/C_UDMI(c,t,14))-(CV*CU/C_UDMI(c,t,15))-(CU/TS))
                    *TV(GR,MR,GD,LMU,gdu);
      C_UDMI(c,t,7)=(C_UDMI(c,t,6)-CU);
      C_UDMI(c,t,8)=GF*(CU+C_UDMI(c,t,7));
    }
    end_c_loop (c,t)
/* slip, drift and discrete phase velocities for the gas phase in the vertical direction */
    begin_c_loop (c,t)
    {
      C_UDMI(c,t,9)=(CG-(CU*CV/C_UDMI(c,t,14))-(CV*CV/C_UDMI(c,t,15))-(CV/TS))
                    *TV(GR,MR,GD,LMU,gdv);
      C_UDMI(c,t,10)=(C_UDMI(c,t,9)-CV);
      C_UDMI(c,t,11)=GF*(CV+C_UDMI(c,t,10));
    }
    end_c_loop (c,t)

```

```

begin_c_loop (c,t)
{
  C_UDMI(c,t,12)=((MR*CU)-((GR*GF*C_UDMI(c,t,8)+(SR*SF*C_UDMI(c,t,2))))
    /(LR*GLF);/* liquid phase horizontal velocity */
  C_UDMI(c,t,13)=((MR*CV)-((GR*GF*C_UDMI(c,t,11)+(SR*SF*C_UDMI(c,t,5))))
    /(LR*GLF);/*liquid phase vertical velocity */
  C_U(c,t)=((LR*GLF*C_UDMI(c,t,12)+(GR*GF*C_UDMI(c,t,8)
    +(SR*SF*C_UDMI(c,t,2)))/MR);/* mixture horizontal velocity */
  C_V(c,t)=((LR*GLF*C_UDMI(c,t,13)+(GR*GF*C_UDMI(c,t,11)
    +(SR*SF*C_UDMI(c,t,5)))/MR);/*mixture phase vertical velocity */
}
end_c_loop (c,t)
/* deviatoric stress tensor components udm-16: i=j=1; udm-17: i=1, j=2; udm-18: i=2, j=1; udm-19: i=j=2; */
begin_c_loop (c,t)
{
  C_UDMI(c,t,16)=CU*MUE*((CU/C_UDMI(c,t,14)+CU/C_UDMI(c,t,14))
    -((C1*C2/C3)*(CU/C_UDMI(c,t,14))));
  C_UDMI(c,t,17)=CV*MUE*((CU/C_UDMI(c,t,15)+CV/C_UDMI(c,t,14))
    -((C0*C2/C3)*(CU/C_UDMI(c,t,14))));
  C_UDMI(c,t,18)=CU*MUE*((CV/C_UDMI(c,t,14)+CU/C_UDMI(c,t,15))
    -((C0*C2/C3)*(CV/C_UDMI(c,t,15))));
  C_UDMI(c,t,19)=CV*MUE*((CV/C_UDMI(c,t,15)+CV/C_UDMI(c,t,15))
    -((C1*C2/C3)*(CV/C_UDMI(c,t,15))));
}
end_c_loop (c,t)
begin_c_loop (c,t)
{
  real r1,r2,r3,r4;
  I
  if(RC<=C0)
  {
    r1=C0;
    r2=C0;
    r3=C0;
    r4=C0;
  }
  else if(RC>C0)
  {
    r1=SGR;
    r2=RCR;
    r3=PFR;
    r4=SGF;
  }
  C_UDMI(c,t,20)=GLF;
  C_UDMI(c,t,21)=GV;
  C_UDMI(c,t,22)=SV;
  C_UDMI(c,t,23)=LV;
  C_UDMI(c,t,24)=r1;
  C_UDMI(c,t,25)=r2;
  C_UDMI(c,t,26)=r3;
  C_UDMI(c,t,27)=r4;
  C_UDMI(c,t,28)=SC;
}
end_c_loop (c,t)
}
}
DEFINE_INIT(b_gls_s1_calc,domain)
{
  Node *n0; /* local mesh array variable definition */
  Thread *t,*t0,*tf;
  cell_t c;
}

```

```

face_t f;
int c0,n;
real xc[ND_ND];          /* local dimension variable definition */
thread_loop_c (t,domain)
{
    begin_c_loop (c,t)
    {
        c_face_loop(c,t,n)
        {
            f=C_FACE(c,t,n);          /* identifying face f */
            tf=C_FACE_THREAD(c,t,n); /* Identifying thread tf for f */
            c0=F_C0(f,tf);           /* Identifying cell c0 for f and tf */
            t0=THREAD_T0(tf);        /* extracting tf as t0 */
            c_node_loop(c,t,n)
            {
                C_CENTROID(xc,c,t);
                n0=C_NODE(c0,t0,n);
                C_UDMI(c,t,14)=C17*sqrt(SQR(NODE_X(n0)-xc[0]));
                C_UDMI(c,t,15)=C17*sqrt(SQR(NODE_Y(n0)-xc[1]));
            }
            /* Calculating the difference between the cell nodes and the cell centroids to act as the spatial derivatives */
        }
    }
    end_c_loop (c,t)
}
}

```

## 12.0 APPENDIX 3: CASE SPECIFICATIONS

### 12.1 Physical properties

Table 1: Material properties for all cases between §3.0 and §6.0.

<i>Material</i>	<i>Property</i>	<i>Units</i>	<i>Method</i>	<i>Value</i>
Aluminium (solid)	Density	kg m <sup>-3</sup>	constant	2719
	Specific Heat Capacity	J kg <sup>-1</sup> K <sup>-1</sup>	constant	871
	Thermal Conductivity	W m <sup>-1</sup> K <sup>-1</sup>	constant	202.4
Air (fluid)	Density	kg m <sup>-3</sup>	constant	1.225
	Viscosity	kg m <sup>-1</sup> s <sup>-1</sup>	constant	1.7894*10 <sup>-5</sup>
	Diameter	m	constant	0.005
Water-Liquid (fluid)	Density	kg m <sup>-3</sup>	constant	998.2
	Viscosity	kg m <sup>-1</sup> s <sup>-1</sup>	constant	0.001003
Air (fluid) for thermal convection	Density	kg m <sup>-3</sup>	boussinesq	1.225
	Specific Heat Capacity	J kg <sup>-1</sup> K <sup>-1</sup>	constant	1006.43
	Thermal Conductivity	W m <sup>-1</sup> K <sup>-1</sup>	constant	0.0242
	Viscosity	kg m <sup>-1</sup> s <sup>-1</sup>	constant	1.7894*10 <sup>-5</sup>
	Thermal Expansion Coefficient	K <sup>-1</sup>	constant	1.7661*10 <sup>-8</sup>
Mixture Phase - for scalar gas- liquid mixtures	Density	kg m <sup>-3</sup>	function	gl2d_mu1
	Viscosity	kg m <sup>-1</sup> s <sup>-1</sup>	function	gl2d_rho
	Diffusivity	-	gas uds-0	0.1
Mixture Phase - for scalar solid- liquid mixtures	Density	kg m <sup>-3</sup>	function	sl2d_mu
	Viscosity	kg m <sup>-1</sup> s <sup>-1</sup>	function	sl2d_rho
	Diffusivity	-	solid uds-0	0.1
Particulate Solid (fluid) - for algebraic slip mixture model	Density	kg m <sup>-3</sup>	constant	1080
	Viscosity	kg m <sup>-1</sup> s <sup>-1</sup>	constant	1
	Diameter	m	constant	0.0001
Mixture Phase - for scalar gas- liquid-solid mixtures	Density	kg m <sup>-3</sup>	function	gls2d_mu
	Viscosity	kg m <sup>-1</sup> s <sup>-1</sup>	function	gls2d_rho
	Diffusivity	-	solid uds-0	0.1
			gas uds-1	0.1
Mixture Phase - for gas-liquid- solid flow with the reaction and transport of scalar species	Density	kg m <sup>-3</sup>	function	gls2d_mu
	Viscosity	kg m <sup>-1</sup> s <sup>-1</sup>	function	gls2d_rho
	Diffusivity	-	solid uds-0	0.1
			gas uds-1	0.1
			substrate uds-2	1*10 <sup>-3</sup>
			product uds-3	1*10 <sup>-3</sup>

## 12.2 User defined functions

Table 2: External functions used in §3.0<sup>i</sup> and §4.0<sup>ii,iii</sup>.

<i>Function</i>	<i>Type</i>	<i>Description</i>
adj_vofandv	Adjust	Updates velocity profile for the gas-liquid flow with Reynolds stresses turbulence model
velo_calc1	On Demand	Updates velocity profile for the thermal convection problem after each time-step
velo_calc2	On Demand	Updates velocity and temperatures profiles for thermal convection problem after each time-step
velo_calc3	Adjust	Updates velocity profile for the thermal convection problem before each iteration
velo_calc4	Adjust	Updates velocity and temperatures profiles for the thermal convection problem before each iteration
velo_calc5	Init	Initialises velocity profile for the thermal convection problem
velo_calc6	Init	Initialises velocity and temperatures profiles for thermal convection problem
gl2d_mu1	Property	Gas-liquid mixture viscosity
gl2d_rho	Property	Gas-liquid mixture density
gl2d_xmom	Source	Gas-liquid x-momentum source
gl2d_ymom	Source	Gas-liquid y-momentum source
gl2d_vof	Source	Source term for the volume fraction of gas phase with two-phase flow
gl2da_calc	On Demand	Updates velocity profile for the scalar mixture model for gas-liquid flow
gl2db_calc	Init	Initialises the domain for the scalar gas-liquid flow
gl2dc_calc	Init	Initialises velocity profile and the domain for the gas-liquid flow model
gl2dd_calc	Adjust	Calculates drift, mixture, phase and slip velocity for the gas-liquid scalar mixture model before each iteration with velocity updating for gl2db_calc
gl2de_calc	Adjust	Calculates drift, mixture, phase and slip velocity for the gas-liquid scalar mixture model before each iteration
gl2df_calc	On Demand	Updates velocity profile for the standard mixture model <sup>9</sup> for gas-liquid flow

<sup>i</sup> See §3.0 for discussion of the velocity updating, for the standard mixture model<sup>9</sup>

<sup>ii</sup> See §4.0, §10.5 and §11.1 for equations and examples of the lateral convection subroutines, velo\_calc1 to velo\_calc6

<sup>iii</sup> See §4.0 for discussion of the gas-liquid flow mixture model equations and coding in §10.1, §10.4 and §10.7 where the discrete phase is a bubbly gas phase

Table 3: External functions used in §5.0 for solid-liquid flow<sup>i</sup> and gas-liquid-solid flow<sup>ii</sup>.

<i>Function</i>	<i>Type</i>	<i>Description</i>
sl2d_mu	Property	Solid-liquid mixture viscosity
sl2d_rho	Property	Solid-liquid mixture density
sl2d_xmom	Source	Solid -liquid x-momentum source
sl2d_ymom	Source	Solid -liquid y-momentum source
sl2d_vof	Source	Solid-liquid volume fraction equation source
sl2da_calc	Adjust	Calculates drift, slip velocities for the discrete phase, each phase velocity plus the mixture velocity
sl2db_calc	Init	Initialises the domain for the solid-liquid flow model
gls2d_mu	Property	Gas-liquid-solid mixture viscosity
gls2d_rho	Property	Gas-liquid-solid mixture density
gls2d_xmom	Source	Gas-liquid-solid x-momentum source
gls2d_ymom	Source	Gas-liquid-solid y-momentum source
gls2d_vof	Source	Source term for the volume fraction of gas phase with three-phase flow models
slg2d_vof	Source	Source term for the volume fraction of solid phase with three-phase flow models
gls2da_calc	Adjust	Calculates drift, slip velocities for each discrete phase, each phase velocity plus the mixture velocity
gls2db_calc	Init	Initialises the domain

<sup>i</sup> See §5.0 for discussion of the solid-liquid flow mixture model equations and coding in §10.1, §10.4 and §10.7 where the discrete phase is a bubbly gas phase.

<sup>ii</sup> See §5.0 for a description of the gas-liquid-solid flow models, also find for an example of the coding for three-phase flow in §11.3.

Table 4: External functions used in §6.0 for three-phase flow and reaction<sup>1</sup>.

<i>Function</i>	<i>Type</i>	<i>Description</i>
gls_s1_mu	Property	Gas-liquid-solid mixture viscosity
gls_s1_rho	Property	Gas-liquid-solid mixture density
gls_s1_xmom	Source	Gas-liquid-solid x-momentum source
gls_s1_ymom	Source	Gas-liquid-solid y-momentum source
gas_s1_vof	Source	Source term for the volume fraction of gas phase with three-phase flow models
sol_s1_vof	Source	Source term for the volume fraction of solid phase with three-phase flow models, modelling the transport of the cell culture where the specific growth rate is $6.500 \cdot 10^{-5} \text{ s}^{-1}$
sub_s1_conc	Source	Source term for the concentration of the substrate, where the yield coefficients are 0.118 and 0.442 $\text{kg kg}^{-1} \text{ s}^{-1}$
prod_s1_conc	Source	Source term for the concentration of the product, where the yield coefficient is 3.752 $\text{kg kg}^{-1} \text{ s}^{-1}$
a_gls_s1_calc	Adjust	Calculates drift, slip velocities for each discrete phase, each phase velocity plus the mixture velocity
b_gls_s1_calc	Init	Initialises the domain and the volume fraction of the solid phase
gls_s2_mu	Property	Gas-liquid-solid mixture viscosity
gls_s2_rho	Property	Gas-liquid-solid mixture density
gls_s2_xmom	Source	Gas-liquid-solid x-momentum source
gls_s2_ymom	Source	Gas-liquid-solid y-momentum source
gas_s2_vof	Source	Source term for the volume fraction of gas phase with three-phase flow models
sol_s2_vof	Source	Source term for the volume fraction of solid phase with three-phase flow models, modelling the transport of the cell culture where the specific growth rate is $1.522 \cdot 10^{-4} \text{ s}^{-1}$
sub_s2_conc	Source	Source term for the concentration of the substrate, where the yield coefficients are 0.148 and 1.087 $\text{kg kg}^{-1} \text{ s}^{-1}$
prod_s2_conc	Source	Source term for the concentration of the product, where the yield coefficient is 7.360 $\text{kg kg}^{-1} \text{ s}^{-1}$
a_gls_s2_calc	Adjust	Calculates drift, slip velocities for each discrete phase, each phase velocity plus the mixture velocity
b_gls_s2_calc	Init	Initialises the domain and the volume fraction of the solid phase

<sup>1</sup> See §6.0 for discussion of the solid-liquid flow mixture model equations §10.1 and §10.4, also see §10.7 for the species transport and reaction models. The coding in for the implementation of these models is found in §11.3.

## 12.3 Domain specifications

Table 5: Boundaries for the 5:1 height to width ratio plane mesh (§3.0, §4.0 and §6.0).

<b>Boundary Condition Definition</b>						
<i>Zone</i>	<i>ID</i>	<i>Type</i>			<i>Mesh</i>	
fluid.1	1	fluid			2000	
vertical leftwall	2	wall			100	
horizontal base leftwall	2	wall			4	
vertical rightwall	3	wall			100	
horizontal base rightwall	3	wall			4	
outlet	4	pressure-inlet			20	
inlet	5	velocity-inlet			16	
<b>Boundary Condition Dimensions</b>						
<i>Zone</i>	$x_0$	$x_1$	$y_0$	$y_1$	$z_0$	$z_1$
fluid.1	-0.1	0.1	0	1	0	0
vertical leftwall	-0.1	-0.1	0	1	0	0
horizontal base leftwall	-0.1	-0.08	0	0	0	0
vertical rightwall	0.08	0.1	0	1	0	0
horizontal base rightwall	0.1	0.1	0	0	0	0
outlet	-0.1	0.1	1	1	0	0
inlet	-0.08	0.08	0	0	0	0

Table 6: Boundaries for the 5:1 height to diameter ratio, 3D cylinder used in §3.0.

<b>Boundary Condition Definition</b>						
<i>Zone</i>	<i>ID</i>	<i>Type</i>			<i>Mesh Cells</i>	
fluid.3	1	fluid			12375	
velocity_inlet.4	2	velocity-inlet			125	
pressure_inlet.6	3	pressure-inlet			165	
wall	4	wall			1440	
<b>Boundary Condition Dimensions</b>						
<i>Zone</i>	$r_0$	$r_1$	$t_0$	$t_1$	$z_0$	$z_1$
fluid.3 (3D volume, cylinder)	0	0.1	0	360	0	1
velocity_inlet.4 (2D surface at bottom of grid)	0	0.08	0	360	0	0
pressure_inlet.6 (2D surface at top of grid)	0	0.1	0	360	1	1
wall (2D vertical surface)	0.1	0.1	0	360	0	1
wall (2D horizontal surface)	0.08	0.1	0	360	0	0

Table 7: Boundaries for the 3D rectangular mesh used in §3.0.

<b>Boundary Condition Definition</b>						
<i>Zone</i>	<i>ID</i>	<i>Type</i>			<i>Mesh Cells</i>	
fluid	1	fluid			13200	
base	2	wall			144	
outlet	3	pressure-inlet			400	
inlet	4	velocity-inlet			256	
rightwall	5	wall			660	
leftwall	6	wall			660	
frontwall	7	wall			660	
backwall	8	wall			660	
<b>Boundary Condition Dimensions</b>						
<i>Zone</i>	$x_0$	$x_1$	$y_0$	$y_1$	$z_0$	$z_1$
Fluid (3D volume, rectangle)	-0.1	0.1	0	1	-0.1	0.1
Base (2D surface four strips about inlet bottom of grid)	-0.1	-0.08	0	0	-0.1	0.1
	-0.08	0.08	0	0	-0.1	-0.08
	-0.08	-0.08	0	0	0.08	0.1
	0.08	0.1	0	0	-0.1	0.1
outlet (2D surface at top of grid)	-0.1	0.1	1	1	-0.1	0.1
inlet (2D surface between base strips bottom of grid)	-0.08	0.08	0	0	-0.08	0.08
rightwall (2D surface)	0.1	0.1	0	1	-0.1	0.1
leftwall (2D surface)	-0.1	-0.1	0	1	-0.1	0.1
frontwall (2D surface)	-0.1	0.1	0	1	0.1	0.1
backwall (2D surface)	-0.1	0.1	0	1	-0.1	-0.1

Table 8: Boundaries for the 50:1 height to width ratio mesh used in §4.0.

<b>Boundary Condition Definition</b>						
<i>Zone</i>	<i>ID</i>	<i>Type</i>			<i>Mesh</i>	
fluid.1	1	fluid			2000	
left.2	2	wall			500	
right.3	3	wall			500	
top.4	4	wall			10	
base.5	5	wall			10	
<b>Boundary Condition Dimensions</b>						
<i>Zone</i>	$x_0$	$x_1$	$y_0$	$y_1$	$z_0$	$z_1$
fluid.1	-0.5	0.5	0	50	0	0
left.2	-0.5	-0.5	0	50	0	0
right.3	0.5	0.5	0	50	0	0
top.4	-0.5	0.5	50	50	0	0
base.5	-0.5	0.5	0	0	0	0

Table 9: Boundaries for the 5:1 height to width ratio plane used for solid-liquid flow.

<b>Boundary Condition Definition</b>						
<i>Zone</i>	<i>ID</i>	<i>Type</i>			<i>Mesh</i>	
fluid	1	fluid			2000	
vertical wall	2	wall			100	
horizontal wall	2	wall			20	
lefttop	3	velocity-inlet/outflow			9	
inlet	4	velocity-inlet/outflow			2	
righttop	5	velocity-inlet/outflow			9	
<b>Boundary Condition Dimensions</b>						
<i>Zone</i>	$x_0$	$x_1$	$y_0$	$y_1$	$z_0$	$z_1$
fluid	-0.1	0.1	0	1	0	0
vertical wall	-0.1	-0.1	0	1	0	0
	0.1	0.1	0	1	0	0
horizontal wall	-0.1	0.1	0	0	0	0
lefttop	-0.1	-0.01	1	1	0	0
inlet	-0.01	0.01	1	1	0	0
righttop	0.01	0.1	1	1	0	0

Table 10: Boundaries for the 5:1 height to width ratio plane used for gas-liquid-solid flow.

<b>Boundary Condition Definition</b>						
<i>Zone</i>	<i>ID</i>	<i>Type</i>			<i>Mesh</i>	
fluid	1	fluid			2000 cells	
vertical leftwall	2	wall			100 nodes	
horizontal leftwall	2	wall			2 nodes	
vertical rightwall	3	wall			100 nodes	
horizontal rightwall	3	wall			2 nodes	
gasinlet	4	wall/velocity-inlet			16 nodes	
solidinlet	5	velocity/pressure-inlet			20 nodes	
lefttop	6	velocity/pressure-inlet			9 nodes	
righttop	7	velocity/pressure-inlet			9 nodes	
<b>Boundary Condition Dimensions</b>						
<i>Zone</i>	$x_0$	$x_1$	$y_0$	$y_1$	$z_0$	$z_1$
fluid	-0.1	0.1	0	1	0	0
vertical leftwall	-0.1	-0.1	0	1	0	0
horizontal leftwall	-0.1	0.08	0	0	0	0
vertical rightwall	0.1	0.1	0	1	0	0
horizontal rightwall	0.08	0.1	0	0	0	0
gasinlet	-0.08	0.08	0	0	0	0
solidinlet	-0.01	0.01	1	1	0	0
lefttop	-0.1	-0.01	1	1	0	0
righttop	0.01	0.1	1	1	0	0

Table 11: Boundaries for the 20:1 height to width ratio plane used in §6.0.

<b>Boundary Condition Definition</b>						
<i>Zone</i>	<i>ID</i>	<i>Type</i>			<i>Mesh</i>	
fluid.1	1	fluid			4500	
left	2	wall			300	
right	3	wall			300	
bottom	4	velocity-inlet			15	
top	5	pressure-inlet			15	
<b>Boundary Condition Dimensions</b>						
<i>Zone</i>	$x_0$	$x_1$	$y_0$	$y_1$	$z_0$	$z_1$
fluid.1	-0.075	0.075	0	3	0	0
left	-0.075	-0.075	0	3	0	0
right	0.075	0.075	0	3	0	0
bottom	-0.075	0.075	0	0	0	0
top	-0.075	0.075	3	3	0	0

## 12.4 Solver specifications

Table 12: Laminar mixture models for 2D and 3D domains described in §3.0.

<b>Model Settings</b>		
Time	Unsteady, 1st-Order Implicit	
Viscous	Laminar	
Multiphase	Algebraic Slip Mixture Model	
	Primary Phase	Water-liquid
	Secondary Phase	Air
	Implicit Body Forces	On (0, -9.81, 0) m s <sup>-2</sup>
<b>Boundary Conditions</b>		
<i>Zone Type</i>	<i>Condition</i>	<i>Value</i>
fluid	Default Specifications	-
wall	Default Specifications	-
pressure-inlet	Gas Phase Fraction	0
velocity-inlet	Vertical Component Velocity	0.032 m s <sup>-1</sup>
	Gas Phase Fraction	1
<b>Solver Controls</b>		
<i>Control</i>	<i>Type</i>	<i>Value</i>
Equations	Flow, Slip Velocity, Volume Fraction	Yes
Time Dependency	Time Step	0.1 s
Under-relaxation	Pressure	0.3
	Momentum	0.7
	Slip Velocity	0.1
	Volume Fraction	0.5
	Density	1
	Body Forces	1
Discretization Scheme	Pressure	Body Force Weighted
	Momentum	QUICK
	Pressure-Velocity Coupling	SIMPLEC
	Volume Fraction	First Order Upwind

Table 13: k-ε turbulence mixture model for 2D and 3D domains described in §3.0.

<b>Model Settings</b>		
Time	Unsteady, 1st-Order Implicit	
Viscous	Standard k-ε turbulence model	
Wall Treatment	Standard Wall Functions	
Multiphase	Algebraic Slip Mixture Model	
	Primary Phase	Water-liquid
	Secondary Phase	Air
	Implicit Body Forces	On (0, -9.81, 0) m s <sup>-2</sup>
<b>Boundary Conditions</b>		
<i>Zone Type</i>	<i>Condition</i>	<i>Value</i>
Fluid	Default Specifications	-
Wall	Default Specifications	-
pressure-inlet	Gas Phase Fraction	0
velocity-inlet	Vertical Component Velocity	0.032 m s <sup>-1</sup>
	Gas Phase Fraction	1
<b>Solver Controls</b>		
<i>Control</i>	<i>Type</i>	<i>Value</i>
Equations	Flow, Slip Velocity, Volume Fraction, Turbulence	Yes
Time Dependency	Time Step	0.1 s
Under-relaxation	Pressure	0.3
	Momentum	0.7
	Slip Velocity	0.1
	Volume Fraction	0.5
	Turbulence Kinetic Energy	0.8
	Turbulence Dissipation Rate	0.8
	Density	1
	Viscosity	1
	Body Forces	1
Discretization Scheme	Pressure	Body Force Weighted
	Momentum	QUICK
	Pressure-Velocity Coupling	SIMPLEC
	Turbulence Kinetic Energy	First Order Upwind
	Turbulence Dissipation Rate	First Order Upwind
	Volume Fraction	First Order Upwind

Table 14: Reynolds stresses mixture model for 2D and 3D domains described in §3.0.

<b>Model Settings</b>		
Time	Unsteady, 1st-Order Implicit	
Viscous	Reynolds stresses model	
Wall Treatment	Standard Wall Functions	
	RSM Wall Reflection Effects and Wall B.C. (solve k)	
Multiphase	Algebraic Slip Mixture Model	
	Primary Phase	Water-liquid
	Secondary Phase	Air
	Implicit Body Forces	On (0, -9.81, 0) m s <sup>-2</sup>
User Defined	Adjust Function Hook	adj_vofandv
<b>Boundary Conditions</b>		
<i>Zone Type</i>	<i>Condition</i>	<i>Value</i>
fluid	Default Specifications	-
wall	Default Specifications	-
pressure-inlet	Gas Phase Fraction	0
velocity-inlet	Vertical Component Velocity	0.032 m s <sup>-1</sup>
	Gas Phase Fraction	1
<b>Solver Controls</b>		
<i>Control</i>	<i>Type</i>	<i>Value</i>
Equations	Flow, Volume Fraction, Turbulence, Slip Velocity, Reynolds stresses	Yes
Time Dependency	Time Step	0.1 s
Under-relaxation	Pressure	0.3
	Momentum	0.7
	Slip Velocity	0.1
	Volume Fraction	0.5
	Turbulence Kinetic Energy	0.8
	Turbulence Dissipation Rate	0.8
	Viscosity	1
	Reynolds stresses	0.5
	Density	1
Discretization Scheme	Body Forces	1
	Pressure	Body Force Weighted
	Momentum	QUICK
	Pressure-Velocity Coupling	SIMPLEC
	Turbulence Kinetic Energy	First Order Upwind
	Turbulence Dissipation Rate	First Order Upwind
	Reynolds stresses	First Order Upwind
Volume Fraction	First Order Upwind	

Table 15: Lateral convection with under-relaxation adjustment in §4.0.

<b>Model Settings</b>		
Time	Unsteady, 1st-Order Implicit	
Viscous	Reynolds stresses model	
Wall Treatment	Standard Wall Functions	
	RSM Wall Reflection Effects and Wall B.C. (solve k)	
Heat Transfer	Enabled without Radiation Effects	
Implicit Body Forces	On (0, -9.81, 0) m s <sup>-2</sup>	
User Defined	Define On Demand	velo_calc2 (Incl. Temp)
	Initialisation Function Hook	velo_calc6 (Incl. Temp)
<b>Boundary Conditions</b>		
<i>Zone</i>	<i>Condition</i>	<i>Value</i>
fluid.1	Material	Air
	Temperature	Initialised with 305 K
left.2	Material	Aluminium
	Temperature	300 K
	Wall Roughness Constant	0
right.3	Material	Aluminium
	Temperature	310 K
	Wall Roughness Constant	0
top.4, base.5	Material	Aluminium
	Temperature	305 K
	Wall Roughness Constant	0
<b>Solver Controls</b>		
<i>Control</i>	<i>Type</i>	<i>Value</i>
Equations	Flow, Energy, Turbulence, Reynolds stresses	Yes
Time Dependency	Time Step	0.2 s
Under-relaxation	Pressure, Momentum	1
	Energy, Body Forces	1
	Viscosity, Density	1
	Reynolds stresses, Kinetic Energy and Dissipation Rate	0.1, 0.2, 0.3, 0.4, 0.5, 0.6, 0.7, 0.8, 0.9 and 1
Discretization Scheme	Pressure	Body Force Weighted
	Momentum	QUICK
	Pressure-Velocity Coupling	SIMPLEC
	Energy	Second Order Upwind
	Turbulence Kinetic Energy	Second Order Upwind
	Turbulence Dissipation Rate	Second Order Upwind
	Reynolds stresses	Second Order Upwind

Table 16: Lateral convection for a number of k-ε turbulence modelling methods (§4.0).

<b>Model Settings</b>		
Time	Unsteady, 1st-Order Implicit	
Viscous	Standard k-ε turbulence model	
Wall Treatment	Standard Wall Functions	
Heat Transfer	Enabled without Radiation Effects	
Implicit Body Forces	On (0, -9.81, 0) m s <sup>-2</sup>	
User Defined	No Variable Updating	-
User Defined for velocity only	Define On Demand	velo_calc1
	Initialisation Function Hook	velo_calc5
User Defined for velocity and temperature	Define On Demand	velo_calc4
	Initialisation Function Hook	velo_calc6
User Defined for velocity only	Adjust Function Hook	velo_calc3
	Initialisation Function Hook	velo_calc5
User Defined for velocity and temperature	Adjust Function Hook	velo_calc4
	Initialisation Function Hook	velo_calc6
<b>Solver Controls</b>		
<i>Control</i>	<i>Type</i>	<i>Value</i>
Equations	Flow, Energy, Turbulence	Yes
Time Dependency	Time Step	0.2 s
Under-relaxation	Pressure, Momentum	1
	Energy, Body Forces	1
	Viscosity, Density	1
	Turbulent Kinetic Energy and Dissipation Rate	0.1
Discretization Scheme	Pressure	Body Force Weighted
	Momentum	QUICK
	Pressure-Velocity Coupling	SIMPLEC
	Energy	Second Order Upwind
	Turbulence Kinetic Energy	Second Order Upwind
	Turbulence Dissipation Rate	Second Order Upwind

Table 17: Lateral convection for a number of Reynolds stresses modelling methods (§4.0).

<b>Model Settings</b>		
Time	Unsteady, 1st-Order Implicit	
Viscous	Reynolds stresses model	
Wall Treatment	Standard Wall Functions	
	RSM Wall Reflection Effects and Wall B.C. (solve k)	
Heat Transfer	Enabled without Radiation Effects	
Implicit Body Forces	On (0, -9.81, 0) m s <sup>-2</sup>	
User Defined for no updates	No Variable Updating	-
User Defined for velocity only	Define On Demand	velo_calc1
	Initialisation Function Hook	velo_calc5
User Defined for velocity and temperature	Define On Demand	velo_calc2
	Initialisation Function Hook	velo_calc6
User Defined for velocity only	Adjust Function Hook	velo_calc3
	Initialisation Function Hook	velo_calc5
User Defined for velocity and temperature	Adjust Function Hook	velo_calc4
	Initialisation Function Hook	velo_calc6
<b>Solver Controls</b>		
<i>Control</i>	<i>Type</i>	<i>Value</i>
Equations	Flow, Energy, Turbulence and Reynolds stresses	Yes
Time Dependency	Time Step	0.2 s
Under-relaxation	Pressure, Momentum	1
	Energy, Body Forces	1
	Viscosity, Density	1
	Reynolds stresses, Kinetic Energy and Dissipation Rate	0.1
Discretization Scheme	Pressure	Body Force Weighted
	Momentum	QUICK
	Pressure-Velocity Coupling	SIMPLEC
	Energy	Second Order Upwind
	Turbulence Kinetic Energy	Second Order Upwind
	Turbulence Dissipation Rate	Second Order Upwind
	Reynolds stresses	Second Order Upwind

Table 18: Gas-liquid flow using the algebraic slip mixture model in §4.0.

<b>Model Settings</b>		
Time	Unsteady, 1st-Order Implicit	
Viscous	Reynolds stresses model	
Wall Treatment	Standard Wall Functions	
	RSM Wall Reflection Effects and Wall B.C. (solve k)	
Multiphase	Algebraic Slip Mixture Model	
	Primary Phase	Water-liquid
	Secondary Phase	Air
	Implicit Body Forces	On (0, -9.81) m s <sup>-2</sup>
No Profile Updating	-	-
Profile Updating	Define On Demand	gl2db_calc
	Initialisation Function Hook	gl2dc_calc
<b>Boundary Conditions</b>		
<i>Zone</i>	<i>Condition</i>	<i>Value</i>
inlet	Vertical Velocity Component	0.032 m s <sup>-1</sup>
	Gas Fraction	1
left, right	Wall Roughness Constant	0
outlet	Gauge Total Pressure	0
<b>Solver Controls</b>		
<i>Control</i>	<i>Type</i>	<i>Value</i>
Equations	Flow, Turbulence, Reynolds stresses, Volume Fraction, Slip Velocity	Yes
Time Dependency	Time Step	0.1 s
Under-relaxation	Pressure	0.3
	Momentum	0.7
	Reynolds stresses, Slip Velocity, Volume Fraction	0.1
	Body Forces, Density, k-ε Turbulence, Viscosity	1
Discretization Scheme	Pressure	Body Force Weighted
	Momentum	QUICK
	Pressure-Velocity Coupling	SIMPLEC
	Turbulence Models	First Order Upwind
	Volume Fraction	Second Order Upwind

Table 19: Gas-liquid flow using the modified scalar equation mixture model in §4.0.

<b>Model Settings</b>		
Time	Unsteady, 1st-Order Implicit	
Viscous	Reynolds stresses model	
Wall Treatment	Standard Wall Functions	
	RSM Wall Reflection Effects and Wall B.C. (solve k)	
Scalar	Mixture Phase for scalar	gas-liquid
	Primary Phase	Water-liquid
	Secondary Phase	Air
	Implicit Body Forces	On (0, -9.81) m s <sup>-2</sup>
User Defined Sources	X-Momentum	gl2d_xmom
	Y-Momentum	gl2d_ymom
	Scalar Equation	gl2d_vof
Non-Profile Updating	Adjust Function Hook	gl2de_calc
	Initialisation Function Hook	gl2db_calc
Profile Updating Case	Adjust Function Hook	gl2dd_calc
	Define On Demand	gl2da_calc
	Initialisation Function Hook	gl2dc_calc
User Defined Memory	0 to 9	16 arrays
<b>Boundary Conditions</b>		
<i>Zone</i>	<i>Condition</i>	<i>Value</i>
inlet	Vertical Velocity Component	0.032 m s <sup>-1</sup>
	Scalar as a Flux	0.6
left, right	Wall Roughness Constant	0
outflow	Gauge Total Pressure	0
<b>Solver Controls</b>		
<i>Control</i>	<i>Type</i>	<i>Value</i>
Equations	Flow, Turbulence, Reynolds stresses, User defined scalar-0	Yes
Time Dependency	Time Step	0.1 s
Under-relaxation	Pressure	0.3
	Momentum	0.7
	Reynolds stresses, User defined scalar-0	0.1
	Body Forces, Density, k-ε Turbulence, Viscosity	1
Discretization Scheme	Pressure	Body Force Weighted
	Momentum	QUICK
	Pressure-Velocity Coupling	SIMPLEC
	Turbulence Models	First Order Upwind
	User defined scalar-0	Second Order Upwind

Table 20: Solid-liquid flow using the algebraic slip mixture model in §5.0.

<b>Model Settings</b>		
Time	Unsteady, 1st-Order Implicit	
Viscous	Reynolds stresses model	
Wall Treatment	Standard Wall Functions	
	RSM Wall Reflection Effects and Wall B.C. (solve k)	
Multiphase	Algebraic Slip Mixture Model	
	Primary Phase	Water-liquid
	Secondary Phase	Particulate Solid (fluid)
	Implicit Body Forces	On (0, -9.81) m s <sup>-2</sup>
Profile Updating	None	
<b>Boundary Conditions</b>		
<i>Zone</i>	<i>Condition</i>	<i>Value</i>
inlet	Vertical Velocity Component	0.1 m s <sup>-1</sup>
	Solid Fraction	0.1
	Injection Time	0 to 10 seconds
	Convert to outflow condition	At 10 seconds
lefttop, righttop	Convert to outflow condition	At 10 seconds
wall	Wall Roughness Constant	0
<b>Solver Controls</b>		
<i>Control</i>	<i>Type</i>	<i>Value</i>
Equations	Flow, Turbulence, Reynolds stresses, Volume Fraction, Slip Velocity	Yes
Time Dependency	Time Step	0.1 s
Under-relaxation	Pressure	0.3
	Momentum	0.7
	Reynolds stresses, Slip Velocity, Volume Fraction	0.1
	Body Forces, Density, k-ε Turbulence, Viscosity	1
Discretization Scheme	Pressure	Body Force Weighted
	Momentum	QUICK
	Pressure-Velocity Coupling	SIMPLEC
	Turbulence Models	First Order Upwind
	Volume Fraction	Second Order Upwind

Table 21: Solid-liquid flow using the modified scalar equation mixture model in §5.0.

<b>Model Settings</b>		
Time	Unsteady, 1st-Order Implicit	
Viscous	Reynolds stresses model	
Wall Treatment	Standard Wall Functions	
	RSM Wall Reflection Effects and Wall B.C. (solve k)	
Scalar	Mixture Phase for scalar	solid-liquid
	Primary Phase	Water-liquid
	Secondary Phase	Particulate Solid (fluid)
	Implicit Body Forces	On (0, -9.81) m s <sup>-2</sup>
User Defined Sources	X-Momentum	sl2d_xmom
	Y-Momentum	sl2d_ymom
	Scalar Equation	sl2d_vof
Other User Defined Functions	Adjust Function Hook	sl2da_calc
	Initialisation Function Hook	sl2db_calc
	User Defined Memory, 0 to 9	16 arrays
<b>Boundary Conditions</b>		
<i>Zone</i>	<i>Condition</i>	<i>Value</i>
inlet	Vertical Velocity Component	0.1 m s <sup>-1</sup>
	Scalar as a Flux	0.1
	Injection Time	0 to 10 seconds
wall	Wall Roughness Constant	0
<b>Solver Controls</b>		
<i>Control</i>	<i>Type</i>	<i>Value</i>
Equations	Flow, Turbulence, Reynolds stresses, User defined scalar-0	Yes
Time Dependency	Time Step	0.1 s
Under-relaxation	Pressure	0.3
	Momentum	0.7
	Reynolds stresses, User defined scalar-0	0.1
	Body Forces, Density, k-ε Turbulence, Viscosity	1
Discretization Scheme	Pressure	Body Force Weighted
	Momentum	QUICK
	Pressure-Velocity Coupling	SIMPLEC
	Turbulence Models	First Order Upwind
	User defined scalar-0	Second Order Upwind

Table 22: Gas-liquid-solid flow for the GLS1 case described in §5.0.

<b>Model Settings</b>		
Time	Unsteady, 1st-Order Implicit	
Viscous	Reynolds stresses Model	
Wall Treatment	Standard Wall Functions	
	RSM Wall Reflection Effects and Wall B.C. (solve k)	
Implicit Body Forces	On (0, -9.81) m s <sup>-2</sup>	
<b>Discrete Phase 1: Gas</b>		
Scalar	G-L Mixture Phase	gas-liquid
	Primary Phase	Water-liquid
	Secondary Phase	Air (fluid)
User Defined Functions	X-Momentum	gl2d_xmom
	Y-Momentum	gl2d_ymom
	Scalar Equation	gl2d_vof
	Adjust Function Hook	gl2de_calc
	Initialisation Function Hook	gl2db_calc
	User Defined Memory	16 arrays
<b>Discrete Phase 2: Solid</b>		
Algebraic Slip Mixture Model	Primary Phase	S-L Mixture Phase
	Secondary Phase	Solid (fluidized)
<b>Boundary Conditions</b>		
<i>Zone</i>	<i>Condition</i>	<i>Value</i>
solidinlet	Vertical Velocity Component	0.1 m s <sup>-1</sup>
	Secondary Phase Fraction	0.1
	Injection Time	0 to 10 s
	Convert zone from velocity-inlet to pressure-inlet	20 s
lefttop, righttop	Convert zone from velocity-inlet to pressure-inlet	20 s
gasinlet	Vertical Velocity Component	0.032 m s <sup>-1</sup>
	Scalar as a Flux Rate	0.6
	Injection Time	20 to 200 s
leftwall, rightwall	Wall Roughness Constant	0
	Scalar as a Constant Value	0

Table 23: Gas-liquid-solid flow for the GLS2 case described in §5.0.

<b>Model Settings</b>		
Time	Unsteady, 1st-Order Implicit	
Viscous	Reynolds stresses Model	
Wall Treatment	Standard Wall Functions	
	RSM Wall Reflection Effects and Wall B.C. (solve k)	
Implicit Body Forces	On (0, -9.81) m s <sup>-2</sup>	
<b>Discrete Phase 1: Solid</b>		
Scalar	S-L Mixture Phase	solid-liquid
	Primary Phase	Water-liquid
	Secondary Phase	Particulate Solid (fluid)
User Defined Functions	X-Momentum	sl2d_xmom
	Y-Momentum	sl2d_ymom
	Scalar Equation	sl2d_vof
	Adjust Function Hook	sl2da_calc
	Initialisation Function Hook	sl2db_calc
	User Defined Memory	16 arrays
<b>Discrete Phase 2: Gas</b>		
Algebraic Slip Mixture Model	Primary Phase	G-L Mixture Phase
	Secondary Phase	Air (fluid)
<b>Boundary Conditions</b>		
<i>Zone</i>	<i>Condition</i>	<i>Value</i>
solidinlet	Vertical Velocity Component	0.1 m s <sup>-1</sup>
	Scalar as a Flux	0.1
	Injection Time	0 to 10 s
	Convert zone from velocity-inlet to pressure-inlet	20 s
lefttop, righttop	Convert zone from velocity-inlet to pressure-inlet	20 s
gasinlet	Vertical Velocity Component	0.032 m s <sup>-1</sup>
	Secondary Phase Fraction	1
	Injection Time	20 to 200 s
leftwall, rightwall	Wall Roughness Constant	0
	Scalar as a Constant Value	0

Table 24: Solver controls for the GLS1 and GLS2 cases (Table 22 and Table 23).

<b>Solver Controls</b>		
<i>Control</i>	<i>Type</i>	<i>Value</i>
Equations	Flow, Turbulence, Reynolds stresses, Slip Velocity, Volume Fraction, User defined scalar-0	Yes
Time Dependency	Time Step	0.1 s
Under-relaxation	Pressure	0.3
	Momentum	0.7
	Reynolds stresses, Slip Velocity, Volume Fraction, User defined scalar-0	0.1
	Body Forces, Density, k- $\epsilon$ Turbulence, Viscosity	1
Discretization Scheme	Pressure	Body Force Weighted
	Momentum	QUICK
	Pressure-Velocity Coupling	SIMPLEC
	Turbulence Models	First Order Upwind
	User defined scalar-0, Volume Fraction	Second Order Upwind

Table 25: Solver conditions for the GLS3 case (Table 26).

<b>Solver Controls</b>		
<i>Control</i>	<i>Type</i>	<i>Value</i>
Equations	Flow, Turbulence, Reynolds stresses, Scalar-0, Scalar-1 (switched off before 20 s)	Yes
Time Depend.	Time Step	0.1 s
Under-relaxation	Pressure	0.3
	Momentum	0.7
	Reynolds stresses, Scalar-0, Scalar-1 (switched off before 20 s)	0.1
	Body Forces, Density, k- $\epsilon$ Turbulence, Viscosity	1
Discretization Scheme	Pressure	Body Force Weighted
	Momentum	QUICK
	Pressure-Velocity Coupling	SIMPLEC
	Turbulence Models	First Order Upwind
	Scalar-0, Scalar-1 (switched off before 20 s)	Second Order Upwind

Table 26: Gas-liquid-solid flow for the GLS3 case described in §5.0.

<b>Model Settings</b>		
Time	Unsteady, 1st-Order Implicit	
Viscous	Reynolds stresses Model	
Wall Treatment	Standard Wall Functions, Wall Reflection Effects & Wall B.C.	
Implicit Body Forces	On (0, -9.81) m s <sup>-2</sup>	
<b>Phases</b>		
Mixture Phase	Subroutines gls2d_mu and gls2d_rho predict the properties	
Liquid Phase	Water-liquid	-
Gas Phase	Air (fluid)	Scalar-1
Solid Phase	Particulate Solid (fluid)	Scalar-0
User Defined Functions	X-Momentum	gls2d_xmom
	Y-Momentum	gls2d_ymom
	Scalar-0	slg2d_vof
	Scalar-1, not switched on for first 20 s	gls2d_vof
	Adjust Function Hook	gls2da_calc
	Initialisation Function Hook	gls2db_calc
	User Defined Memory	22 arrays
<b>Boundary Conditions</b>		
<i>Zone</i>	<i>Condition</i>	<i>Value</i>
solidinlet	Vertical Velocity Component	0.1 m s <sup>-1</sup>
	Scalar-0 as a Specified Value	0.1
	Injection Time	0 to 10 s
	Convert zone from velocity-inlet to pressure-inlet	At 20 s
lefttop, righttop	Convert zone from velocity-inlet to pressure-inlet	At 20 s
gasinlet	Convert zone velocity inlet to wall	Only from 0 to 20 s
	Vertical Velocity Component	0.032 m s <sup>-1</sup>
	Scalar-1 as a Flux Rate	0.6
	Injection Time	20 to 200 s
leftwall, rightwall	Wall Roughness Constant	0
	Scalar as a Constant Value	0

Table 27: Gas-liquid-solid flow and reaction for the 5:1 aspect ratio bubble column.

<b>Model Settings</b>		
Mesh	5:1 height to diameter aspect ratio mesh, see Table 5	
Time	Unsteady, 1st-Order Implicit	
Viscous	Reynolds stresses Model	
Wall Treatment	Standard Wall Functions, Wall Reflection Effects & Wall B.C.	
Implicit Body Forces	On (0, -9.81) m s <sup>-2</sup>	
<b>Phases</b>		
Mixture Phase	Subroutines gls_s1_mu and gls_s1_rho predict the properties	
Liquid Phase	Water-liquid	-
Gas Phase	Air (fluid)	Scalar-1
Solid Phase	Cell culture as a particulate solid	Scalar-0
Substrate	Solute, molasses	Scalar-2
Product	Solute, citric acid	Scalar-3
User Defined Functions	X-Momentum	gls_s1_xmom
	Y-Momentum	gls_s1_ymom
	Scalar-0	sol_s1_vof
	Scalar-1	gas_s1_vof
	Scalar-2	sub_s1_vof
	Scalar-3	prod_s1_vof
	Adjust Function Hook	a_gls_s1_calc
	Initialisation Function Hook	b_gls_s1_calc
User Defined Memory	29 arrays	
<b>Boundary Conditions</b>		
<i>Zone</i>	<i>Condition</i>	<i>Value</i>
outlet	Scalar-1 as a Flux Rate	0
	Scalars 0, 2 and 3 as Specified Values	0
inlet	Vertical Velocity Component	0.032 m s <sup>-1</sup>
	Scalar-1 as a Flux Rate	0.6
	Scalars 0, 2 and 3 as Specified Values	0
leftwall, rightwall	Wall Roughness Constant	0
	Scalars 0-3 as Specified Values	0
fluid.1	Scalar-0 volume fraction initialised as	0.005
	Scalar-2 volume fraction initialised as	150

Table 28: Gas-liquid-solid flow and reaction for the 5:1 aspect ratio bubble column.

<b>Model Settings</b>		
Mesh	5:1 height to diameter aspect ratio mesh, see Table 5	
Time	Unsteady, 1st-Order Implicit	
Viscous	Reynolds stresses Model	
Wall Treatment	Standard Wall Functions, Wall Reflection Effects & Wall B.C.	
Implicit Body Forces	On (0, -9.81) m s <sup>-2</sup>	
<b>Phases</b>		
Mixture Phase	Subroutines <code>gls_s2_mu</code> and <code>gls_s2_rho</code> predict the properties	
Liquid Phase	Water-liquid	-
Gas Phase	Air (fluid)	Scalar-1
Solid Phase	Cell culture as a particulate solid	Scalar-0
Substrate	Solute, molasses	Scalar-2
Product	Solute, citric acid	Scalar-3
User Defined Functions	X-Momentum	<code>gls_s2_xmom</code>
	Y-Momentum	<code>gls_s2_ymom</code>
	Scalar-0	<code>sol_s2_vof</code>
	Scalar-1	<code>gas_s2_vof</code>
	Scalar-2	<code>sub_s2_vof</code>
	Scalar-3	<code>prod_s2_vof</code>
	Adjust Function Hook	<code>a_gls_s2_calc</code>
	Initialisation Function Hook	<code>b_gls_s2_calc</code>
User Defined Memory	29 arrays	
<b>Boundary Conditions</b>		
<i>Zone</i>	<i>Condition</i>	<i>Value</i>
outlet	Scalar-1 as a Flux Rate	0
	Scalars 0, 2 and 3 as Specified Values	0
inlet	Vertical Velocity Component	0.032 m s <sup>-1</sup>
	Scalar-1 as a Flux Rate	0.6
	Scalars 0, 2 and 3 as Specified Values	0
leftwall, rightwall	Wall Roughness Constant	0
	Scalars 0-3 as Specified Values	0
fluid.1	Scalar-0 volume fraction initialised as	0.005
	Scalar-2 volume fraction initialised as	150

Table 29: Gas-liquid-solid flow and reaction for the 20:1 aspect ratio bubble column.

<b>Model Settings</b>		
Mesh	20:1 height to diameter aspect ratio mesh, see Table 11	
Time	Unsteady, 1st-Order Implicit	
Viscous	Reynolds stresses Model	
Wall Treatment	Standard Wall Functions, Wall Reflection Effects & Wall B.C.	
Implicit Body Forces	On (0, -9.81) m s <sup>-2</sup>	
<b>Phases</b>		
Mixture Phase	Subroutines gls_s1_mu and gls_s1_rho predict the properties	
Liquid Phase	Water-liquid	-
Gas Phase	Air (fluid)	Scalar-1
Solid Phase	Cell culture as a particulate solid	Scalar-0
Substrate	Solute, molasses	Scalar-2
Product	Solute, citric acid	Scalar-3
User Defined Functions	X-Momentum	gls_s1_xmom
	Y-Momentum	gls_s1_ymom
	Scalar-0	sol_s1_vof
	Scalar-1	gas_s1_vof
	Scalar-2	sub_s1_vof
	Scalar-3	prod_s1_vof
	Adjust Function Hook	a_gls_s1_calc
	Initialisation Function Hook	b_gls_s1_calc
User Defined Memory	29 arrays	
<b>Boundary Conditions</b>		
<i>Zone</i>	<i>Condition</i>	<i>Value</i>
top	Scalar-1 as a Flux Rate	0
	Scalars 0, 2 and 3 as Specified Values	0
bottom	Vertical Velocity Component	0.036 m s <sup>-1</sup>
	Scalar-1 as a Flux Rate	0.6
	Scalars 0, 2 and 3 as Specified Values	0
left, right	Wall Roughness Constant	0
	Scalars 0-3 as Specified Values	0
fluid.1	Scalar-0 volume fraction initialised as	0.005
	Scalar-2 volume fraction initialised as	150

Table 30: Gas-liquid-solid flow and reaction for the 20:1 aspect ratio bubble column.

<b>Model Settings</b>		
Mesh	20:1 height to diameter aspect ratio mesh, see Table 11	
Time	Unsteady, 1st-Order Implicit	
Viscous	Reynolds stresses Model	
Wall Treatment	Standard Wall Functions, Wall Reflection Effects & Wall B.C.	
Implicit Body Forces	On (0, -9.81) m s <sup>-2</sup>	
<b>Phases</b>		
Mixture Phase	Subroutines gls_s2_mu and gls_s2_rho predict the properties	
Liquid Phase	Water-liquid	-
Gas Phase	Air (fluid)	Scalar-1
Solid Phase	Cell culture as a particulate solid	Scalar-0
Substrate	Solute, molasses	Scalar-2
Product	Solute, citric acid	Scalar-3
User Defined Functions	X-Momentum	gls_s2_xmom
	Y-Momentum	gls_s2_ymom
	Scalar-0	sol_s2_vof
	Scalar-1	gas_s2_vof
	Scalar-2	sub_s2_vof
	Scalar-3	prod_s2_vof
	Adjust Function Hook	a_gls_s2_calc
	Initialisation Function Hook	b_gls_s2_calc
User Defined Memory	29 arrays	
<b>Boundary Conditions</b>		
<i>Zone</i>	<i>Condition</i>	<i>Value</i>
top	Scalar-1 as a Flux Rate	0
	Scalars 0, 2 and 3 as Specified Values	0
bottom	Vertical Velocity Component	0.036 m s <sup>-1</sup>
	Scalar-1 as a Flux Rate	0.6
	Scalars 0, 2 and 3 as Specified Values	0
left, right	Wall Roughness Constant	0
	Scalars 0-3 as Specified Values	0
fluid.1	Scalar-0 volume fraction initialised as	0.005
	Scalar-2 volume fraction initialised as	150

Table 31: Solver conditions for gas-liquid-solid flow and reaction (Table 27 to Table 30).

<b>Solver Controls</b>		
<i>Control</i>	<i>Type</i>	<i>Value</i>
Equations	Flow, Turbulence, Reynolds stresses, Scalar 0-3	Yes
Time Depend.	Time Step	0.1 s
Under-relaxation	Pressure	0.3
	Momentum	0.7
	Reynolds stresses, Scalar 0-4	0.1
	Body Forces, Density, k- $\epsilon$ Turbulence, Viscosity	1
Discretization Scheme	Pressure	Body Force Weighted
	Momentum	QUICK
	Pressure-Velocity Coupling	SIMPLEC
	Turbulence Models	First Order Upwind
	Scalar 0-4	Second Order Upwind

## 13.0 APPENDIX 4: RESULTS

Results from §3.0 to §6.0 are presented here.

### 13.1 Gas-liquid results

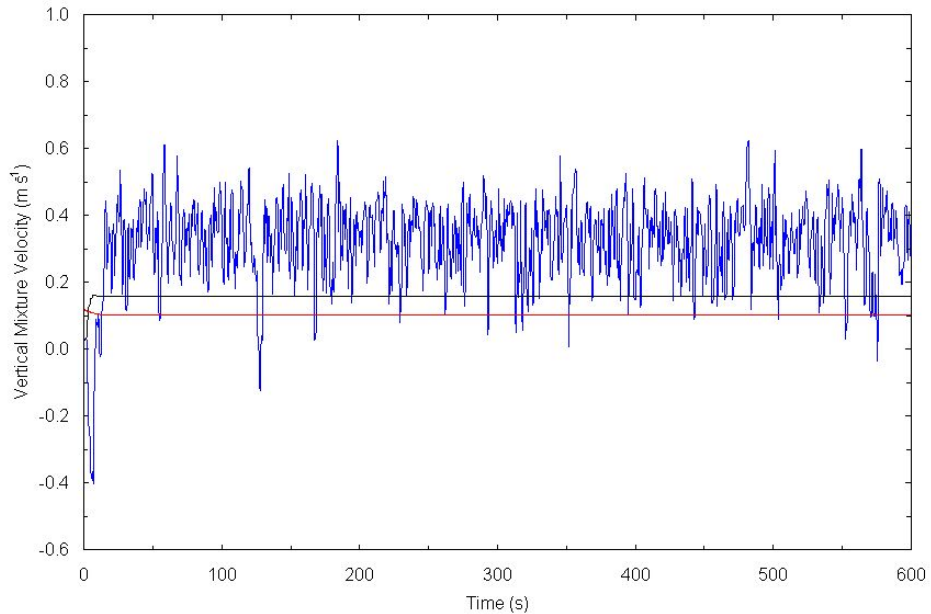


Figure 3: Time series of the vertical mixture velocity ( $\text{m s}^{-1}$ ) for plane gas-liquid flow; Point series recorded on the column centre line at a height of 2.5 column diameters for Blue: laminar (Blue), k- $\epsilon$  turbulence (Black), Reynolds stresses (Red) cases;

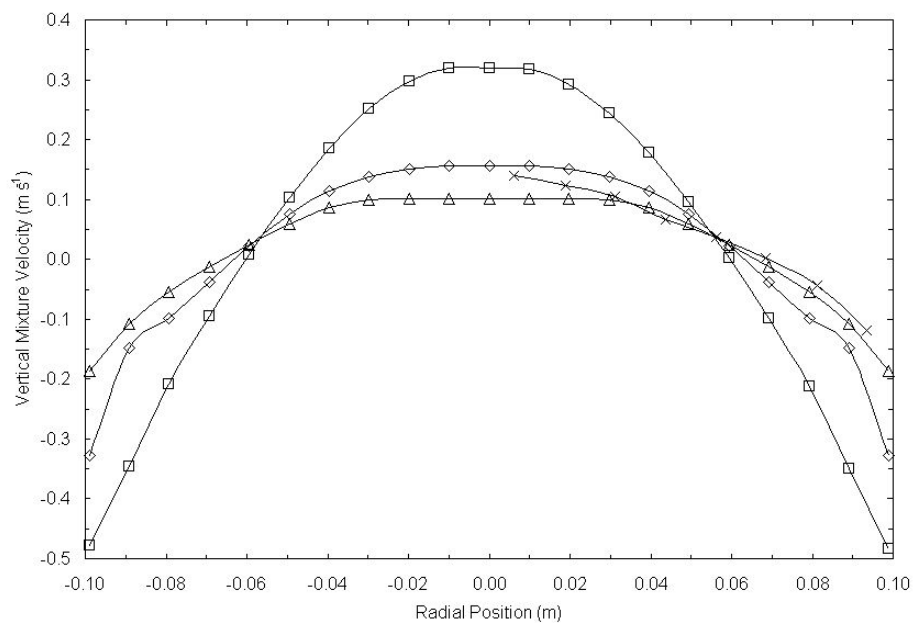


Figure 4: Vertical mixture velocity profile ( $\text{m s}^{-1}$ ) for plane gas-liquid flow; At a height of 2.5 column diameters;  $\square$ : laminar case;  $\diamond$ : k- $\epsilon$  turbulence case;  $\triangle$ : Reynolds stresses case;  $\times$  Experimental column<sup>35-37</sup>;

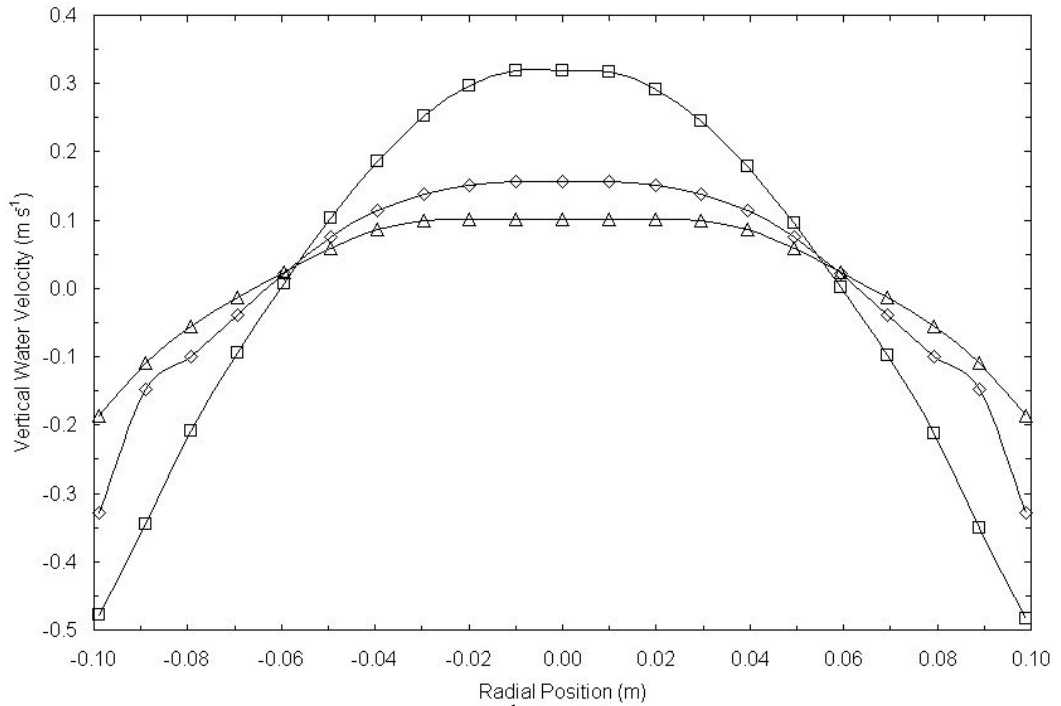


Figure 5: Vertical liquid velocity profile ( $\text{m s}^{-1}$ ) for plane gas-liquid flow; At a height of 2.5 column diameters; □: laminar case; ◇: k- $\epsilon$  turbulence case; △: Reynolds stresses case;

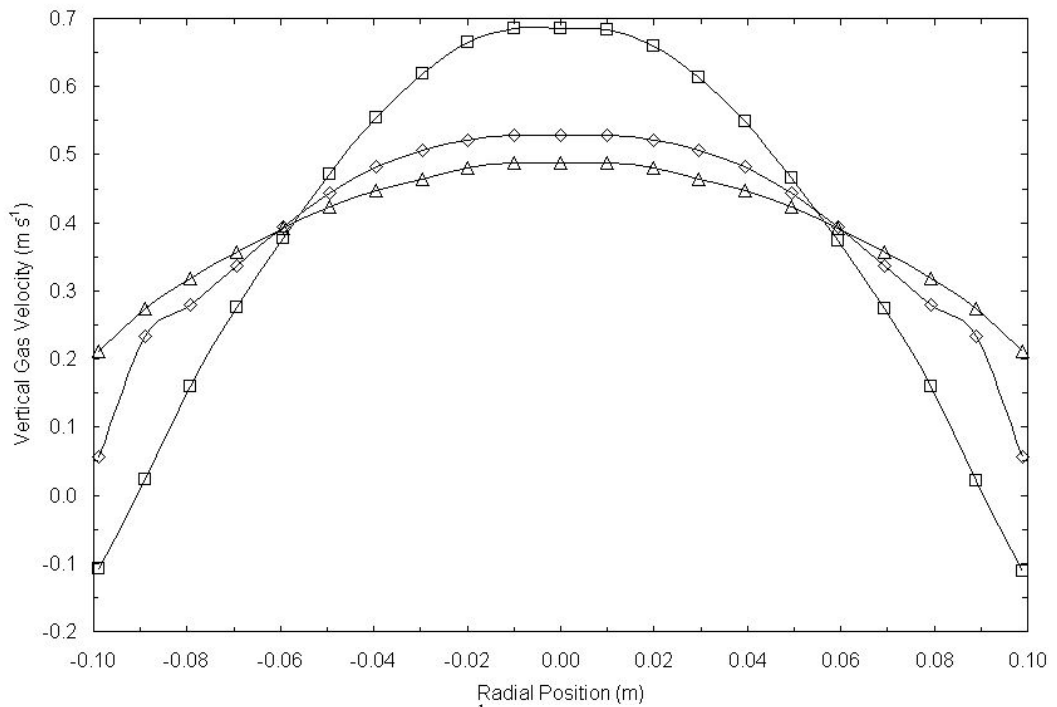


Figure 6: Vertical gas velocity profile ( $\text{m s}^{-1}$ ) for plane gas-liquid flow; At a height of 2.5 column diameters; □: laminar case; ◇: k- $\epsilon$  turbulence case; △: Reynolds stresses case;

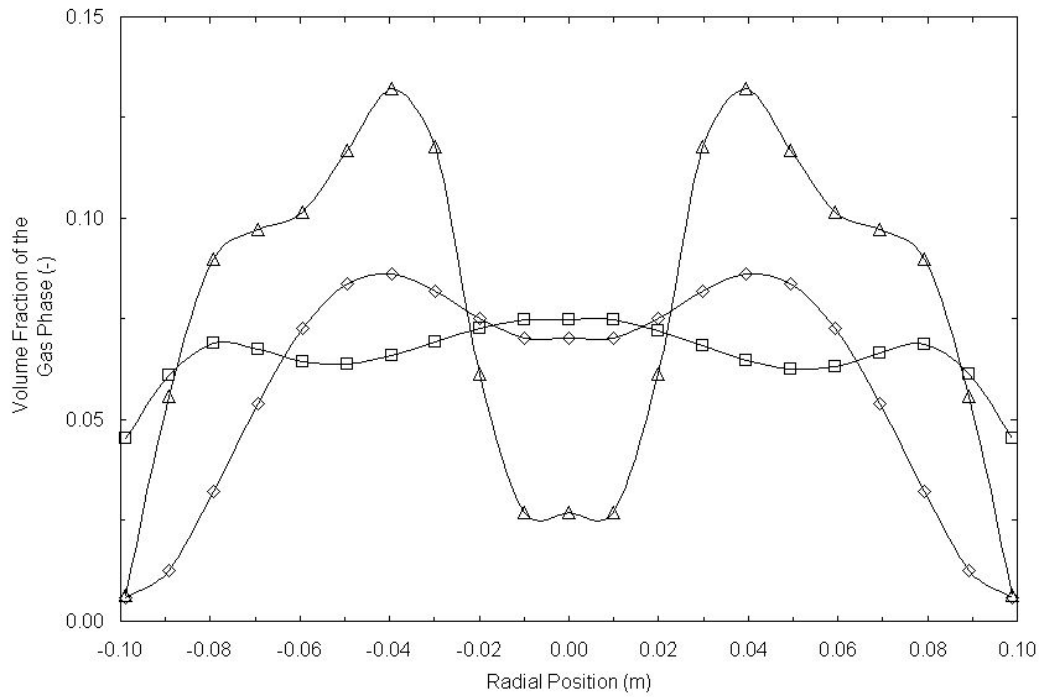


Figure 7: Volume fraction of the gas phase profile (-) for plane gas-liquid flow; At a height of 2.5 column diameters; □: laminar case; ◇: k- $\epsilon$  turbulence case; △: Reynolds stresses case;

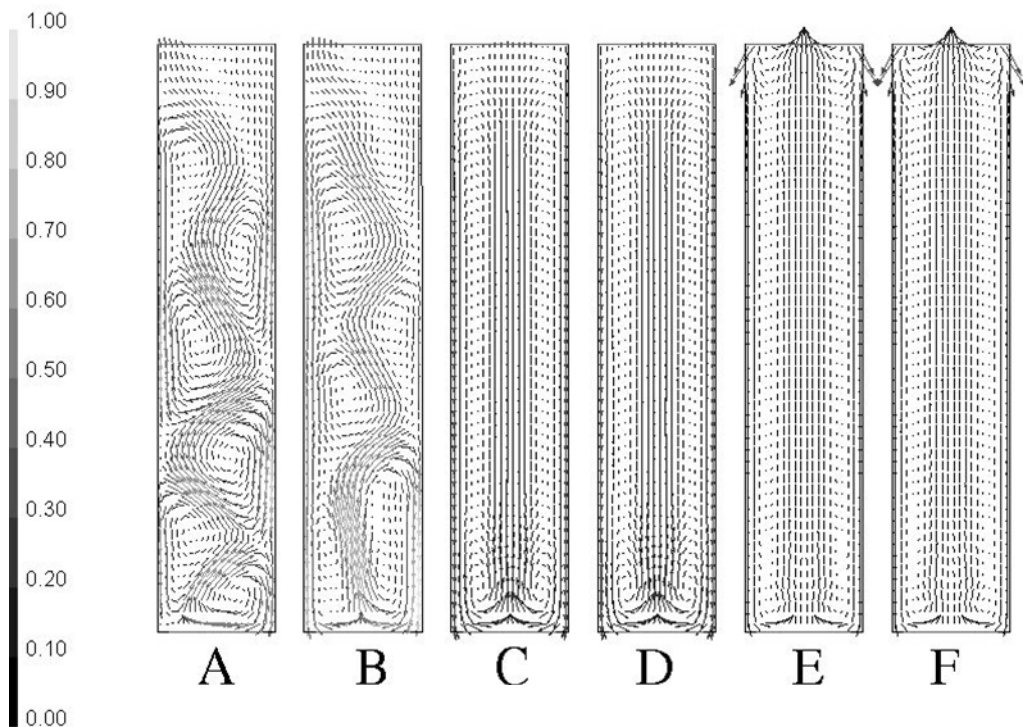


Figure 8: Vectors of mixture velocity magnitude ( $\text{m s}^{-1}$ ) for plane gas-liquid flow; A: laminar flow at 300 s; B: laminar flow at 600 s; C: k- $\epsilon$  turbulence at 300 s; D: k- $\epsilon$  turbulence at 600 s; E: Reynolds stresses at 300 s; F: Reynolds stresses at 600 s;

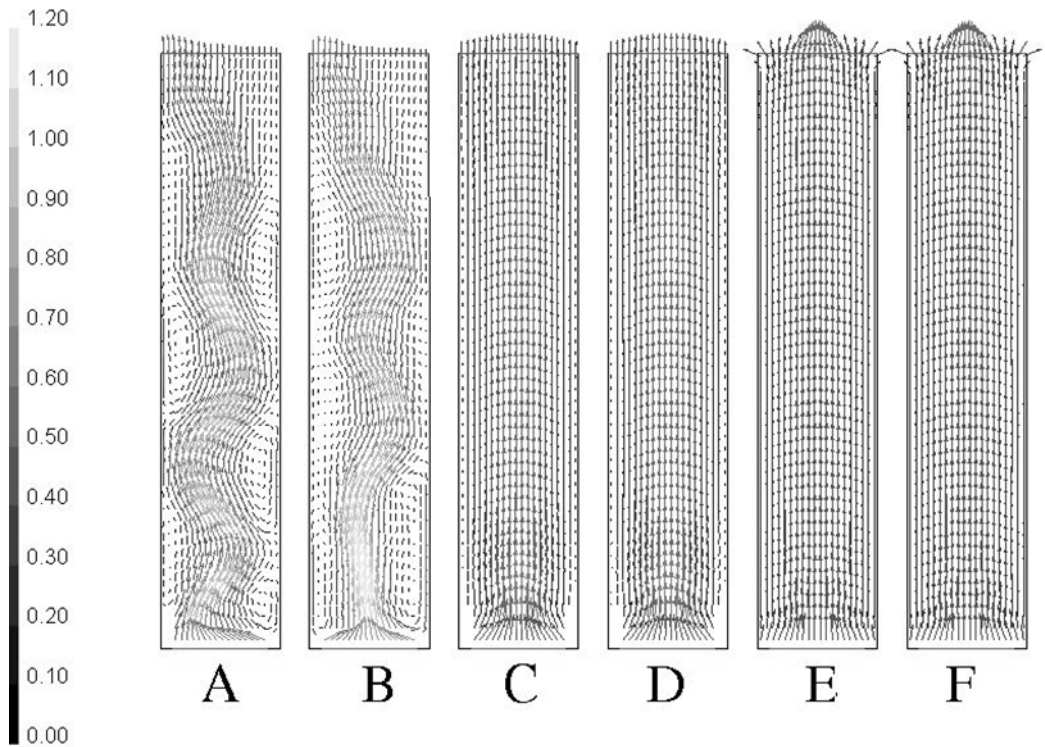


Figure 9: Vectors of gas velocity magnitude ( $\text{m s}^{-1}$ ) for plane gas-liquid flow;  
 A: laminar flow at 300 s; B: laminar flow at 600 s; C: k- $\epsilon$  turbulence at 300 s; D: k- $\epsilon$  turbulence at 600 s; E: Reynolds stresses at 300 s; F: Reynolds stresses at 600 s;

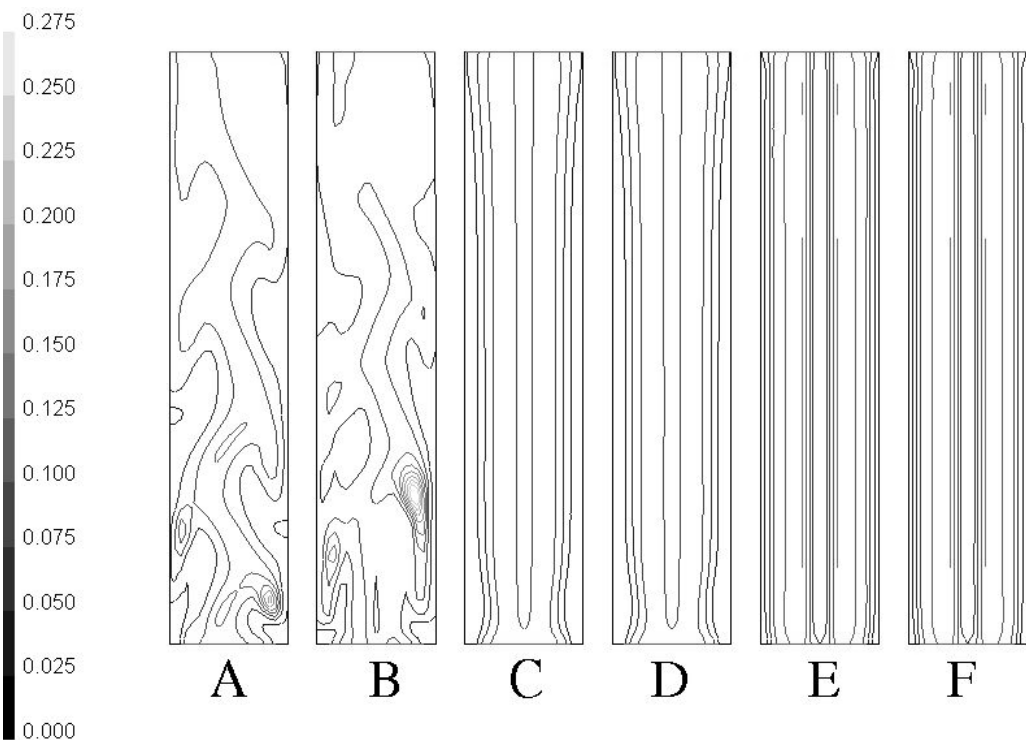


Figure 10: Contours of volume fraction of gas (-) for plane gas-liquid flow;  
 A: laminar flow at 300 s; B: laminar flow at 600 s; C: k- $\epsilon$  turbulence at 300 s; D: k- $\epsilon$  turbulence at 600 s; E: Reynolds stresses at 300 s; F: Reynolds stresses at 600 s;

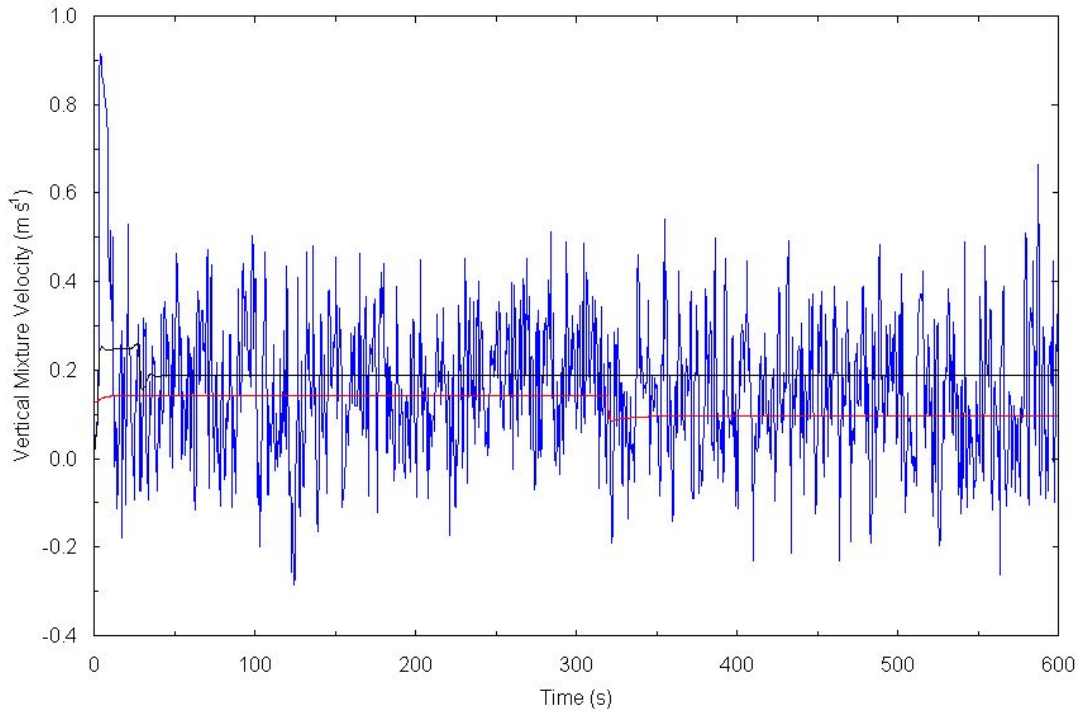


Figure 11: Time series of the vertical mixture velocity ( $\text{m s}^{-1}$ ) for rectangular gas-liquid flow; Point series recorded on the column centre line at a height of 2.5 column widths for Blue: laminar (Blue),  $k-\varepsilon$  turbulence (Black), Reynolds stresses (Red) cases;

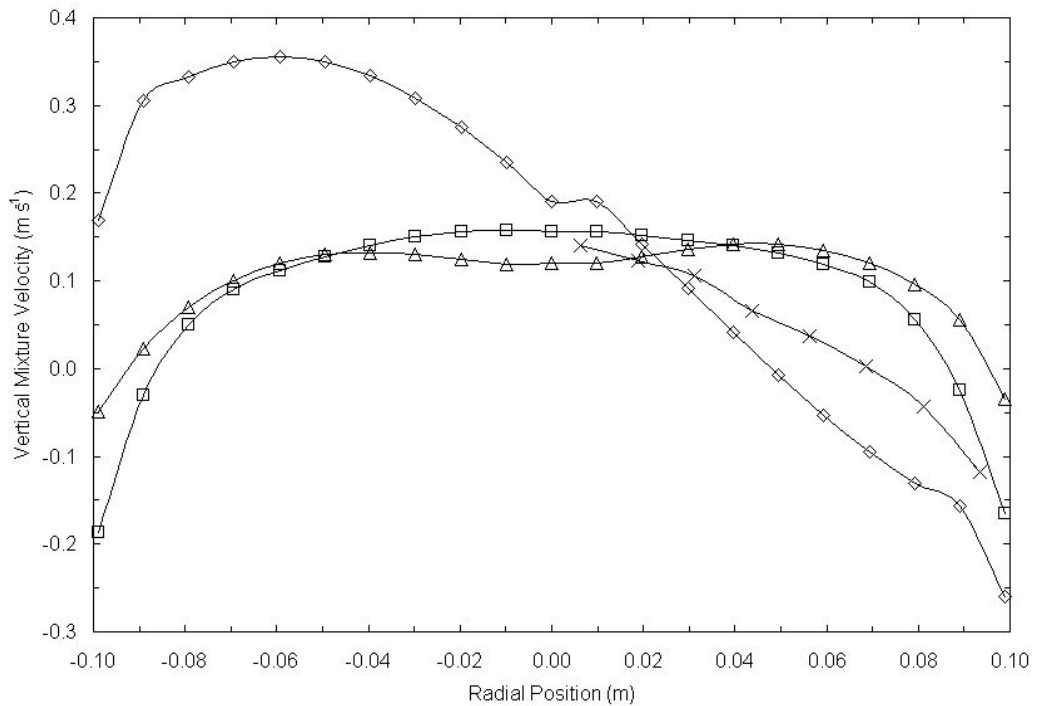


Figure 12: Vertical mixture velocity profile ( $\text{m s}^{-1}$ ) for rectangular gas-liquid flow; At a height of 2.5 column widths;  $\square$ : laminar case;  $\diamond$ :  $k-\varepsilon$  turbulence case;  $\triangle$ : Reynolds stresses case;  $\times$  Experimental column<sup>35-37</sup>;

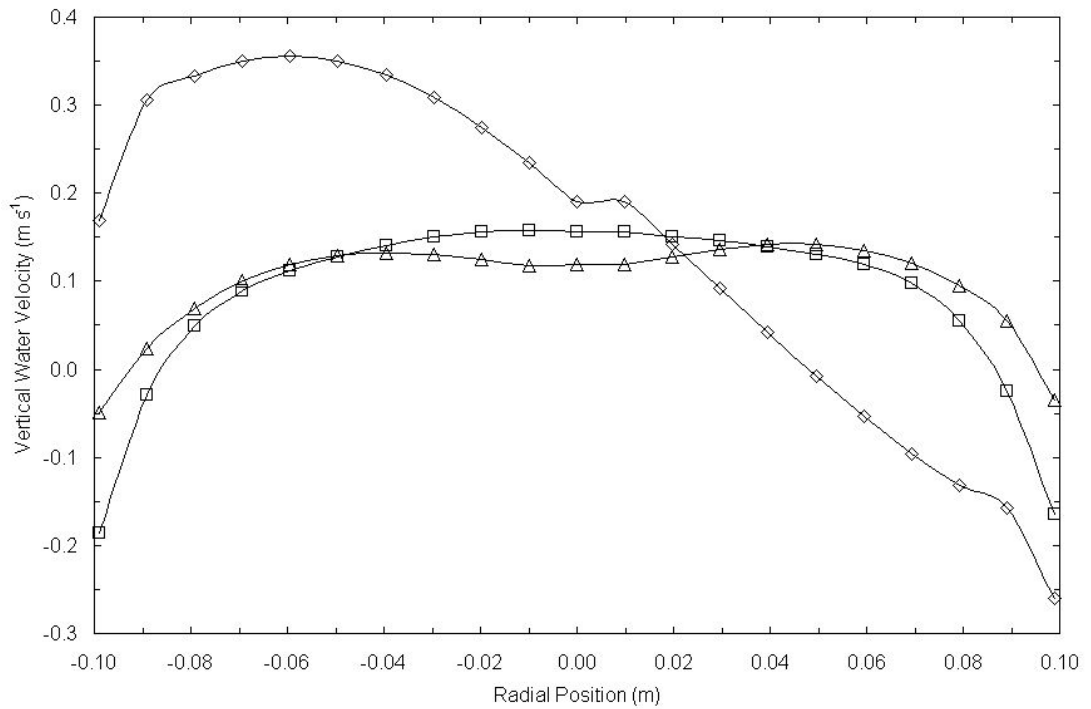


Figure 13: Vertical liquid velocity profile ( $\text{m s}^{-1}$ ) for rectangular gas-liquid flow; At a height of 2.5 column widths;  $\square$ : laminar case;  $\diamond$ : k- $\epsilon$  turbulence case;  $\triangle$ : Reynolds stresses case;

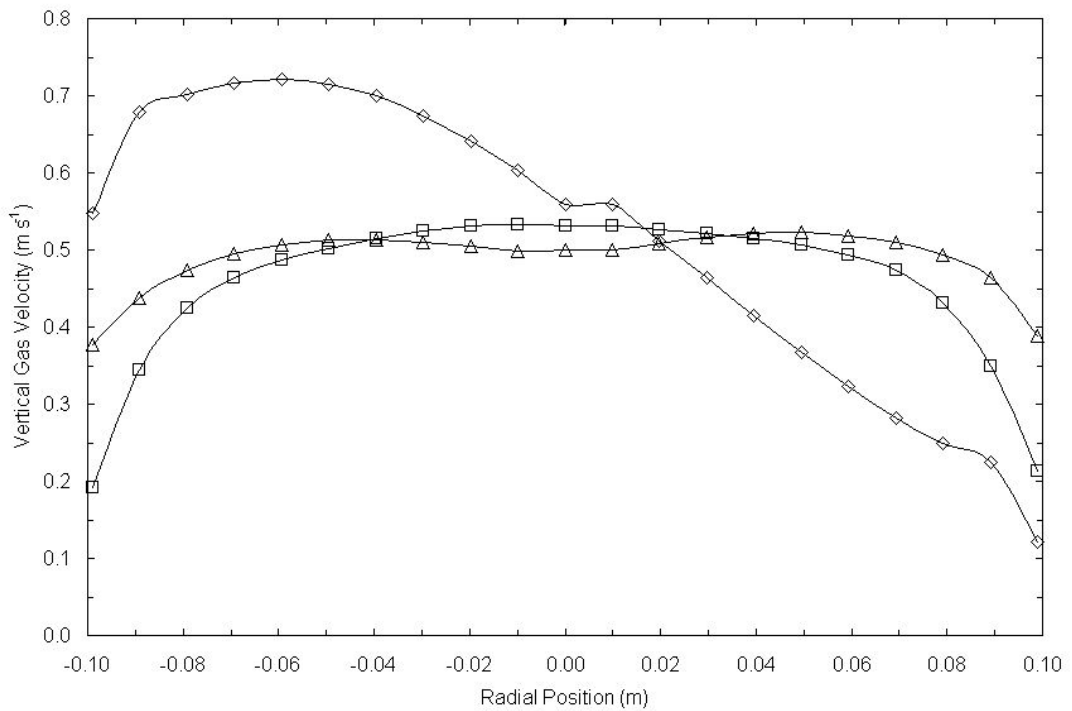


Figure 14: Vertical gas velocity profile ( $\text{m s}^{-1}$ ) for rectangular gas-liquid flow; At a height of 2.5 column widths;  $\square$ : laminar case;  $\diamond$ : k- $\epsilon$  turbulence case;  $\triangle$ : Reynolds stresses case;

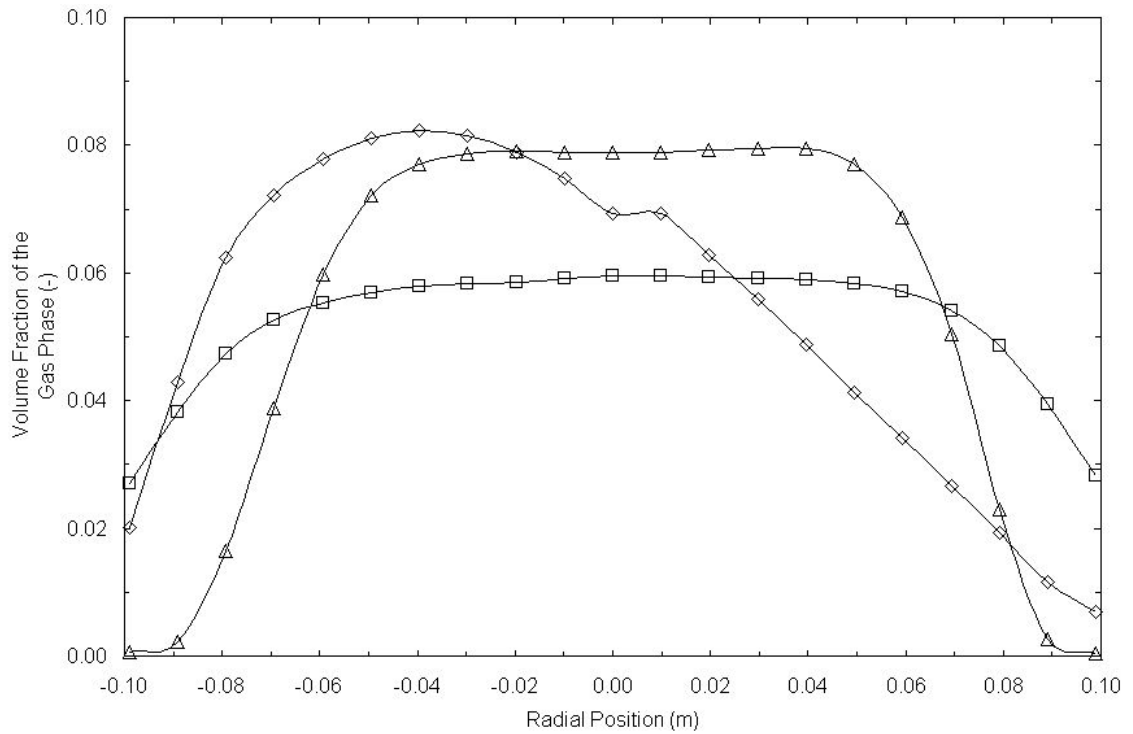


Figure 15: Volume fraction of gas phase profile (-) for rectangular gas-liquid flow; At a height of 2.5 column widths;  $\square$ : laminar case;  $\diamond$ : k- $\epsilon$  turbulence case;  $\triangle$ : Reynolds stresses case;

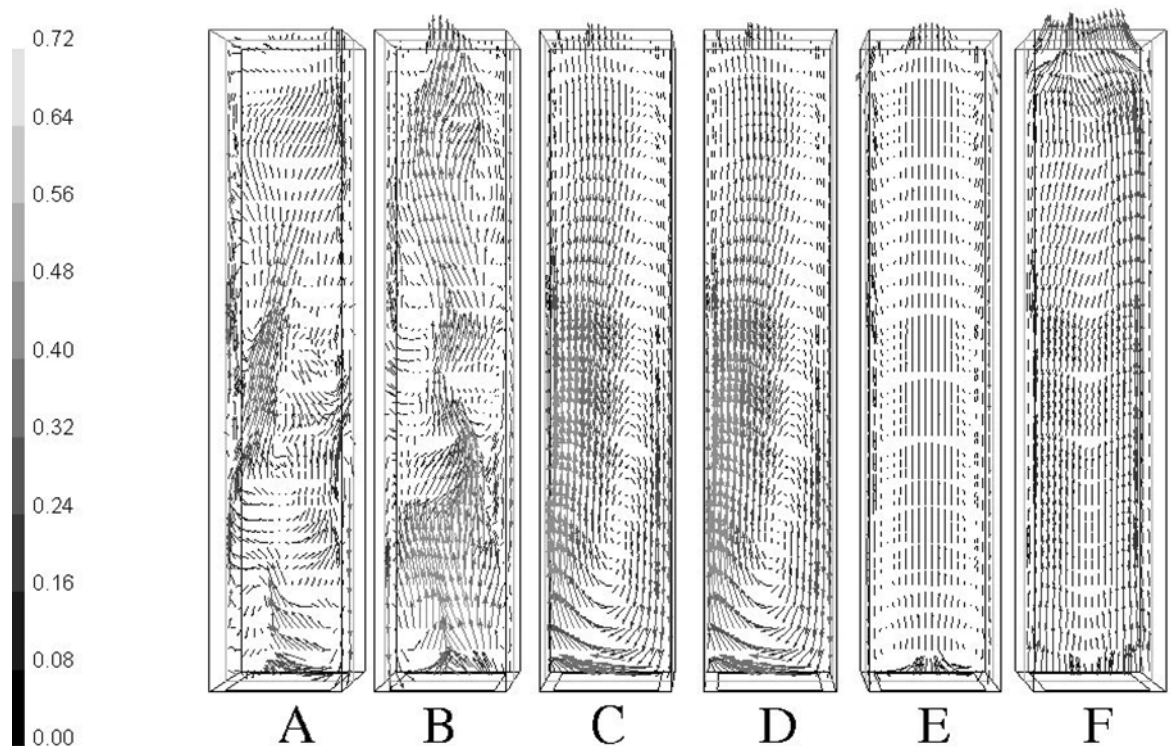


Figure 16: Vectors of mixture velocity magnitude ( $\text{m s}^{-1}$ ) for rectangular gas-liquid flow; A: laminar flow at 300 s; B: laminar flow at 600 s; C: k- $\epsilon$  turbulence at 300 s; D: k- $\epsilon$  turbulence at 600 s; E: Reynolds stresses at 300 s; F: Reynolds stresses at 600 s;

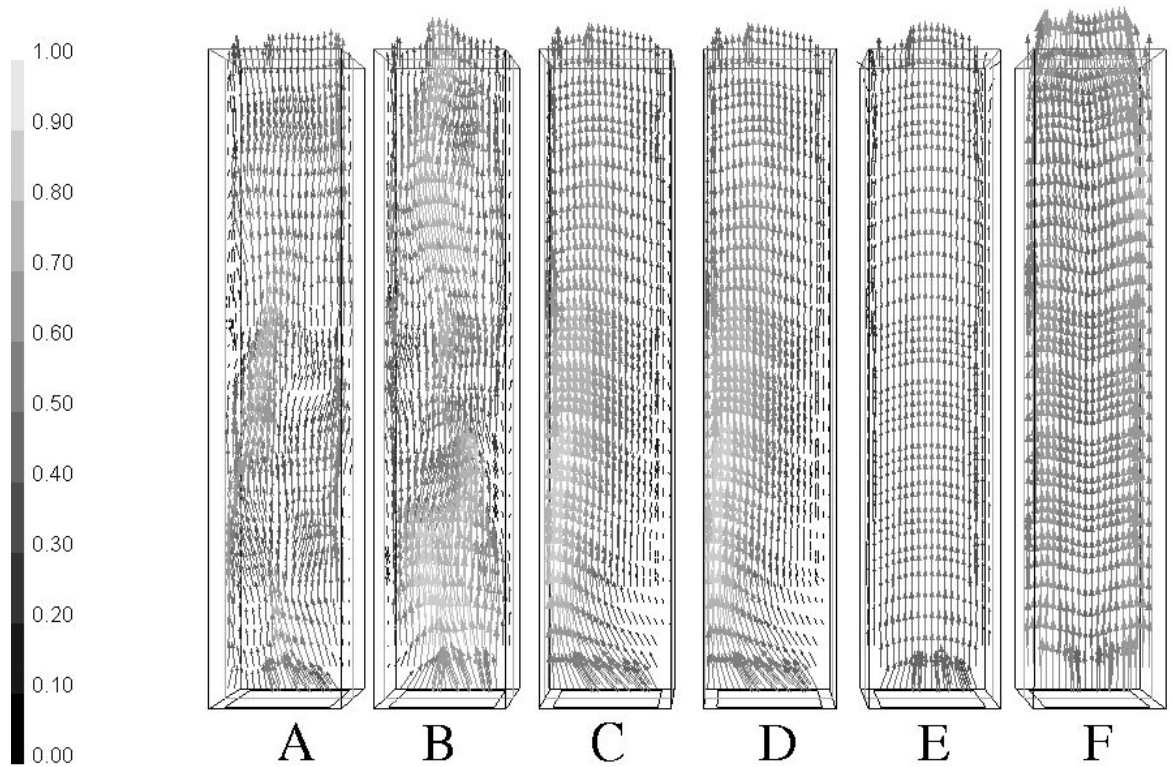


Figure 17: Vectors of gas velocity magnitude ( $\text{m s}^{-1}$ ) for rectangular gas-liquid flow; A: laminar flow at 300 s; B: laminar flow at 600 s; C: k- $\epsilon$  turbulence at 300 s; D: k- $\epsilon$  turbulence at 600 s; E: Reynolds stresses at 300 s; F: Reynolds stresses at 600 s;

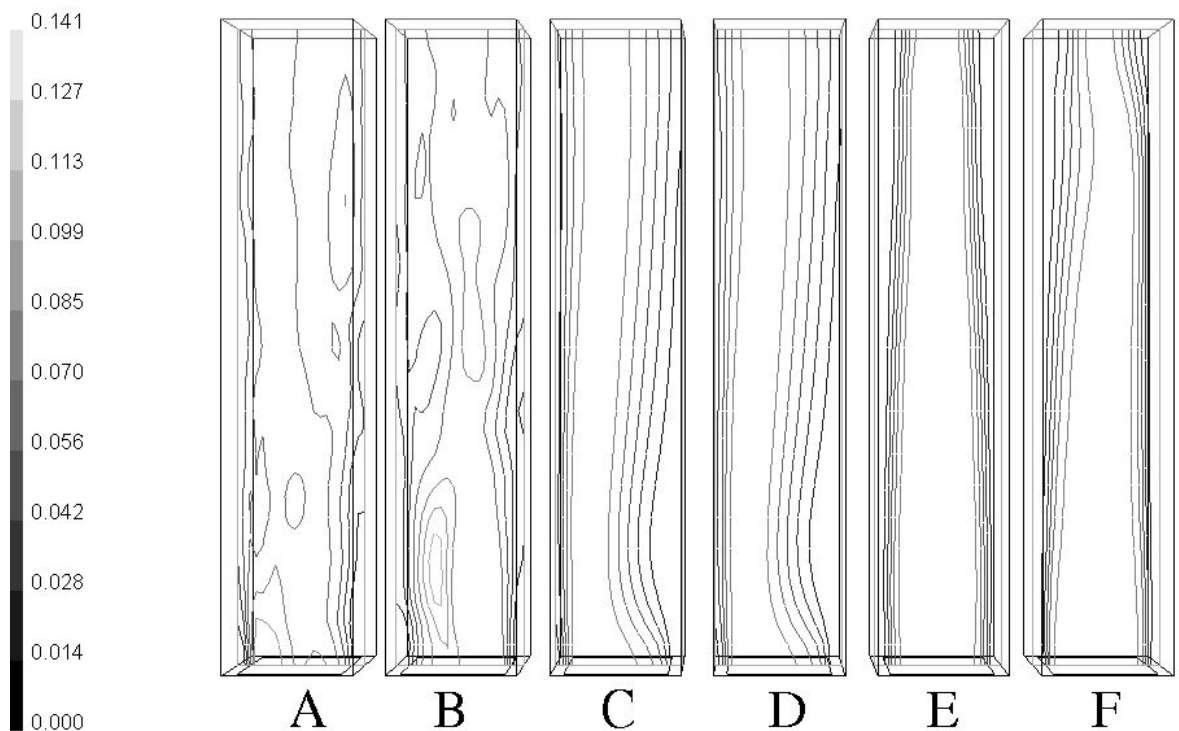


Figure 18: Contours of gas phase volume fraction (-) for rectangular gas-liquid flow; A: laminar flow at 300 s; B: laminar flow at 600 s; C: k- $\epsilon$  turbulence at 300 s; D: k- $\epsilon$  turbulence at 600 s; E: Reynolds stresses at 300 s; F: Reynolds stresses at 600 s;

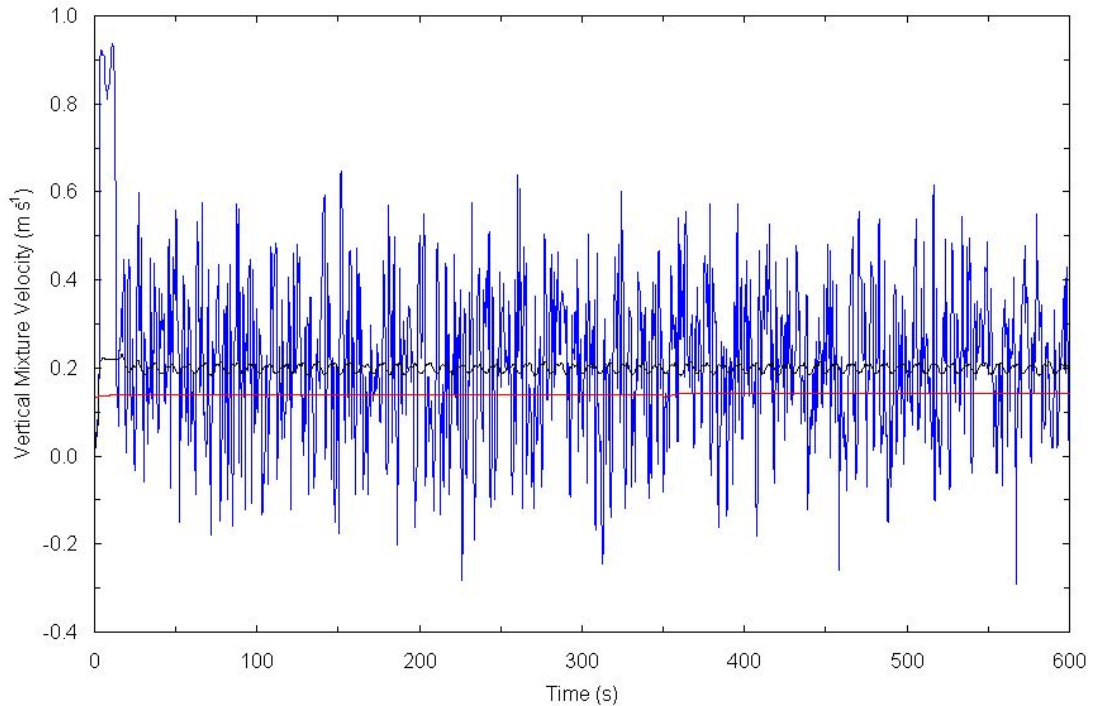


Figure 19: Time series of the vertical mixture velocity ( $\text{m s}^{-1}$ ) for cylindrical gas-liquid flow; Point series recorded on the column centre line at a height of 2.6 column diameters for Blue: laminar (Blue),  $k\text{-}\epsilon$  turbulence (Black), Reynolds stresses (Red) cases;

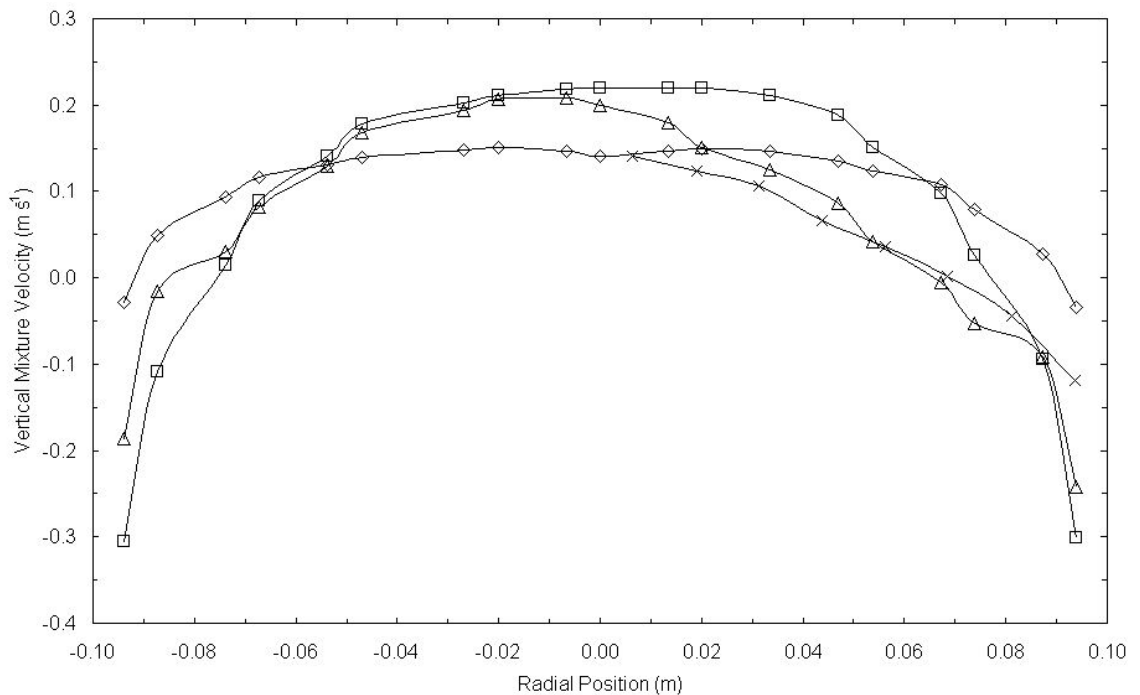


Figure 20: Vertical mixture velocity profile ( $\text{m s}^{-1}$ ) for cylindrical gas-liquid flow; At a height of 2.6 column diameters;  $\square$ : laminar case;  $\diamond$ :  $k\text{-}\epsilon$  turbulence case;  $\triangle$ : Reynolds stresses case;  $\times$  Experimental column<sup>35-37</sup>;

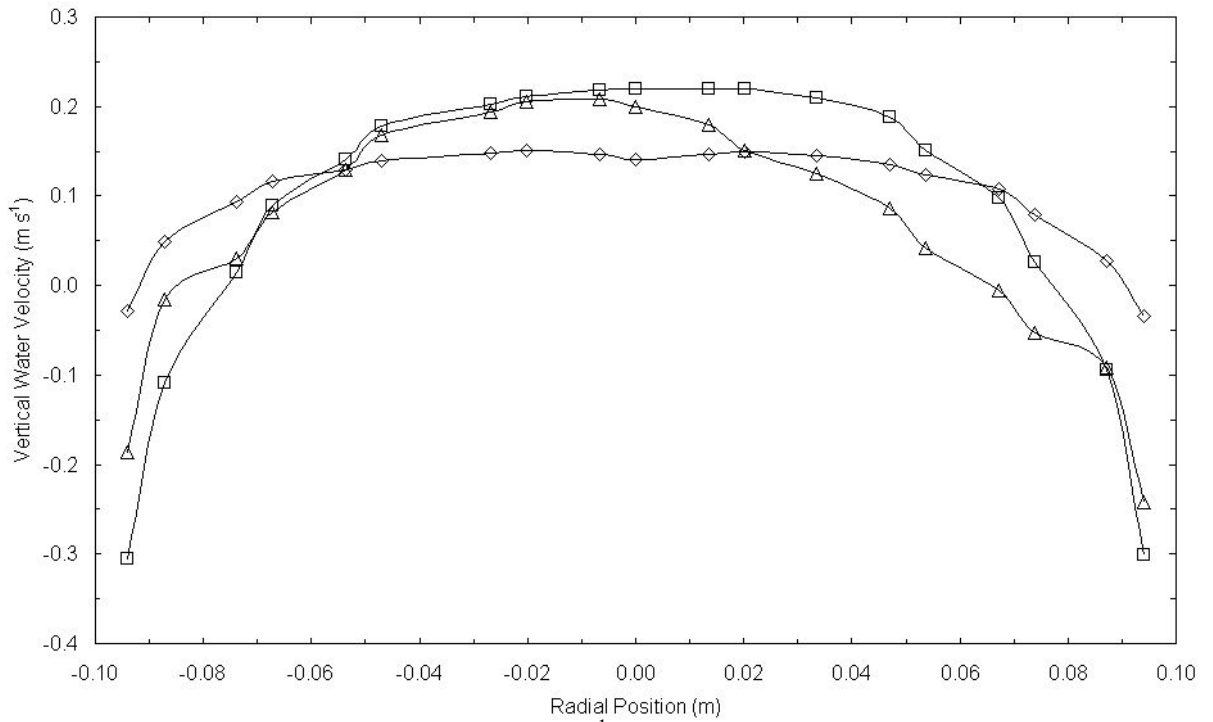


Figure 21: Vertical liquid velocity profile ( $\text{m s}^{-1}$ ) for cylindrical gas-liquid flow; At a height of 2.6 column diameters;  $\square$ : laminar case;  $\diamond$ : k- $\epsilon$  turbulence case;  $\triangle$ : Reynolds stresses case;

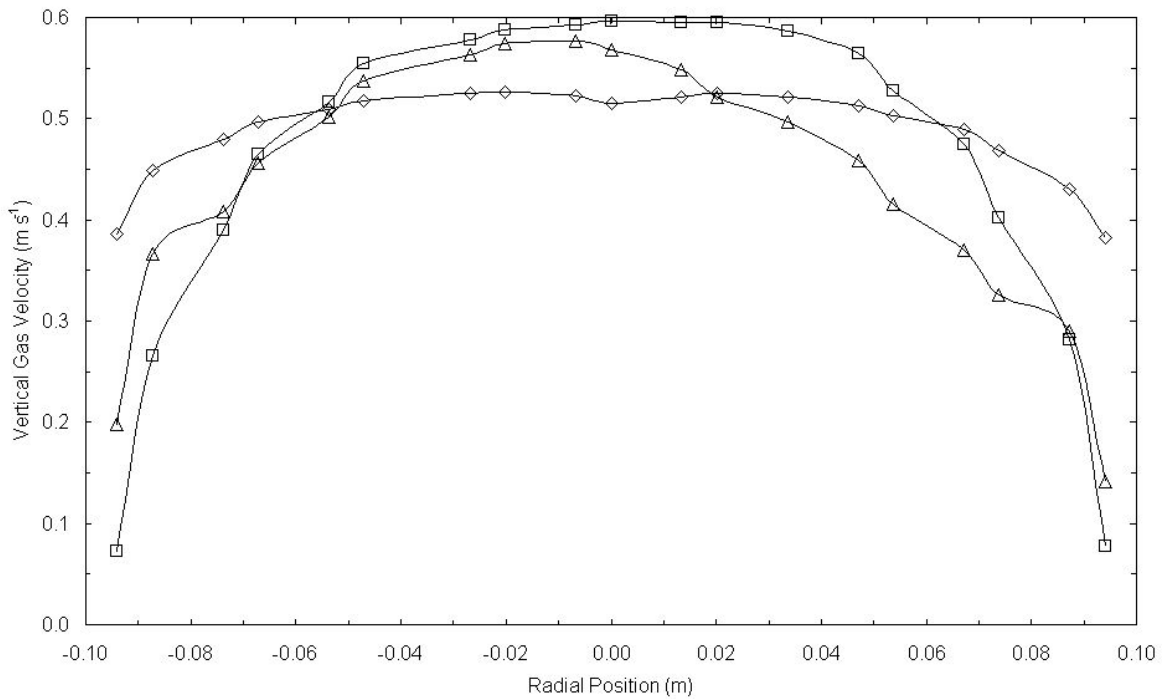


Figure 22: Vertical gas velocity profile ( $\text{m s}^{-1}$ ) for cylindrical gas-liquid flow; At a height of 2.6 column diameters;  $\square$ : laminar case;  $\diamond$ : k- $\epsilon$  turbulence case;  $\triangle$ : Reynolds stresses case;

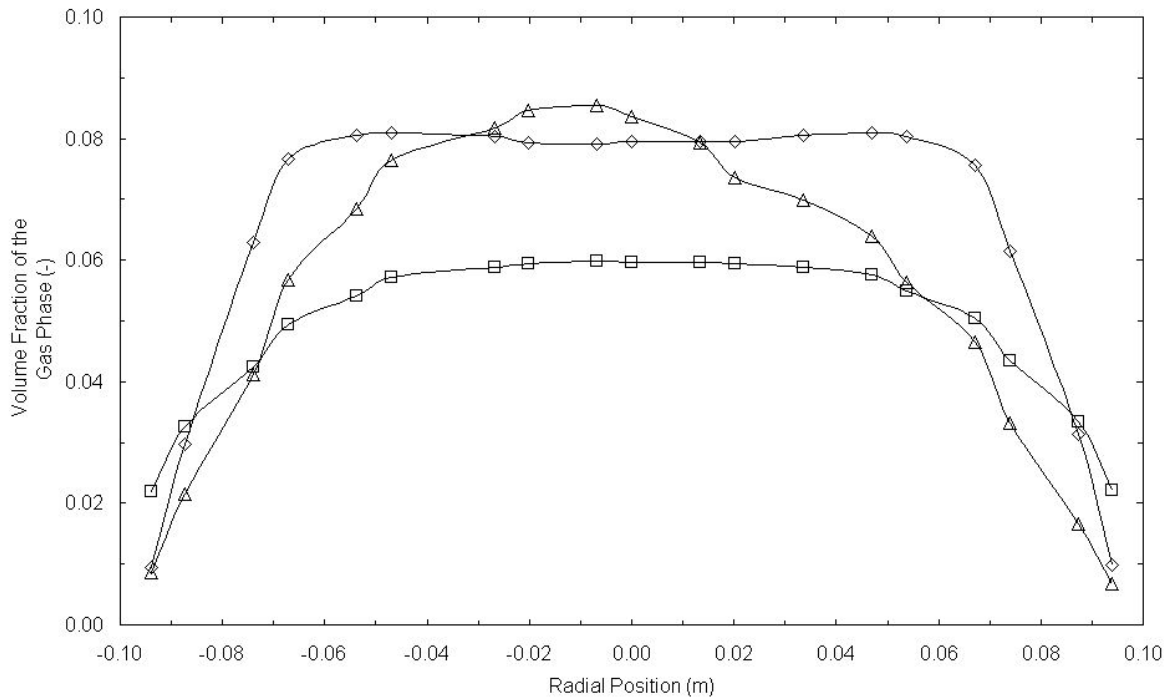


Figure 23: Volume fraction of gas phase profile (-) for cylindrical gas-liquid flow; At a height of 2.6 column diameters; □: laminar case; ◇: k- $\epsilon$  turbulence case; △: Reynolds stresses case;

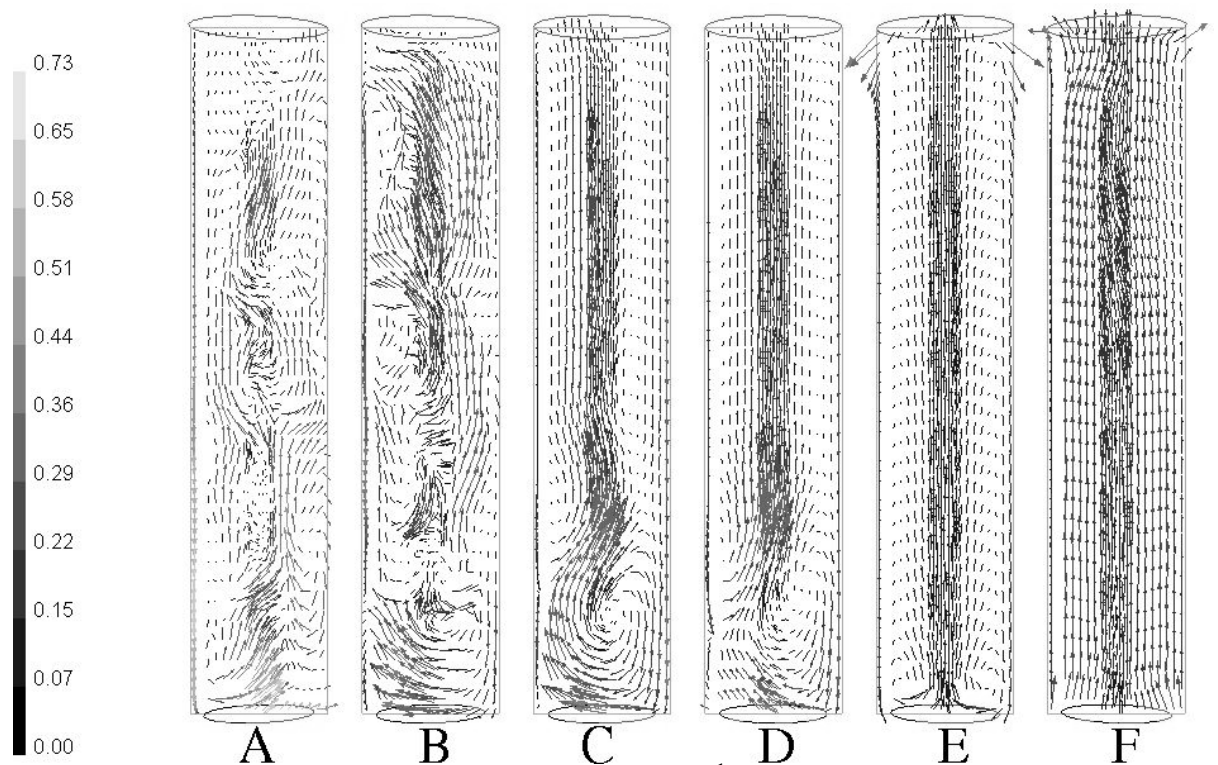


Figure 24: Vectors of mixture velocity magnitude ( $\text{m s}^{-1}$ ) for cylindrical gas-liquid flow; A: laminar flow at 300 s; B: laminar flow at 600 s; C: k- $\epsilon$  turbulence at 300 s; D: k- $\epsilon$  turbulence at 600 s; E: Reynolds stresses at 300 s; F: Reynolds stresses at 600 s;

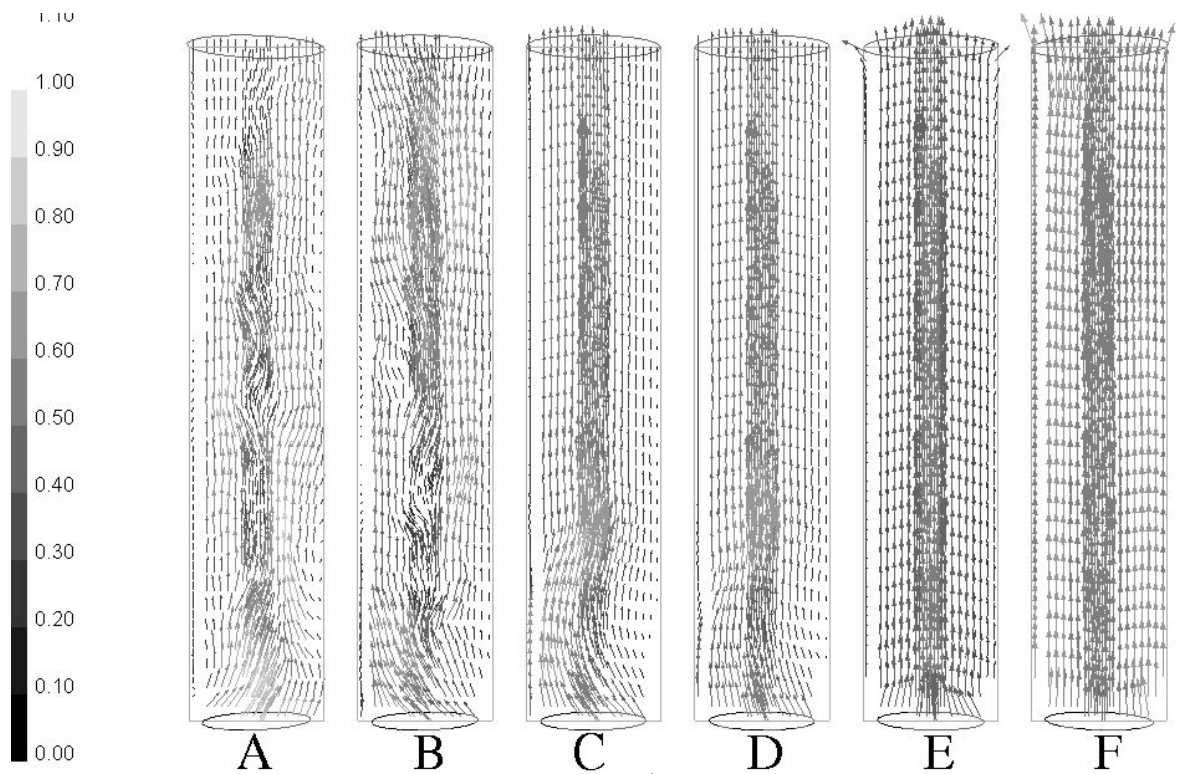


Figure 25: Vectors of gas velocity magnitude ( $\text{m s}^{-1}$ ) for cylindrical gas-liquid flow; A: laminar flow at 300 s; B: laminar flow at 600 s; C: k- $\epsilon$  turbulence at 300 s; D: k- $\epsilon$  turbulence at 600 s; E: Reynolds stresses at 300 s; F: Reynolds stresses at 600 s;

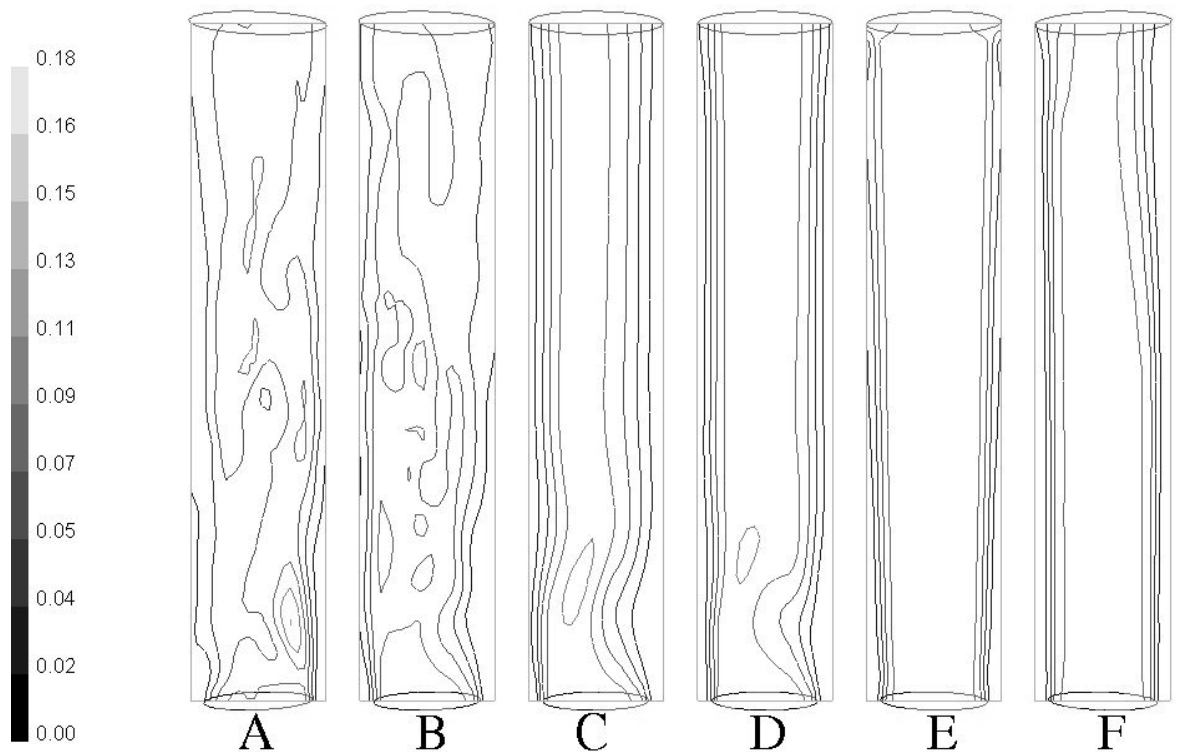


Figure 26: Contours of volume fraction of gas (-) for cylindrical gas-liquid flow; A: laminar flow at 300 s; B: laminar flow at 600 s; C: k- $\epsilon$  turbulence at 300 s; D: k- $\epsilon$  turbulence at 600 s; E: Reynolds stresses at 300 s; F: Reynolds stresses at 600 s;

## 13.2 Turbulence modelling of buoyancy driven flows results

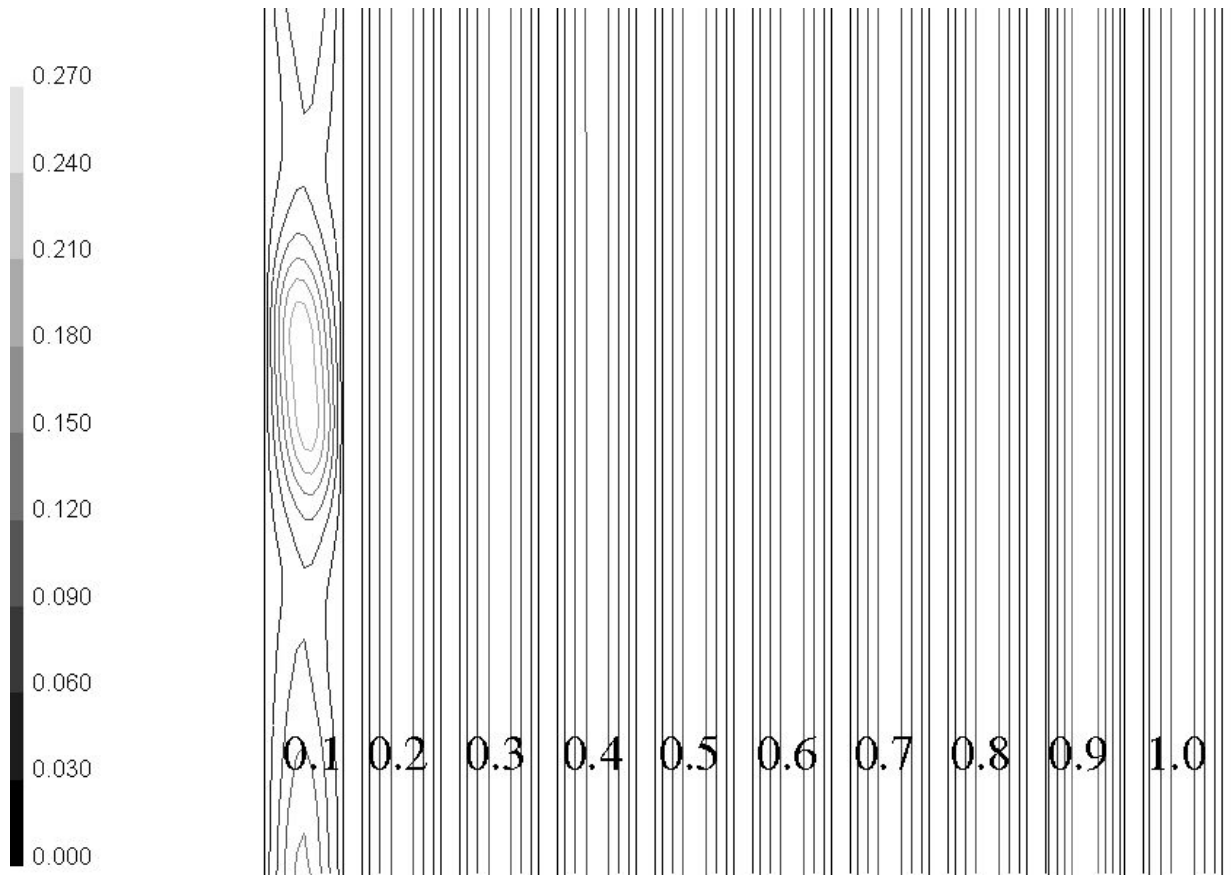


Figure 27: Contours of stream function ( $\text{kg s}^{-1}$ ) for lateral convection; Using turbulent Reynolds stresses in a 50:1 height to width aspect ratio mesh, where each number corresponds to the under-relaxation factor applied to the turbulence transport equations;

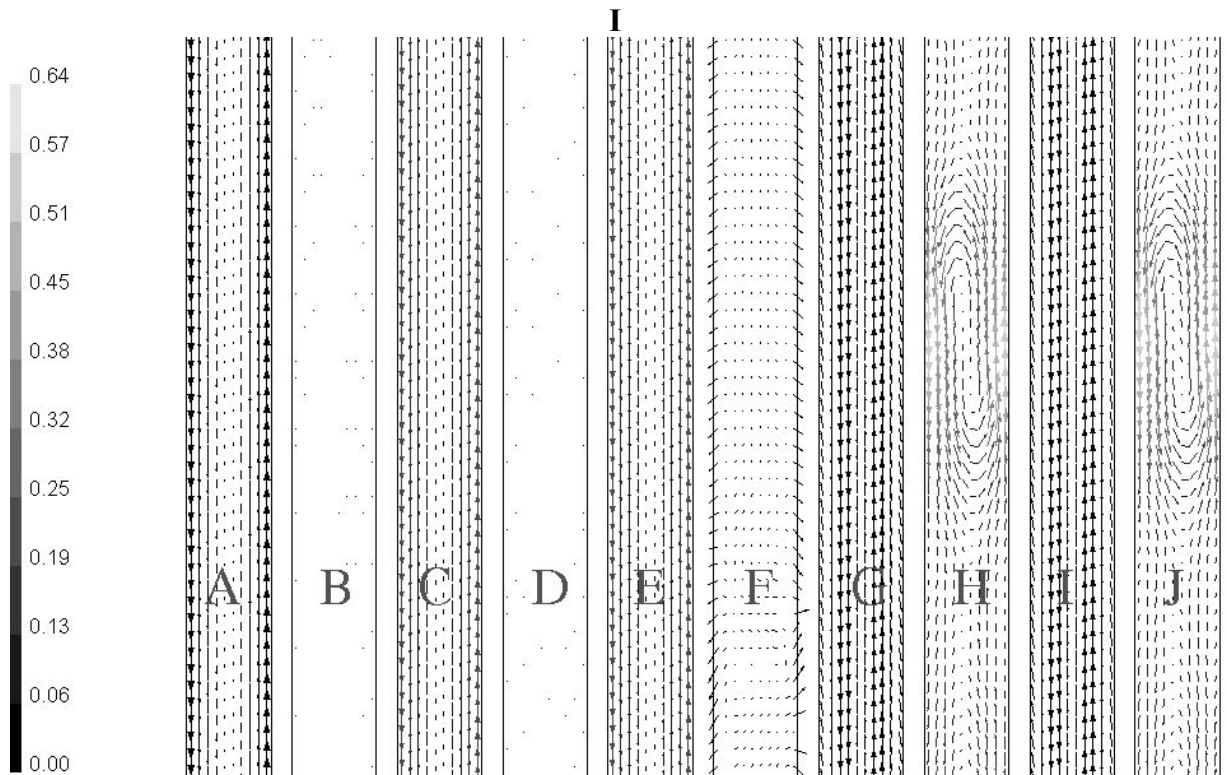


Figure 28: Lateral convection plots for the 50:1 height to width aspect ratio mesh;  
**I**: Vectors of velocity ( $\text{m s}^{-1}$ ), the scale on the left is for the colour of the vectors;  
 Overleaf:

**II**: Contours of stream function ( $\text{kg s}^{-1}$ ), the scale on the left is for the colour of the stream function contours;

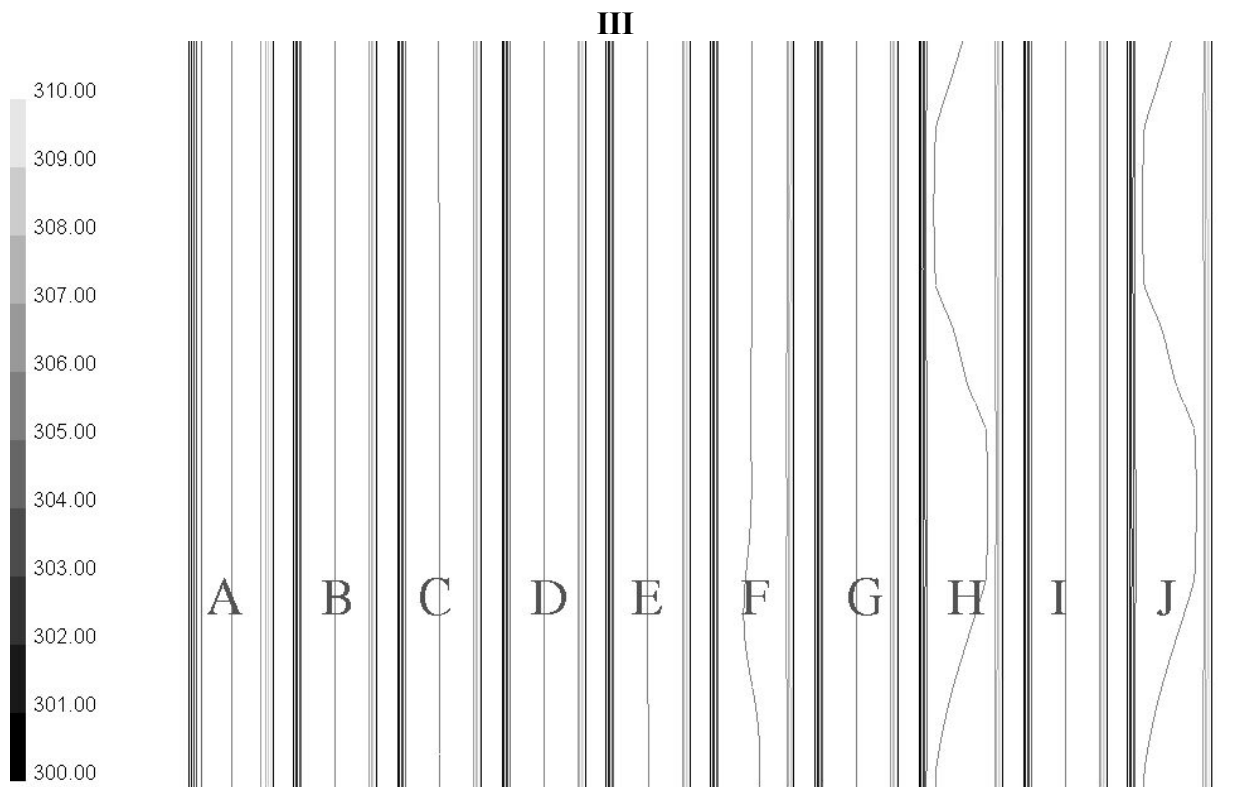
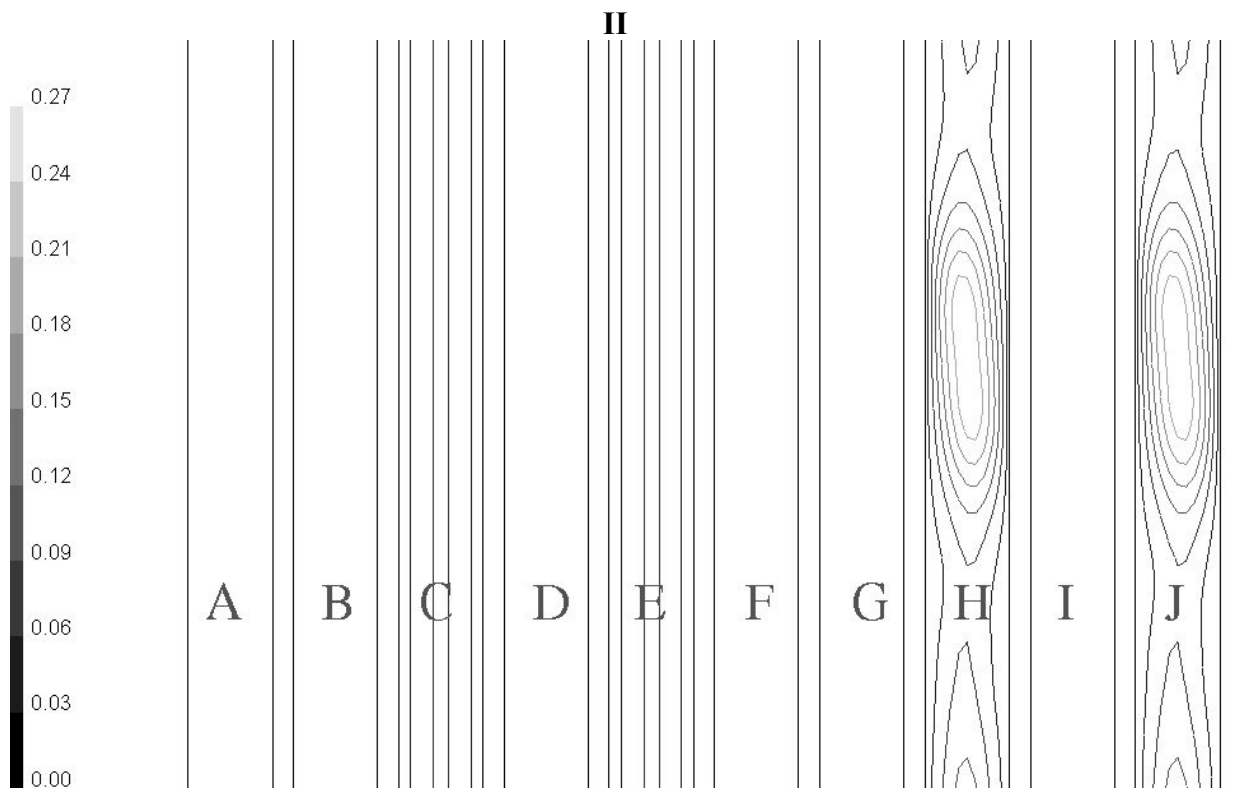
**III**: Contours of static temperature (K), the scale on the left is for the colour of the temperature contours;

#### k- $\epsilon$ turbulence model

A: no basic flow profiles; B: velocity profile updated for all iterations; C: velocity profile updated after each time-step; D: velocity and temperature profiles updated for all iterations; E: velocity and temperature profiles updated after each time-step;

#### Reynolds stresses model

F: no basic flow profiles; G: velocity profile updated for all iterations; H: velocity profile updated after each time-step; I: velocity and temperature profiles updated for all iterations; J: velocity and temperature profiles updated after each time-step;



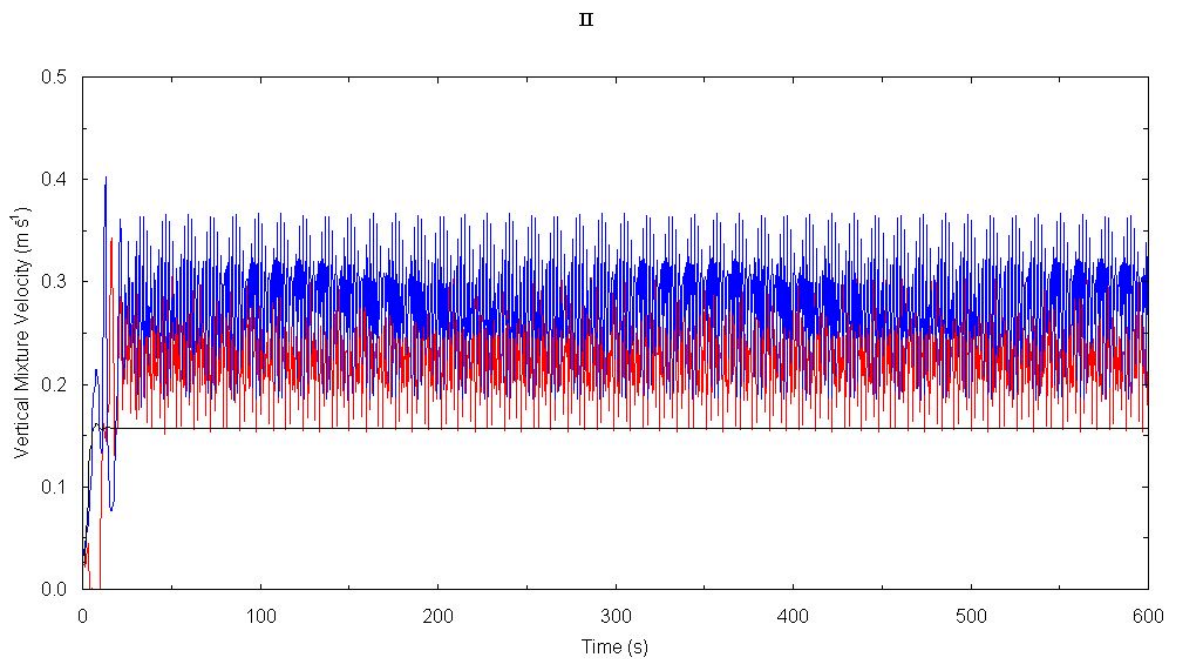
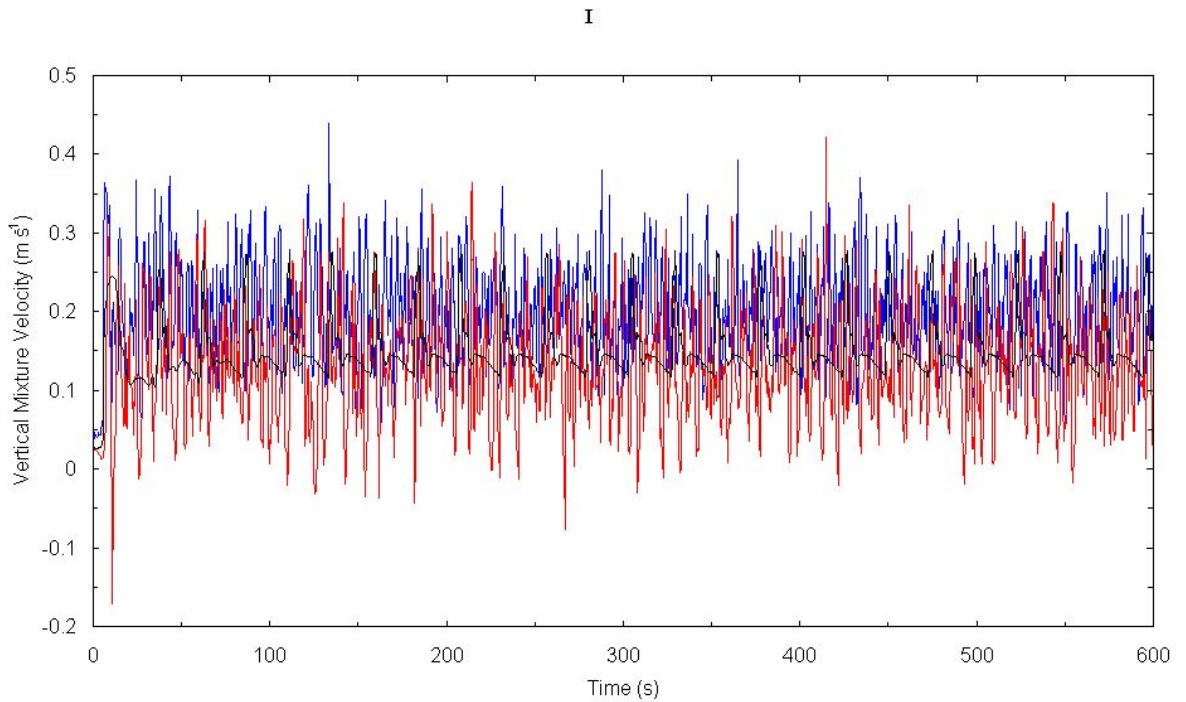


Figure 29: Time series of the vertical mixture velocity ( $\text{m s}^{-1}$ ) for gas-liquid flow; **I**: Scalar transport equation represents the gas phase volume fraction; **II**: Algebraic slip mixture model<sup>9</sup> were recorded on the column centre line at a height of 2.5 column widths; Black line:  $k$ - $\epsilon$  turbulence transport; Red line: Reynolds stresses turbulence transport; Blue line: Reynolds stresses turbulence transport with vertical velocity updating;

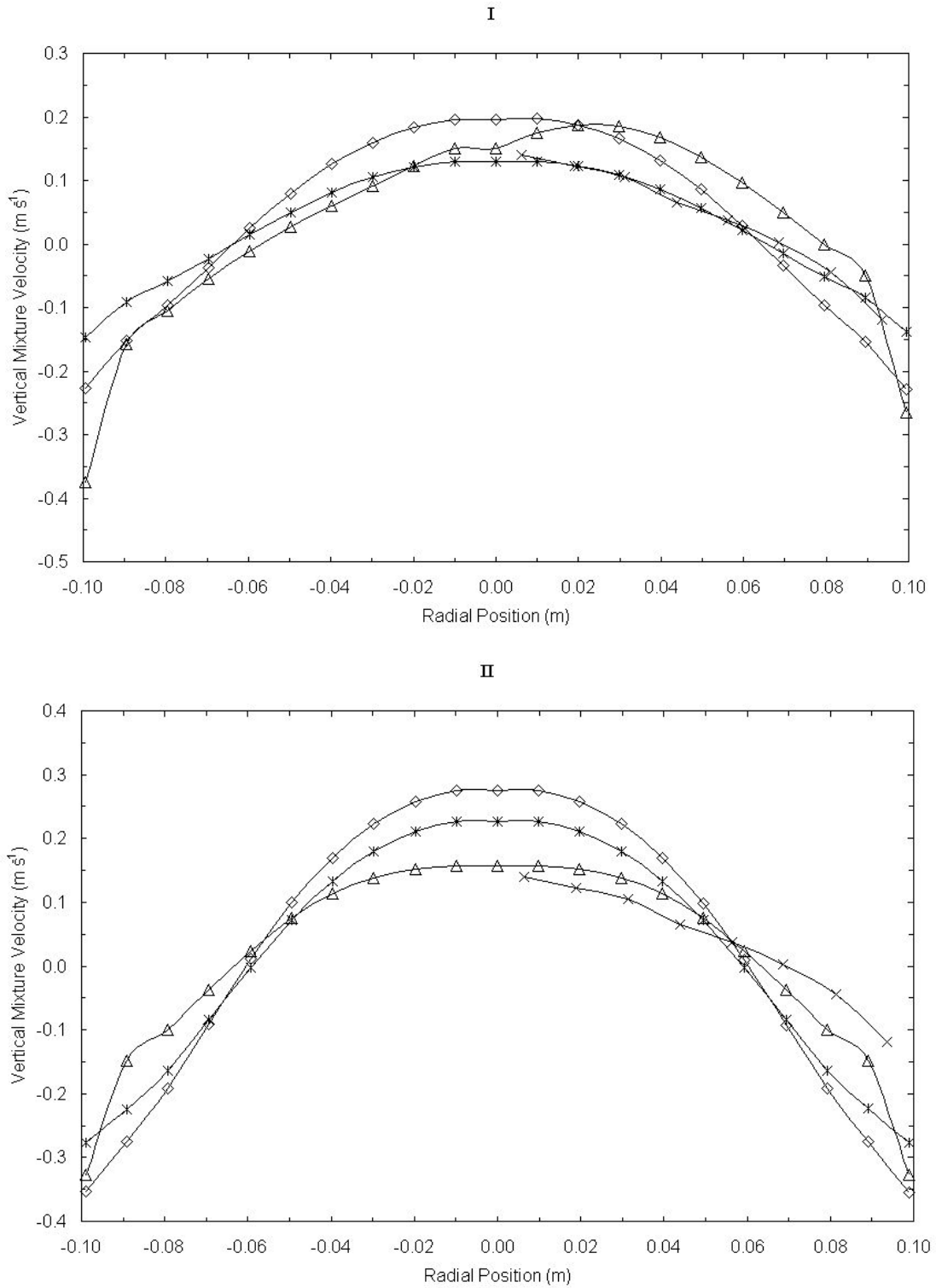


Figure 30: Profile plots of the vertical mixture velocity ( $\text{m s}^{-1}$ ) for gas-liquid flow;  
**I**: Scalar transport equation represents the gas phase volume fraction; **II**: Algebraic slip mixture model<sup>9</sup>;  
 At a height of 2.5 column widths;  $\Delta$ :  $k$ - $\epsilon$  turbulence transport;  $*$ : Reynolds stresses turbulence transport;  $\diamond$ : Reynolds stresses turbulence transport with vertical velocity updating;  $\times$  Experimental column<sup>35-37</sup>;

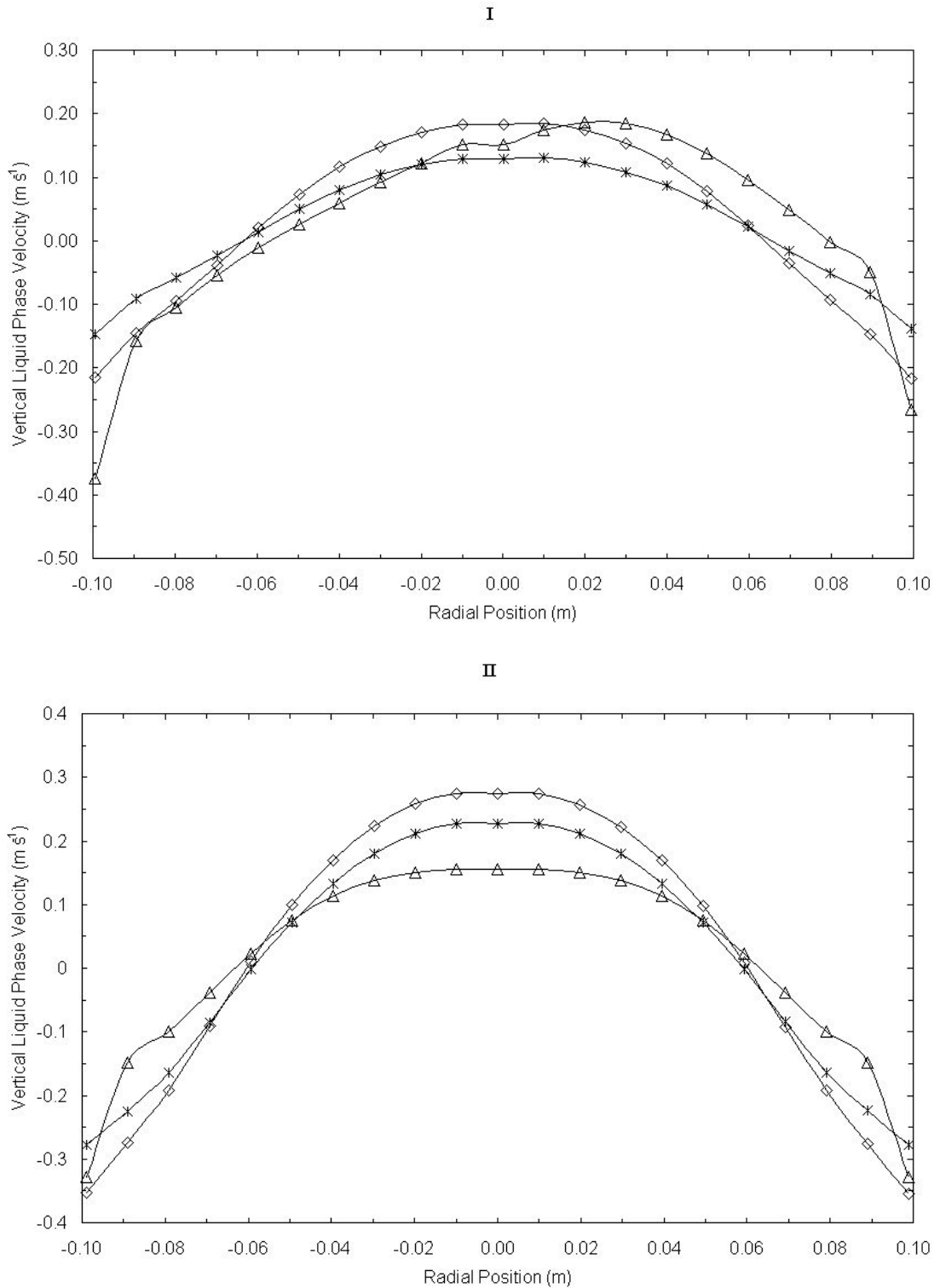


Figure 31: Profile plots of the vertical liquid velocity ( $\text{m s}^{-1}$ ) for gas-liquid flow;  
**I:** Scalar transport equation represents the gas phase volume fraction; **II:** Algebraic slip mixture model<sup>9</sup>;  
 At a height of 2.5 column widths;  $\triangle$ : k- $\epsilon$  turbulence transport;  $*$ : Reynolds stresses turbulence transport;  $\diamond$ : Reynolds stresses turbulence transport with vertical velocity updating;

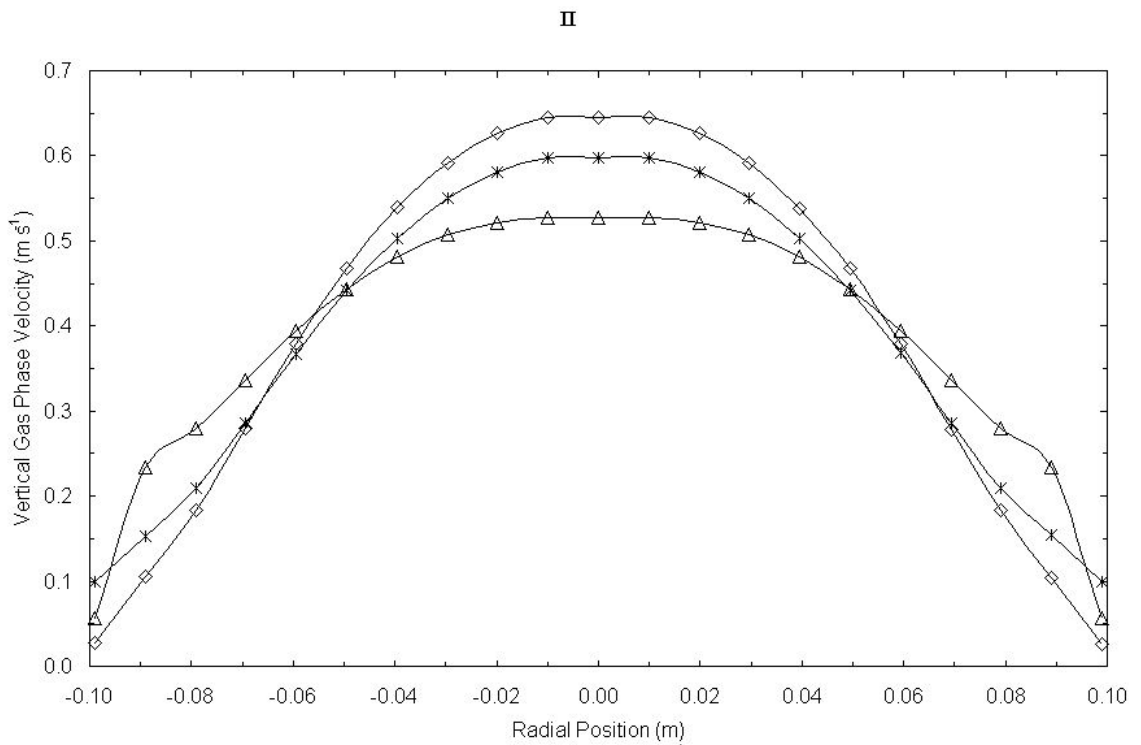
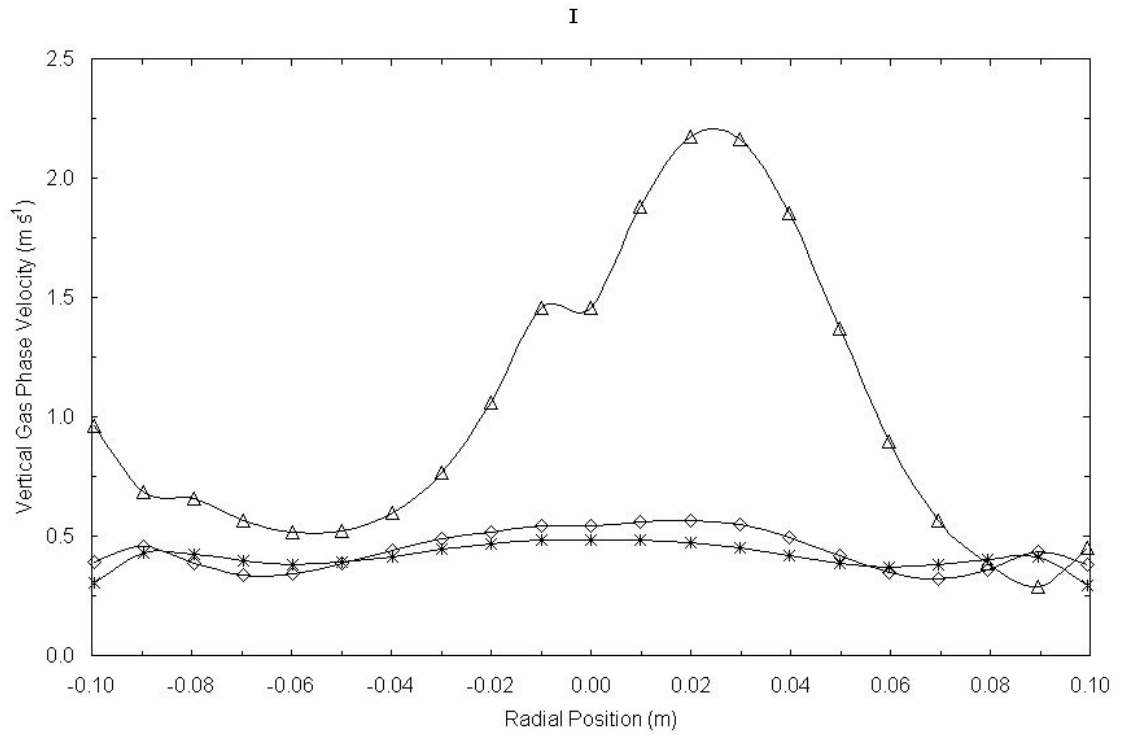


Figure 32: Profile plots of the vertical gas velocity ( $\text{m s}^{-1}$ ) for gas-liquid flow; **I**: Scalar transport equation represents the gas phase volume fraction; **II**: Algebraic slip mixture model<sup>9</sup>; At a height of 2.5 column widths;  $\Delta$ : k- $\epsilon$  turbulence transport; \*: Reynolds stresses turbulence transport;  $\diamond$ : Reynolds stresses turbulence transport with vertical velocity updating;

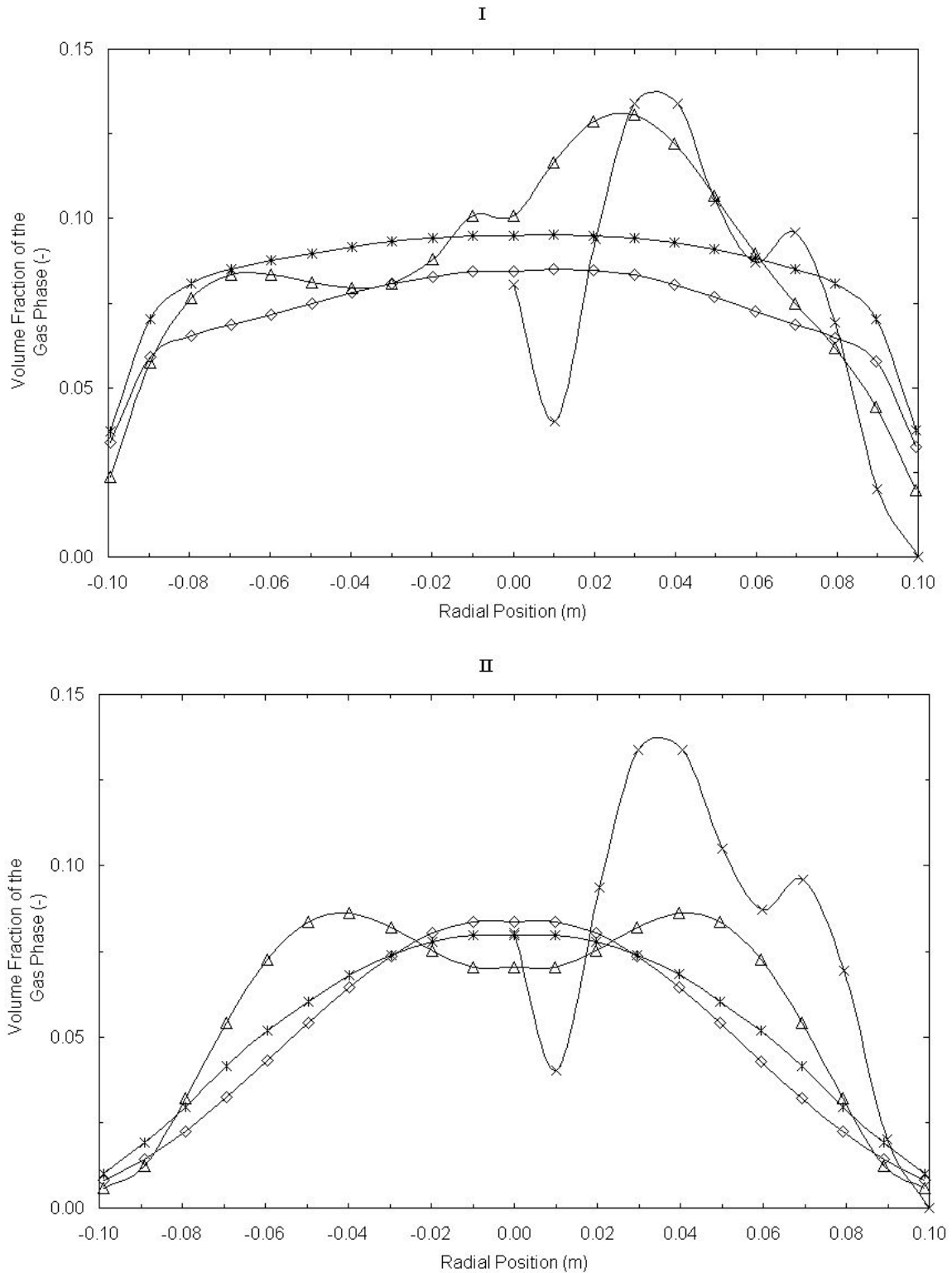


Figure 33: Profile plots of the gas volume fraction (-) for gas-liquid flow;  
**I:** Scalar transport equation represents the gas phase volume fraction; **II:** Algebraic slip mixture model<sup>9</sup>;  
 At a height of 2.5 column widths;  $\Delta$ : k- $\epsilon$  turbulence transport;  $*$ : Reynolds stresses turbulence transport;  $\diamond$ : Reynolds stresses turbulence transport with vertical velocity updating;  $\times$  Experimental column<sup>35-37</sup>;

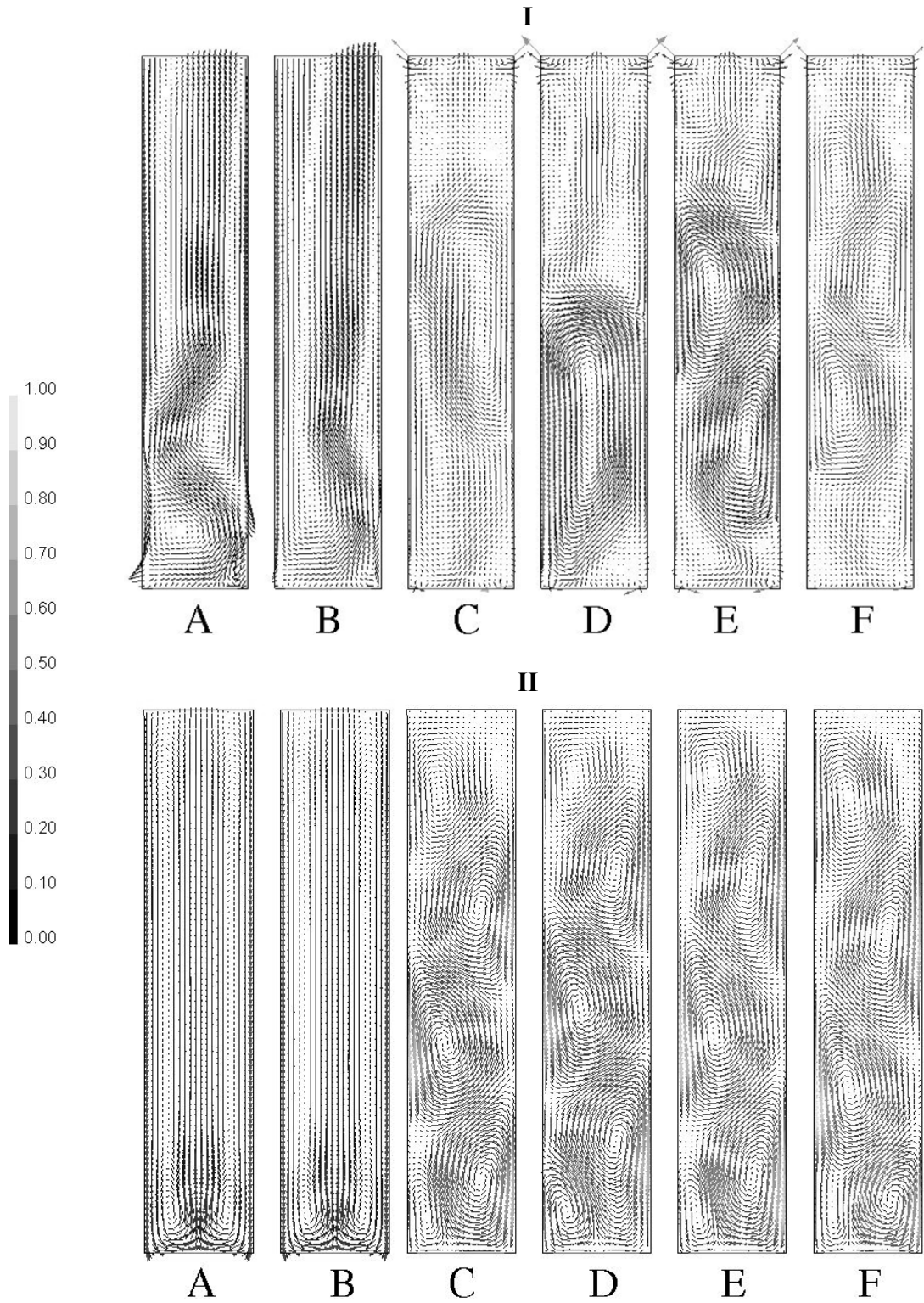


Figure 34: Vectors of mixture velocity magnitude ( $\text{m s}^{-1}$ ) for gas-liquid flow; **I**: modified scalar equation; **II**: standard mixture model<sup>9</sup>; A: k- $\epsilon$  turbulence transport at 300 s; B: k- $\epsilon$  turbulence transport at 600 s; C: Reynolds stresses at 300 s; D: Reynolds stresses at 600 s; E: Reynolds stresses with velocity updating at 300 s; F: Reynolds stresses with velocity updating at 600 s;

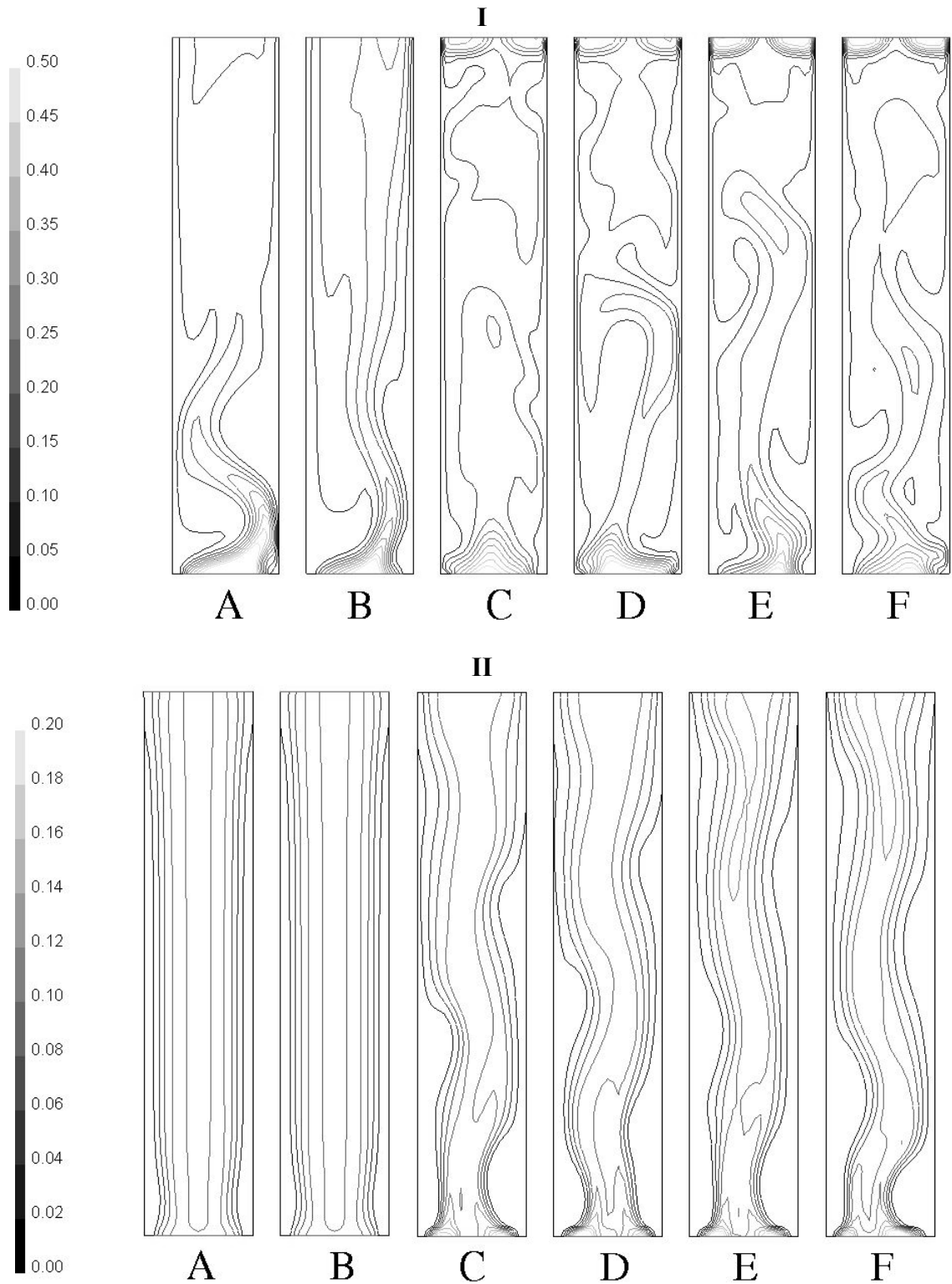


Figure 35: Contours of gas phase volume fraction (-) for gas-liquid flow;  
**I**: modified scalar equation; **II**: standard mixture model<sup>9</sup>;  
 A: k- $\epsilon$  turbulence transport at 300 s; B: k- $\epsilon$  turbulence transport at 600 s; C: Reynolds stresses at 300 s; D: Reynolds stresses at 600 s; E: Reynolds stresses with velocity updating at 300 s; F: Reynolds stresses with velocity updating at 600 s;

### 13.3 Gas-liquid-solid flow results

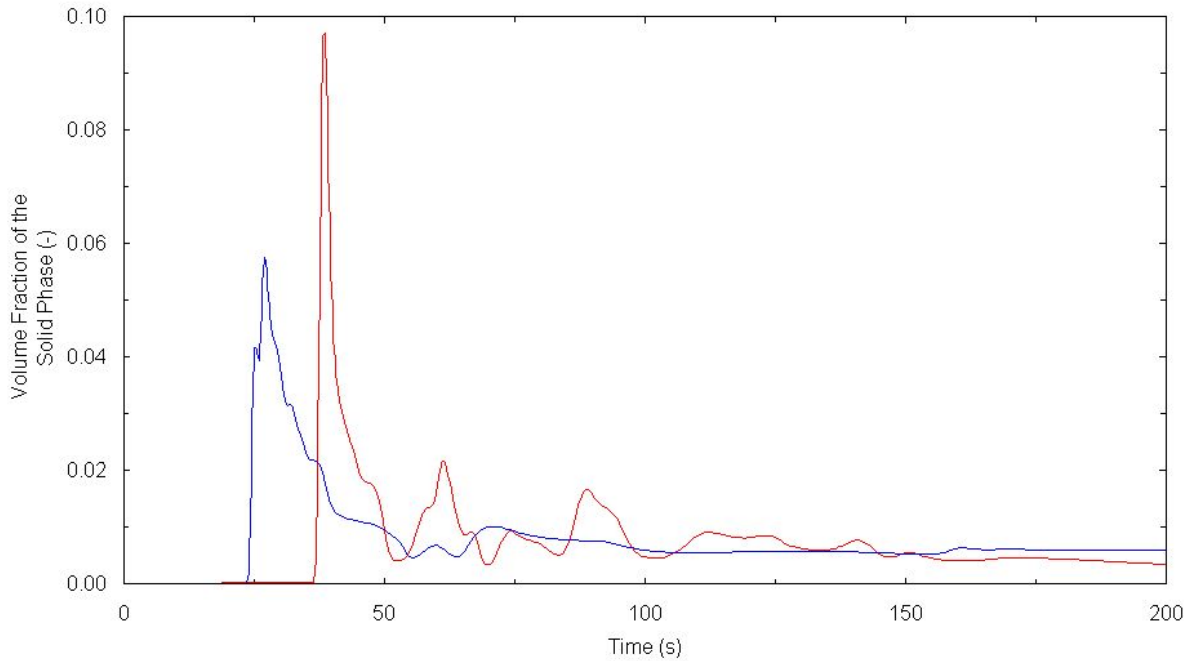


Figure 36: Time series of the solid phase volume fraction (-) for solid-liquid flow; At 2.5 mesh widths on the column centreline recorded fractions for: Red: Scalar transport equation represents the solid phase volume fraction; Blue: Algebraic slip mixture model<sup>9</sup>;

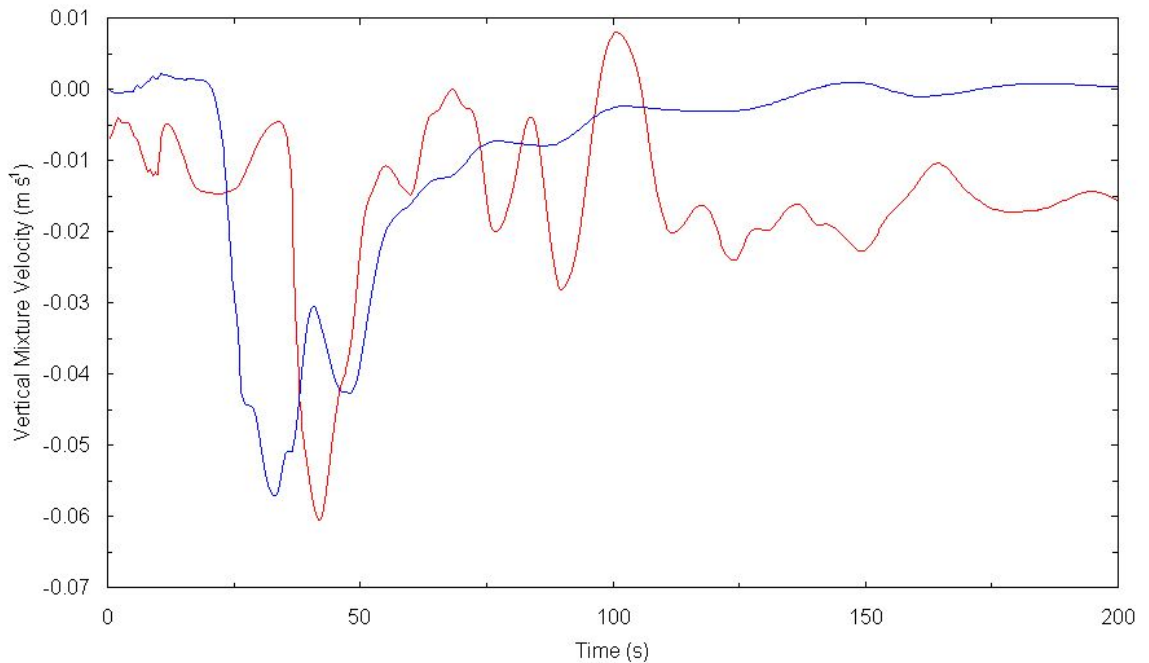


Figure 37: Time series of the vertical mixture velocity ( $\text{m s}^{-1}$ ) for solid-liquid flow; At 2.5 mesh widths on the column centreline recorded velocities for: Red: Scalar transport equation represents the solid phase volume fraction; Blue: Algebraic slip mixture model<sup>9</sup>;

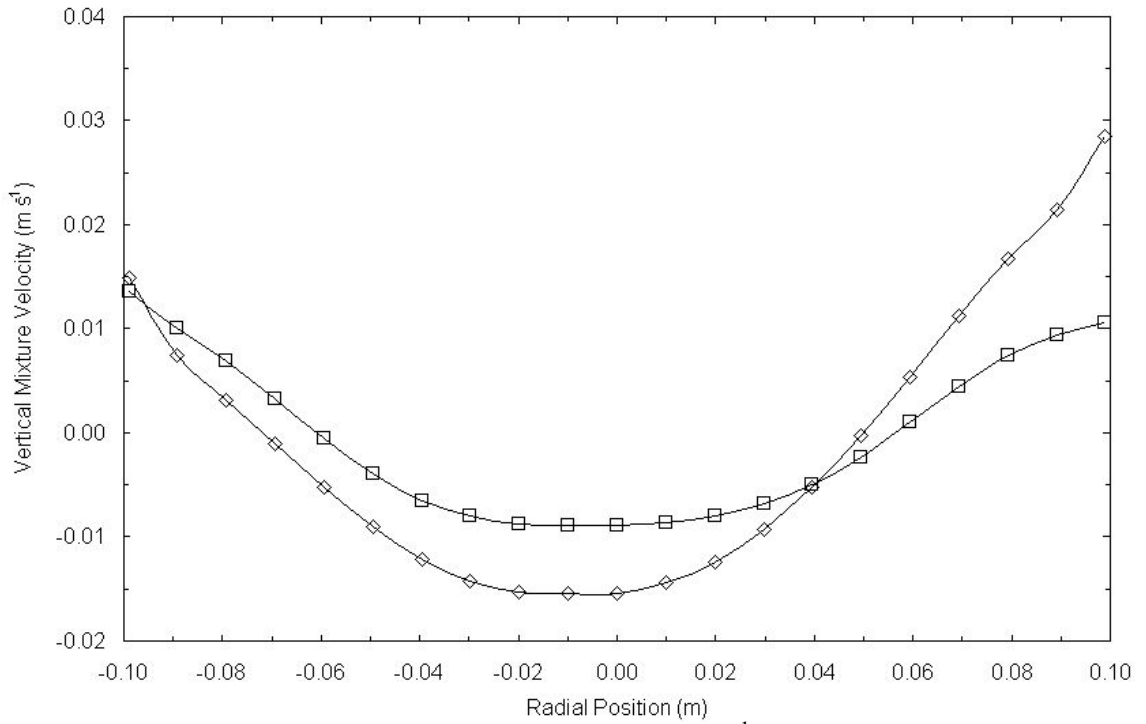


Figure 38: Profile plots of the vertical mixture velocity ( $\text{m s}^{-1}$ ) for solid-liquid flow; At a height of 2.5 mesh widths; ◇: Scalar transport equation represents the solid phase volume fraction; □: Algebraic slip mixture model<sup>9</sup>;

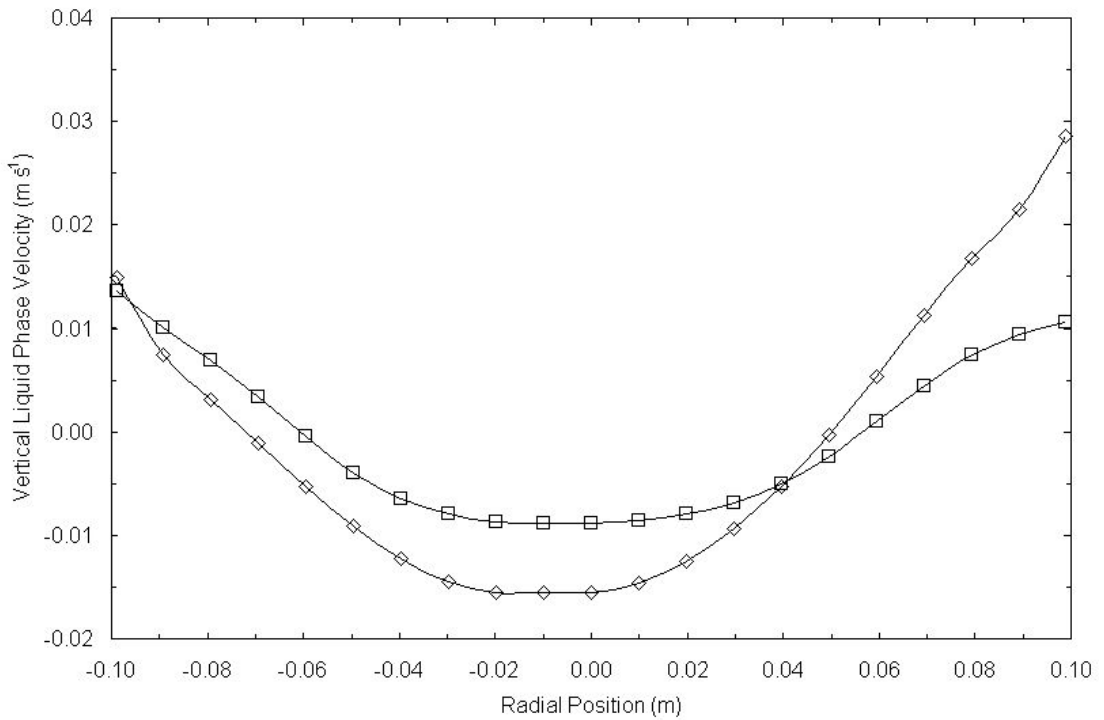


Figure 39: Profile plots of the vertical liquid phase velocity ( $\text{m s}^{-1}$ ) for solid-liquid flow; At a height of 2.5 mesh widths; ◇: Scalar transport equation representing the solid phase volume fraction; □: Algebraic slip mixture model<sup>9</sup>;

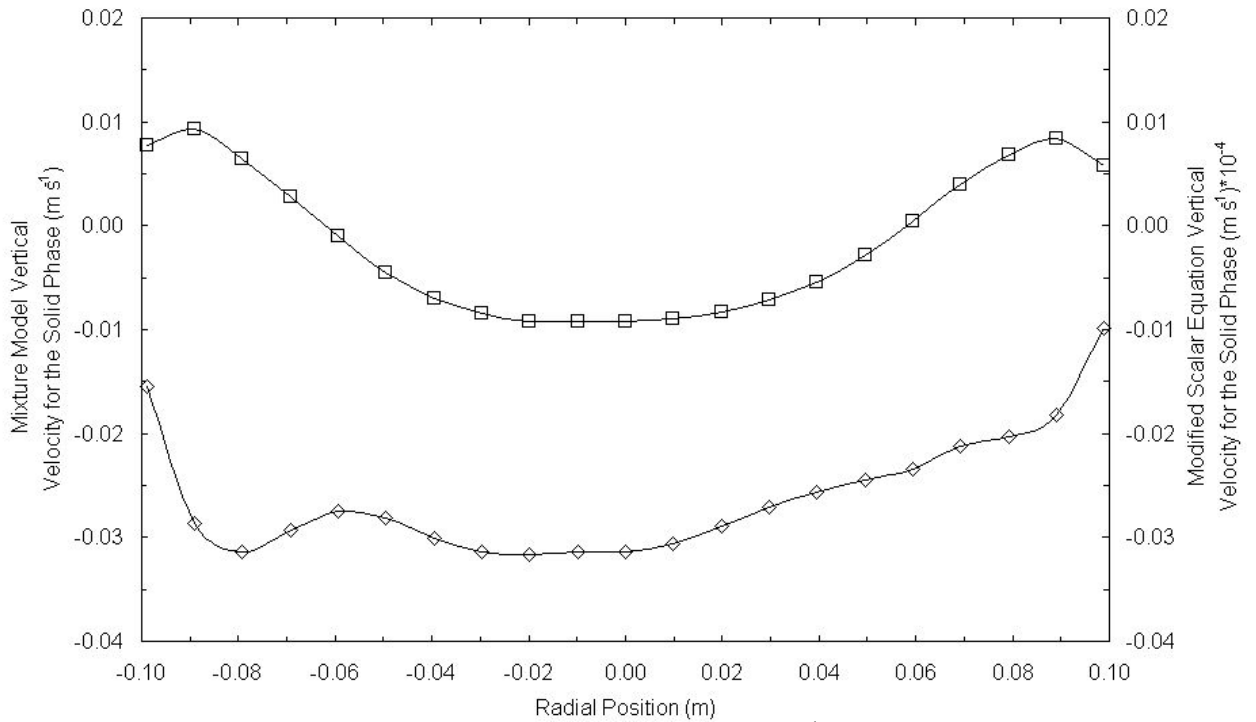


Figure 40: Profile plots of the vertical solid phase velocity ( $\text{m s}^{-1}$ ) for solid-liquid flow; At a height of 2.5 mesh widths;  $\diamond$ : Scalar transport equation representing the solid phase volume fraction;  $\square$ : Algebraic slip mixture model<sup>9</sup>;

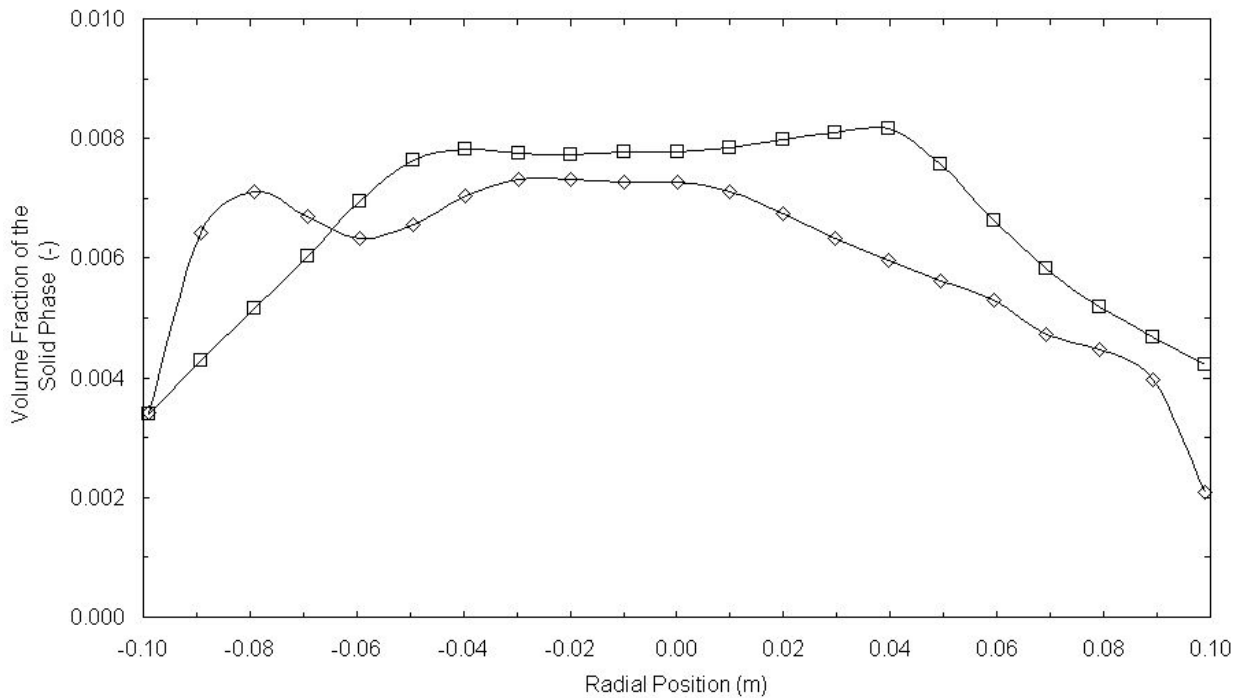


Figure 41: Profile plots of the solid phase volume fraction (-) for solid-liquid flow; At a height of 2.5 mesh widths;  $\diamond$ : Scalar transport equation representing the solid phase volume fraction;  $\square$ : Algebraic slip mixture model<sup>9</sup>;

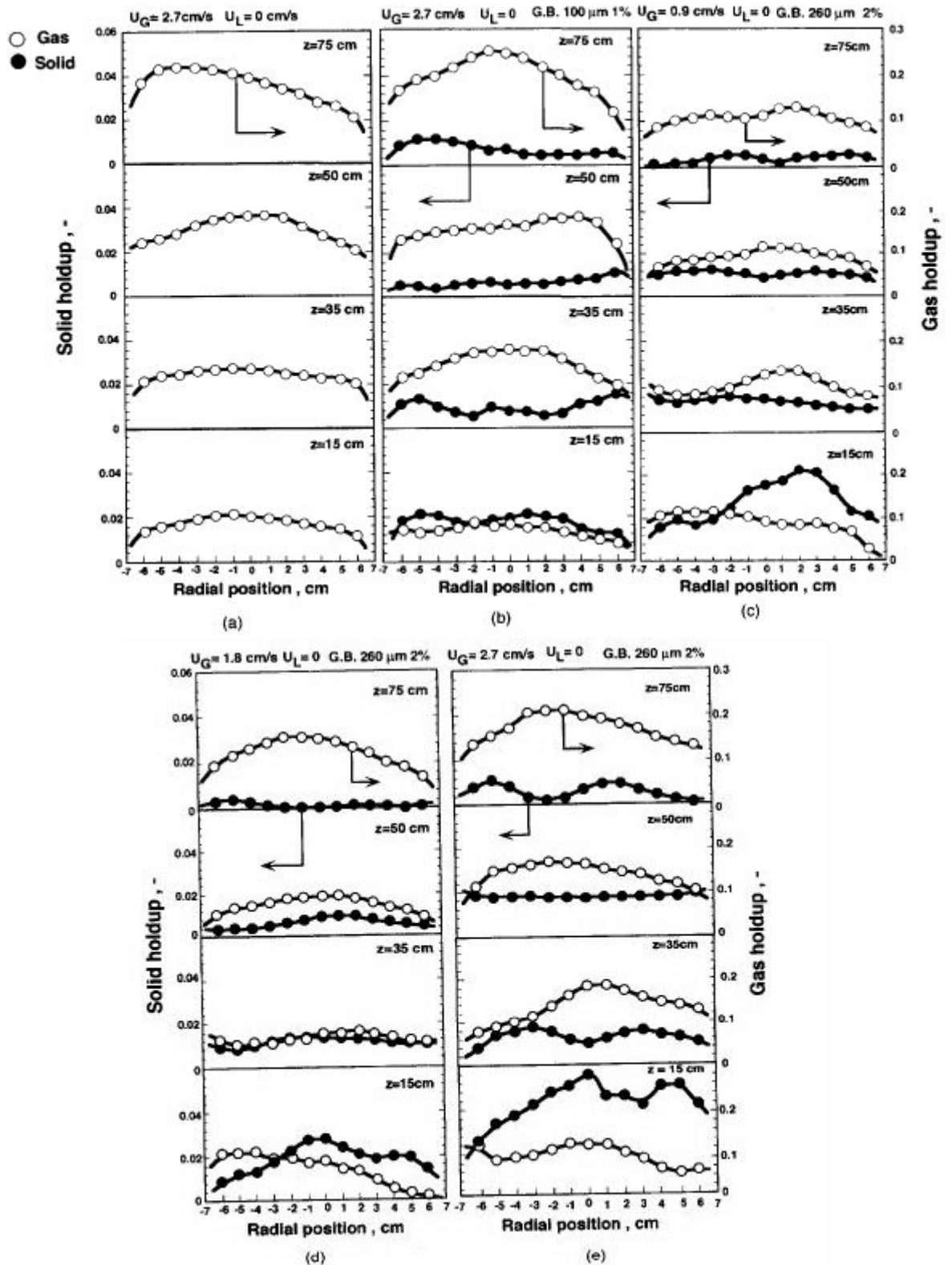


Figure 42: Experimental gas and solid phase extracted from Warsito<sup>56</sup>. Chart B describes the solid holdup for a similarly size particle to the particles used in the scalar transport and algebraic slip mixture models<sup>9</sup> found in Figure 41.

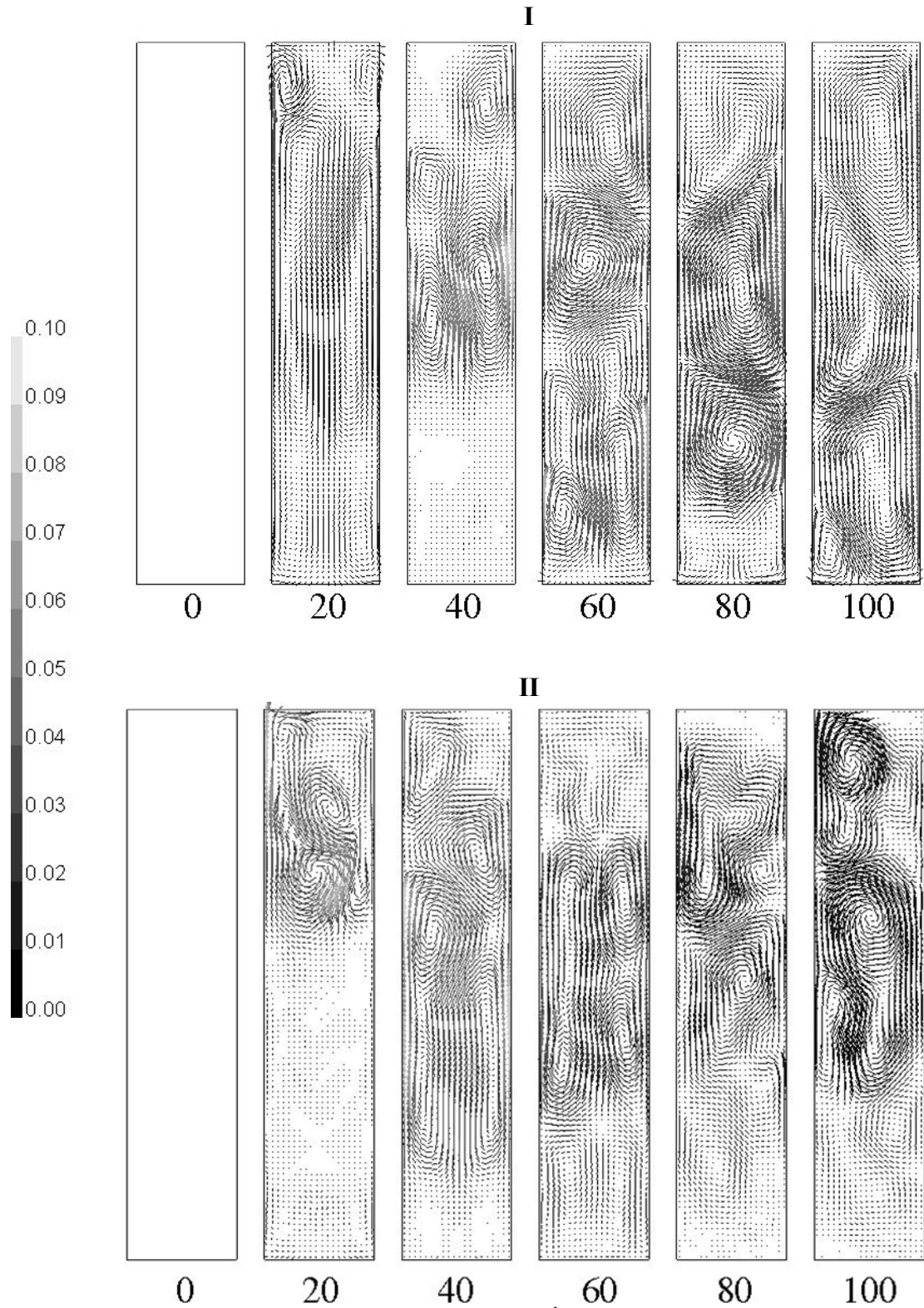


Figure 43: Vectors of mixture velocity magnitude ( $\text{m s}^{-1}$ ) for solid-liquid flow; Between 0 and 100 seconds of time for the **I**: modified-scalar equation; **II**: standard mixture model<sup>9</sup>;

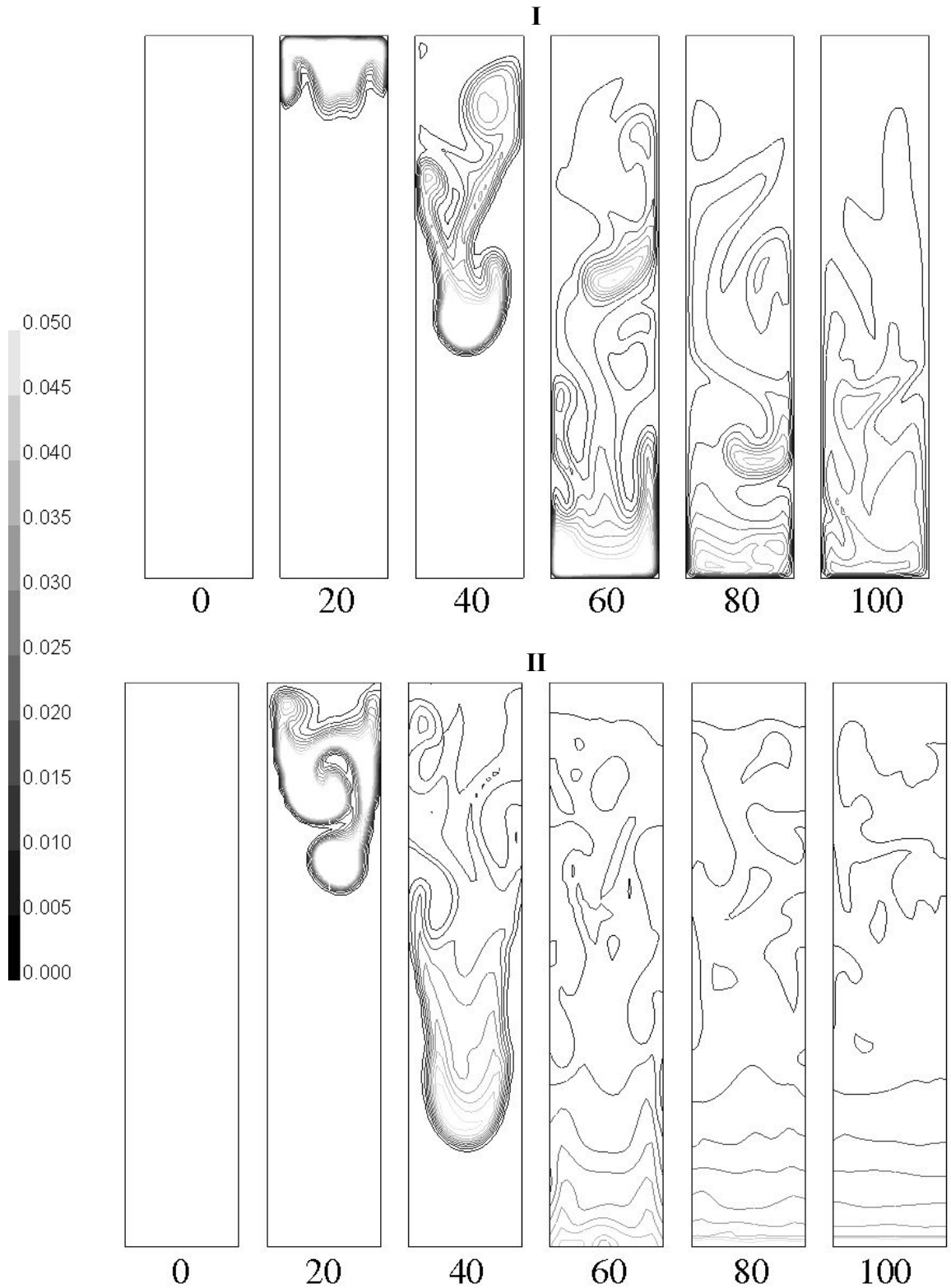


Figure 44: Contours of solid phase volume fraction (-) for solid-liquid flow; Between 0 and 100 seconds of time for the **I**: modified-scalar equation; **II**: standard mixture model<sup>9</sup>;

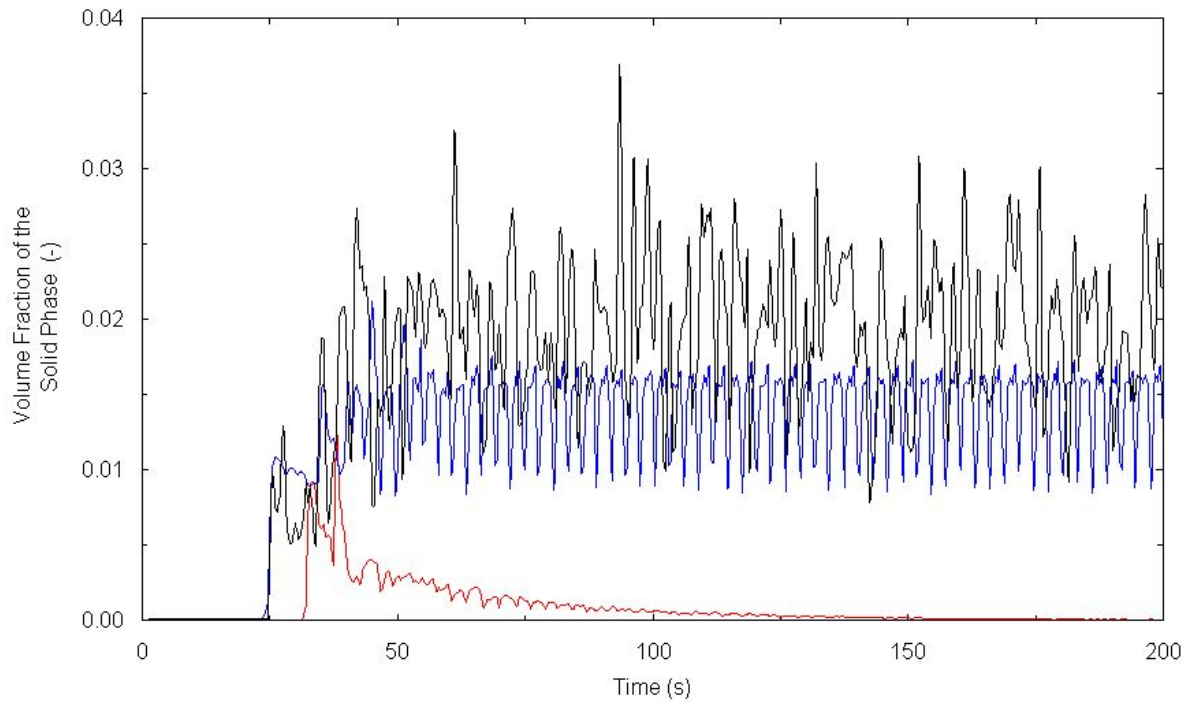


Figure 45: Time series of the solid phase volume fraction (-) for gas-liquid-solid flow; Red: GLS1; Blue: GLS2; Black: GLS3;

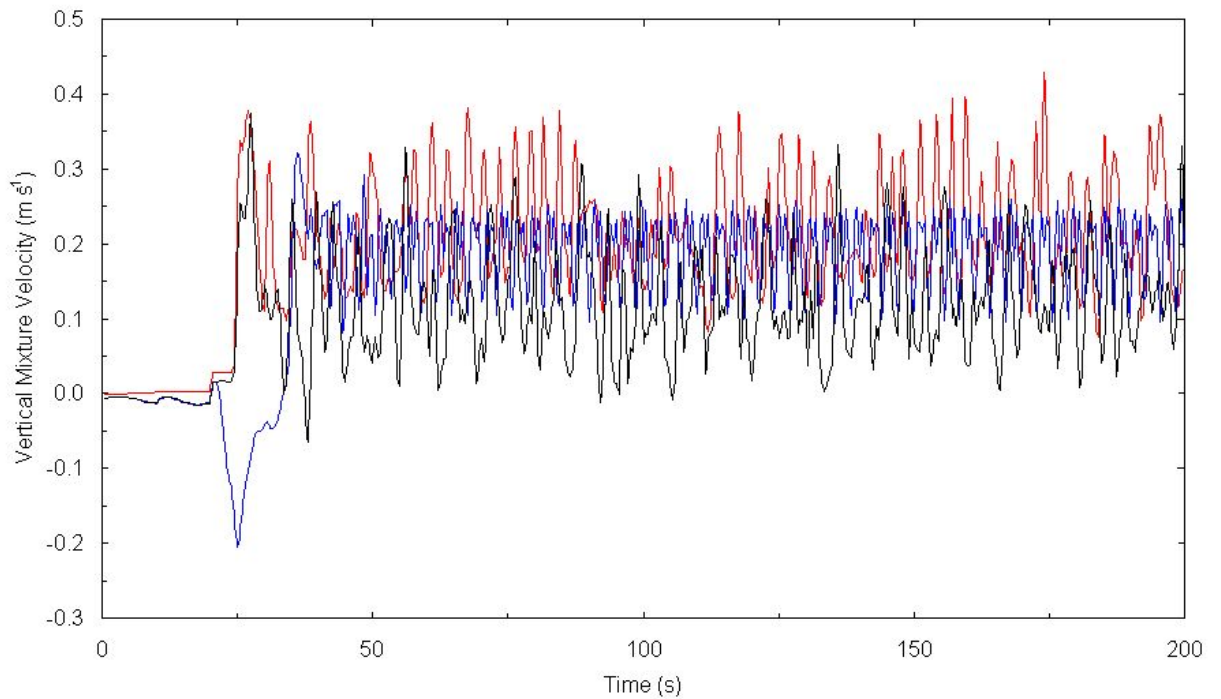


Figure 46: Time series of the vertical mixture velocity ( $\text{m s}^{-1}$ ) for gas-liquid-solid flow; Red: GLS1; Blue: GLS2; Black: GLS3;

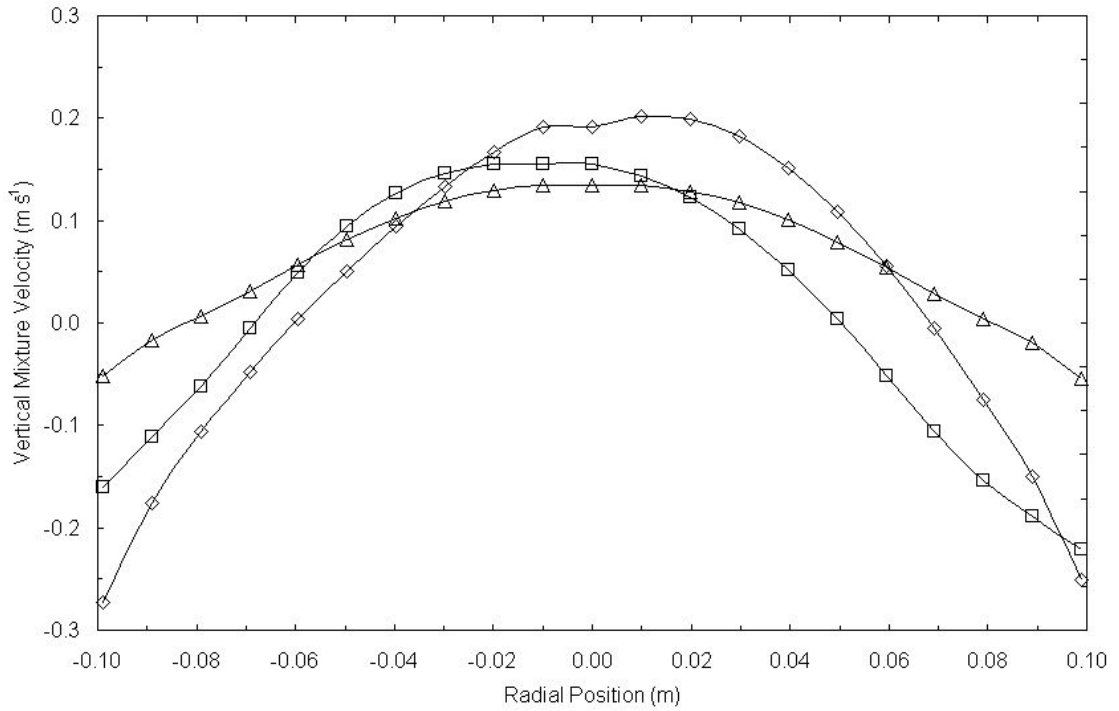


Figure 47: Profiles of the vertical mixture velocity ( $\text{m s}^{-1}$ ) for gas-liquid-solid flow;  
 ◇: GLS1; □: GLS2; △: GLS3;

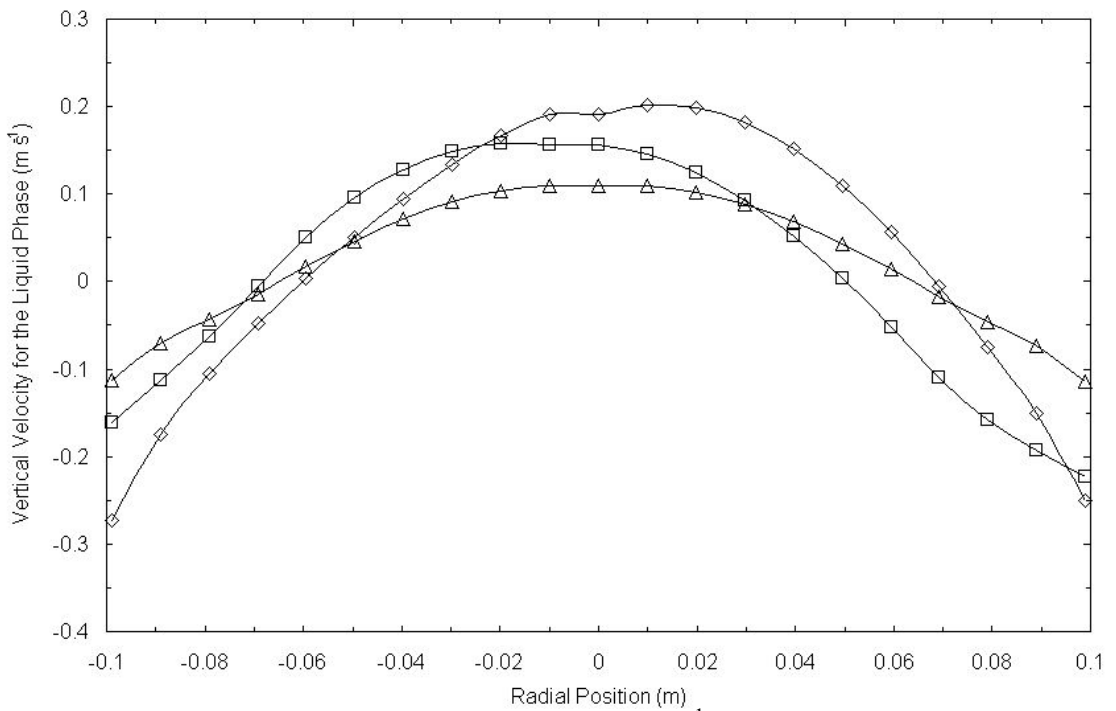


Figure 48: Profiles of liquid-phase vertical velocities ( $\text{m s}^{-1}$ ) for gas-liquid-solid flow;  
 ◇: GLS1; □: GLS2; △: GLS3;

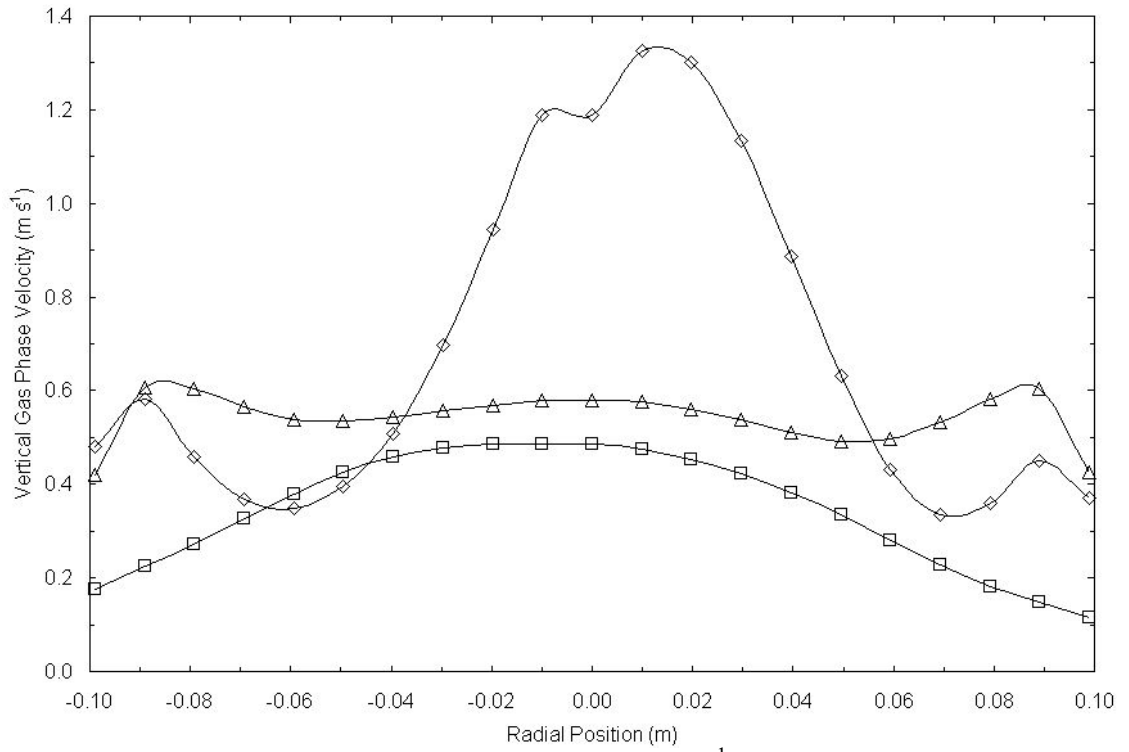


Figure 49: Profiles of the gas-phase vertical velocities ( $\text{m s}^{-1}$ ) for gas-liquid-solid flow;  $\diamond$ : GLS1;  $\square$ : GLS2;  $\triangle$ : GLS3;

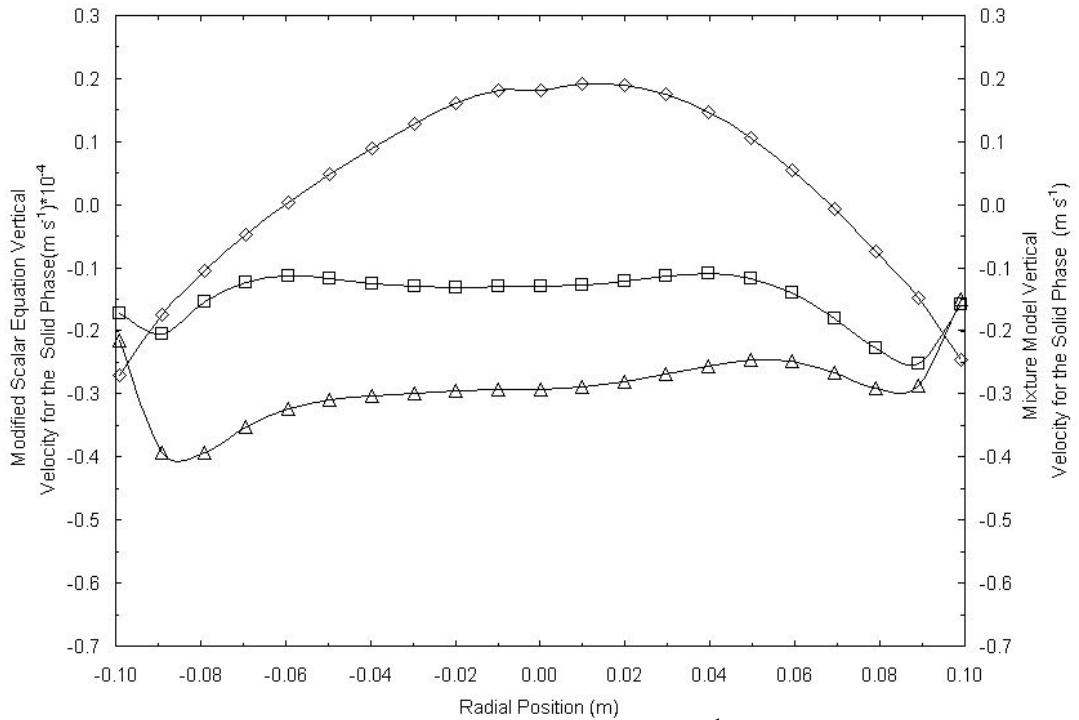


Figure 50: Profiles of the solid-phase vertical velocities ( $\text{m s}^{-1}$ ) for gas-liquid-solid flow;  $\diamond$ : GLS1;  $\square$ : GLS2;  $\triangle$ : GLS3;

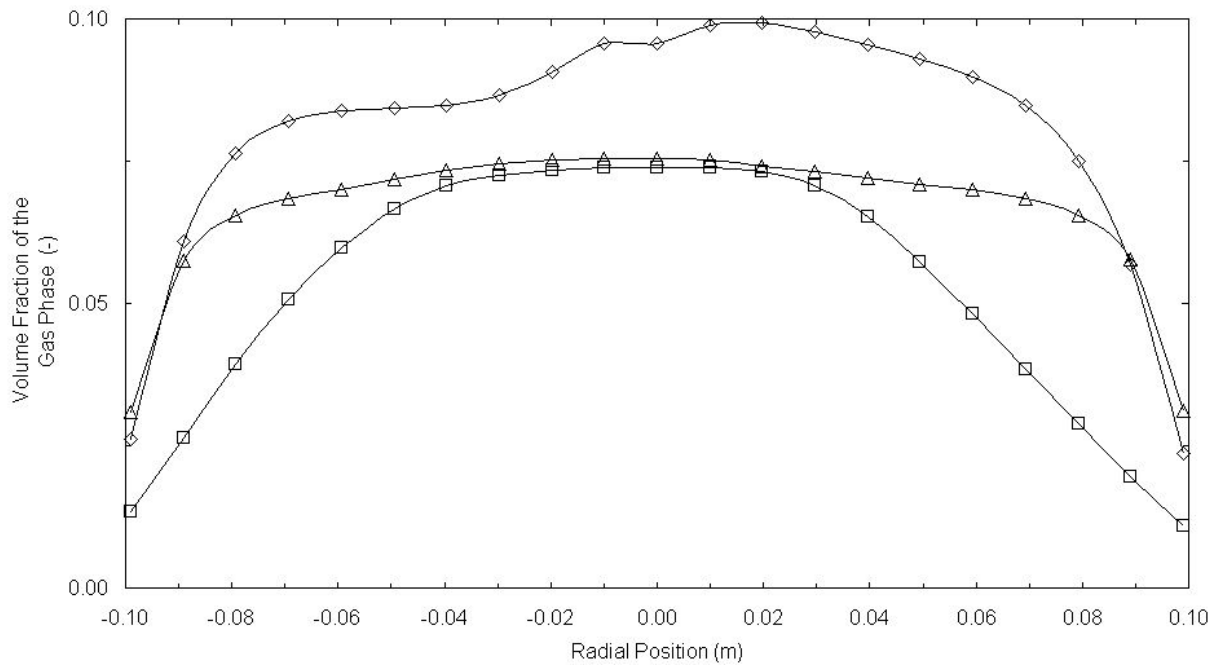


Figure 51: Profiles of the gas phase volume fraction (-) for gas-liquid-solid flow;  
 ◇: GLS1; □: GLS2; △: GLS3;

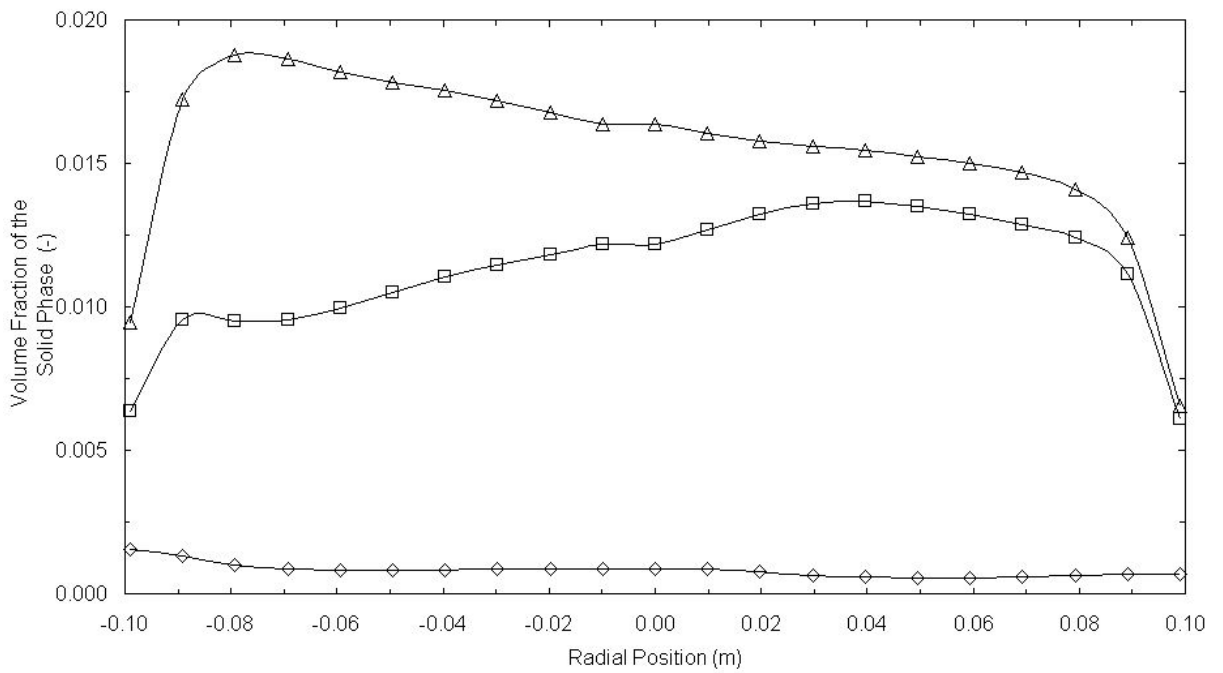


Figure 52: Profiles of the solid phase volume fraction (-) for gas-liquid-solid flow;  
 ◇: GLS1; □: GLS2; △: GLS3;

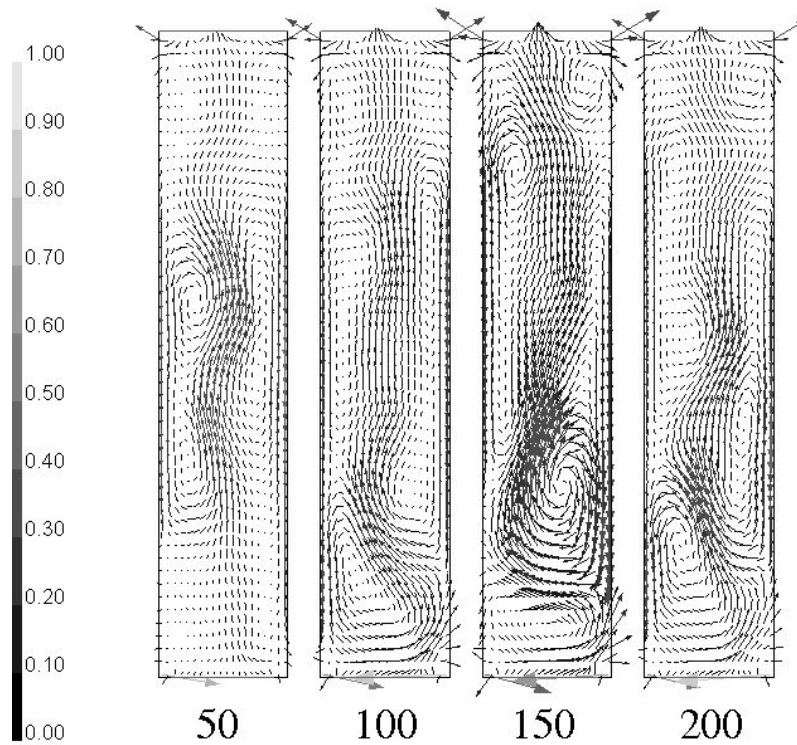


Figure 53: Vectors of mixture velocity magnitude ( $\text{m s}^{-1}$ ) for GLS1 gas-liquid-solid flow; The standard model<sup>9</sup> characterises the solid phase and the gas phase is represented modified scalar model for flow times between 50 and 200 seconds;

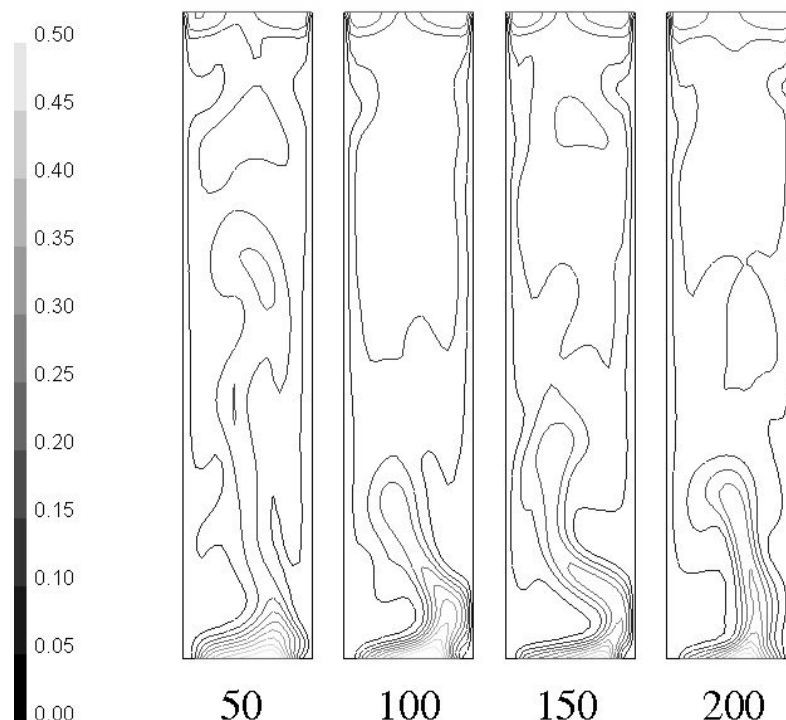


Figure 54: Contours of gas phase volume fraction (-) for GLS1 gas-liquid-solid flow; The standard model<sup>9</sup> characterises the solid phase and the gas phase is represented modified scalar model for flow times between 50 and 200 seconds;

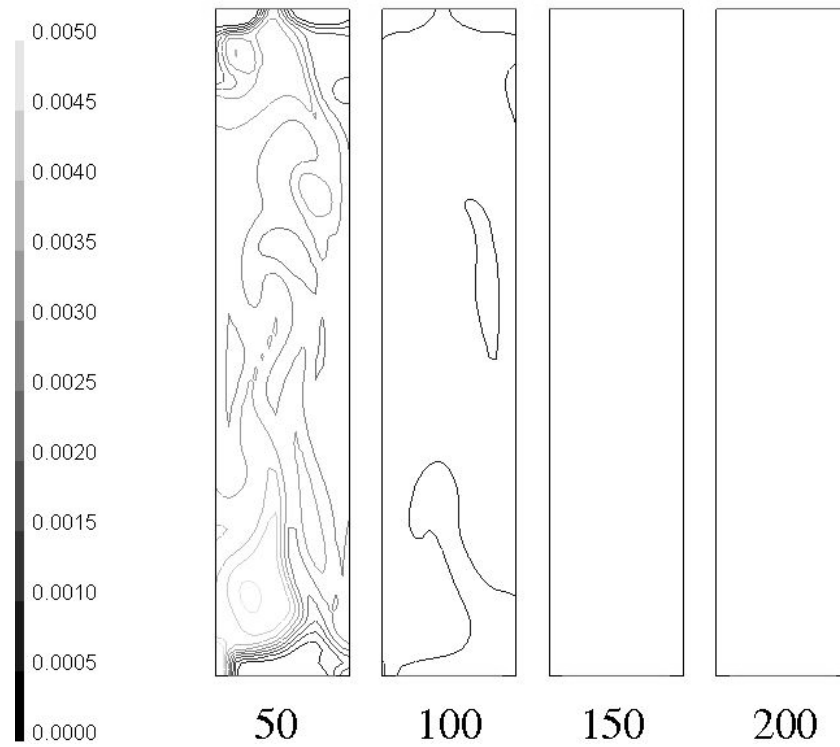


Figure 55: Contours of solid phase volume fraction (-) for GLS1 gas-liquid-solid flow; The standard model<sup>9</sup> characterises the solid phase and the gas phase is represented modified scalar model for flow times between 50 and 200 seconds;

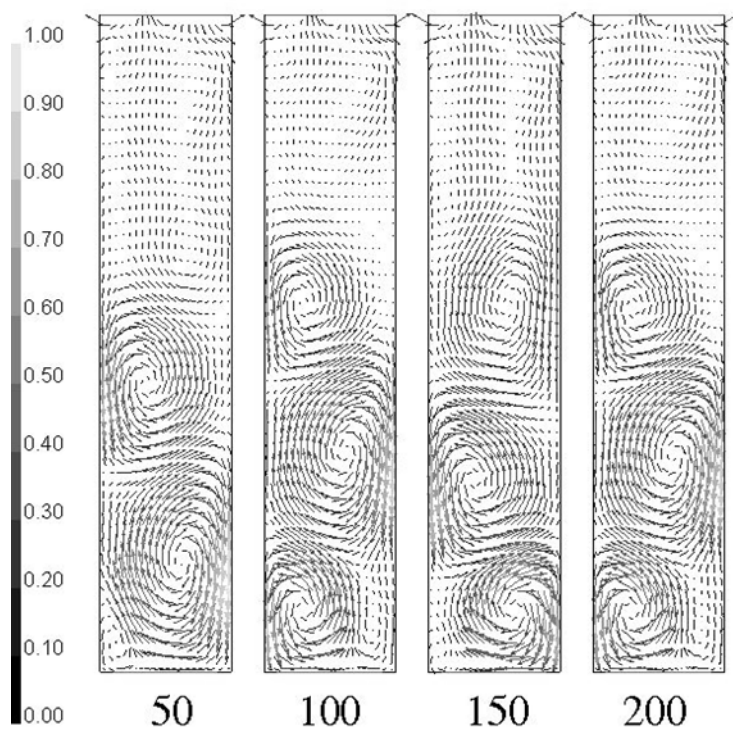


Figure 56: Vectors of mixture velocity magnitude ( $\text{m s}^{-1}$ ) for GLS2 gas-liquid-solid flow; The standard model<sup>9</sup> characterises the gas phase and the solid phase is represented modified scalar model for flow times between 50 and 200 seconds;

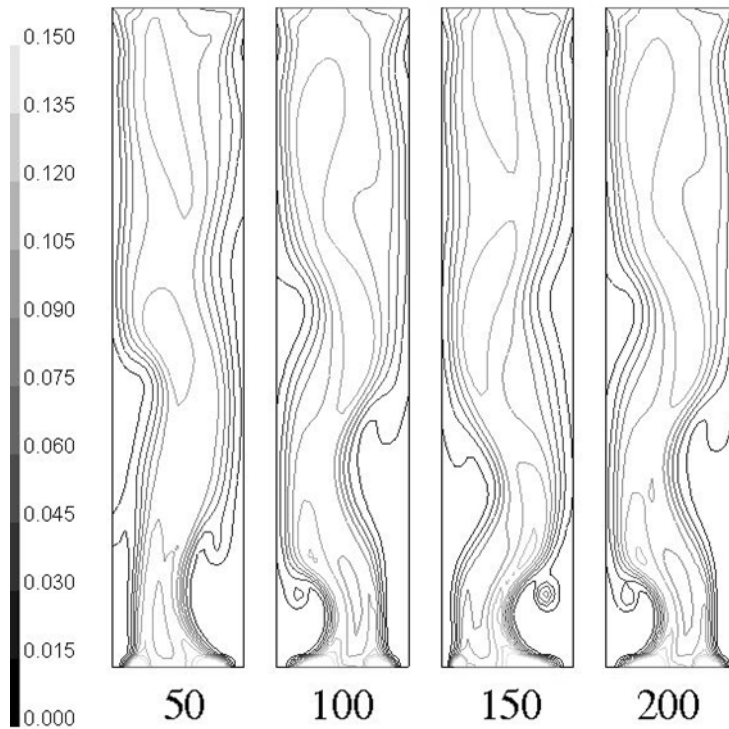


Figure 57: Contours of gas phase volume fraction (-) for GLS2 gas-liquid-solid flow; The standard model<sup>9</sup> characterises the gas phase and the solid phase is represented modified scalar model for flow times between 50 and 200 seconds;

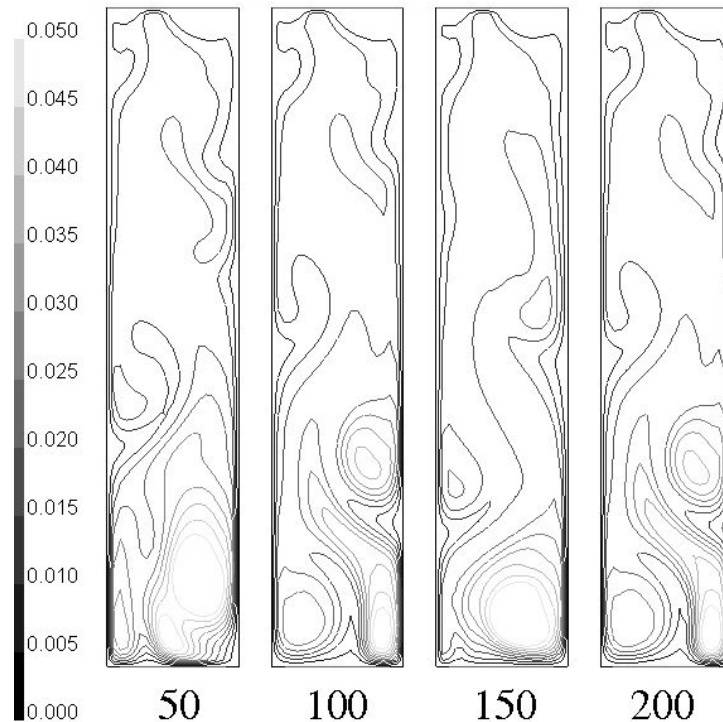


Figure 58: Contours of solid phase volume fraction (-) for GLS2 gas-liquid-solid flow; The standard model<sup>9</sup> characterises the gas phase and the solid phase is represented modified scalar model for flow times between 50 and 200 seconds;

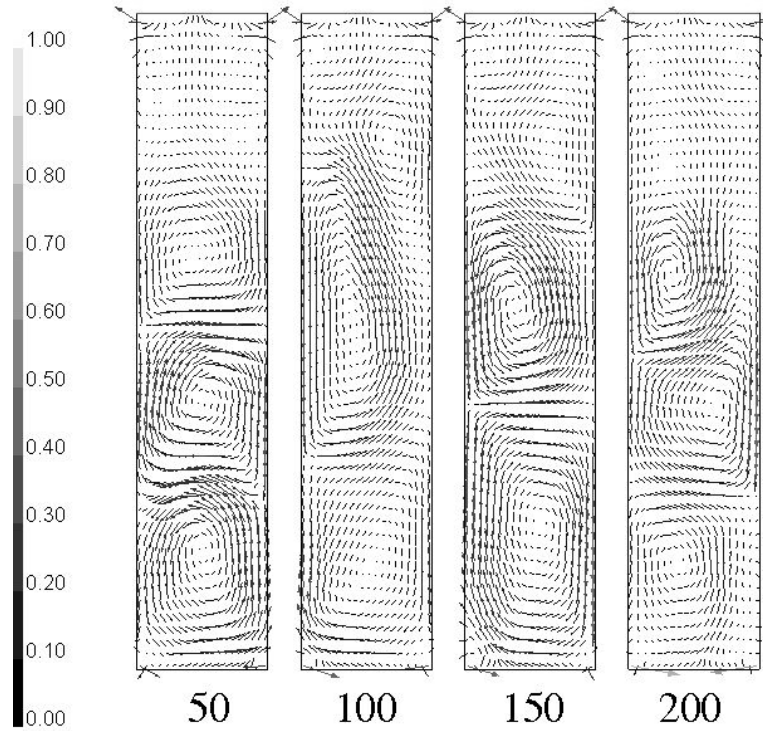


Figure 59: Vectors of mixture velocity magnitude ( $\text{m s}^{-1}$ ) for GLS3 gas-liquid-solid flow; Both discrete phases are modelled by a modified scalar equation for each phase between flow times of 50 and 200 seconds;

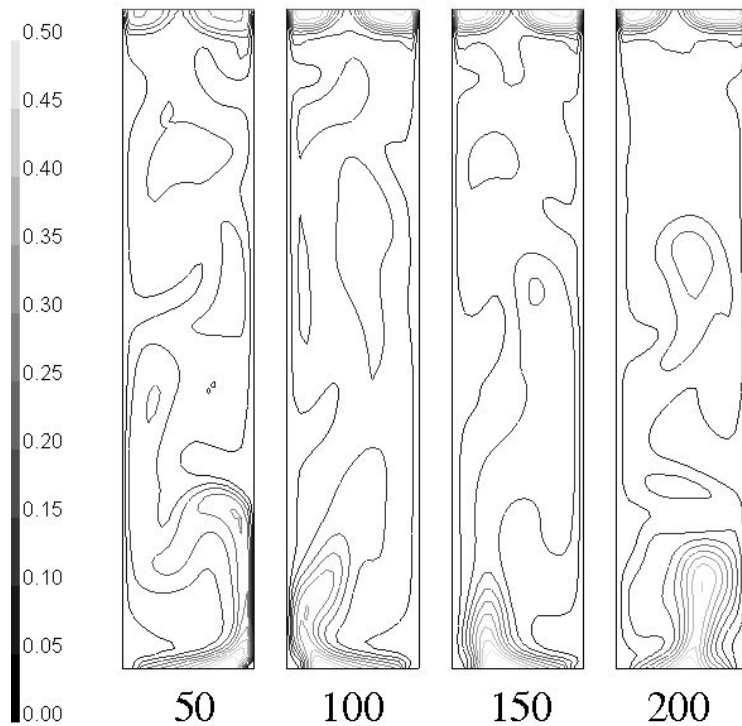


Figure 60: Contours of gas phase volume fraction (-) for GLS3 gas-liquid-solid flow; Both discrete phases are modelled by a modified scalar equation for each phase between flow times of 50 and 200 seconds;

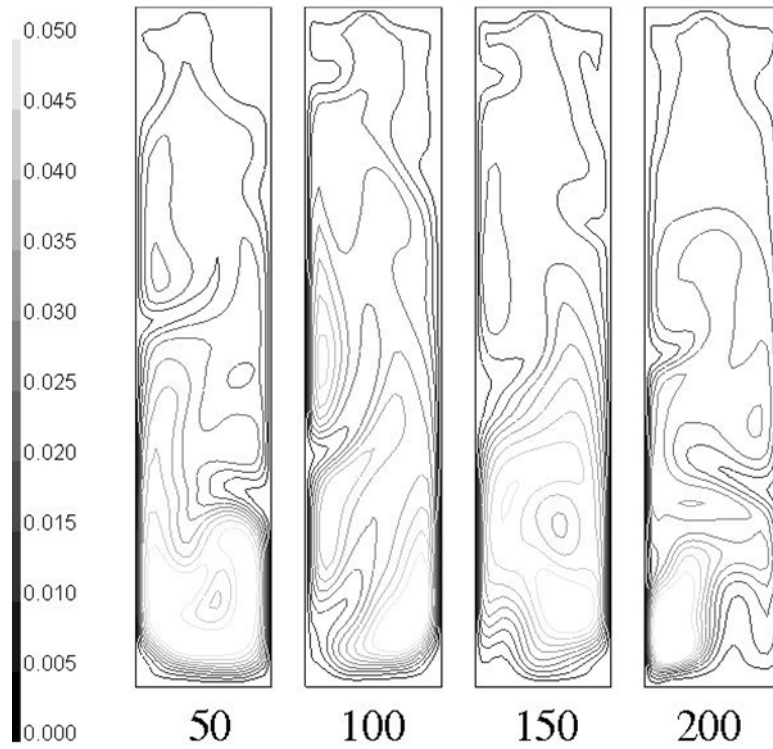


Figure 61: Contours of solid phase volume fraction (-) for GLS3 gas-liquid-solid flow; Both discrete phases are modelled by a modified scalar equation for each phase between flow times of 50 and 200 seconds;

## 13.4 Biochemical reaction results

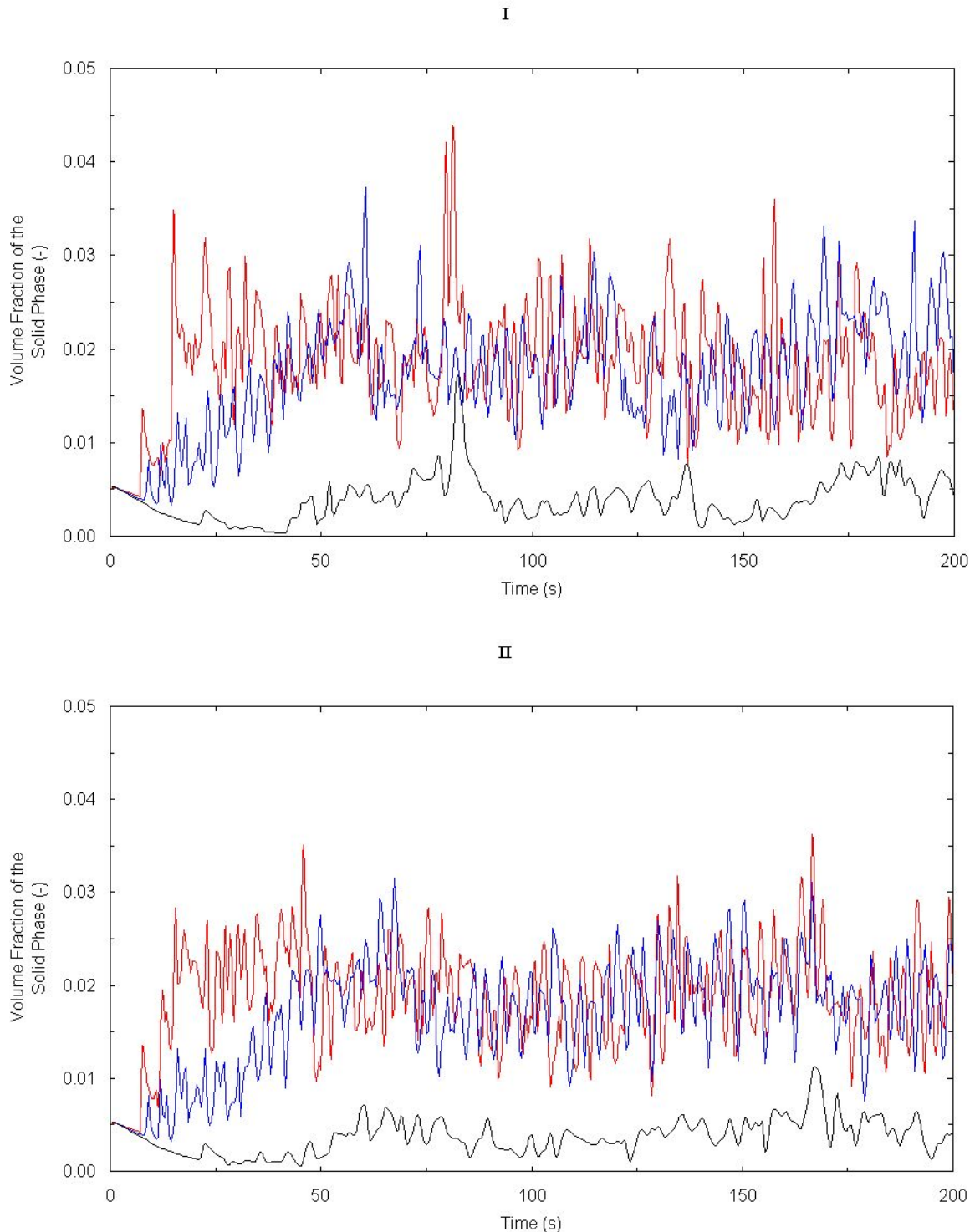


Figure 62: Time series for the volume fraction of the solid phase (-) for both gas-liquid-solid flow and reaction models;

**I:** specific growth rate was  $6.5 \cdot 10^{-5} \text{ s}^{-1}$ ; **II:** specific growth rate was  $1.52 \cdot 10^{-4} \text{ s}^{-1}$ ; Red: 5:1 height to diameter (H/D) ratio column; Blue: 20:1 H/D ratio column at a height of 2.5 column diameters; Black: 20:1 H/D ratio column at a height of 10 column diameters;

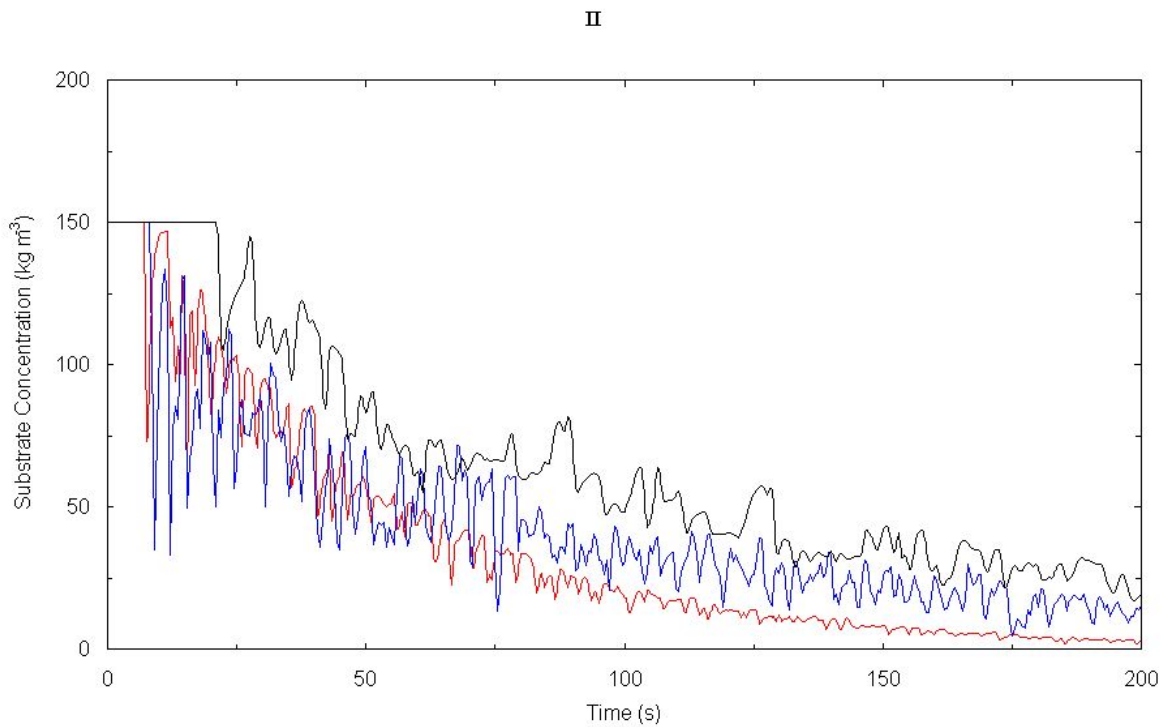
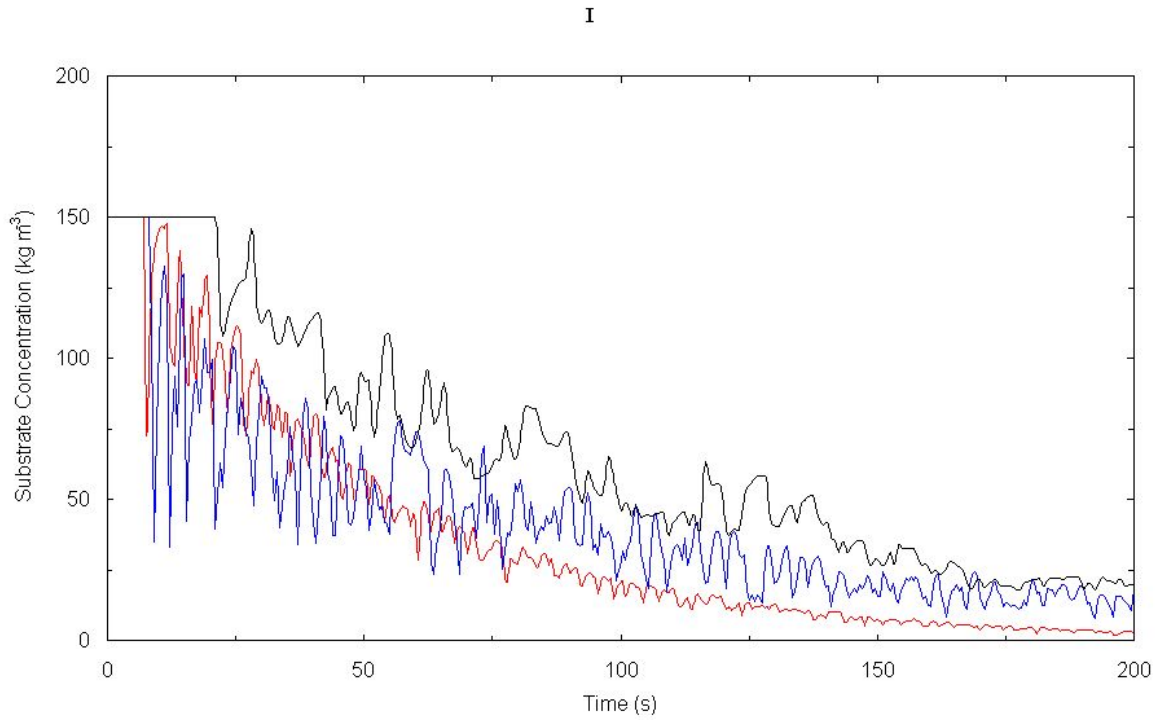


Figure 63: Time series for the substrate concentration ( $\text{kg m}^{-3}$ ) for both gas-liquid-solid flow and reaction models;

**I**: specific growth rate was  $6.5 \cdot 10^{-5} \text{ s}^{-1}$ ; **II**: specific growth rate was  $1.52 \cdot 10^{-4} \text{ s}^{-1}$ ; Red: 5:1 height to diameter (H/D) ratio column; Blue: 20:1 H/D ratio column at a height of 2.5 column diameters; Black: 20:1 H/D ratio column at a height of 10 column diameters;

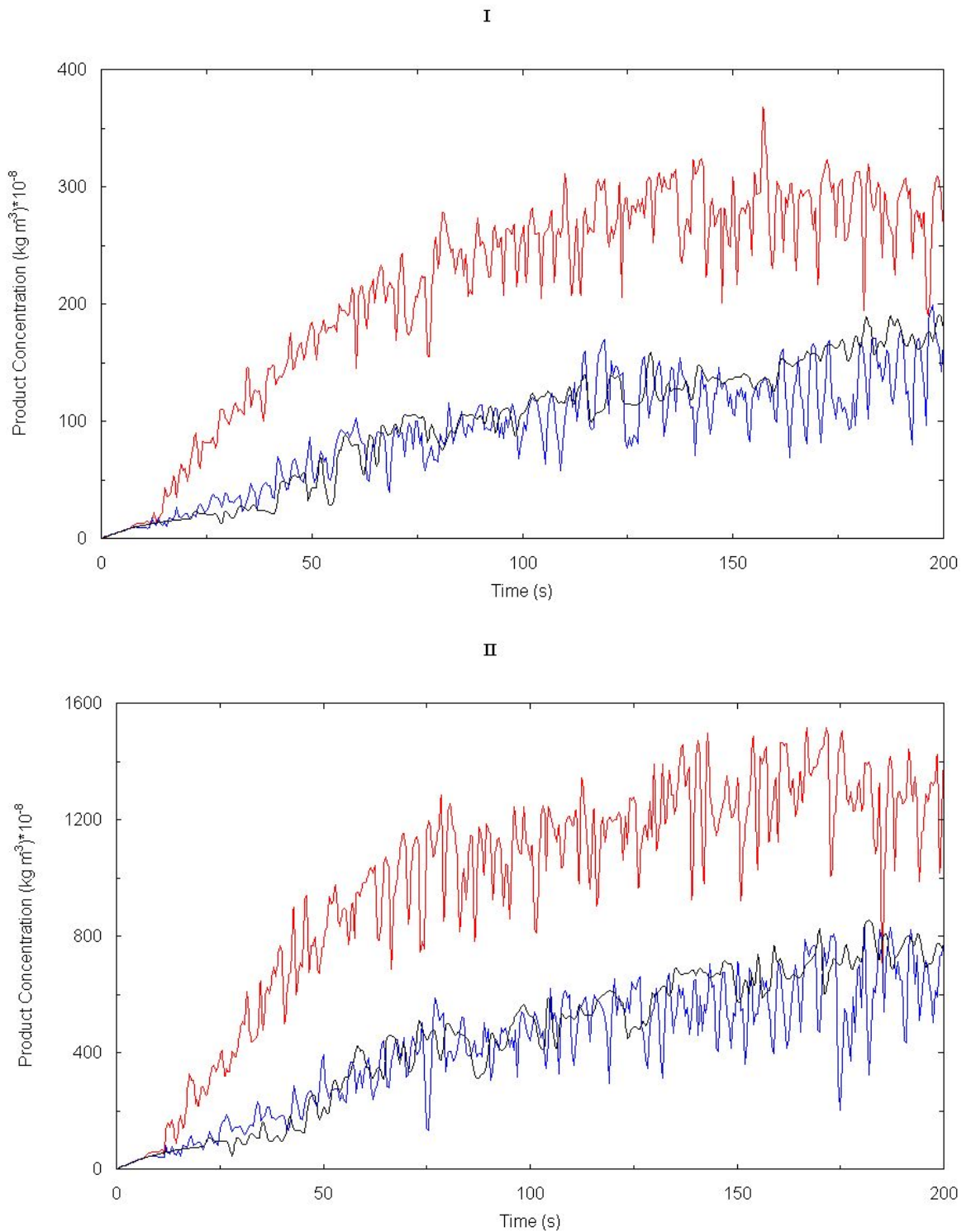


Figure 64: Time series for the product concentration ( $\text{kg m}^{-3}$ ) for both gas-liquid-solid flow and reaction models;

**I**: specific growth rate was  $6.5 \cdot 10^{-5} \text{ s}^{-1}$ ; **II**: specific growth rate was  $1.52 \cdot 10^{-4} \text{ s}^{-1}$ ; Red: 5:1 height to diameter (H/D) ratio column; Blue: 20:1 H/D ratio column at a height of 2.5 column diameters; Black: 20:1 H/D ratio column at a height of 10 column diameters;

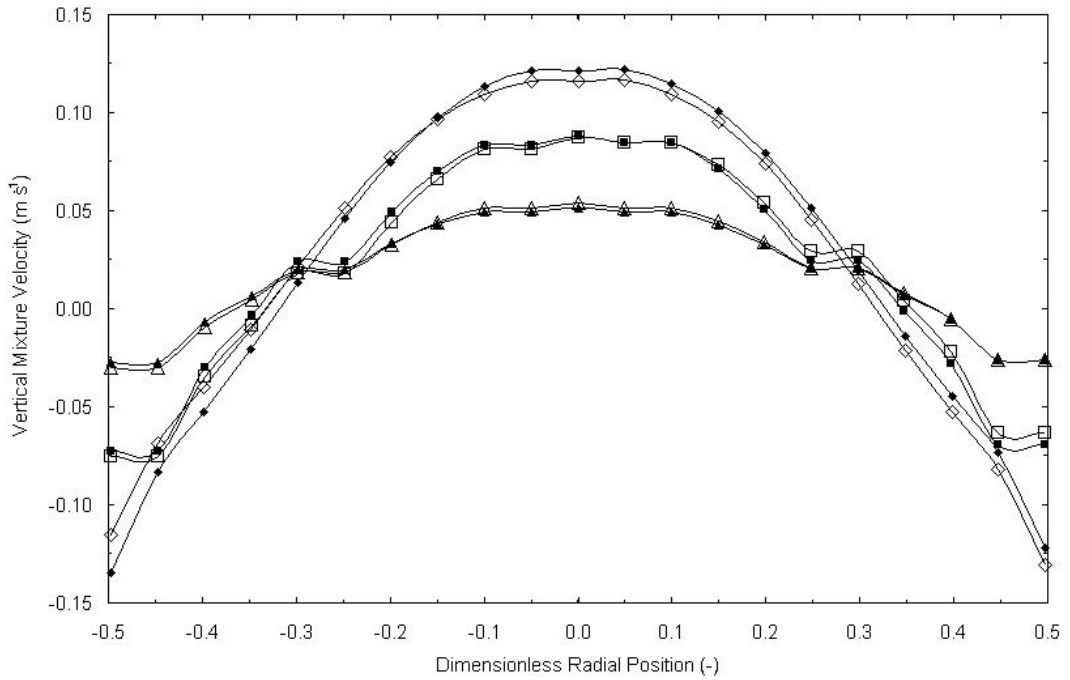


Figure 65: Profiles of vertical mixture velocity ( $\text{m s}^{-1}$ ) for both gas-liquid-solid flow and reaction models;  
 Specific growth rate was  $6.5 \cdot 10^{-5} \text{ s}^{-1}$  for the open markers and  $1.52 \cdot 10^{-4} \text{ s}^{-1}$  for the closed markers;  $\diamond, \blacklozenge$ : 5:1 height to diameter (H/D) ratio column;  $\square, \blacksquare$ : 20:1 H/D ratio column at a height of 2.5 column diameters;  $\triangle, \blacktriangle$ : 20:1 H/D ratio column at a height of 10 column diameters;

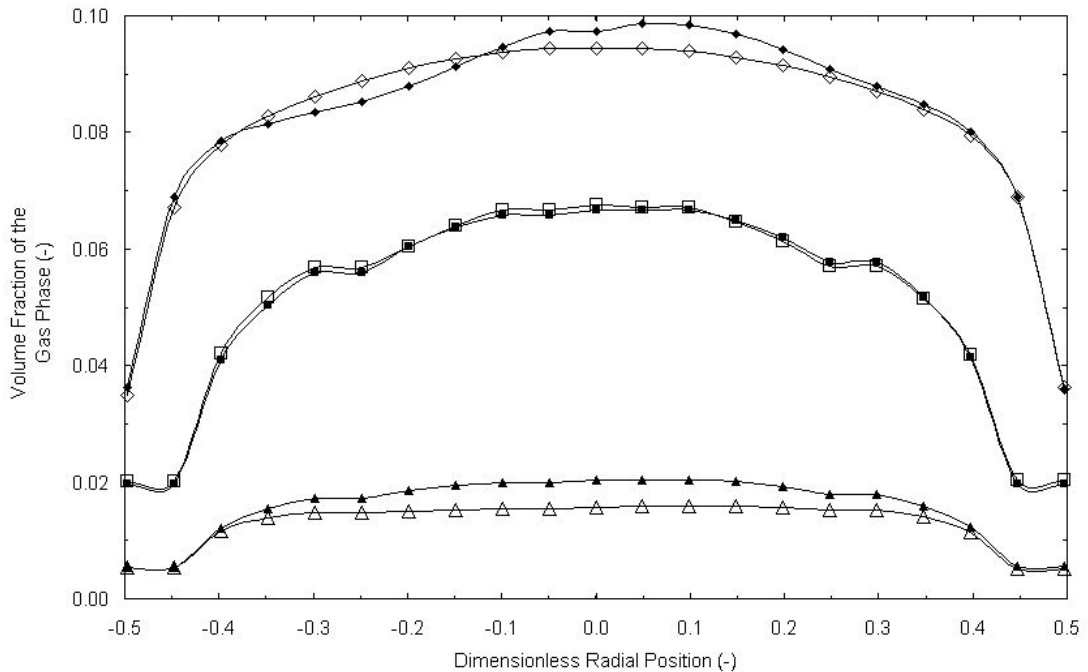


Figure 66: Profiles of volume fraction of the gas phase (-) for both gas-liquid-solid flow and reaction models;  
 Specific growth rate was  $6.5 \cdot 10^{-5} \text{ s}^{-1}$  for the open markers and  $1.52 \cdot 10^{-4} \text{ s}^{-1}$  for the closed markers;  $\diamond, \blacklozenge$ : 5:1 height to diameter (H/D) ratio column;  $\square, \blacksquare$ : 20:1 H/D ratio column at a height of 2.5 column diameters;  $\triangle, \blacktriangle$ : 20:1 H/D ratio column at a height of 10 column diameters;

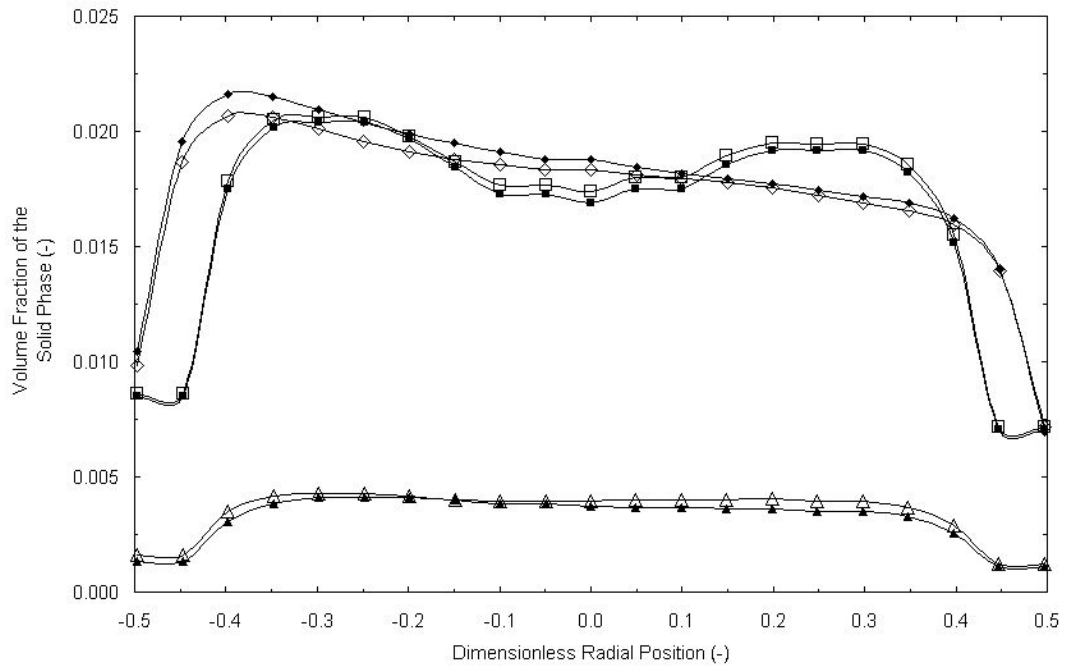


Figure 67: Profiles of volume fraction of the solid phase (-) for both gas-liquid-solid flow and reaction models;

Specific growth rate was  $6.5 \cdot 10^{-5} \text{ s}^{-1}$  for the open markers and  $1.52 \cdot 10^{-4} \text{ s}^{-1}$  for the closed markers;  $\diamond, \blacklozenge$ : 5:1 height to diameter (H/D) ratio column;  $\square, \blacksquare$ : 20:1 H/D ratio column at a height of 2.5 column diameters;  $\triangle, \blacktriangle$ : 20:1 H/D ratio column at a height of 10 column diameters;

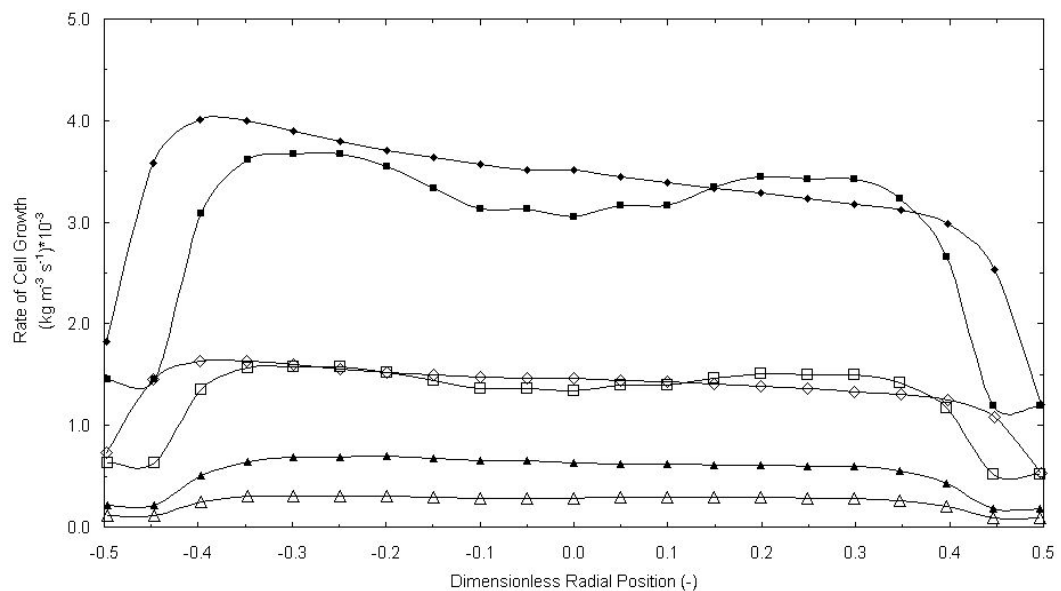


Figure 68: Profiles of cell growth rate ( $\text{kg m}^{-3} \text{ s}^{-1}$ ) for both gas-liquid-solid flow and reaction models;

Specific growth rate was  $6.5 \cdot 10^{-5} \text{ s}^{-1}$  for the open markers and  $1.52 \cdot 10^{-4} \text{ s}^{-1}$  for the closed markers;  $\diamond, \blacklozenge$ : 5:1 height to diameter (H/D) ratio column;  $\square, \blacksquare$ : 20:1 H/D ratio column at a height of 2.5 column diameters;  $\triangle, \blacktriangle$ : 20:1 H/D ratio column at a height of 10 column diameters;

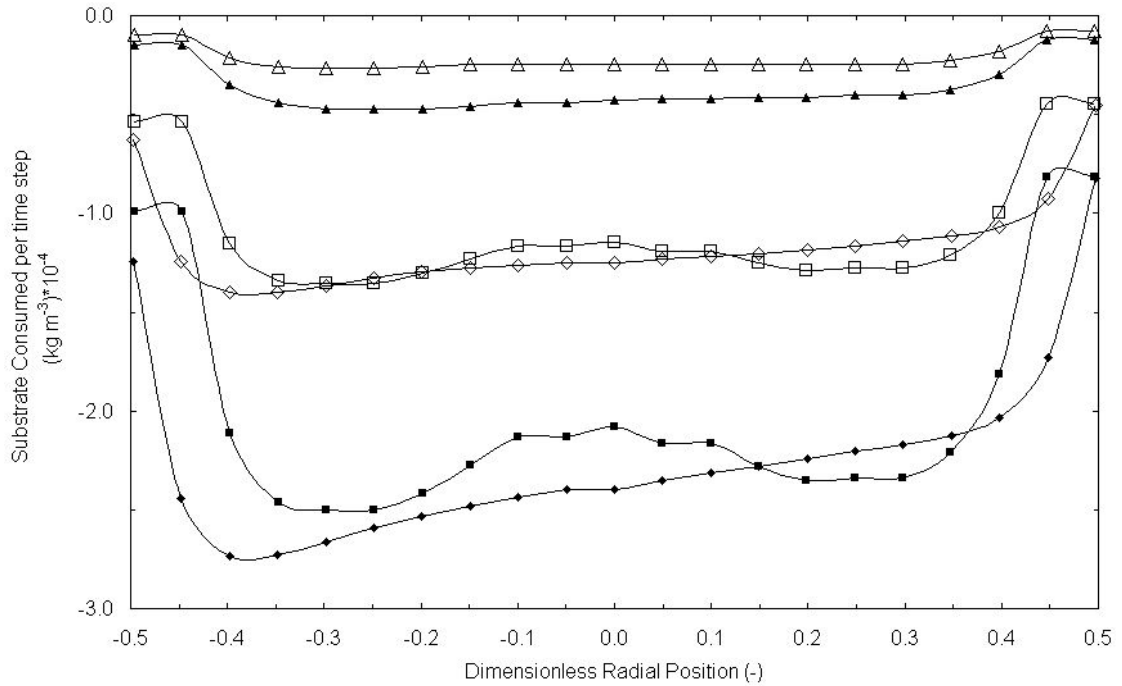


Figure 69: Profiles of substrate consumed per time step ( $\text{kg m}^{-3}$ ) for both gas-liquid-solid flow and reaction models;  
 Specific growth rate was  $6.5 \cdot 10^{-5} \text{ s}^{-1}$  for the open markers and  $1.52 \cdot 10^{-4} \text{ s}^{-1}$  for the closed markers;  $\diamond, \blacklozenge$ : 5:1 height to diameter (H/D) ratio column;  $\square, \blacksquare$ : 20:1 H/D ratio column at a height of 2.5 column diameters;  $\triangle, \blacktriangle$ : 20:1 H/D ratio column at a height of 10 column diameters;

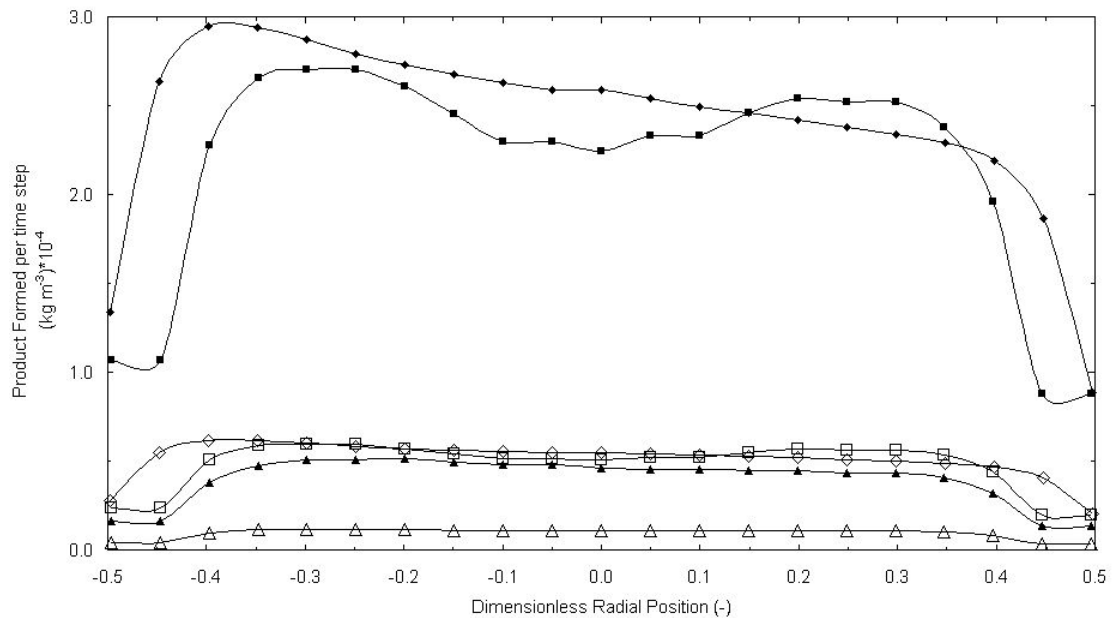


Figure 70: Profiles of product formed per time step ( $\text{kg m}^{-3}$ ) for both gas-liquid-solid flow and reaction models;  
 Specific growth rate was  $6.5 \cdot 10^{-5} \text{ s}^{-1}$  for the open markers and  $1.52 \cdot 10^{-4} \text{ s}^{-1}$  for the closed markers;  $\diamond, \blacklozenge$ : 5:1 height to diameter (H/D) ratio column;  $\square, \blacksquare$ : 20:1 H/D ratio column at a height of 2.5 column diameters;  $\triangle, \blacktriangle$ : 20:1 H/D ratio column at a height of 10 column diameters;

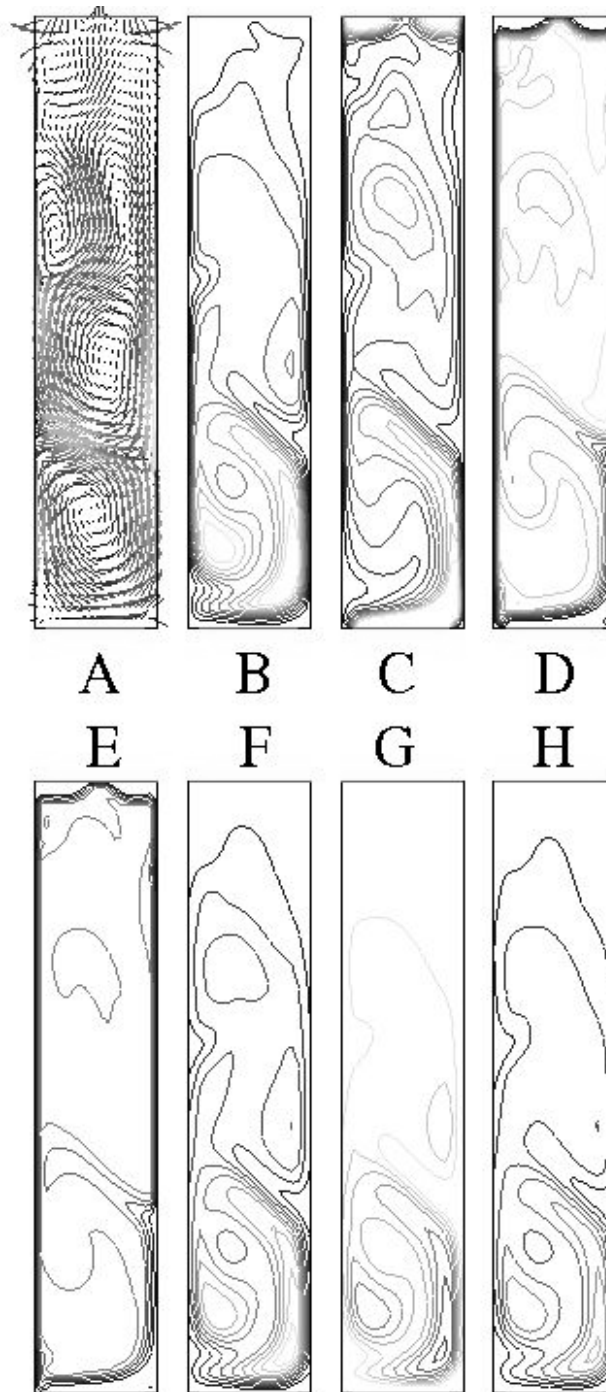


Figure 71: Fields of the gas-liquid-solid flow and reaction models for the 5:1 bubble column after 100 s, where  $\lambda=6.5 \cdot 10^{-5} \text{ s}^{-1}$ ;

A: Velocity vectors between 0 (small) and  $0.5 \text{ m s}^{-1}$  (large); B: Contours of the volume fraction of the solid phase (-) between 0 (black) and 0.05 (light grey); C: Contours of the volume fraction of the gas phase (-) between 0 (black) and 0.25 (light grey); D: Contours of the substrate concentration between 0 (black) and  $25 \text{ kg m}^{-3}$  (light grey); E: Contours of the product concentration between 0 (black) and  $5 \cdot 10^{-6} \text{ kg m}^{-3}$  (light grey); F: Contours of the cells grown between 0 (black) and  $5 \cdot 10^{-3} \text{ kg m}^{-3}$  (light grey); G: Contours of the substrate consumed between  $-5 \cdot 10^{-4}$  (black) and  $0 \text{ kg m}^{-3}$  (light grey); H: Contours of the product formed between 0 (black) and  $2.5 \cdot 10^{-4} \text{ kg m}^{-3}$  (light grey);

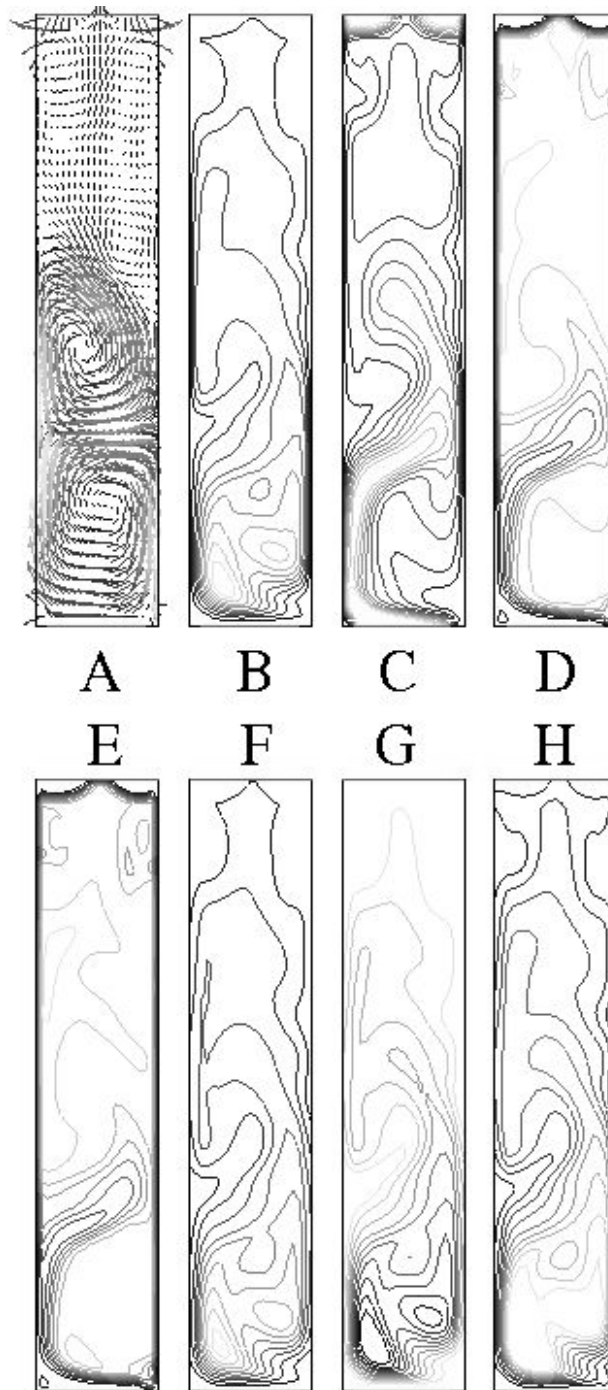


Figure 72: Fields of the gas-liquid-solid flow and reaction models for the 5:1 bubble column after 100 s, where  $\lambda=1.52 \cdot 10^{-4} \text{ s}^{-1}$ ;

A: Velocity vectors between 0 (small) and  $0.5 \text{ m s}^{-1}$  (large); B: Contours of the volume fraction of the solid phase (-) between 0 (black) and 0.05 (light grey); C: Contours of the volume fraction of the gas phase (-) between 0 (black) and 0.25 (light grey); D: Contours of the substrate concentration between 0 (black) and  $25 \text{ kg m}^{-3}$  (light grey); E: Contours of the product concentration between 0 (black) and  $1.5 \cdot 10^{-5} \text{ kg m}^{-3}$  (light grey); F: Contours of the cells grown between 0 (black) and  $1.5 \cdot 10^{-2} \text{ kg m}^{-3}$  (light grey); G: Contours of the substrate consumed between  $-5 \cdot 10^{-4}$  (black) and  $0 \text{ kg m}^{-3}$  (light grey); H: Contours of the product formed between 0 (black) and  $5 \cdot 10^{-4} \text{ kg m}^{-3}$  (light grey);

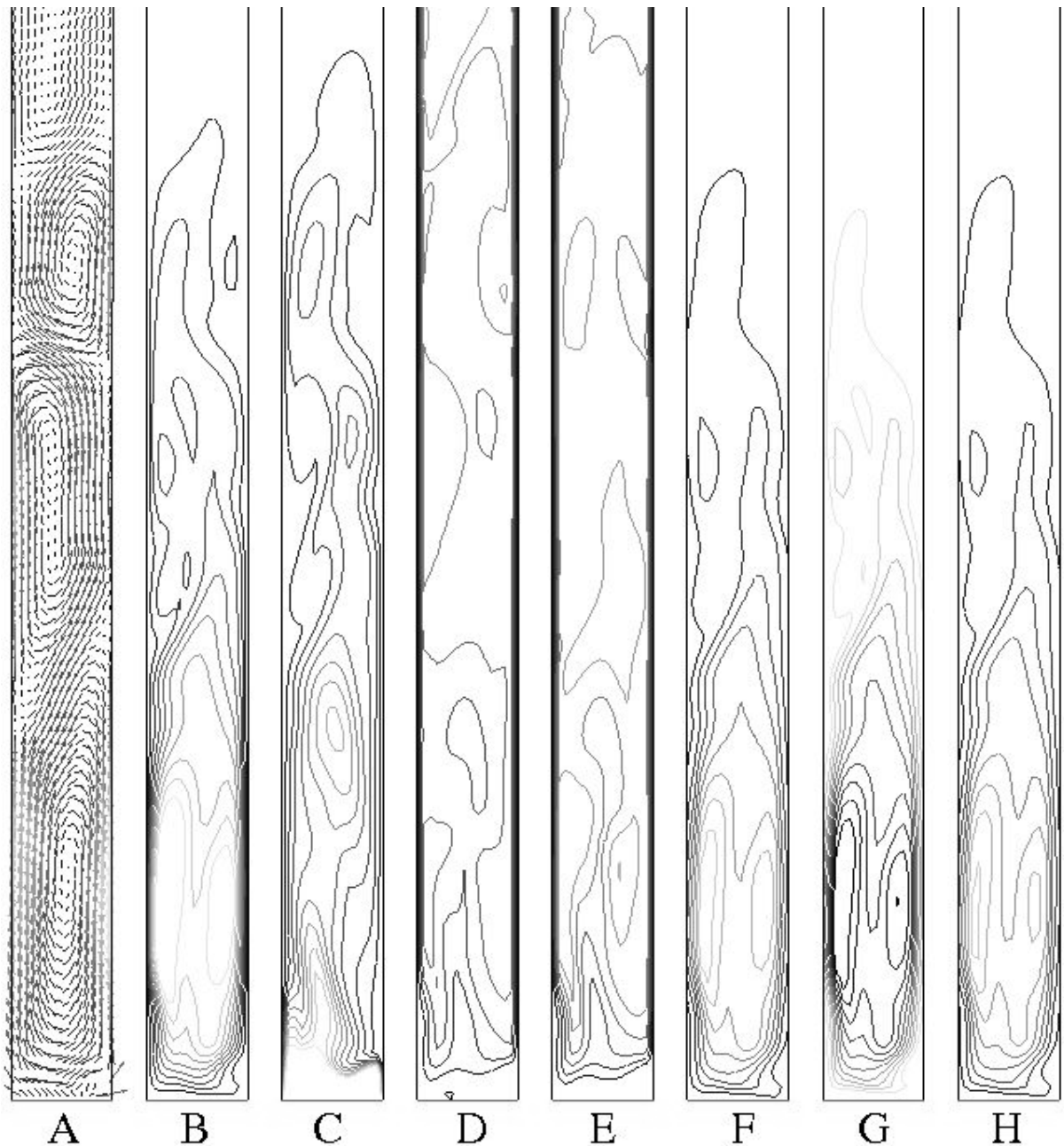


Figure 73: Bottom half of the fields for the gas-liquid-solid flow and reaction models in the 20:1 bubble column after 100 s, where  $\lambda=6.5 \cdot 10^{-5} \text{ s}^{-1}$ ;

A: Velocity vectors between 0 (small) and  $0.5 \text{ m s}^{-1}$  (large); B: Contours of the volume fraction of the solid phase (-) between 0 (black) and 0.025 (light grey); C: Contours of the volume fraction of the gas phase (-) between 0 (black) and 0.15 (light grey); D: Contours of the substrate concentration between 0 (black) and  $100 \text{ kg m}^{-3}$  (light grey); E: Contours of the product concentration between 0 (black) and  $2 \cdot 10^{-6} \text{ kg m}^{-3}$  (light grey); F: Contours of the cells grown between 0 (black) and  $2.5 \cdot 10^{-3} \text{ kg m}^{-3}$  (light grey); G: Contours of the substrate consumed between  $-1.5 \cdot 10^{-4}$  (black) and  $0 \text{ kg m}^{-3}$  (light grey); H: Contours of the product formed between 0 (black) and  $1 \cdot 10^{-4} \text{ kg m}^{-3}$  (light grey);



Figure 74: Top half of the fields for the gas-liquid-solid flow and reaction models in the 20:1 bubble column after 100 s, where  $\lambda=6.5 \cdot 10^{-5} \text{ s}^{-1}$ ;  
 A: Velocity vectors between 0 (small) and  $0.5 \text{ m s}^{-1}$  (large); B: Contours of the volume fraction of the solid phase (-) between 0 (black) and  $5 \cdot 10^{-3}$  (light grey); C: Contours of the volume fraction of the gas phase (-) between 0 (black) and 0.025 (light grey); D: Contours of the substrate concentration between 0 (black) and  $100 \text{ kg m}^{-3}$  (light grey); E: Contours of the product concentration between 0 (black) and  $1.5 \cdot 10^{-6} \text{ kg m}^{-3}$  (light grey); F: Contours of the cells grown between 0 (black) and  $5 \cdot 10^{-4} \text{ kg m}^{-3}$  (light grey); G: Contours of the substrate consumed between  $-1 \cdot 10^{-5}$  (black) and  $0 \text{ kg m}^{-3}$  (light grey); H: Contours of the product formed between 0 (black) and  $1.5 \cdot 10^{-5} \text{ kg m}^{-3}$  (light grey);

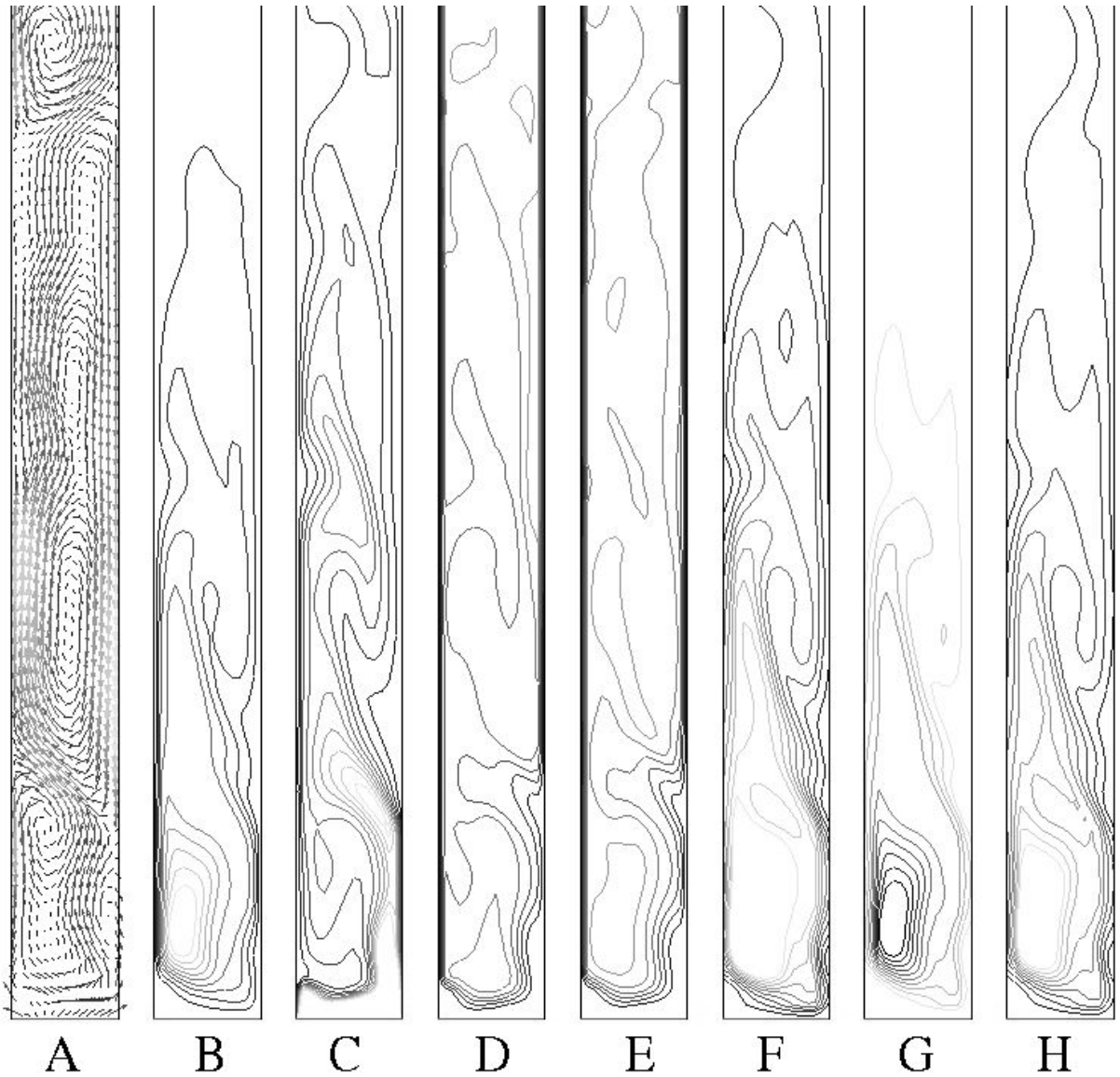


Figure 75: Bottom half of the fields for the gas-liquid-solid flow and reaction models in the 20:1 bubble column after 100 s, where  $\lambda=1.52 \cdot 10^{-4} \text{ s}^{-1}$ ;

A: Velocity vectors between 0 (small) and  $0.4 \text{ m s}^{-1}$  (large); B: Contours of the volume fraction of the solid phase (-) between 0 (black) and 0.05 (light grey); C: Contours of the volume fraction of the gas phase (-) between 0 (black) and 0.15 (light grey); D: Contours of the substrate concentration between 0 (black) and  $100 \text{ kg m}^{-3}$  (light grey); E: Contours of the product concentration between 0 (black) and  $1 \cdot 10^{-5} \text{ kg m}^{-3}$  (light grey); F: Contours of the cells grown between 0 (black) and  $5 \cdot 10^{-3} \text{ kg m}^{-3}$  (light grey); G: Contours of the substrate consumed between  $-5 \cdot 10^{-4}$  (black) and  $0 \text{ kg m}^{-3}$  (light grey); H: Contours of the product formed between 0 (black) and  $5 \cdot 10^{-4} \text{ kg m}^{-3}$  (light grey);

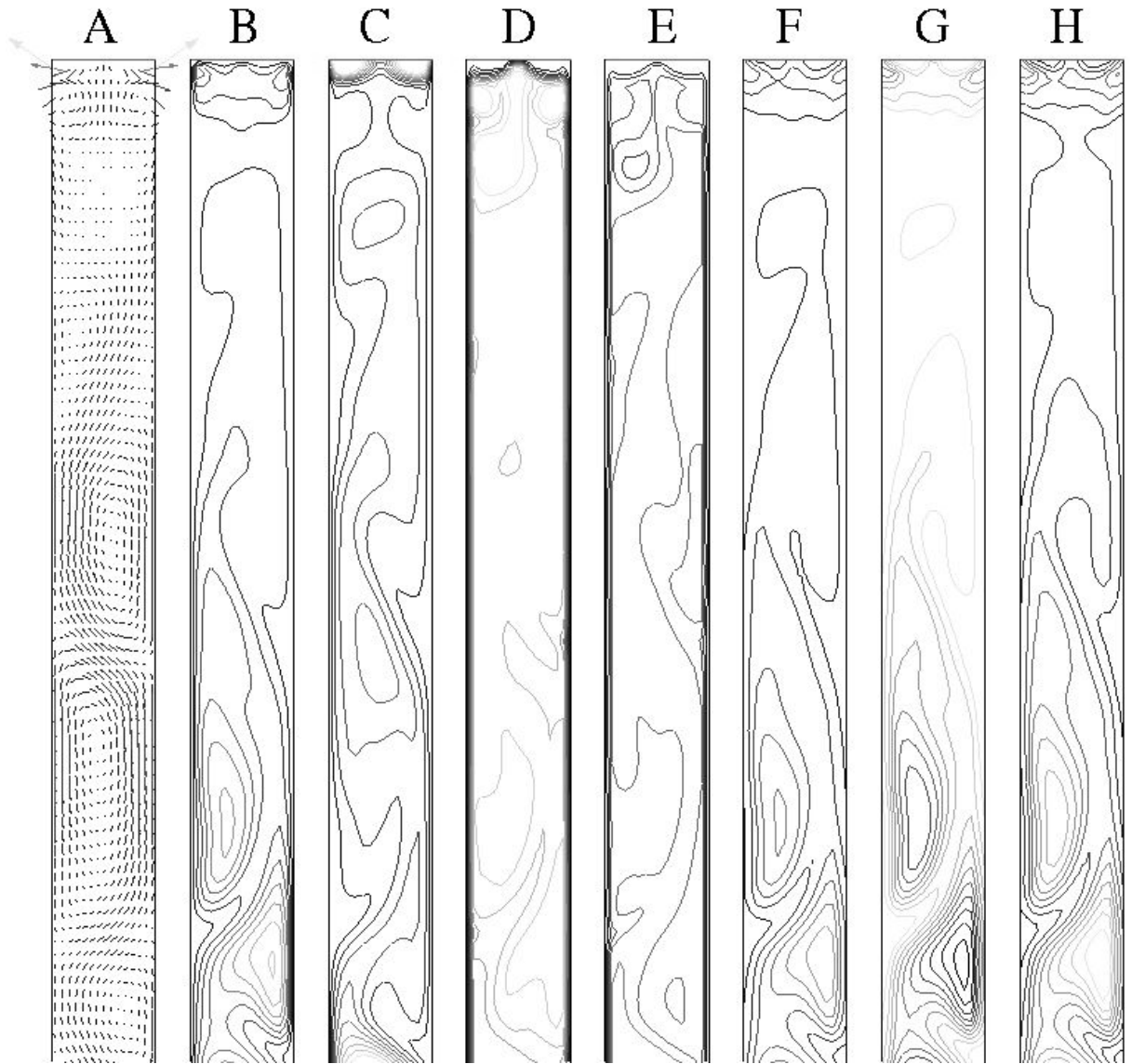


Figure 76: Top half of the fields for the gas-liquid-solid flow and reaction models in the 20:1 bubble column after 100 s, where  $\lambda=1.52 \cdot 10^{-4} \text{ s}^{-1}$ ;

A: Velocity vectors between 0 (small) and  $0.4 \text{ m s}^{-1}$  (large); B: Contours of the volume fraction of the solid phase (-) between 0 (black) and  $5 \cdot 10^{-3}$  (light grey); C: Contours of the volume fraction of the gas phase (-) between 0 (black) and 0.05 (light grey); D: Contours of the substrate concentration between 0 (black) and  $100 \text{ kg m}^{-3}$  (light grey); E: Contours of the product concentration between 0 (black) and  $1 \cdot 10^{-5} \text{ kg m}^{-3}$  (light grey); F: Contours of the cells grown between 0 (black) and  $5 \cdot 10^{-4} \text{ kg m}^{-3}$  (light grey); G: Contours of the substrate consumed between  $-4 \cdot 10^{-5}$  (black) and  $0 \text{ kg m}^{-3}$  (light grey); H: Contours of the product formed between 0 (black) and  $5 \cdot 10^{-5} \text{ kg m}^{-3}$  (light grey);